

Quasi-static cyclic tests on different types of masonry spandrels

Katrin Beyer
Ahmad Abo-El-Ezz
Alessandro Dazio

Institute of Structural Engineering
Swiss Federal Institute of Technology

Zürich
September 2010

Preface

Unreinforced masonry (URM) is a popular construction material since thousands of years and today the vast majority of dwellings worldwide is built using URM in one of its different types. Over and over again, earthquakes have induced significant damage to many URM structures claiming countless lives. However, during the same earthquakes other URM structures were able to survive even intense shaking suggesting that through appropriate conceptual design, constructive detailing and quality of the materials it is possible to build safe masonry structures even in earthquake prone regions featuring an important seismicity. Yet, this need for an engineering approach has been neglected for a long time due to the traditional vernacular character of masonry. As a consequence scientific research in this field was long not so popular compared to more mainstream fields like reinforced concrete or steel construction, leading to a lag that urgently needs to be closed.

Recognising the importance of horizontal structural elements (spandrels) connecting vertical piers to the seismic behaviour of URM walls, and considering the scarcity of information regarding their inelastic cyclic performance, nine full-scale quasi-static tests on spandrels have been designed and carried out. This report presents extensively the results of the five composite spandrels typical of modern buildings and of the four masonry spandrels typical of buildings stemming from the end of the nineteenth century. The tests reproduced failure mechanisms observed during real earthquakes and shall provide sound experimental evidence for the development and calibration of much needed reliable mechanical models describing the behaviour of spandrels under seismic action.

Minusio, September 2010

Alessandro Dazio

Summary

In unreinforced masonry (URM) walls the vertical piers are connected by horizontal spandrel elements. Numerical simulations have shown that spandrels influence significantly the global wall behaviour under seismic loading. Despite their importance, experimental data on the cyclic behaviour of these spandrels is very scarce. For this reason a research programme was initiated in which the cyclic behaviour of masonry spandrels was investigated experimentally and numerically. Within this programme different configurations of masonry spandrels were tested under quasi-static monotonic and cyclic loading. The spandrel configurations that were investigated included pure masonry spandrels and masonry spandrels which also comprised a reinforced concrete (RC) beam or slab ("composite spandrels"). The latter represent spandrels in newer masonry buildings with RC slabs or RC ring beams while the former can be found in older brick masonry buildings. This report presents the results of quasi-static tests on five full-scale composite and four masonry spandrels.

The five composite spandrels consisted of a RC beam and a masonry spandrel. The parameters investigated were: (i) the loading history (monotonic / cyclic), (ii) the brick type and (iii) the longitudinal reinforcement content of the RC beam. Comparison of the spandrel shear force-deformation curves obtained from the monotonic and cyclic tests showed that the monotonic tests envelopes the cyclic test rather well. The two brick types investigated differed concerning the web layout of the bricks. While brick type 1 had staggered webs, the webs of brick type 2 were continuous. The brick type had a considerable influence on the crack pattern of the masonry spandrel but only relatively little influence on the force-deformation curve of the spandrel. Cyclic tests were performed on three test units with different longitudinal reinforcement content of the RC beam. The longitudinal reinforcement content strongly influenced the force-deformation characteristics of the spandrel including the failure mode. The latter ranged from flexural failure of the plastic hinges in the RC beam to shear failure of the RC beam. At the point of failure of the RC beam the damage state of the masonry spandrel varied significantly between the test units. Over the entire test series the masonry spandrel affected significantly the load bearing mechanism of the composite spandrels. For this reason the masonry spandrel should not be neglected when striving for a realistic hysteretic model of the composite spandrels.

The four masonry spandrels were all subjected to quasi-static cyclic loading and comprised two different spandrel configurations. The first configuration consisted of a masonry spandrel with a timber lintel and the second configuration of a masonry spandrel on a shallow masonry arch. For each configuration two specimens were tested. The first was tested with a constant axial load in the spandrel while for the second specimen the axial load in the spandrel depended on the axial elongation of the spandrel. The failure mechanisms that were obtained for the four test units corresponded well to those observed for spandrels after recent seismic events. One spandrel failed in flexure, two in shear and one featured a mixed shear-flexural failure mode. In general, spandrels

with small axial loads were prone to flexural failure and spandrels with large axial loads prone to shear failure.

The lack of experimental data prevented in the past the validation of numerical and mechanical models regarding the cyclic behaviour of masonry spandrels. The nine tests on full-scale spandrel elements represent a contribution towards filling this gap and allow a further development of spandrel models, which will eventually lead to a more rational design and assessment of URM buildings.

Zusammenfassung

In unbewehrten Mauerwerksfassaden sind vertikale Wände mit horizontalen Riegeln verbunden. Numerische Berechnungen haben gezeigt, dass die Mauerwerksriegel einen grossen Einfluss auf das globale Kraft-Verformungsverhalten der Mauerwerksfassade unter Erdbebenbelastung haben. Trotz ihrer Wichtigkeit gibt es praktisch keine Versuche zum Kraft-Verformungsverhalten von Mauerwerksriegeln. Aus diesem Grund wurde ein Forschungsprogramm initiiert, in welchem das zyklische Verhalten von Mauerwerksriegeln experimentell und numerisch untersucht wurde. Im Rahmen dieses Programms wurden verschiedene Konfigurationen von Mauerwerksriegeln unter quasi-statisch monotonischer und zyklischer Last getestet. Die Riegelkonfigurationen, die getestet wurden, waren reine Mauerwerksriegel und Mauerwerksriegel, die auch einen Stahlbetonbalken oder Streifen einer Stahlbetondecke umfassten (zusammengesetzte oder "composite" Riegel). Letzterer Riegeltyp ist repräsentativ für neuere Gebäude mit Stahlbetondecke oder Stahlbetonringbalken während reine Mauerwerksriegel in älteren Gebäuden anzutreffen sind. Dieser Bericht präsentiert die Ergebnisse von fünf quasi-statischen Versuchen an zusammengesetzten Riegeln und vier Versuchen an Mauerwerksriegeln.

Die fünf zusammengesetzten Riegel bestanden je aus einem Stahlbetonbalken und einem Mauerwerksriegel. Die Parameter, die mittels der fünf Versuche untersucht wurden, waren: (i) die Belastungsgeschichte (monoton / zyklisch), (ii) die Backstein-Typen, und (iii) der Längsbewehrungsgehalt des Stahlbetonbalkens. Der Vergleich der Kraft-Verformungskurve, von zwei identischen Riegeln, von denen einer unter monotoner und einer unter zyklischer Belastung getestet worden war, zeigt, dass die monotone Kurve sehr gut mit der Umhüllenden des zyklischen Tests übereinstimmt. Die zwei Backstein-Typen, die untersucht wurden, unterschieden sich hinsichtlich der Form der inneren Stege. Während Backstein-Typ 1 versetzte innere Stege hatte, waren die inneren Stege von Backstein-Typ 2 durchgehend. Der Backstein-Typ hatte einen grossen Einfluss auf das Rissebild des Mauerwerksriegels, jedoch nur einen beschränkten Einfluss auf die Kraft-Verformungskurve des Riegels. Drei Riegel mit unterschiedlichem Längsbewehrungsgehalt des Stahlbetonbalkens wurden unter quasi-statisch zyklischer Last geprüft. Der Längsbewehrungsgehalt hatte einen grossen Einfluss auf die Kraft-Verformungshysterese und den Versagensmechanismus. Beobachtete Versagensmechanismen waren Schub- und Biegemechanismen des Stahlbetonbalkens. Zum Versagenszeitpunkt des Stahlbetonbalkens unterschied sich der Schadensgrad des Mauerwerksriegels sehr stark zwischen den verschiedenen Versuchskörpern. Bei allen getesteten Riegelemente hatte der Mauerwerksriegel einen grossen Einfluss auf den Kraftfluss im zusammengesetzten Riegel. Aus diesem Grund sollte der Mauerwerksriegel nicht vernachlässigt werden, wenn ein realistisches hysteretisches Modell des zusammengesetzten Riegels angestrebt wird.

Die vier Mauerwerksriegel wurden alle unter quasi-statisch zyklischer Last geprüft und umfassten zwei unterschiedliche Riegelkonfigurationen. Die erste Konfiguration bestand aus einem Mauerwerksriegel auf Holzbalken, die die Riegelspannweite überbrückten, und die zweite Kon-

figuration aus einem Mauerwerksriegel auf einem flachen Mauerwerksbogen. Für jede Konfiguration wurden zwei Versuchskörper gebaut und getestet. Der erste Versuchskörper wurde mit einer konstanten Axialkraft im Riegel getestet während beim zweiten Versuchskörper die Axialkraft von der axialen Verlängerung des Versuchskörpers abhing. Die Versagensmechanismen der vier Versuchskörper stimmten gut mit denen überein, die nach Erdbeben in Schadensgebieten beobachtet wurden. Ein Mauerwerksriegel versagte auf Schub, zwei zeigten einen gemischten Biege-Schub-Versagensmechanismus und einer einen Biegemechanismus. Im Allgemeinen waren Mauerwerksriegel mit kleinen Axialkräften anfällig für Biegeversagen während Mauerwerksriegel mit grösseren Axialkräften eher auf Schub versagten.

Das Fehlen von Versuchen an zusammengesetzten Riegeln und Mauerwerksriegeln verunmöglichte in der Vergangenheit die Validierung von numerischen und mechanischen Modellen für das zyklische Verhalten der Riegel. Die neun Versuche an voll-massstäblichen Riegelementen sind ein Beitrag, um diese Lücke zu schliessen, und ermöglichen eine Weiterentwicklung der Riegelmodelle, welche schlussendlich zu einem rationaleren Entwurf und einer weniger konservativen Erdbebenbemessung bzw. -überprüfung von unbewehrten Mauerwerksbauten führen wird.

Contents

Preface	i
Summary	ii
Zusammenfassung	v
Table of contents	vii
I. Overview	1
1. Introduction	3
1.1. Problem statement	3
1.2. Different types of spandrels	4
1.3. Damage to spandrels during earthquakes	6
1.4. Objectives and scope of the test programme	7
1.5. Outline of the test report	10
2. Test programme	11
2.1. Tests on composite spandrels	11
2.2. Tests on masonry spandrels	13
3. Summary of test results	15
3.1. Test results for composite spandrels	15
3.2. Test results for masonry spandrels	17
4. Conclusions and outlook	23
Acknowledgments	28
Bibliography	29
II. Composite spandrels	31
1. Test units, test setup, instrumentation and testing procedure	33
1.1. Test units	33
1.1.1. Properties of test units	33
1.1.2. Construction of test units	35
1.2. Test setup	36
1.3. Instrumentation	39
1.3.1. Hard-wired channels	39

1.3.2.	Optical measurements	40
1.4.	Testing procedure	44
2.	Material tests for composite spandrels	49
2.1.	Reinforcement steel	49
2.1.1.	Testing procedure	50
2.1.2.	Test results	51
2.2.	Concrete	52
2.2.1.	Testing procedure	53
2.2.2.	Test results	53
2.3.	Mortar	54
2.3.1.	Testing procedure	55
2.3.2.	Test results	55
2.4.	Bricks	56
2.4.1.	Testing procedure	57
2.4.2.	Test results	59
2.5.	Compression tests on masonry wallettes	63
2.5.1.	Test setup, testing procedure and instrumentation	64
2.5.2.	Failure modes	67
2.5.3.	Test results	67
2.6.	Shear tests on masonry wallettes	75
2.6.1.	Test setup, testing procedure and instrumentation	75
2.6.2.	Failure modes	77
2.6.3.	Test results	78
3.	Test results for composite spandrels	81
3.1.	Definition of force and deformation quantities	81
3.2.	Composite spandrel TU1	85
3.2.1.	Test observations	85
3.2.2.	Test results	89
3.2.3.	Deformation plot	93
3.3.	Composite spandrel TU2	95
3.3.1.	Test observations	95
3.3.2.	Test results	98
3.3.3.	Deformation plots	101
3.4.	Composite spandrel TU3	104
3.4.1.	Test observations	104
3.4.2.	Test results	107
3.4.3.	Deformation plots	111
3.5.	Composite spandrel TU4	116
3.5.1.	Test observations	116
3.5.2.	Test results	121
3.5.3.	Deformation plots	129
3.6.	Composite spandrel TU5	132
3.6.1.	Test observations	132
3.6.2.	Test results	133
3.6.3.	Deformation plots	142

III. Masonry spandrels	143
1. Test units, test setup, instrumentation and testing procedure	145
1.1. Test units	145
1.1.1. Properties of test units	145
1.1.2. Construction of test units	148
1.1.3. True dimensions and constructive imperfections of test units	151
1.2. Test setup	153
1.3. Instrumentation	157
1.3.1. Hard-wired channels	157
1.3.2. Optical measurements	160
1.4. Testing procedure	164
2. Material tests for masonry spandrels	167
2.1. Mortar	167
2.1.1. Testing procedure	168
2.1.2. Test results	168
2.2. Bricks	169
2.2.1. Testing procedure	169
2.2.2. Test results	170
2.3. Compression tests on masonry wallettes	176
2.3.1. Test setup and testing procedure	176
2.3.2. Failure modes	177
2.3.3. Test results	177
2.4. Shear tests on masonry wallettes	182
2.4.1. Test setup and testing procedure	182
2.4.2. Failure modes	183
2.4.3. Test results	184
2.5. Threaded steel bars	188
2.5.1. Testing procedure	188
2.5.2. Test results	189
2.6. Timber	190
2.6.1. Test setup and testing procedure	191
2.6.2. Failure modes	192
2.6.3. Test results	193
3. Test results for masonry spandrels	197
3.1. Definition of force and deformation quantities	197
3.2. Masonry spandrel TUA	200
3.2.1. Specific test setup	200
3.2.2. Test observations	201
3.2.3. Test results	206
3.2.4. Deformation plots	213
3.3. Masonry spandrel TUB	216
3.3.1. Specific test setup	216
3.3.2. Test observations	216
3.3.3. Test results	219
3.3.4. Deformation plots	225

3.4. Masonry spandrel TUC	228
3.4.1. Specific test setup	228
3.4.2. Test observations	228
3.4.3. Test results	233
3.4.4. Deformation plots	235
3.5. Masonry spandrel TUD	240
3.5.1. Specific test setup	240
3.5.2. Test observations	240
3.5.3. Test results	245
3.5.4. Deformation plots	247

Part I.

Overview

1 Introduction

1.1 Problem statement

Most of the design approaches for unreinforced masonry (URM) structures in today's design codes are rather conservative. For example, most design approaches neglect the framing action due to the horizontal spandrel elements and consider only the vertical pier elements when calculating the strength and stiffness of a URM wall. Numerical simulations have, however, shown that the spandrel elements influence significantly the force-deformation characteristics of a URM wall. An example of such a calculation is shown in Fig. 1.1. A three-storey URM wall consisting of three piers was analysed. The piers were interconnected by spandrels that consisted of a reinforced concrete (RC) beam and masonry spandrels. The RC beam can represent either a RC ring beam as it is, for example, present in many Italian URM houses or a strip of a RC slab. In a first analysis the coupling action of the spandrels was neglected while in a second analysis the coupling action of the horizontal elements was considered. The analyses were conducted using the finite element program "Atena" [Cer07]. This program was chosen since it includes very advanced material models for concrete and reinforcing steel. In addition, in Atena masonry can be modelled by means of a simple heterogenous micro model where each brick is modelled as an elastic unit and the mortar joints are represented by contact elements with a Mohr-Coulomb friction constitutive law [Loe05]. More information on this analysis can be found in [BAD10]. Figure 1.1b compares the pushover curve of the URM wall in Fig. 1.1a to the pushover curve of three uncoupled piers, i.e. the curve when the coupling action of the spandrel elements is neglected. The figure shows that the spandrel elements have a significant influence on the initial stiffness as well as on the resistance of the URM wall. It seems therefore desirable to include the spandrel elements when analysing the URM wall. Over the past decades the seismic action defined in the Swiss design codes has steadily increased. For this reason and as a consequence of the conservative design approach – despite the moderate seismicity of Switzerland – it is today virtually impossible to design URM buildings for seismic loading or to verify the seismic safety of existing URM buildings. This applies to some extent even to zones of low seismicity with design peak ground accelerations of 10% g and less.

A major reason why spandrel elements are not considered in the design of URM structures is the lack of experimental evidence for the behaviour of masonry spandrels under seismic loading. Without experimental data, numerical and mechanical models, which are required for the realistic design of new and the assessment of old buildings, cannot be calibrated. The wide range of different types of spandrels that are present in old and new URM structures renders the problem for the engineer even more difficult. To structure the problem, the next section gives an overview on different types of spandrels.

1. Introduction

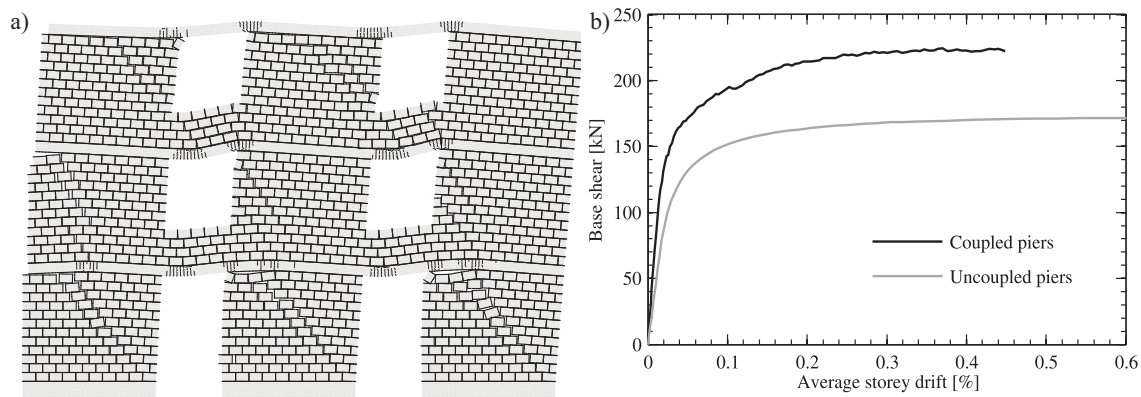


Figure 1.1: Deformed shape of the URM wall at an average storey drift of $\theta = 0.4\%$ (a, displacements are magnified by a factor of 20) and pushover curve of the URM wall in comparison to the pushover curve of uncoupled piers (b).

1.2 Different types of spandrels

Different types of spandrels have been used in the past to bridge window and door openings in URM buildings. This section gives a broad classification of the spandrels in URM buildings. Note that only brick masonry is considered here. Other types of masonry, such as for example stone masonry, is not included in this study. The examples of spandrel types given in this section are all drawn from countries within Europe. It is, however, believed, that brick construction in other areas of the world features very similar spandrel types. Three different classes of spandrels in URM construction were identified:

- Masonry spandrels with a masonry arch bridging the opening.
- Masonry spandrels with lintels where the lintels can be stone, timber, steel or RC lintels.
- Spandrels consisting of a RC beam or a RC slab alone.
- Spandrels consisting of a RC beam or a RC slab and a masonry spandrel (“composite spandrels”).

Masonry arches were often used in buildings of exposed brickwork since they are more ornamental than lintels. An example of such a building is shown in Fig. 1.2. It is an old storehouse in the city centre of Copenhagen.

One of the oldest types of lintels that has been used in masonry construction is the timber lintel. Figure 1.3 shows a building in the city centre of Basel (Switzerland) at the shore of the river Rhine, which was refurbished at the time of the visit (building behind scaffolding in Fig. 1.3a). The building was constructed around 1300 and modified over the centuries. For this reason the construction material is very inhomogenous ranging from rubble masonry over stone masonry to brick masonry. In particular the walls of the lower storeys are very thick. Figure 1.3b shows a lintel in one of these storeys. It is a timber lintel made of several timber beams, which are laid next to each other to cover the entire width of the wall. The support length on either side of the opening depends on the width of the opening but varies typically between 10 and 20 cm. This is a very typical way of constructing a timber lintel, which has been observed in several old buildings.



Figure 1.2: Old URM masonry house with masonry arches in the city centre of Copenhagen (Denmark): Entire building (a) and arches bridging the window openings (b).

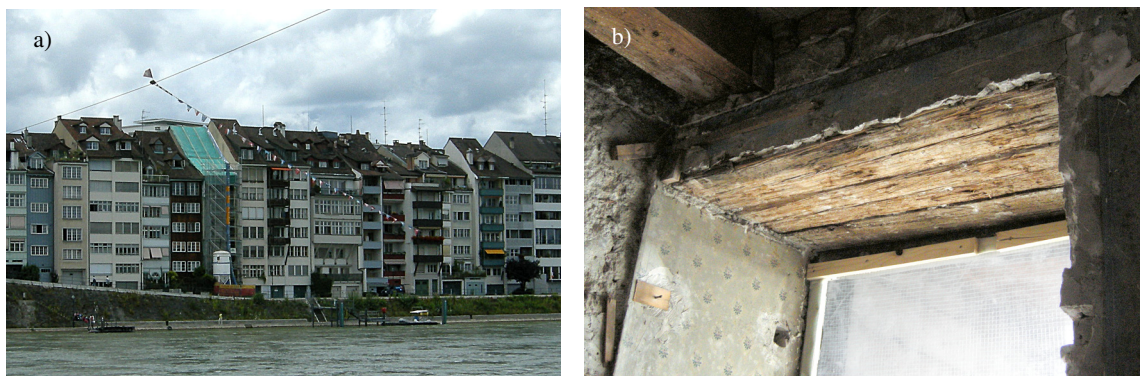


Figure 1.3: Old URM masonry house with timber lintel in Basel (Switzerland): Entire building (a) and lintel detail (b).

In more modern URM buildings timber lintels have been often replaced by RC lintels. An example of such a construction is shown in Fig. 1.4. Modern large bricks with holes have been used for the construction of the masonry. The window openings are bridged by RC lintels. RC slabs are not visible and it is possible that either a timber slab or a Hourdis slab system was used for the construction of the floors. A type of lintel that is more modern than the RC lintel is the prestressed brick lintel developed by Stahlton AG. Stahlton AG is a company located in Zürich (Switzerland) founded in 1945¹. One of the first products of the company was the prestressed brick spandrel, which was filed as a patent in Switzerland. In the brick lintel, the brick serves as a lost formwork in which prestressed wires are embedded. The formwork is filled with concrete and upon hardening of the concrete the wires are released and finally cut. This type of spandrel has been used in many URM buildings in Switzerland after World War II.

Modern URM buildings feature RC or Hourdis slabs. In the latter case a RC ring beam is typically present at every storey and runs along the perimeter of the building. Both, RC slab and RC ring beam contribute to the resistance of the spandrel element. In very modern buildings window opening might reach over the entire storey height. In this case the masonry spandrel disappears and the spandrel element consists solely of the RC beam or slab (Fig. 1.5a). Where the

¹Telephone call with Mr. Curiger, Stahlton AG, 26th of June, 2009

1. Introduction

window opening is smaller, a masonry spandrel is located on top of the RC beam (Fig. 1.5b). In the following this type of spandrel is referred to as "composite spandrel".



Figure 1.4: URM building with RC lintel serving as a gravel plant in Alt St. Johann (Switzerland): Entire building (a) and lintel detail (b).

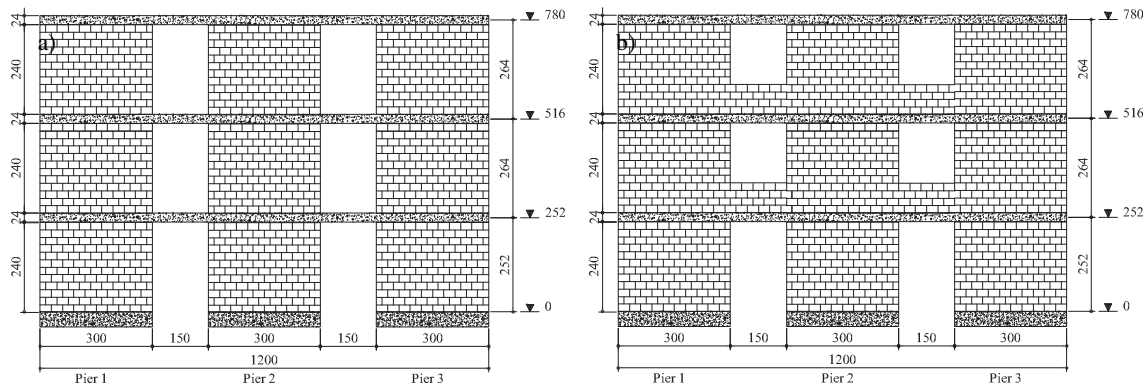


Figure 1.5: A modern URM building with spandrels consisting of a RC beam alone (a) and with composite spandrels (b).

1.3 Damage to spandrels during earthquakes

Spandrels have been subjected to extensive damage during earthquakes and are often the first elements within a URM building to crack or fail. In the following two types of failure modes of spandrels that were observed after the $M_w = 6.3$ earthquake in L'Aquila (Italy) on April 6th, 2009 are briefly discussed [DBB⁺09]. A typical failure mode of URM spandrels with masonry arches is shown in Fig. 1.6. It is a URM building in the city centre of L'Aquila. All the spandrels between window openings have failed in shear and show the characteristic X-crack pattern. The horizontal stiffness and strength of the building are therefore very much reduced. In this case the spandrels are heavily restrained by both the relatively wide piers as well as by tension ties running along the facade embedded in the masonry. When looking at the building from the side, it was possible to see the anchorage of those ties. The anchorage of the ties running perpendicular to the facade can be easily identified on Fig. 1.6a. A different example is shown in Fig. 1.7. This building stood also close to the city centre of L'Aquila. In this case tension ties were definitely not present. In addition the piers were very slender providing only a minor restraint to the axial elongation of

the spandrels. As a consequence the spandrels failed in flexure by means of wide vertical cracks at both ends of the spandrel. Due to out-of-plane accelerations one of the spandrels collapsed completely. This building was a complete loss and was pulled down after the earthquake. Only one building with composite spandrels was identified during the Swiss reconnaissance mission to L'Aquila [DBB⁺09]. It was a very small building and remained undamaged. For this reason damage to composite spandrels has not yet been observed by the authors.

1.4 Objectives and scope of the test programme

It is obviously impossible to test all existing spandrel configurations. Only selected configurations can be investigated by means of experimental methods. However, the test results can be used to verify the results of numerical models, which can then be used to analyse further spandrel configurations. Three types of spandrels were chosen to be tested. These were: (i) masonry spandrels with arches, (ii) masonry spandrels with timber lintels and (iii) composite spandrels. Masonry spandrels with other types of lintels were not tested since it was assumed that if a numerical or mechanical model is able to capture the behaviour of masonry spandrels with timber lintels, it is also likely to perform well for masonry spandrels with other types of lintels. A similar consideration concerned the spandrels consisting of a RC beam or a RC slab alone: For these types of spandrels it was assumed that models that work for composite spandrels will also work for the simpler spandrels with RC beam or RC slab alone. The test units were divided into two groups. In the first part of the test programme composite spandrels were tested, i.e. spandrels consisting of a RC beam and a masonry spandrel. In total five composite spandrels were tested, two of these were subjected to monotonic and three to cyclic loading. The investigated variables concerned the type of brick, the type of loading and the longitudinal reinforcement ratio of the RC beam. In the second part of the test programme four masonry spandrels were subjected to quasi-static cyclic loading. Two of these test units included a masonry spandrel and a timber lintel and the other two a masonry spandrel with a shallow masonry arch. Apart from the configuration of the spandrel the horizontal load, which partially restrained the elongation of the spandrel, was varied between the test units. Care was taken to design a test setup which imposed a demand on the spandrels which was as realistic as possible and which led for the masonry spandrels to the failure modes observed after the L'Aquila earthquake.

The objective of the research programme initiated at the ETH Zürich was to provide high-quality experimental evidence for the seismic behaviour of composite and masonry spandrels under in-plane loading. To do so, several full-scale test units of different types of spandrels were tested under quasi-static monotonic and cyclic loading. Apart from the forces, detailed measurements of global and local deformation quantities were taken using both hard-wired instruments and a new optical measurement system. The results of the experimental programme will be used to develop mechanical models for the load-bearing and deformation behaviour of spandrels in URM buildings as well as to refine the global analysis of URM walls. The final goal is to develop practice-oriented guidelines for the modelling of spandrels when performing pushover analyses of URM walls with and without reinforced concrete slabs. The results of the pushover analyses can be used to remove some of the conservatism of current force-based design approaches or they can form the basis for the displacement-based design of URM walls; the latter has the potential to lead to more rational and economic structures compared to force-based design.

1. Introduction



Figure 1.6: Shear failure of spandrels in an old URM building with masonry arches during the L'Aquila earthquake on April 6th, 2009: Entire building (a) and detail of a spandrel (b).



Figure 1.7: Flexural failure of spandrels in an old URM building with lintels during the L'Aquila earthquake on April 6th, 2009: Entire building (a) and detail of a spandrel (b).

1. Introduction

The results herein form a substantial basis of experimental evidence for composite and masonry spandrels. To the knowledge of the authors, further tests are currently underway in Italy at the University of Trieste [GCMN08] and at the EUCENTRE in Pavia. Research groups of these institutions investigate experimentally the behaviour of URM and stone masonry spandrels, respectively. A different test setup was used for these tests compared to the setup used for the tests at the ETH Zürich. They will therefore allow to make a first judgment concerning the repeatability of the tests and the sensitivity of the results concerning the chosen test setup.

1.5 Outline of the test report

This report summarises the results of the two series of spandrel tests that were conducted at the structural engineering laboratory of the ETH Zürich between February 2009 and January 2010. The report is organised in three parts. The first part gives an overview on the research initiative. Within this part this first chapter outlined the problem statement and the objectives of the research (Chapter 1). Chapter 2 gives an overview on the test programme while Chapter 3 includes a short summary of the test results. The findings of the test programme and an outlook on future research are given in Chapter 4. The other two parts are dedicated to the tests on composite spandrels and masonry spandrels, respectively. Both parts are structured in the same way and stand for their own, i.e. each of these parts is a complete test report in itself. It is therefore possible to consult, for example, only the part on masonry spandrels if the reader is only interested in the cyclic behaviour of these. Each of these two parts is divided into three chapters. The first chapter describes the test units, test setup, instrumentation and testing procedure, the second chapter summarises the results from the material tests that were conducted in parallel to the tests on the spandrel test units and the third chapter presents the test observations and test results from the quasi-static cyclic tests on the spandrel test units.

2 Test programme

The test programme comprised quasi-static tests of five composite spandrels and four masonry spandrels. The test units were full-scale models representing spandrels in modern structures with RC slabs or RC ring beams (composite spandrels) or structures constructed at approximately the beginning of the last century (masonry spandrels).

Each test unit consisted of two piers and the spandrel element. In the test stand (Fig. 2.1) the test unit stood on two stiff steel beams ("lever beams") that were supported on hinges at the centre line of the piers and connected to servo-hydraulic actuators at their ends. The support of the South lever beam allowed next to a rotation also a sliding movement in the direction of the beam. Hence, there was no axial restraint on the beam and for the composite spandrels the total axial force in the spandrel was zero during the entire time. For the masonry spandrels two horizontal rods introduced an axial force into the spandrel, which was either constant throughout the test (TUA and TUC) or depended on the axial elongation of the spandrel (TUB and TUD). Vertical rods that were tensioned by means of hollow core jacks applied a constant axial load to the two piers. During testing the two servo-hydraulic actuators were moved with the same velocity in opposite directions. As a result, the two horizontal lever beams rotated and the piers right and left to the spandrel were subjected to the same drifts, which caused the demand on the spandrel.

The two piers were post-tensioned by four vertical rods each. The forces in the rods were kept constant throughout the test. The purpose of these forces was to simulate the axial force in piers in real buildings. However, it should be noted that the piers of the test units were not subjected to realistic moment and shear demands. The goal of the test programme was not to test the piers but to test the spandrels. The function of the piers was to create realistic boundary conditions for the spandrel. Since the demand on the piers was not realistic, the piers were expected to remain largely undamaged during the test. The test units were subjected either to monotonic loading or to cyclic loading. The forces in the actuators and at the support as well as different global and local deformation quantities were measured during testing by means of hard-wired instruments. In addition, an optical measurement system was used to measure the coordinates of LEDs mounted on one face of the test units.

2.1 Tests on composite spandrels

Five composite spandrels were tested. The variables investigated concerned (i) the type of brick, (ii) the loading regime and (iii) the longitudinal reinforcement content of the RC beams. Two of the spandrels were subjected to monotonic loading (TU1 and TU2) and three to cyclic loading (TU3-5, Table 2.1). The difference between TU1 and TU2 concerned the type of masonry that was used. For the construction of TU1 bricks with staggered longitudinal webs and a mortar with a higher tensile strength were used. TU2-5 were constructed using bricks with continuous longitudinal

2. Test programme

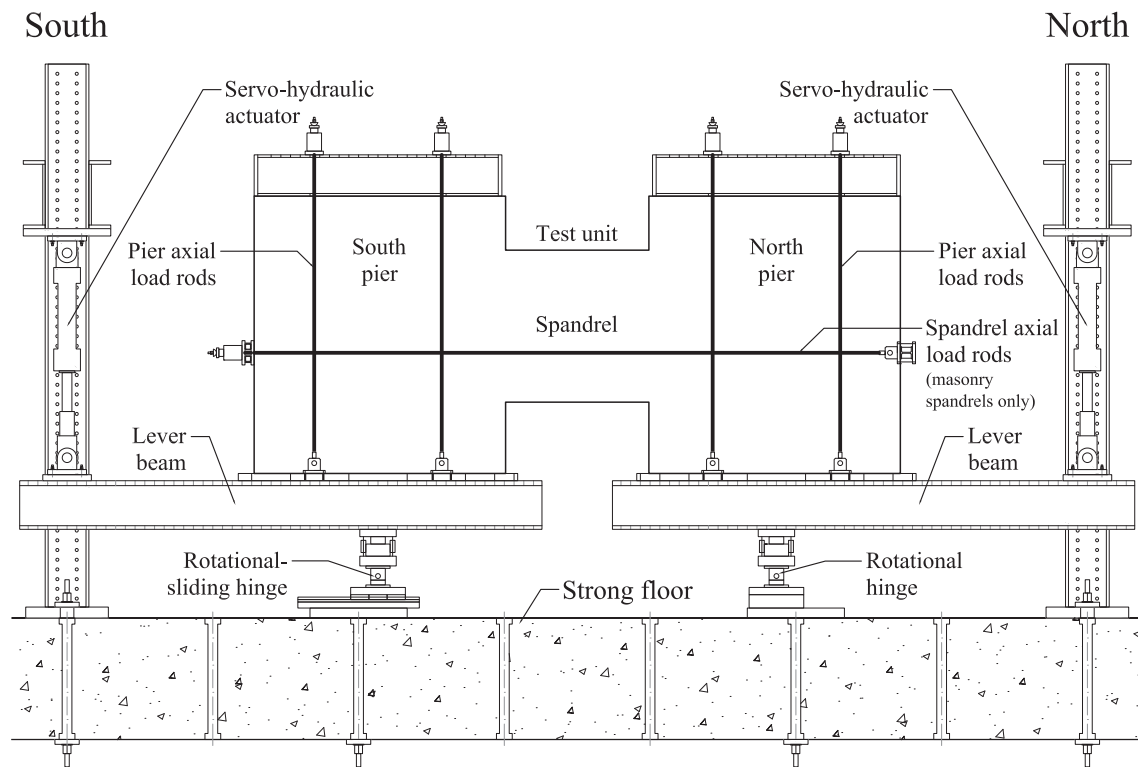
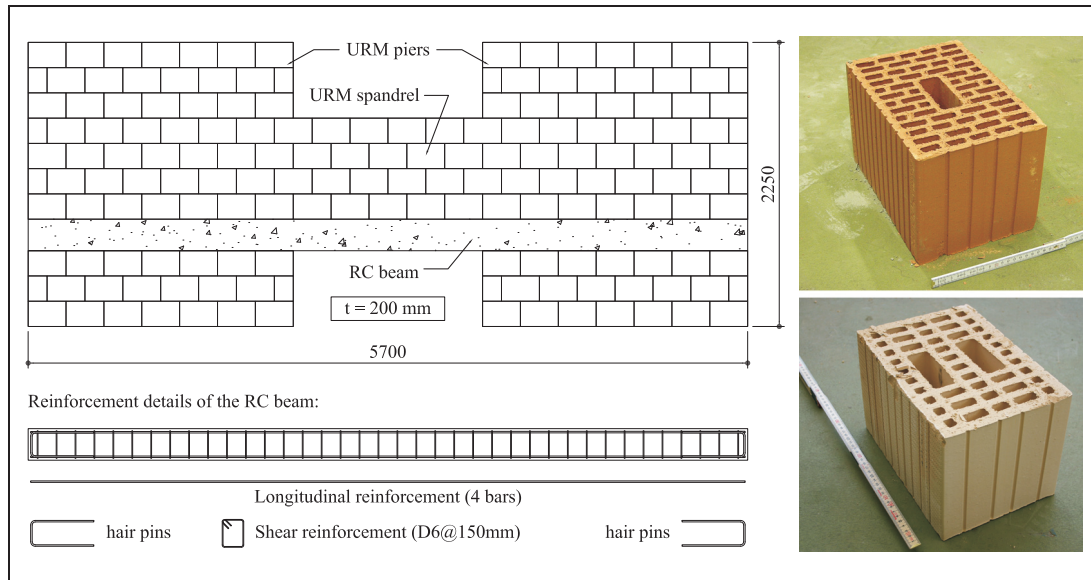


Figure 2.1: Test setup for spandrel tests.

webs and a mortar with a smaller tensile strength, the latter being one of the most commonly used mortars for masonry construction in Switzerland. While for ductile RC structural elements it is known that the force-deformation relationships obtained from a monotonic test corresponds well to the envelope of a cyclic test, this has not yet been shown for tests on spandrels. Such a comparison is important since many analysis and design approaches are based on pushover analysis results, i.e. the force-deformation relationship for monotonic loading. To investigate the difference between monotonic and cyclic behaviour experimentally, two – apart from the natural variations in material properties – identical test units were subjected to the two different loading regimes. These were TU2 (monotonic loading) and TU3 (cyclic loading). The final two test units were subjected to cyclic loading. The parameter variation concerned the longitudinal reinforcement content of the RC beams. The RC beams of TU1-3 had a longitudinal reinforcement of 4D12 mm bars. The RC beam of TU4 had a longitudinal reinforcement which was almost twice as large (4D16 mm) while TU5 had a smaller longitudinal reinforcement (4D10 mm). TU4 satisfied the minimum requirements for a RC ring beam according to the Italian seismic design code [OPC03]; only the shear reinforcement was with D6 mm hoops every 150 mm larger than the required D6 mm hoops every 250 mm. According to the European seismic design code EC8 [CEN04] a ring beam has to be fitted with a minimum longitudinal reinforcement area of 2 cm^2 , which is considerably smaller than the reinforcement area of TU1-4. For this reason a fifth beam was tested with a smaller longitudinal reinforcement area (TU5). Note that EC8 makes no specifications concerning the minimum shear reinforcement content.

Table 2.1: Composite spandrels: Loading scheme, reinforcement and brick details for the five test units.



Test unit	Loading	Longit. reinf. of RC beam	Shear reinf. of RC beam	Axial stress in piers	Brick dimensions and type
TU1	Monotonic	4 D12 mm (4.52 cm ²)	D6 s = 150 mm	0.4 MPa	290x200x190 mm Staggered webs
TU2	Monotonic	4 D12 mm (4.52 cm ²)	D6 s = 150 mm	0.4 MPa	290x200x190 mm Continuous webs
TU3	Cyclic	4 D12 mm (4.52 cm ²)	D6 s = 150 mm	0.4 MPa	290x200x190 mm Continuous webs
TU4	Cyclic	4 D16 mm (8.04 cm ²)	D6 s = 150 mm	0.4 MPa (0.6 MPa) ¹⁾	290x200x190 mm Continuous webs
TU5	Cyclic	4 D10 mm (3.14 cm ²)	D6 s = 150 mm	0.4 MPa	290x200x190 mm Continuous webs

¹⁾ Axial stress in piers was increased for the final cycles.

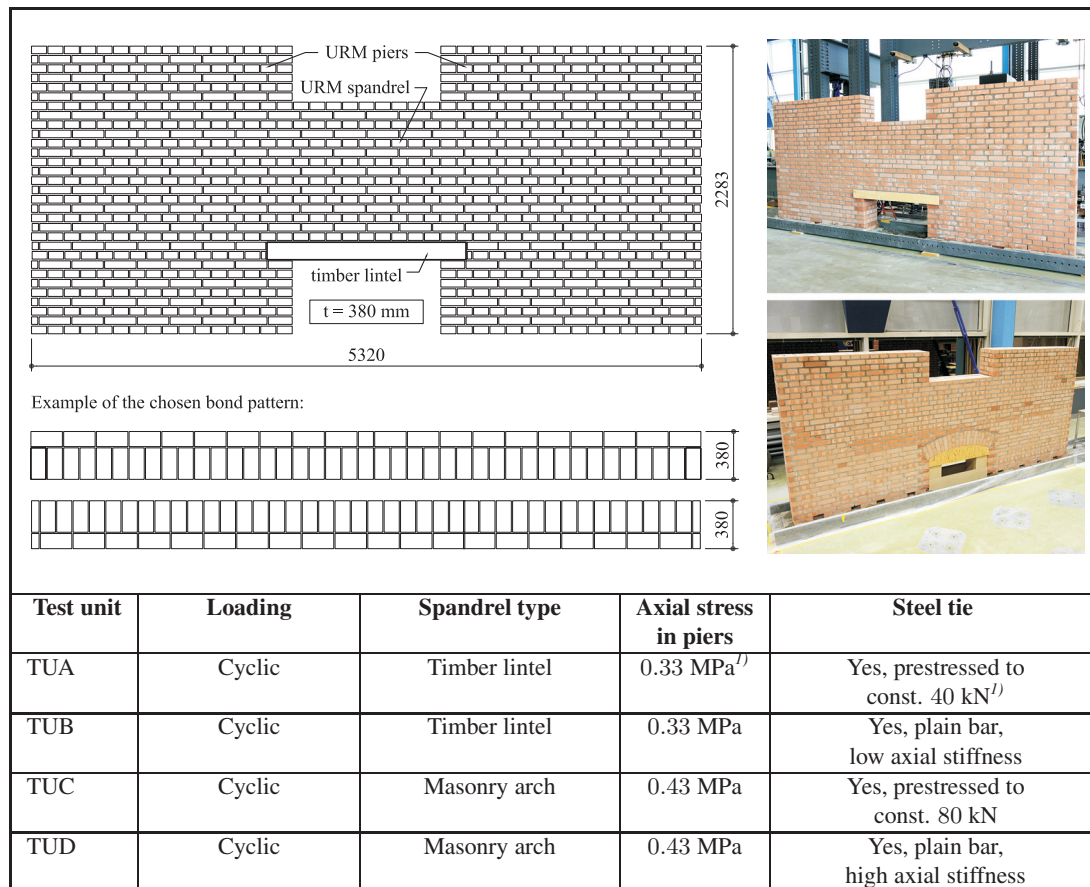
2.2 Tests on masonry spandrels

Four masonry spandrels were tested. They were constructed with full bricks with dimensions of 250x120x60 mm. All spandrels were subjected to cyclic loading. The investigated variables concerned (i) the type of the spandrel and (ii) the axial load applied to the spandrel (Table 2.2). The two types of spandrel investigated were a masonry spandrel with a timber lintel and a masonry spandrel with a shallow arch. As outlined at the beginning of this chapter, the test stand did not provide an axial restraint to the spandrel. An axial load was applied to the masonry spandrel to simulate the restraining action of the framing piers and the axial force created by a steel tie, which is often present in older URM buildings. In the tests the axial force in the spandrel was either constant throughout the test (TUA and TUC) or depended on the axial elongation of the spandrel (TUB and TUD). The latter is a more realistic scenario while the former is easier to model in numerical simulations of the tests. Note that the axial loads to which the piers were subjected were also varied between the tests. They were increased when testing TUA and were further augmented for TUC and TUD. This was done to ensure that even for greater axial spandrel forces, which caused an increase in spandrel capacity, the piers remained largely undamaged. The

2. Test programme

constant axial forces in the spandrels to which TUA and TUC were subjected differed by a factor of two. The axial restraint systems of the spandrels of TUB and TUD had also different stiffnesses. In a more extensive test programme it would have been desirable to change only a single variable at the time. However, due to time constraints it was only possible to test four test units. The objective was therefore to test a wide variety of configurations leading to failure mechanisms of the spandrels that were similar to those observed after the earthquake in L'Aquila (see Section 1.3).

Table 2.2: Masonry spandrels: Loading scheme, spandrel type and details of the axial load application for the four test units.



¹⁾ Final configuration. At the beginning of the test the following two different configurations of axial stress in the piers and axial force applied to the spandrel were investigated: $\sigma = 0.18$ MPa, $H = 80$ kN and $\sigma = 0.33$ MPa, $H = 80$ kN before the test was continued with the final configuration.

3 Summary of test results

3.1 Test results for composite spandrels

The general behaviour of a composite spandrel observed for a positive rotation demand on the piers is depicted in Fig. 3.1: A compression diagonal reached from the South end of the spandrel into the spandrel. The compression diagonal was supported by the RC beam, which was subjected to positive bending at this position. Hence, the positive plastic hinge in the RC beam formed not at the South end of the spandrel but within the span of the spandrel. The negative plastic hinge in the RC beam, on the contrary, formed at the North end of the spandrel. A further difference of the two plastic hinges concerned their length: While the North (negative) plastic hinge was rather short the South (positive) plastic hinge was typically spread over a longer part of the RC beam. This general behaviour of the RC beam applied to all five test units for small rotation demands and it agrees well with the numerical results presented in Fig. 1.1 of Section 1.1. Due to friction in the joints of the masonry spandrel, the masonry contributed to some extent to the shear capacity of the spandrel. In the following the particularities of the five test units are outlined and compared.

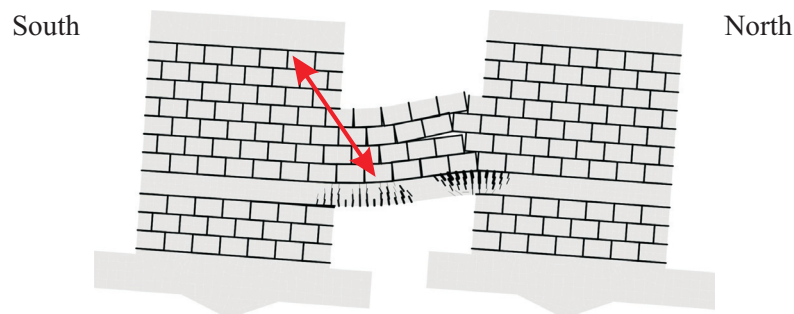


Figure 3.1: Schematic load bearing mechanism of a composite test unit when the piers are subjected to a positive rotation demand.

Out of the five composite spandrels, TU1 showed a very different crack pattern than the others: The masonry spandrel of TU1 showed very pronounced vertical cracks at both ends of the spandrel which extended over the entire height of the spandrel and ran almost straight through bricks (Fig. 3.2a). The body of the masonry spandrel remained virtually undamaged and all the deformation demand on the masonry spandrel was absorbed in the two flexural cracks. At the South end of the spandrel the compression strut reaching into the spandrel (the spandrel was subjected to monotonic loading towards North only) caused crushing of the bricks. Crushing commenced in the top rows of the spandrel. Due to the crushing, the compression diagonal moved to the South leading to crushing of the bricks located below the top row. Eventually, a vertical column about half a brick wide failed. Very early during the test the masonry spandrel separated from the RC beam beneath. Plastic hinges formed at both ends of the beam leading eventually to failure due to rupture of longitudinal reinforcing bars. The difference in behaviour of TU1 from the other

3. Summary of test results

composite test units is due to the different type of masonry used for construction. The bricks had staggered longitudinal internal webs and therefore the shear and tensile strength of these bricks was considerably smaller than that of the bricks with continuous webs, which were used for TU2-5. In addition, the mortar used for the construction of TU1 had a larger tensile strength leading to failure of the bricks rather than the joints.

The crack pattern of the masonry spandrel of TU2 at failure was characterised by two major stair-stepped cracks (Fig. 3.2b). At the beginning of the test, the bricks of TU2 remained largely undamaged and the cracks followed the joints. As the deformation demand increased, crushing of the compression diagonal took place leading to a Southward shift of the positive plastic hinge. The final failure of the test unit was caused by the rupture of longitudinal bars in both the negative and the positive plastic hinge. Although TU1 and TU2 had different masonry properties and exhibited a different masonry behaviour, the force-rotation relationships of TU1 and TU2 were very similar (Fig. 3.2f). For both test units, the initial elastic phase was followed by a zacky branch, which was associated with the formation of cracks in the masonry spandrel and the RC beam. The onset of yielding in the longitudinal reinforcement of the RC beam caused the force-rotation curve to round off. It stayed level for a small range of rotations and began then to drop. This reduction in capacity starting at a rotation of 1 to 1.5% was associated with the crushing of the compression diagonal.

TU3 was the first test unit subjected to cyclic loading. It showed a very stable cyclic behaviour up to a drift of 1.5% (Fig. 3.2f). Afterwards, the capacity of the test unit decreased. This reduction in capacity was again associated with the crushing of the compression diagonals in the masonry spandrel. TU3 failed within the first cycle at a rotation demand of 3% due to shear failure of the RC beam (Fig. 3.2c). On the whole, the envelope of TU3 corresponded very well to the force-deformation relationship of TU2, which had identical properties but had been subjected to monotonic loading. Up to a drift of 1.5% the peak capacities of TU3 exceeded even the curve of TU2. This is most likely due to the slightly larger mortar strength of TU3. TU2 and TU3 were built at the same time. Since TU2 was tested first, the mortar strength at the day of testing was less than the mortar strength of TU3 at the day of testing. For drift demands larger than 1.5% the reduction in capacity was stronger for TU3 than for TU2. It is believed that the cyclic behaviour led to a faster degradation of the compression strut and therefore to a stronger reduction in capacity. The cyclic behaviour also led to a larger growth in length of the RC beam since the plastic strain in the longitudinal reinforcing bars accumulated. As a consequence, at the same drift demand, the crack widths in the RC beam were larger for TU3 than for TU2. The shear reinforcement in the RC beam was not sufficient to carry the entire shear force of the beam. As the contribution of the concrete to the shear capacity reduced below a certain limit, TU3 failed within the positive plastic hinge in shear. When the loading was reversed thereafter, also a longitudinal bar fractured within the positive plastic hinge.

The RC beam of TU4 had a longitudinal reinforcement ratio which was almost twice the ratio of TU3. The RC beam was therefore much stronger. It was also considerably stiffer and had therefore the tendency to remain straight rather than to bend. Since the axial force in the piers was kept constant by means of load followers, the RC beam forced a gap between the bottom of the RC beam and the pier to open up, which reduced the deformation demand on the RC beam itself. For loading in the positive direction (drift towards North) the gap opened in the South pier and only a negative plastic hinge formed in the RC beam at the location of the North end of the spandrel. No

positive hinge formed in the RC beam. For loading in the negative direction (drift towards South) the behaviour was mirrored; i.e. the gap opened up in the North pier and a negative hinge formed in the RC beam at the location of the South edge of the spandrel. No positive hinge formed in the RC beam. Hence, the flattening of the curve at a force level of ~ 60 kN shown in Fig. 3.2g was caused by the rocking of the RC beam on the piers according to the just described mechanism. The force-rotation curve of TU4 was therefore almost bilinear elastic. At the end of the cycles with a rotation of $\pm 2\%$ the axial stress in the piers was increased from 0.4 MPa to 0.6 MPa. As a consequence, the gap between pier and RC beam did not open as much and the RC beam had to deform more. This increased deformation demand on the RC beam led to yielding of the positive plastic hinge and already in the second cycle to shear failure of the RC beam.

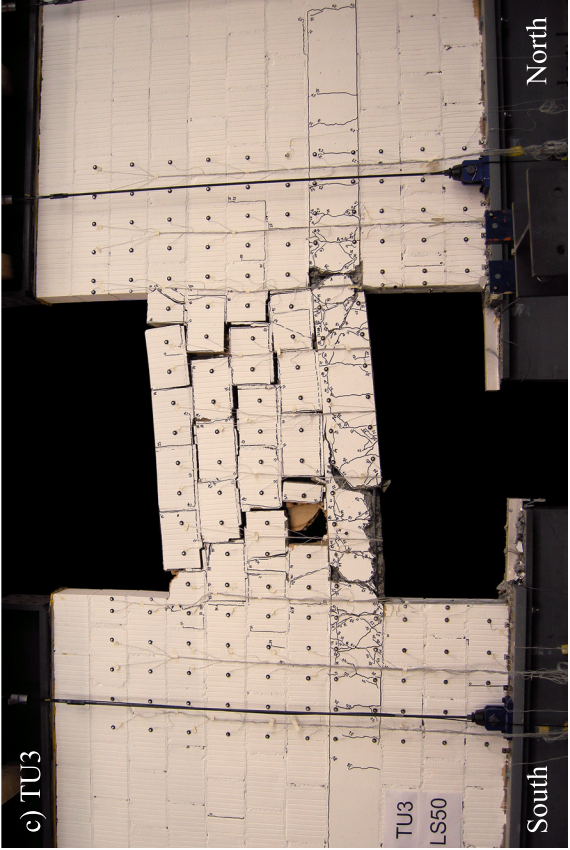
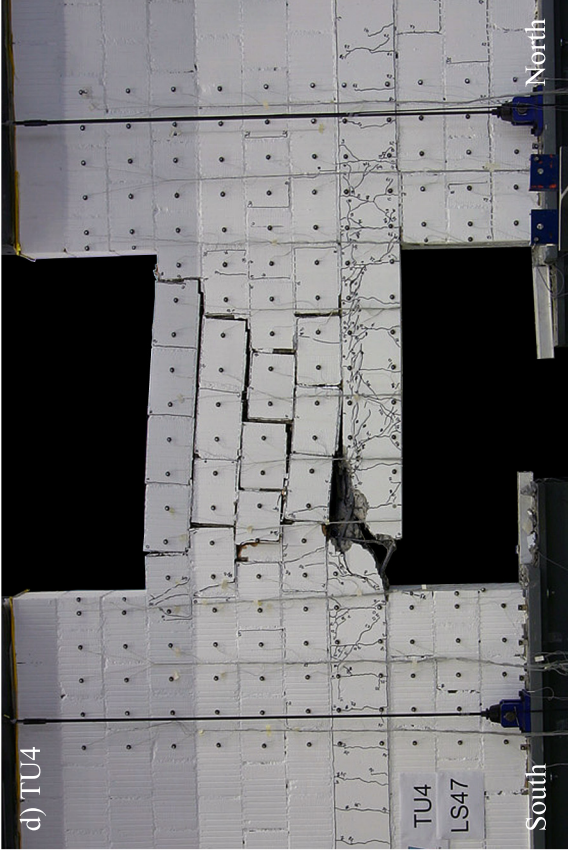
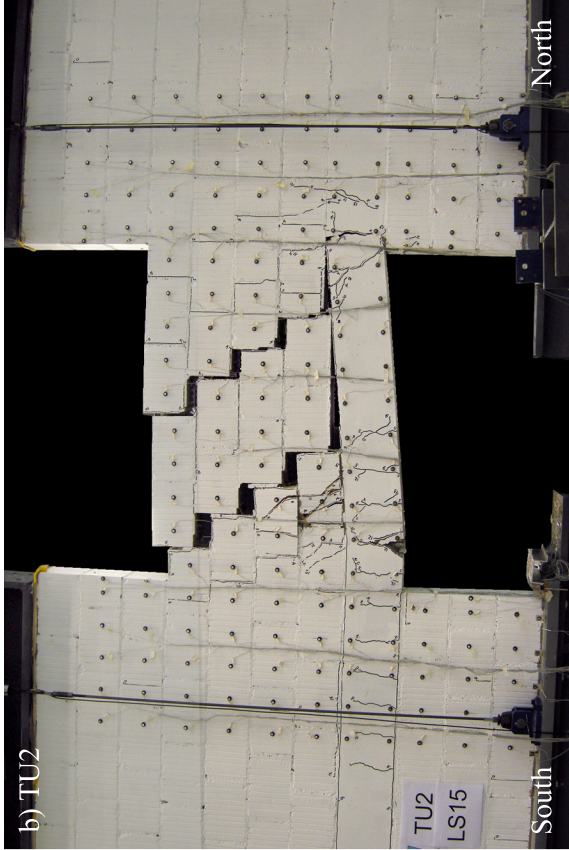
The RC beam of TU5 had of all test units the smallest longitudinal reinforcement (4D10 mm). This had the following effects: (i) The stresses in the compression diagonal of the spandrel were smaller and crushing of the masonry played only a minor role. As a consequence, the drop in the capacity after the peak was reached was less significant (Fig. 3.2h). (ii) The relative contribution of the masonry spandrel to the resistance of the spandrel element might therefore have been larger leading to the more pinched behaviour of the hysteresis curves with stiffnesses recovering at the end of the cycle, which is typical for a behaviour dominated by shear.

The deformation capacity of all test units was considerably larger than the drift limits that are normally assumed for failure of URM piers. EC8 [CEN05] proposes as drift limits at ultimate limit state 0.4% and 0.8% for shear and flexural failure, respectively. Damage to the piers modifies the boundary conditions of the spandrel element. This holds even to some degree if it is assumed that the crossing zones, i.e. the zones at the intersections of spandrels and piers remain largely undamaged. Observations of masonry spandrels after past earthquakes (see Section 1.3) have, however, shown that often either the piers or the spandrels remain largely undamaged. Based on this observations the simplified models of "weak piers, strong spandrels" and "strong piers, weak spandrels" were developed by Tomazevic [Tom99]. Note, however, that even if it is assumed that the boundary conditions applied to the spandrels by the test setup are realistic also at large rotation demands, out-of-plane accelerations might lead to out-of-plane failure of the spandrels once extensive cracking has disjointed the masonry. For this reason, the behaviour of the test unit at large deformation is unlikely to represent an accurate simulation of the true situation during a real earthquake.

3.2 Test results for masonry spandrels

Test unit TUA, which featured a masonry spandrel supported on a timber lintel, was the first masonry spandrel tested within this series. During the small cycles of TUA (up to a maximum rotation of 0.2%) the combination of axial load on the piers and axial load in the spandrel was modified two times. In the following only the behaviour of TUA with the final configurations of axial loads is discussed (In Fig. 3.3e these cycles are plotted using a black line). In this configuration the axial stress on the piers was 0.33 MPa and the axial load on the spandrel 40 kN. The failure of the spandrel was a mixed flexural-shear failure with vertical cracks at the end of the spandrel and shear cracks in the spandrel (Fig. 3.3a). Final failure of the test unit was associated with the failure of the supports of the timber lintel in the piers: They rotated inwards due to the horizontal shear stresses caused by the pull-out forces of the timber lintel.

3. Summary of test results



3.2. Test results for masonry spandrels

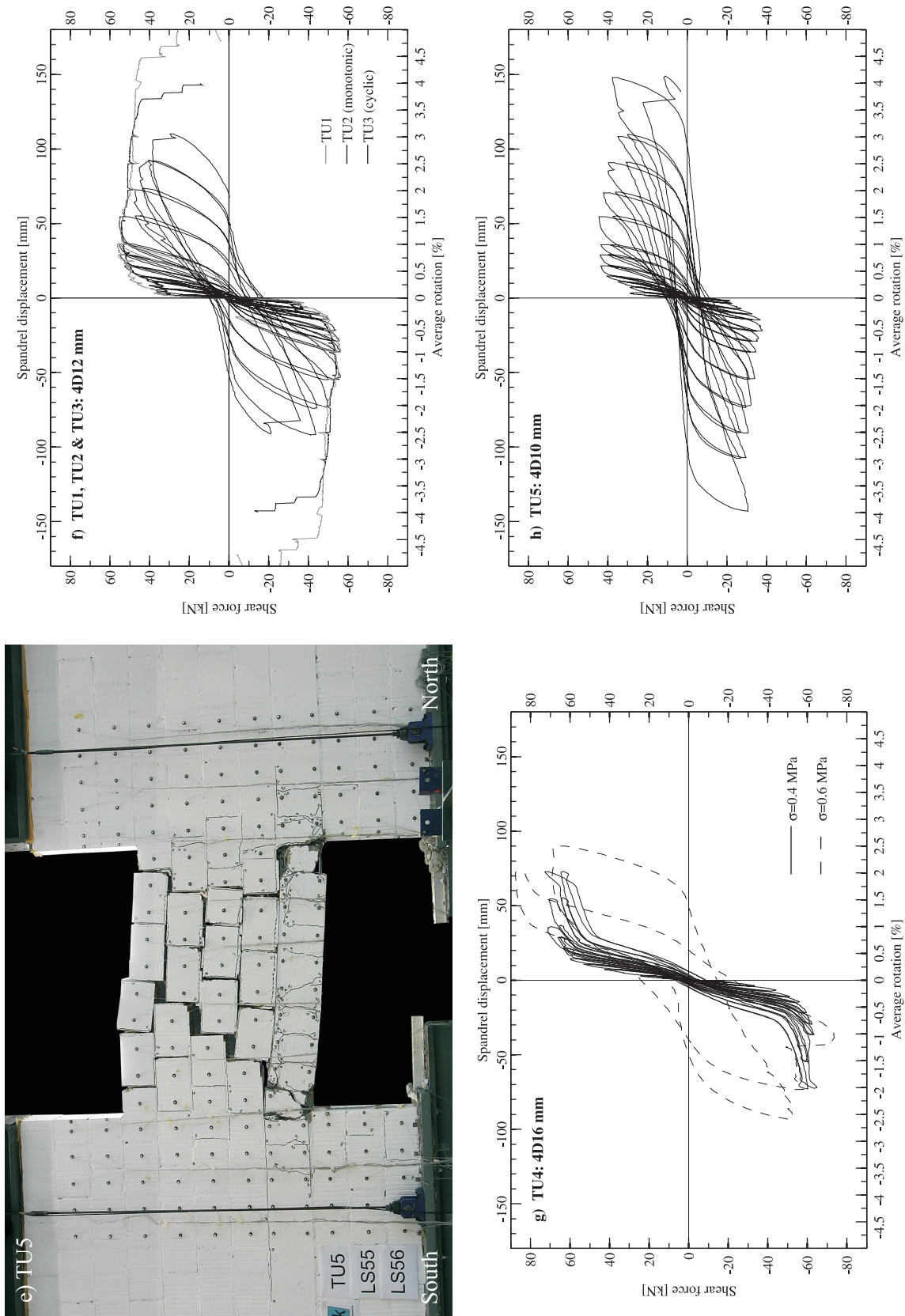
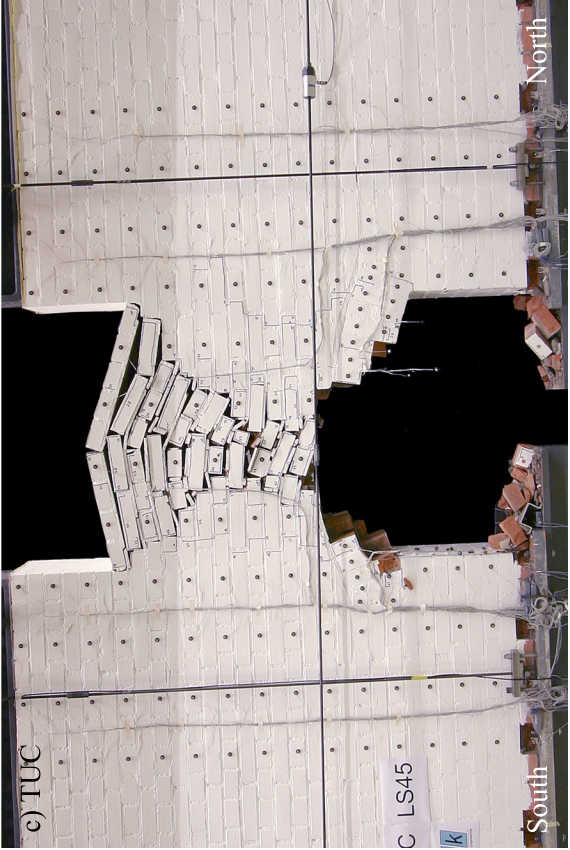
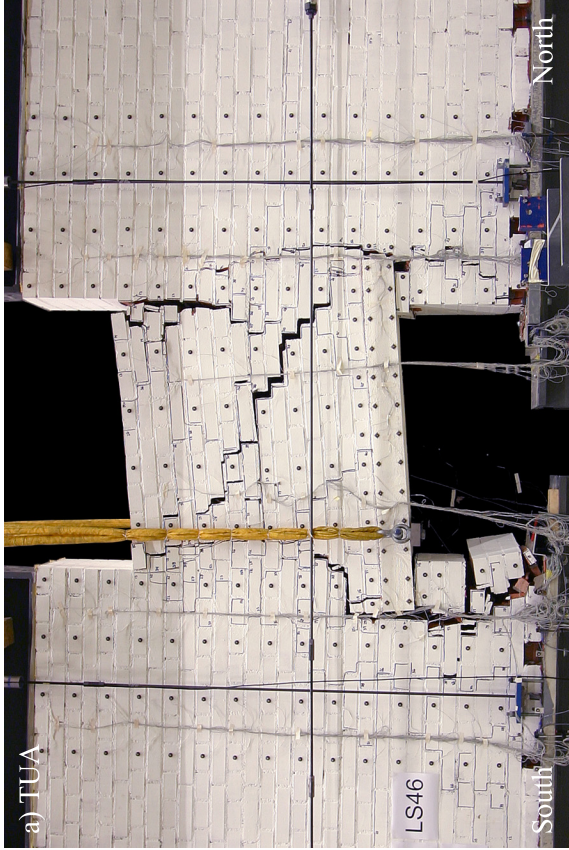
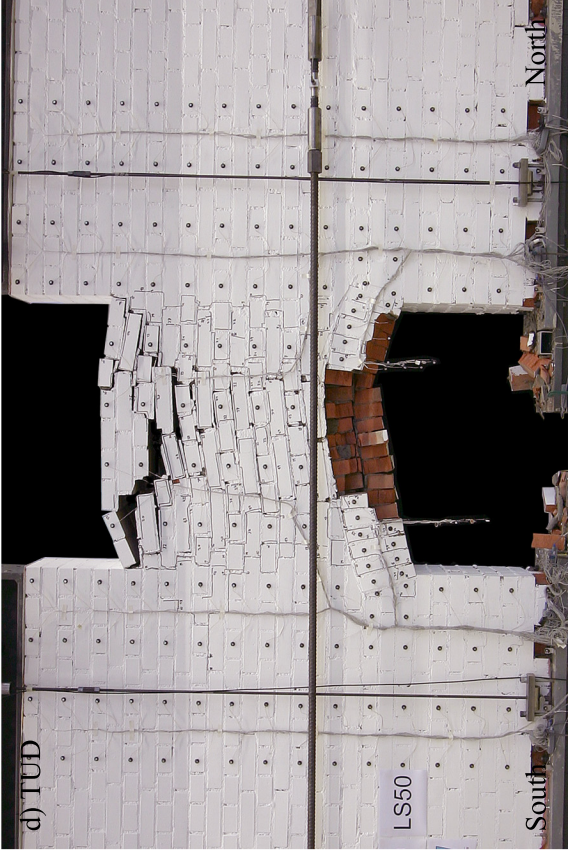
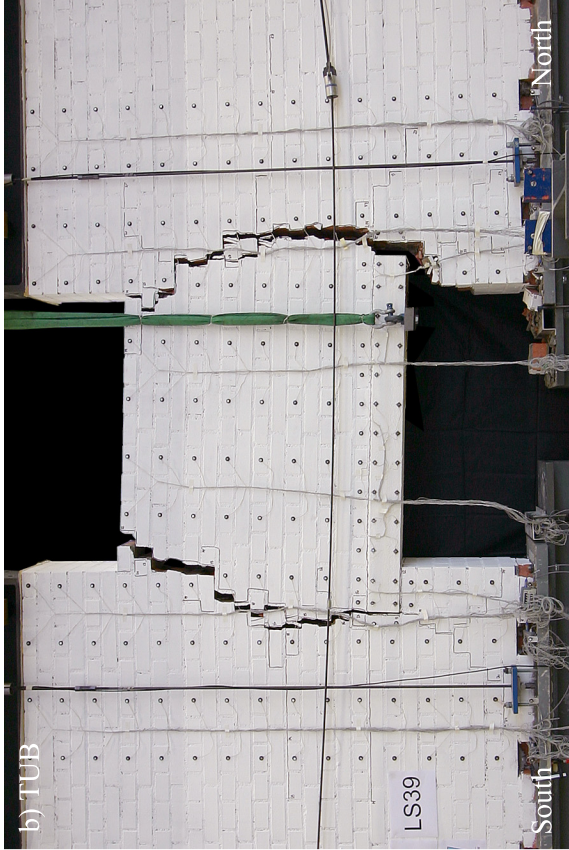


Figure 3.2: Composite spandrels: Failure modes of TU1-5 (a-e) and hysteresis curves of TU1-5 (f-h).

3. Summary of test results



3.2. Test results for masonry spandrels

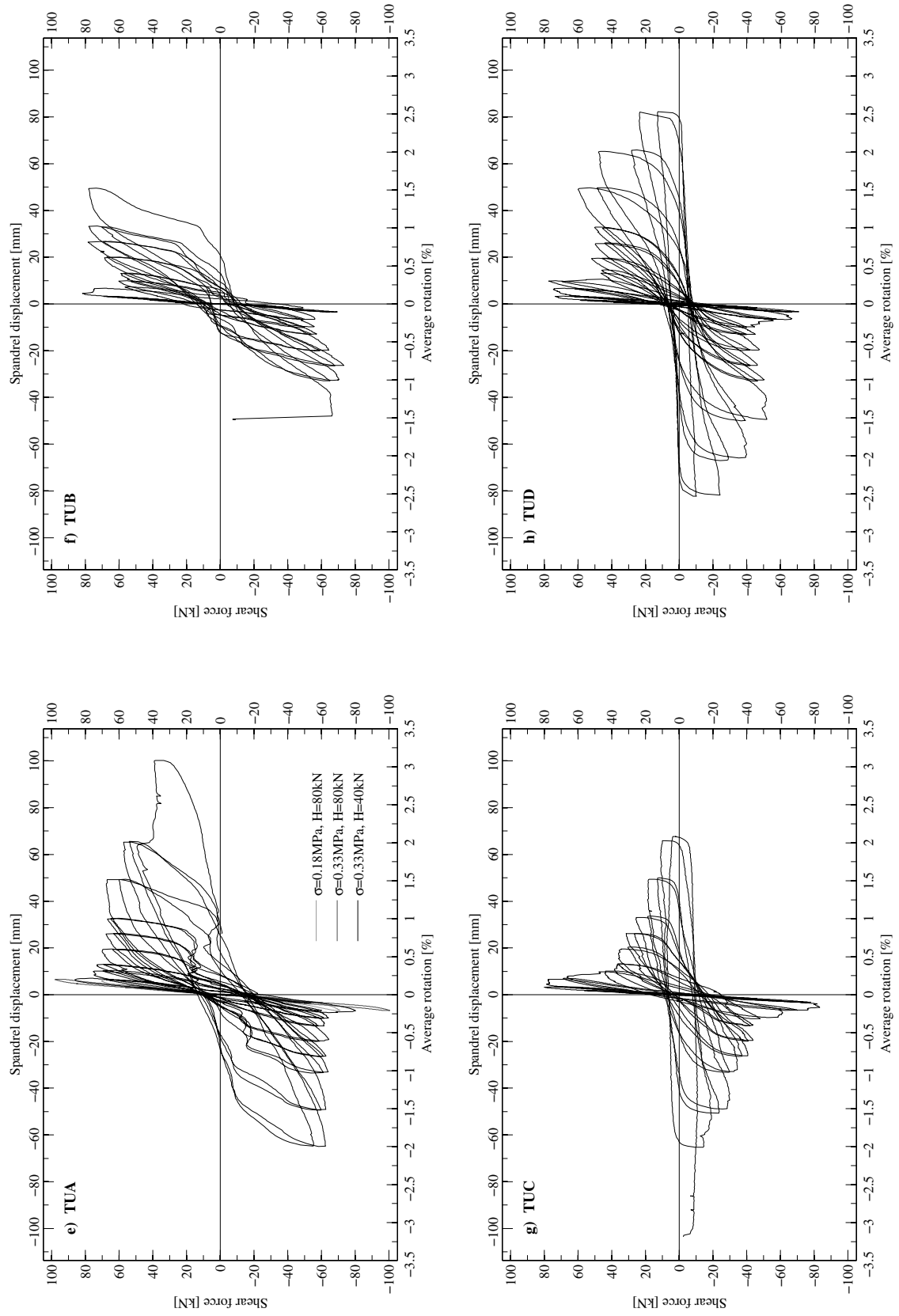


Figure 3.3: Masonry spandrels: Failure modes of TUA-TUD (a-d) and hysteresis curves of TUA-TUD (e-h).

3. Summary of test results

Like TUA, TUB featured a masonry spandrel supported on a timber lintel. Unlike TUA, the axial force in the spandrel was not constant but depended on the axial elongation of the spandrel. Figure 3.3f shows that TUB reached a similar maximum force as TUA with the final configuration of axial loads. At the maximum shear force, the spandrel of TUB had not yet undergone any significant cracking and therefore the axial force in the spandrel was still the initial axial force of 5 kN. The cracks that developed in TUB were pure flexural cracks at both ends of the spandrel (Fig. 3.3b). This crack pattern is typical for spandrels with little axial restraint as shown, for example, in Fig. 1.7. The cracks ran around the ends of the timber lintel leading eventually to large crack widths between the lintel and the piers. After the initial drop in shear force due to the flexural cracking, the shear force increased with the imposed rotation demand. The increasing elongation of the spandrel caused an increase in axial force in the spandrel and therefore an increase in the flexural capacity of the spandrel. However, similar to TUA the axial force in the spandrel did not account for the entire capacity of the spandrel but both the timber lintel and the masonry spandrel must have also contributed to the resistance of the spandrel. The final failure mechanism of TUB was similar to that of TUA: Pull-out forces of the timber lintel caused the supports of the timber lintel to rotate inwards and to fail eventually. Almost at the same time as the North support failed, one of the horizontal bars providing the axial restraint to the spandrel fractured. It was not possible to identify which of the two failure mechanisms occurred first.

Test unit TUC was the first of the two masonry spandrels featuring a shallow arch. Similar to TUA the axial force in the spandrel was kept constant throughout the test but it was doubled to create a failure mode which was different to that of TUA. To reduce unrealistic deformations in the piers, the axial stress in the piers had been increased from 0.33 MPa to 0.43 MPa. TUC reached its peak shear capacity during the cycles with a rotation of 0.2% (Fig. 3.3g). During these cycles the spandrel failed in shear forming the characteristic X-crack pattern, which has also been observed in real buildings (see Fig. 1.6). In the following cycles the capacity of the spandrel reduced significantly. It continued to drop until failure occurred, which was caused by the partial collapse of the arch (Fig. 3.3c). The gradual drop in force shown in Fig. 3.3g was caused by the progressive crushing of the masonry arch, which led to a reduction in the static height of the spandrel.

For TUD, which was the second test unit featuring a shallow arch, the axial force in the spandrel depended again on the axial elongation of the spandrel. Unlike TUB, however, the axial restraint was much stiffer since D32 mm instead of D10 mm rods were used as horizontal restrainers in an attempt to simulate the restraining effect of the vertical piers on the spandrel (Fig. 1.6). The first cracks that formed were flexural cracks in the masonry arch at about one third and two thirds of the span. The drop in shear force occurred during the cycles with maximum pier rotations of $\pm 0.3\%$ (Fig. 3.3h). At this drift level shear cracks formed in the spandrel. Note that the rotations for which cracking occurred were very similar for all four test units, independent whether flexural or shear cracks formed. After the drop in shear force, the shear capacity increased slightly with the rotation demand. The latter caused an axial elongation of the spandrel and therefore an increase in axial force in the spandrel. The shear cracks became the widest cracks although small flexural cracks in the arch and at both ends of the spandrel were also present. During the cycles with $\theta = 1.5\%$ the axial force in the spandrel reached a maximum value of 174 kN (it was 20 kN at the beginning of the test). In the following cycles the axial force in the spandrel reduced due to crushing of the bricks of the masonry arch. The final failure was – similar to TUC – caused by a partial collapse of the masonry arch (Fig. 3.3d).

4 Conclusions and outlook

As part of the research project "Nonlinear deformation behaviour of unreinforced masonry structures through testing and numerical simulations" nine spandrel test units were tested in the structural engineering laboratory of the ETH Zürich. Out of the nine test units, five were composite spandrels consisting of a RC beam and a masonry spandrel and four were masonry spandrels representing two types of spandrels that can be found in construction from the beginning of the last century. This section summarises the most important findings from the two parts of the test programme and gives an outlook on the research work which will be carried out in the future as a continuation of this project.

The main findings of the tests on **composite spandrels** are the following:

- The peak shear force was typically reached for pier rotations of about 1.0%. For larger rotations the shear capacity of the spandrel reduced. This reduction in capacity was associated with a deterioration of the compression strut in the masonry spandrel which for all test units apart from TU5 finally crushed.
- Final failure of all composite spandrels was always associated with the failure of the RC beam. The RC beam failed either in flexure (TU1, TU2, TU5) or in shear (TU4) or exhibited a mixed failure mode (TU3).
- The comparison of monotonic and cyclic tests on test units with the same properties have shown that the envelope obtained from cyclic loading corresponds well over a large range of rotations with the shear force - rotation relationship obtained for monotonic loading. For large rotations the envelope obtained from cyclic loading decreased faster than the shear force - rotation relationship obtained from monotonic loading. This was due to the crushing of the compression diagonal in the masonry, for which the damage accumulated over the cycles.
- The main contribution of the masonry spandrel to the shear capacity of the spandrel was associated with the reduction of the effective span of the RC beam. This was caused by the compression diagonal, which reached from the pier into the spandrel. As a result, the positive plastic hinge in the RC beam shifted from the edge of the spandrel, where it would have been located had a masonry spandrel not been present, to inside the span of the spandrel. Further contributions of the masonry spandrel to the capacity of the spandrel were associated with friction transmitted in the joints of the masonry.
- The shorter effective span of the RC beam induced by the masonry spandrel led to an increase of the maximum shear force acting on the RC beam. If not accounted for, this increase in shear force can cause a brittle shear failure of the RC beam.
- On the whole, all composite spandrels exhibited a very stable shear force - rotation relationship over the rotation demands, which are typically of interest. These correspond to the ultimate state drift limits for piers, which are currently assumed as 0.4% and 0.8% drift for shear and flexural failure, respectively [CEN05]. The tests were continued beyond these limits. However, it is recommended to regard these results with caution when transferring them

4. Conclusions and outlook

to real applications. Reasons for this cautioning are: (i) Possible damage to the piers during real earthquakes might modify the boundary conditions imposed on the spandrel while in the tests, the piers remained over the entire range of rotation demand virtually undamaged. (ii) Out-of-plane accelerations might lead to out-of-plane failure of the masonry spandrels once the in-plane loading has disjointed the masonry spandrel.

The main findings of the tests on the **masonry spandrels** are the following:

- For all masonry spandrels the peak resistance was reached at a rotation demand of approximately 0.2%. Until that point the spandrel was largely uncracked. Afterwards, the shear capacity of the spandrel dropped by a considerable amount due to the formation of large shear or flexural cracks in the spandrel.
- Once the peak shear force was overcome, the spandrel had the tendency to elongate axially. At this point the axial force in the spandrel or the axial restraint on the spandrel played an important role on the overall behaviour of the spandrel. An axial force in the spandrel increased the shear force for which the spandrel cracked.
- The axial force on the spandrel was applied in two different ways: For TUA and TUC the axial force was kept constant throughout the test, i.e. it was independent on the elongation of the spandrel. For TUB and TUD the axial load in the spandrel depended on the axial elongation of the spandrel. The latter is more realistic for real buildings while the former is easier to implement in numerical simulations. The way the axial force was applied to the spandrel had a large effect on the shape of the hysteresis curves.
- The failure mechanisms that were obtained for TUA-TUD corresponded well to those that were observed for spandrels after the earthquake in L'Aquila (see Section 1.3). TUB failed in flexure, TUC and TUD in shear and TUA in a mixed shear-flexural mode. In general, spandrels with small axial loads were prone to flexural failure and spandrels with large axial loads prone to shear failure. This also agrees with the observations after the earthquake in L'Aquila.
- The timber lintel contributed significantly to the integrity of the spandrel at large rotation demands. When the spandrel was damaged it served as a support of the loose parts of the spandrel. The masonry arch on the contrary was prone to damage and collapsed for both test units TUC and TUD.
- The ultimate state drift limits for URM piers are currently assumed as 0.4% and 0.8% drift for shear and flexural failure, respectively [CEN05], independently of the type of URM construction (i.e. modern or old URM). For this range of drifts the spandrels exhibited a large variation of shear capacity, mainly due to the initial strength drop associated with the formation of flexural or shear cracks. If this drop is neglected, the spandrels exhibited a relatively stable hysteretic behaviour over the range of rotations that are of interests. The tests were continued beyond these drift limits until the spandrel failed. The notes of caution that were issued for composite spandrels concerning the transfer of the test results to real buildings for large rotations apply of course also to the results for masonry spandrels.

The two test series together form an extensive data basis for the continuation of the research on the effect of spandrels on the force-deformation behaviour of URM buildings. Aspects that will be investigated in the future are:

- In this test report the test data and a first interpretation of the test results are presented. In the next step an in-depth analysis of the data will be performed which should reveal additional insights into the load-bearing mechanisms of the different spandrels. In addition, numerical and mechanical modelling of the spandrels will be performed. The final objective of this research effort will be the development of new displacement-orientated guidelines for the design and assessment of buildings with composite and masonry spandrels.
- In this project isolated spandrels were tested. The next step is to test spandrels as part of a URM wall. To do so, quasi-static cyclic tests on different URM walls are envisaged (see Fig. 4.1). A final investigation will involve shaking table tests of small buildings with spandrels.
- In buildings with strong piers and weak spandrels, the spandrels are the first elements to fail [Tom99]. As a retrofit measure it is therefore desirable to increase the deformation and force capacity of the spandrels. Different techniques such as FRP wrapping are conceivable. The test stand, which was developed for this project, was reliable and yielded excellent results. For this reason it is envisaged to carry out further tests on spandrels that are retrofitted.

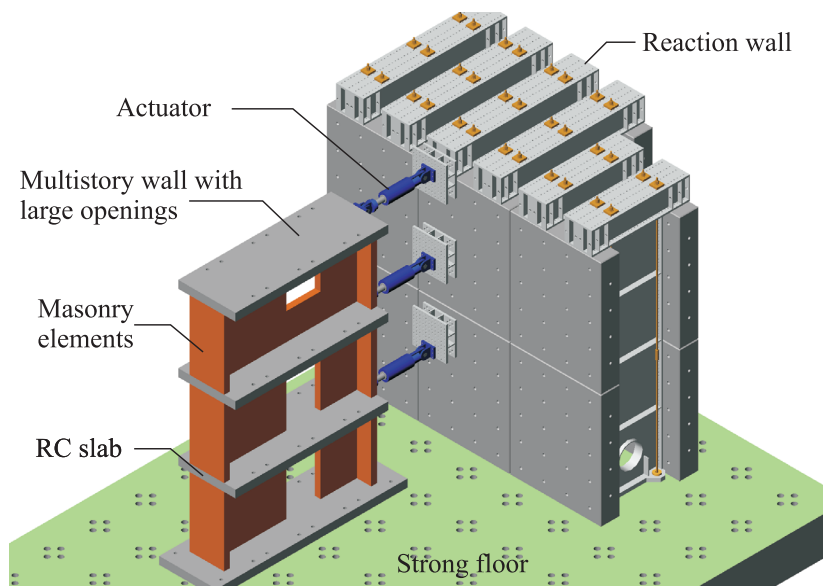


Figure 4.1: Envisaged test setup for quasi-static cyclic tests on an 3-storey URM wall.

Acknowledgments

Funding for this work was provided by the KGV Prevention Foundation in the framework of the research project "Nonlinear deformation behaviour of unreinforced masonry structures through testing and numerical simulations". Dr. Olivier Lateltin supervised the project on behalf of the funding agency while Dr. Thomas Wenk coordinated the research framework in which the project was embedded.

Lively discussions with many researchers have provided very valuable insight into various aspects of this research. In particular we would like to mention Prof. Guido Magenes, Dr. Maria Rota, Dr. Andrea Penna and Prof. Sergio Largomasino. Director Emil Setz (Unterbötzberg, Switzerland) and Dipl.-Arch. Markus Schmid (Office for the preservation of monuments and historic buildings, Basel, Switzerland) helped with the selection of spandrel types for the masonry spandrels.

Keller Ziegeleien (Pfungen, Switzerland) built the test units and Stüssi AG (Dällikon, Switzerland) constructed the RC beams for the composite spandrels. The tests were carried out in the structural engineering laboratory of the ETH Zürich. During the testing the authors were actively supported by staff of the laboratory, in particular by Dipl.-Ing. Dominik Werne, Thomas Jaggi and Christof Gisler. Dominik Werne also prepared the mechanical drawings of the supports of the lever beams. During the second part of the test programme the following students replaced Ahmad Abo-El-Ezz as helping hands in the laboratory: Maja Messerli, Xavier Perrinjaquet and Roman Beck.

Bibliography

- [BAD10] Beyer, K., AboElEzz, A., Dazio, A., “Experimental investigation of the cyclic behaviour of unreinforced masonry spandrels”, in *Proceedings of the 9th US National and 10th Canadian Conference on Earthquake Engineering*, Toronto, Canada, 2010.
- [BDP08] Beyer, K., Dazio, A., Priestley, M., “Quasi-static cyclic tests of two U-shaped reinforced concrete walls”, *Journal of Earthquake Engineering*, vol. 12(7), pp. 1023–1053, 2008.
- [CEN98] CEN, “EN 1052-1: Methods of test for masonry, Part 1: Determination of compressive strength”, *Tech. Rep. EN 1052-1:1998-12*, European Committee for Standardisation, Brussels, Belgium, 1998.
- [CEN00] CEN, “EN 772-1: Methods of test for masonry units, Part 1: Determination of compressive strength”, *Tech. Rep. EN 772-1:2000*, European Committee for Standardisation, Brussels, Belgium, 2000.
- [CEN02a] CEN, “EN 1052-1: Methods of test for masonry, Part 1: Determination of compressive strength”, *Tech. Rep. EN 1052-1:1998-12*, European Committee for Standardisation, Brussels, Belgium, 2002.
- [CEN02b] CEN, “EN 1052-3: Methods of test for masonry, Part 3: Determination of the initial shear strength”, *Tech. Rep. EN 1052-3:2002+A1:2007 D*, European Committee for Standardisation, Brussels, Belgium, 2002.
- [CEN03] CEN, “Eurocode 2: Design of concrete structures - Part 1: General rules and rules for buildings”, *Final Draft prEN 1992-1-1*, European Committee for Standardisation, Brussels, Belgium, 2003.
- [CEN04] CEN, “Eurocode 8: Design of structures for earthquake resistance, Part 1: General rules, seismic actions and rules for buildings”, *Tech. Rep. EN 1998-1*, European Committee for Standardisation, Brussels, Belgium, 2004.
- [CEN05] CEN, “Eurocode 8: Design of structures for earthquake resistance, Part 3: Assessment and retrofitting of buildings”, *Tech. Rep. EN 1998-3*, European Committee for Standardisation, Brussels, Belgium, 2005.
- [Cer07] Cervenka, V., “Atena – Computer Program for Nonlinear Finite Element Analysis of Reinforced Concrete Structures”, *Tech. rep.*, Cervenka Consulting, Prague, Czech Republic, 2007.
- [Che70] Chen, W., “Double punch test for tensile strength of concrete”, *ACI Journal*, vol. 67(12), pp. 993–995, 1970.
- [DBB⁺09] Dazio, A., Beyer, K., Braune, F., Fritsche, S., Mittaz, X., “Das $M_w=6.3$ Erdbeben von L’Aquila am 6. April 2009 (The $M_w=6.3$ L’Aquila Earthquake on April 6, 2009). Report of

Bibliography

- the April 15-18 2009 SGEB-reconnaissance mission.”, *Tech. rep.*, Swiss Society for Earthquake Engineering and Structural Dynamics, Zürich, Switzerland, 2009, available online: <http://www.sgeb.ch/erkundungsmissionen/Aquila.pdf>.
- [DIN09] DIN, “DIN EN 408: Timber structures - Structural timber and glued laminated timber: Determination of some physical and mechanical properties (in German)”, *Tech. Rep. DIN EN 408:2004-08*, DIN German Committee for Standardisation e.V., Berlin, Germany, 2009.
- [GCMN08] Gattesco, N., Clemente, I., Macorini, L., Noè, S., “Experimental investigation of the behaviour of spandrels in ancient masonry buildings”, in *Proceedings of the 14th World Conference on Earthquake Engineering*, Beijing, China, 2008.
- [Loe05] Loering, S., “Zum Tragverhalten von Mauerwerksbauten unter Erdbebeneinwirkung”, Ph.D. thesis, Universität Dortmund, Germany, 2005.
- [NDI09] NDI, *Optotrak Certus HD*, Northern Digital Inc., Waterloo, Ontario, Canada, <http://www.ndigital.com/industrial/certushd.php>, 2009.
- [OPC03] OPCM, “Primi elementi in materia di criteri generali per la classificazione sismica del territorio nazionale e di normative tecniche per le costruzioni in zona sismica, allegato 2: Norme tecniche per il progetto, la valutazione e l’adeguamento sismico degli edifici”, *Tech. Rep. OPCM 3274*, Consiglio dei ministri, Rome, Italy, 2003.
- [SIA95] SIA, “SIA162/1 Concrete Structures: Material Testing”, *Building code*, Swiss Society of Engineers and Architects (SIA), Zürich, Switzerland, 1995.
- [SIA03a] SIA, “SIA262/1: Concrete Structures – Supplementary Specifications”, *Building code*, Swiss Society of Engineers and Architects (SIA), Zürich, Switzerland, 2003.
- [SIA03b] SIA, “SIA266/1: Masonry – Supplementary Specifications”, *Building code*, Swiss Society of Engineers and Architects, Zürich, Switzerland, 2003.
- [SIA05] SIA, “SIA266: Masonry”, *Building code*, Swiss Society of Engineers and Architects, Zürich, Switzerland, 2005.
- [Tom99] Tomazevic, M., *Earthquake-Resistant Design of Masonry Structures*, Imperial College Press, London, United Kingdom, 1999.

Part II.

Composite spandrels

1 Test units, test setup, instrumentation and testing procedure

1.1 Test units

1.1.1 Properties of test units

In the first part of the test programme five full-scale composite spandrels were tested. The test units represent a typical spandrel that can be found in modern masonry buildings and consists of basically three parts as shown in Fig. 1.1: (i) the unreinforced masonry (URM) piers, (ii) the reinforced concrete (RC) beam, and (iii) the URM spandrel. In the following the sum of the latter two parts is referred to either as "composite spandrel" or more simply as "spandrel". In the test units, the dimensions of the piers are smaller compared to the dimensions of the piers found in real buildings. They were chosen to provide realistic boundary conditions for the spandrel based on engineering judgment and taking into account the geometric constraints given by the pattern of the tie-down holes within the strong floor of the laboratory.

The dimensions of all test units were identical. The piers and the URM spandrel were made of standard hollow clay bricks 29 cm long, 19 cm high and 20 cm thick, with 1 cm bed and head mortar joints, i.e. one brick plus half of the adjacent mortar joints features the dimensions: 30x20x20 cm (LxHxT). The RC beam had a rectangular cross-section 20 cm wide and 25 cm high with a nominal concrete cover of 1.5 cm. The four longitudinal reinforcement bars were deformed and had a nominal diameter ranging from 10 to 16 mm depending on the test unit. The shear reinforcement of the RC beam of all test units consisted of D6 closed hoops spaced at 150 mm and made of deformed bars featuring a 135 degrees seismic hook. Table 1.1 lists for the five test units the type of loading, the longitudinal reinforcement of the RC beam, the type of the bricks that was used for the construction of the test units and the construction and testing dates.

Table 1.1: Composite spandrels: Loading scheme, reinforcement and brick details as well as construction and testing dates for the five test units.

Test unit	Loading	Reinforcement of RC beam	Brick	Construction date	Testing date
TU1	Monotonic	4 D12 mm (4.52 cm ²)	Type 1	28.10.2008	02-03.03.2009
TU2	Monotonic	4 D12 mm (4.52 cm ²)	Type 2	20+23.03.2009	22.04.2009
TU3	Cyclic	4 D12 mm (4.52 cm ²)	Type 2	20+23.03.2009	28.05-02.06.2009
TU4	Cyclic	4 D16 mm (8.04 cm ²)	Type 2	14+15.05.2009	15-18.06.2009
TU5	Cyclic	4 D10 mm (3.14 cm ²)	Type 2	14+15.05.2009	9-10.07.2009

TU1 and TU2 were both subjected to monotonic loading and the only difference consists basically in the type of bricks used for their construction. While the bricks of TU1 had non-continuous longitudinal webs, the bricks of TU2 had continuous longitudinal webs. Figure 1.2 shows the two types of bricks and details on their mechanical properties are given in Section 2.4. Additionally,

1. Test units, test setup, instrumentation and testing procedure

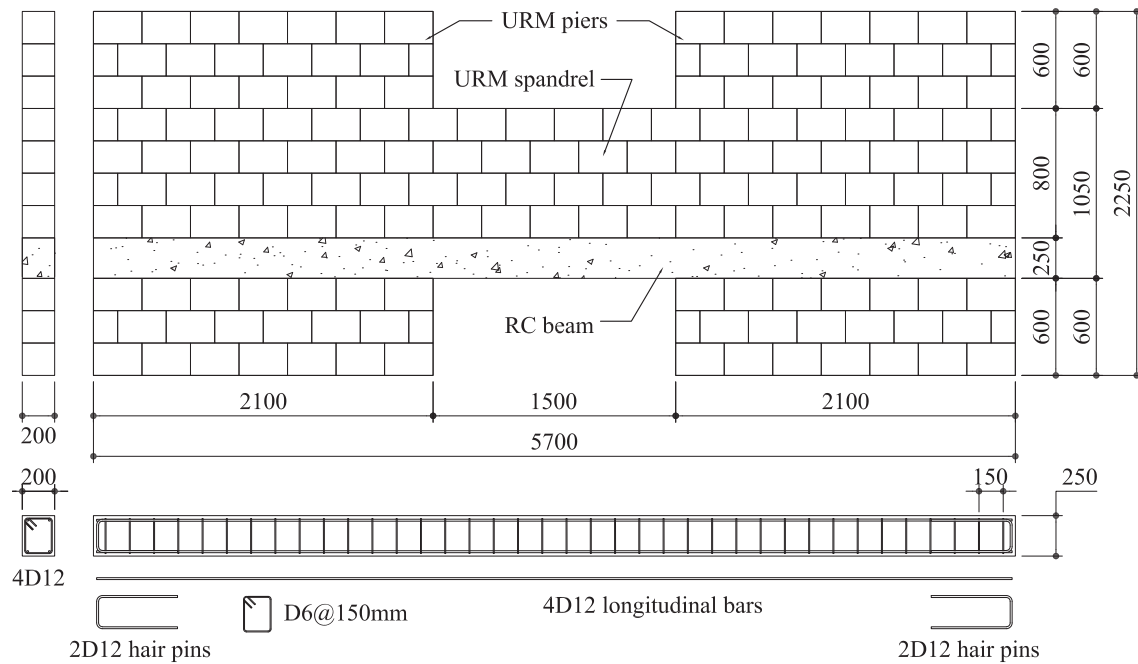


Figure 1.1: Composite spandrels: Dimensions of the test units and reinforcement layout of the RC beams. The longitudinal reinforcement varied according to Table 1.1. All dimensions are in [mm].

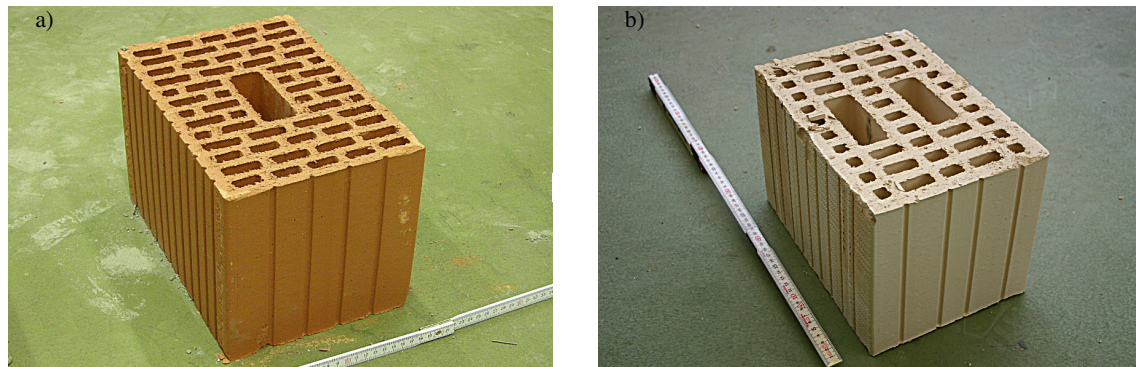


Figure 1.2: Hollow clay bricks used for the construction of the composite spandrels: Brick type 1 (a) was used for TU1, brick type 2 (b) for TU2-5.

also the mortar properties differed slightly between the two test units (see Section 2.3). The Swiss masonry design code [SIA05] does not regulate the shape of the webs. Therefore both types of bricks are commonly used in Switzerland for any kind of application, and the design engineer has no influence on the type of brick that is actually delivered on the construction site. On the contrary, for example the Italian seismic design code [OPC03] specifies that for seismic applications only bricks with continuous longitudinal webs may be used. Intuitively, the shear behaviour of brick with continuous longitudinal webs seems to be superior yielding a better seismic performance. Considering that in Switzerland such bricks are readily available at no additional cost and that in other countries they may be mandatory, they were used to build TU2-5. A comparison of the behaviour of TU1 and TU2 in terms of brick performance is presented in Section 3.1 of Part I.

TU3 differs from TU2 regarding the loading history: While TU2 was tested under monotonic loading, TU3 was subjected to cyclic loading. When assessing the seismic behaviour of a real structure, cyclic loading is surely more representative. Design approaches, however, are often based on pushover analyses addressing only the monotonic behaviour of the structure. While it is known that for ductile RC elements the pushover curve obtained from monotonic loading corresponds well to the envelope obtained from cyclic loading, at the beginning of the testing campaign due to the scarcity of relevant experimental evidence it was not possible to conclude that the same assumption holds true also for URM spandrels. In order to evaluate the difference between the two types of loading and the case being to justify this assumption, two identical test units (TU2 and TU3) were subjected to monotonic and cyclic loading, respectively.

TU4 and TU5 differ from the other test units regarding the longitudinal reinforcement of the RC beam, which was 4 D16 mm for TU4 and 4D10 mm for TU5. For TU1-3 the longitudinal reinforcement consisted of 4 D12 mm bars. The Italian seismic design code [OPC03] requires for RC ring beams a minimum longitudinal reinforcement area of 8 cm^2 , which correspond to 4 D16 mm bars, and a minimum beam width equal to the width of the masonry wall. For the shear reinforcement a minimum of D6 mm hoops every 250 mm must be provided. TU4 therefore satisfies all the minimum requirements for a ring beam according to [OPC03]; only the shear reinforcement is with D6 mm hoops every 150 mm larger than required. According to the European seismic design code EC8 [CEN04] a ring beam has to be fitted with a minimum longitudinal reinforcement area of 2 cm^2 , which is considerably smaller than the reinforcement area of TU1-4. For this reason a fifth beam was tested with a smaller longitudinal reinforcement area (TU5). Note that in EC8 no indications concerning the minimum shear reinforcement content are given.

1.1.2 Construction of test units

The test units were not constructed directly on the test stand but on the laboratory floor. In this way several test units could be constructed at the same time. For the construction of each test unit two base plates were aligned on the floor (see Fig. 1.3). An epoxy mortar was applied on the base plates where the piers were to be constructed. The construction of the piers started with a mortar layer. Particular attention was paid to the distance between the piers, i.e. the length of the spandrel of 1.5 m, and the alignment of the two piers to avoid any out-of-plane loading. The single-leaf masonry was laid in running bond by professional masons, the bed and the head joints were fully filled using a technique called "Doppelspatz" which represents the standard in Switzerland. A "Doppelspatz" is shown in Fig. 1.3c. Two strips of mortar are laid on the brick close to the edges and when the brick is put in place the mortar fills approximately 2/3 of the joint. In Switzerland this is considered as a "fully filled" joint. The RC beams were built by an external precast company and transported to the laboratory by truck. After the first three rows of bricks were built, the reinforced concrete beam was placed onto a layer of mortar by the masons (Fig. 1.3a). A further mortar layer followed and the next four rows of bricks were built over the entire length of the test unit, i.e. the two piers and the spandrel. The last three rows were only constructed over the piers.

After two weeks or more, the load transfer beams (see Fig. 1.5) were mounted on the test unit. To do so, the load transfer beams were bolted to two long steel beams. The long steel beams were needed for moving the test unit onto the test stand. Capacity-wise one beam would have been sufficient. A second beam was added for additional stiffness to ensure that the test unit would not

1. Test units, test setup, instrumentation and testing procedure

be damaged during the lifting. A mortar bed was prepared on top of the piers. The load transfer beams were placed together with the long beams onto the test unit. By means of eight vertical rods the load transfer beams were prestressed against the base plates. The total prestressing force in the rods was $8 \times 20 \text{ kN} = 160 \text{ kN}$ and therefore significantly larger than the weight of the test unit, which was including base plates and load distribution beams, approximately 53 kN . The test unit was lifted by means of one of the 10 t laboratory cranes onto the test stand (Fig. 1.4). On the test stand the base plates were bolted onto the lever beams (see Fig. 1.5) and finally the two long beams were removed. During the mounting of the test unit on the lever beams and the removing of the long beams, the channels measuring the forces at the supports and the rotations of the lever beams were continuously recorded. Once the test unit was installed on the test stand the forces in the vertical rods were released. This load condition was called LS 0 and marked the onset of the loading history.



Figure 1.3: Construction of composite spandrels.

1.2 Test setup

A drawing and a photo of the test setup are shown in Fig. 1.5 and Fig. 1.6, respectively. The test unit stood on two stiff steel beams ("lever beam") that were supported on hinges at the centre line of the piers and connected to servo-hydraulic actuators at their ends. The actuators had a force capacity of $\pm 250 \text{ kN}$ and a displacement capacity of $\pm 250 \text{ mm}$. Both actuators were displacement-controlled. The support of the South lever beam allowed next to a rotation also a sliding movement in the direction of the beam. Hence, there was no axial restraint on the beam and for the composite spandrels the total axial force in the spandrel was zero during the entire time. During testing the two servo-hydraulic actuators were moved with the same velocity in opposite directions. As a



Figure 1.4: Lifting the test unit onto the test stand.

result, the two horizontal lever beams rotated and the piers right and left to the spandrel were subjected to the same drifts, which caused the demand on the spandrel. Note that, since the velocity of the actuators was controlled via the displacement transducers mounted on the actuators themselves, the actual drifts of the two lever beams could differ slightly. This was mainly due to some small backlash within the actuators' hinges.

At the supports of the two lever beams the reaction forces were measured. Since the axial elongation of the spandrel was not restrained by the test setup only vertical forces developed at the supports. Within the cyclic tests, the vertical force of each support could potentially change sign (tension-compression) twice during every loading cycle. Considering that no tension-compression load cells were readily available, to measure the reaction force at each support such a load cell was assembled from one compression load cell and four tension load cells. The compression load cell was mounted between two steel plates by means of four D13 mm Stahlton rods where the force in the rods was measured by means of the four tension load cells. The total pretension force was about 200 kN and therefore larger than the expected maximum reaction force in tension. From the actuator forces and the reaction forces at the supports the shear force within the spandrel could be computed. The measured forces were redundant since the shear force in the spandrel could be once computed from the force of the North actuator and the North support and once from the force of the South actuator and the South support (see Section 3.1). This allowed to double-check the crucial quantity of the shear force in the spandrel.

The axial load on the piers was applied by means of four prestressed D13 mm Stahlton rods per pier. If it was expected that the height of the piers at the location of the rods would not vary

1. Test units, test setup, instrumentation and testing procedure

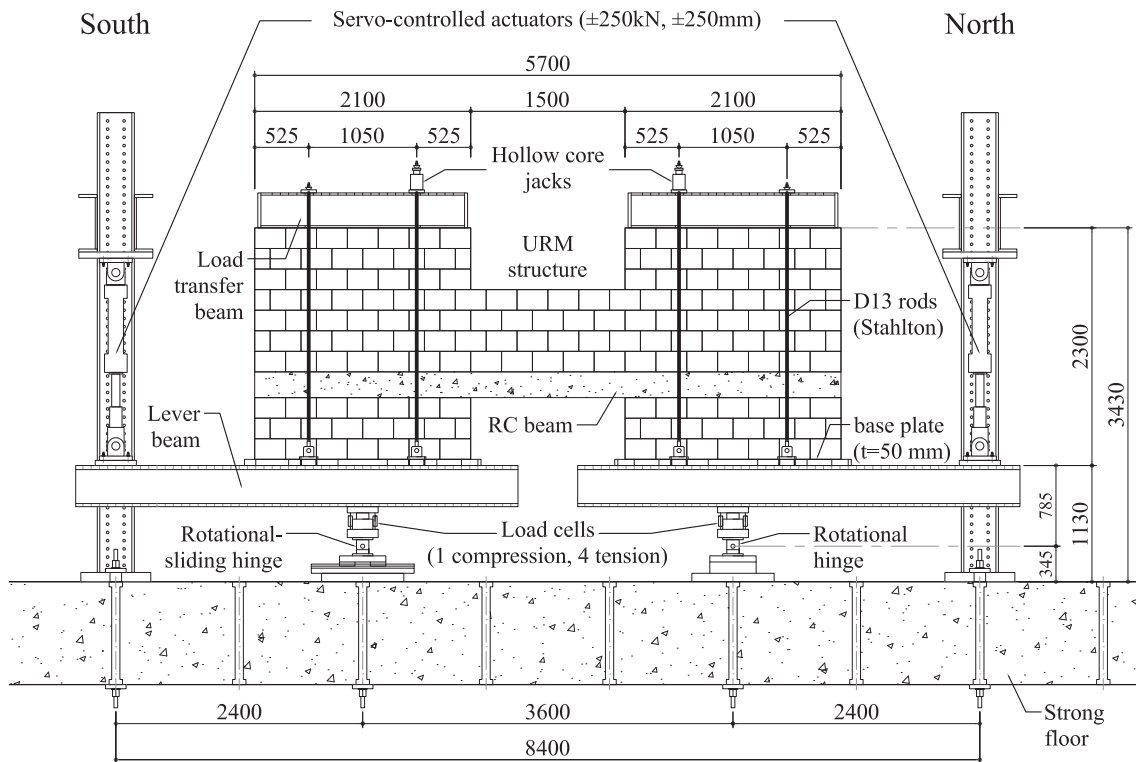


Figure 1.5: Drawing of the test setup for the composite spandrels. View from the East without side restraint. All dimensions in [mm].

much during testing, the rods were prestressed by hand and locked-in afterwards. This applied with the exception of TU4 to the outer rods. For the inner rods it was expected that the height of the piers at their location would vary during testing due to the opening and closing of cracks. For this reason the rods were prestressed by means of hollow core jacks which were mounted on top of the load transfer beams. The hollow core jacks on one pier were connected to one load follower, which ensured that the prestressing in the rods and hence the axial load applied to the piers during testing remained approximately constant despite the opening and closing of cracks in the piers. For TU4 it was found that also the force in the outer rods varied considerably during testing. For this reason, hollow core jacks were also used to prestress the outer rods. The four hollow core jacks on one pier were then connected to the same load follower. Since it was in fact easier to prestress the outer rods by means of the hollow core jacks than by hand, for the following tests all vertical rods were always pretensioned by means of the jacks rather than by hand, even if a significant variation of forces in the outer rods was not expected.

To avoid out-of-plane movements of the test unit two lateral support systems were mounted: The first lateral support system restrained excessive out-of-plane movement of the lever beams. This was accomplished by steel plates that guided the web of the lever beams. The steel plates were fixed to the four inner columns shown on Fig. 1.6 by means of threaded bars. At the beginning of testing the clear distance between steel plates and web of the lever beams was approximately 1 cm. Checks during testing showed that the out-of-plane movement of the lever beams was rather small and therefore this lateral support system served only as a safety measure. The second lateral support system restrained the load transfer beams on top of the piers from moving out-of-plane.

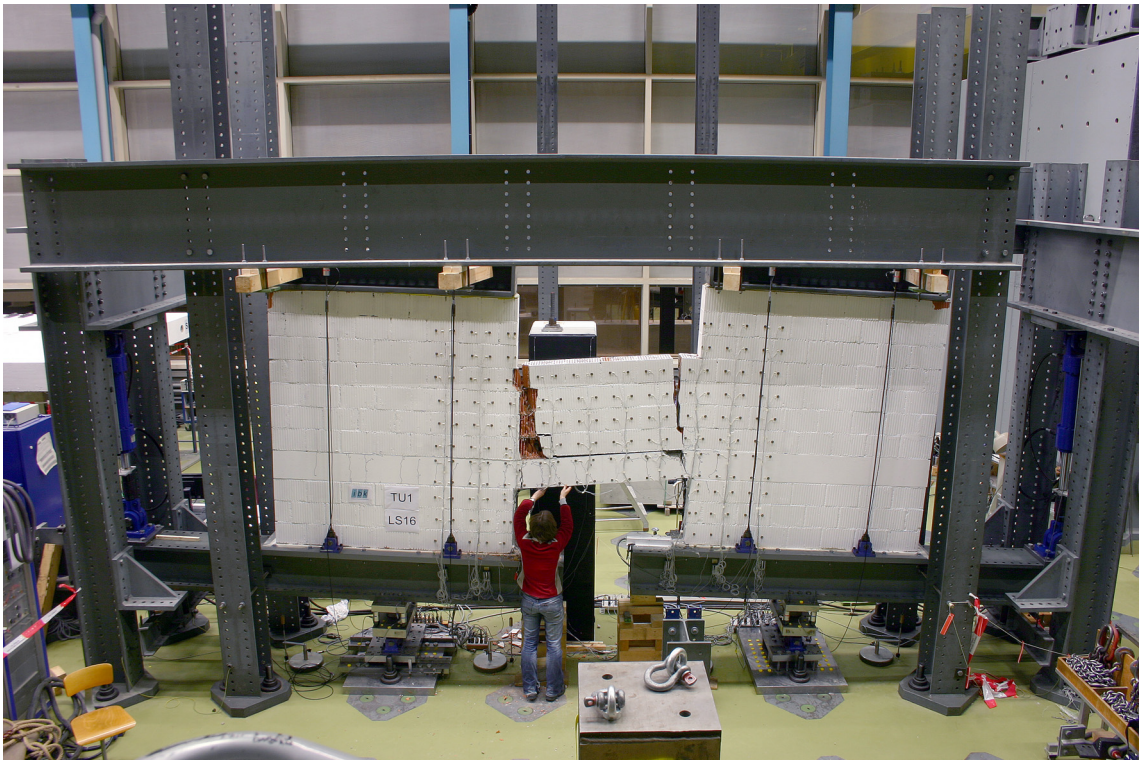


Figure 1.6: Photo of the test setup for the composite spandrels. View from the East.

On each side of the test unit a steel frame consisting of two columns and a large horizontal beam were set up. Timber beams with a cross section of approximately 14x14 cm were clamped to the lower edge of the horizontal beam. Stiff plastic rollers were mounted on the end cross-sections of the timber beams close to the test unit. The rollers were approximately 8 cm in diameter and are commonly used as heavy duty wheels. The axis of the rollers was vertical so that when the load transfer beam moved horizontally due to the applied pier rotation the rollers could roll on the web of the load transfer beams. Also for this lateral support system the clear distance between rollers and web of the load transfer beams at the beginning of testing was approximately 1 cm.

1.3 Instrumentation

Different global and local deformation quantities were measured during testing by means of hard-wired instruments. In addition, an optical measurement system was used to measure the coordinates of LEDs mounted on the East face of the test units. In the following, the quantities measured with the two measurement systems are described in detail.

1.3.1 Hard-wired channels

For TU2-5 hard-wired instruments were used to measure three different sets of quantities:

- The actuator forces and the reaction forces at the supports of the lever beams.

1. Test units, test setup, instrumentation and testing procedure

- Global deformation quantities, i.e. the rotation of the lever beams and the movement of the sliding support of the South lever beam.
- Local deformation of the RC beams by means of two LVDT chains running along the longitudinal edges of the beam at approximately the height of the top and bottom reinforcement layer.

In total 59 hard-wired instruments were used to monitor the behaviour of TU2-5: 38 displacement transducers (LVDTs), 20 load cells (LC) and 1 voltmeter.

For TU1 a different instrumentation layout was used. Since TU1 was the first real test in the structural engineering laboratory at the ETH Zürich for which the optical measurement system presented in Section 1.3.2 was used, additional hard-wired instruments on the West face of the test unit measured the deformation of the spandrel and of the adjacent zones in the piers. In total 68 hard-wired instruments were used to monitor the behaviour of TU1: 47 displacement transducers (LVDTs), 20 load cells (LC) and 1 voltmeter.

Tables 1.2 and 1.3 summarise the hard-wired instruments for TU2-5 and TU1, respectively. Figures 1.7 and 1.8 show the layout of the instrumentation and the labelling of the individual instruments. The hard-wired instruments were recorded at 2 s intervals.

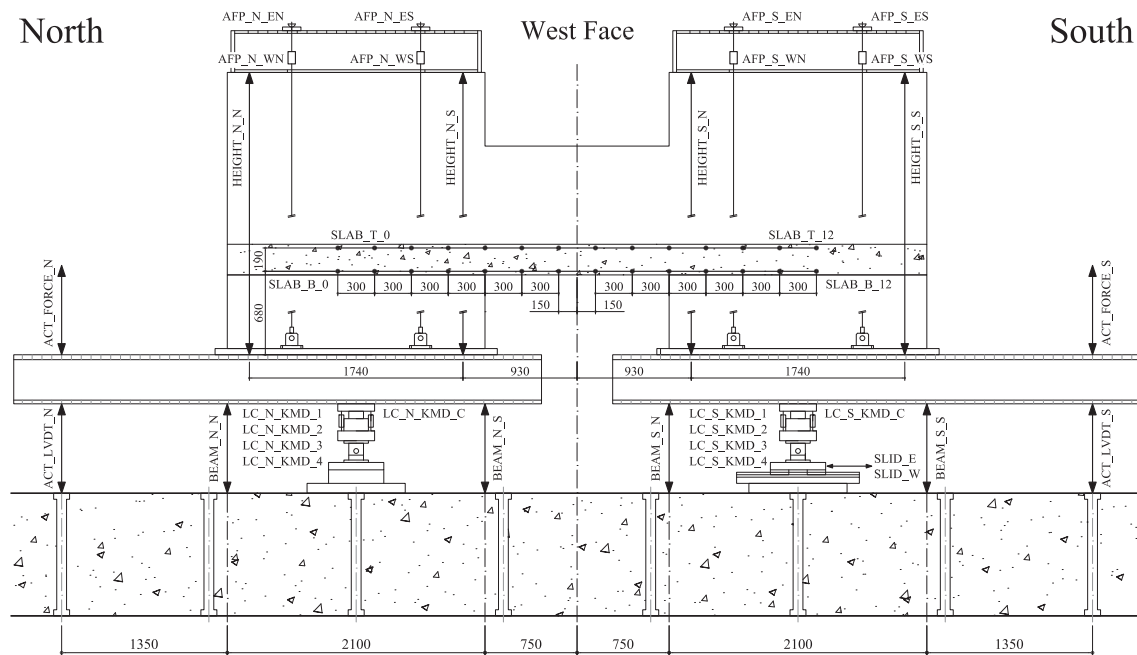


Figure 1.7: Layout of the hard-wired instruments for TU2-5. West face, all dimensions in [mm].

1.3.2 Optical measurements

In addition to the hard-wired instruments, an optical measurement system (NDI Optotrak Certus HD [NDI09]) was used to measure the local deformations of the test unit. The system works with a position sensor consisting of three cameras which measured the 3D-coordinates of LEDs glued onto the test unit and the base plates. The position sensor shown on the right of Fig. 1.10 was

Table 1.2: Hard-wired channels measured for TU2-5.

Channel name	Instrument type	Description of measured quantity
ACT_FORCE_N	± 250 kN LC	Actuator force of North actuator
ACT_FORCE_S	± 250 kN LC	Actuator force of South actuator
ACT_LVDT_N	LVDT HBM W50 ± 50 mm	Vertical displ. of lever beam at the position of the North actuator
ACT_LVDT_S	LVDT HBM W50 ± 50 mm	Vertical displ. of lever beam at the position of the South actuator
BEAM_N_N	LVDT Precisor TK50 ± 50 mm	Vertical displ. of lever beam at the position of the North edge of the North pier
BEAM_N_S	LVDT Precisor TK50 ± 50 mm	Vertical displ. of lever beam at the position of the South edge of the North pier
BEAM_S_N	LVDT Precisor TK50 ± 50 mm	Vertical displ. of lever beam at the position of the North edge of the South pier
BEAM_S_S	LVDT Precisor TK50 ± 50 mm	Vertical displ. of lever beam at the position of the South edge of the South pier
SLID_E	LVDT Precisor TK25 ± 25 mm	Sliding displacement at support of South lever beam measured at the East rail
SLID_W	LVDT Precisor TK25 ± 25 mm	Sliding displacement at support of South lever beam measured at the West rail
LC_N_KMD_C	Compression LC	Support of North lever beam, Compression LC (original name: LC_N_C)
LC_N_KMD_1	Tension LC	Support of North lever beam, Tension LC 1 (original name: LC_N_17)
LC_N_KMD_2	Tension LC	Support of North lever beam, Tension LC 2 (original name: LC_N_16)
LC_N_KMD_3	Tension LC	Support of North lever beam, Tension LC 3 (original name: LC_N_19)
LC_N_KMD_4	Tension LC	Support of North lever beam, Tension LC 4 (original name: LC_N_08)
LC_S_KMD_C	Compression LC	Support of South lever beam, Compression LC (original name: LC_S_C)
LC_S_KMD_1	Tension LC	Support of South lever beam, Tension LC 1 (original name: LC_S_15)
LC_S_KMD_2	Tension LC	Support of South lever beam, Tension LC 2 (original name: LC_S_0)
LC_S_KMD_3	Tension LC	Support of South lever beam, Tension LC 3 (original name: LC_S_24)
LC_S_KMD_4	Tension LC	Support of South lever beam, Tension LC 4 (original name: LC_S_22)
AFP_N_EN	Tension LC	Axial force on North pier, North rod on East face
AFP_N_ES	Tension LC	Axial force on North pier, South rod on East face
AFP_N_WN	Tension LC	Axial force on North pier, North rod on West face
AFP_N_WS	Tension LC	Axial force on North pier, South rod on West face
AFP_S_EN	Tension LC	Axial force on South pier, North rod on East face
AFP_S_ES	Tension LC	Axial force on South pier, South rod on East face
AFP_S_WN	Tension LC	Axial force on South pier, North rod on West face
AFP_S_WS	Tension LC	Axial force on South pier, South rod on West face
SLAB_T_0	LVDT Precisor TK25 ± 25 mm	Elongation of RC beam, top row (measured on the West face)
SLAB_T_1	LVDT Precisor TK10 ± 10 mm	
SLAB_T_2	LVDT Precisor TK10 ± 10 mm	
SLAB_T_3	LVDT Precisor TK10 ± 10 mm	
SLAB_T_4	LVDT Precisor TK10 ± 10 mm	
SLAB_T_5	LVDT Precisor TK10 ± 10 mm	
SLAB_T_6	LVDT Precisor TK10 ± 10 mm	
SLAB_T_7	LVDT HBM WSF20 ± 10 mm	
SLAB_T_8	LVDT HBM WSF20 ± 10 mm	
SLAB_T_9	LVDT HBM WSF20 ± 10 mm	
SLAB_T_10	LVDT HBM WSF20 ± 10 mm	
SLAB_T_11	LVDT HBM WSF20 ± 10 mm	
SLAB_T_12	LVDT Precisor TK10 ± 10 mm	
SLAB_B_0	LVDT Precisor TK25 ± 25 mm	Elongation of RC beam, bottom row (measured on the West face)
SLAB_B_1	LVDT Precisor TK10 ± 10 mm	
SLAB_B_2	LVDT Precisor TK10 ± 10 mm	
SLAB_B_3	LVDT Precisor TK10 ± 10 mm	
SLAB_B_4	LVDT Precisor TK10 ± 10 mm	
SLAB_B_5	LVDT Precisor TK10 ± 10 mm	
SLAB_B_6	LVDT Precisor TK10 ± 10 mm	
SLAB_B_7	LVDT HBM WSF20 ± 10 mm	
SLAB_B_8	LVDT HBM WSF20 ± 10 mm	
SLAB_B_9	LVDT HBM WSF20 ± 10 mm	
SLAB_B_10	LVDT HBM WSF20 ± 10 mm	
SLAB_B_11	LVDT HBM WSF20 ± 10 mm	
SLAB_B_12	LVDT Precisor TK25 ± 25 mm	
HEIGHT_N_N	LVDT Precisor TK25 ± 25 mm	Displ. betw. transfer beam and base plate at the North end of the North pier (measured on the West face)
HEIGHT_N_S	LVDT Precisor TK25 ± 25 mm	Displ. betw. transfer beam and base plate at the South end of the North pier (measured on the West face)
HEIGHT_S_N	LVDT Precisor TK25 ± 25 mm	Displ. betw. transfer beam and base plate at the North end of the South pier (measured on the West face)
HEIGHT_S_S	LVDT Precisor TK25 ± 25 mm	Displ. betw. transfer beam and base plate at the South end of the South pier (measured on the West face)
Voltage		Volt measurement. The displacement measurement of BEAM_N_N, BEAM_N_S, BEAM_S_N and BEAM_S_S is based on a voltage.

placed approximately 5.3 m away from the East face of the test unit. At this distance LEDs within an area of 3.25x2.45 m could be tracked. Figure 1.9 shows the layout of the LEDs glued onto the test units while Fig. 1.10 shows the position sensor and the stand used to support it. The lowest

1. Test units, test setup, instrumentation and testing procedure

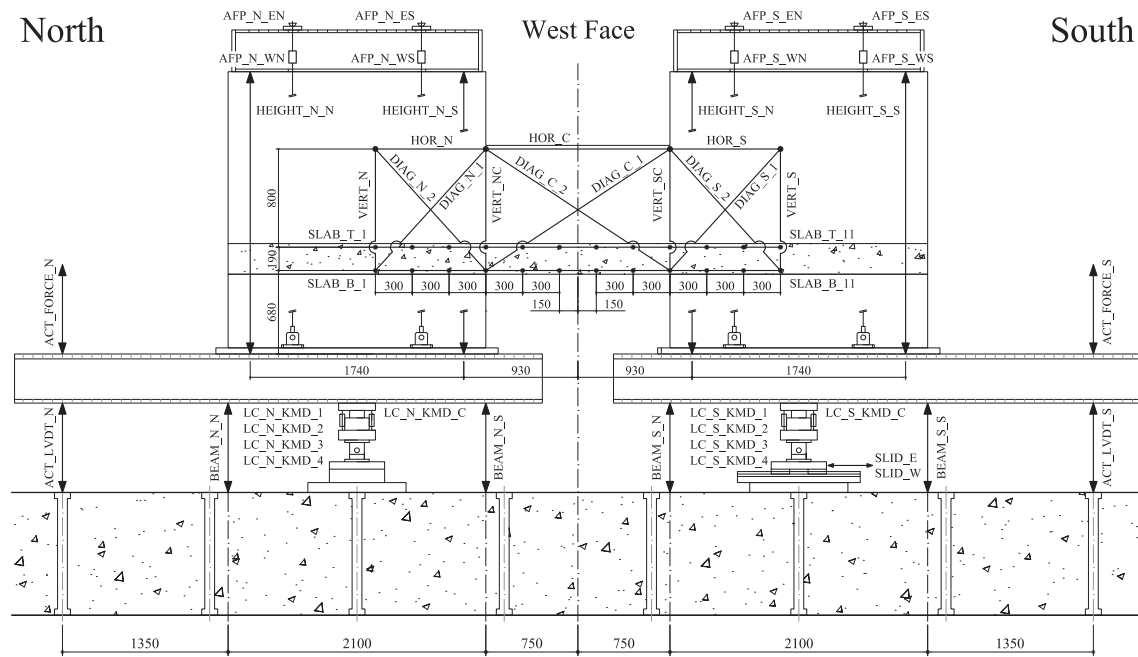


Figure 1.8: Layout of the hard-wired instruments for TU1. West face, all dimensions in [mm].

rows of LEDs was not glued onto the test units but onto angles (L-shapes) that were glued onto the base plates. In addition to the LEDs shown in Fig. 1.9, two LEDs were fixed to a short steel column standing in front of the test unit (see Fig. 1.10) and four LEDs to a concrete block placed behind the test unit (see Fig. 1.6). These six LEDs were used as reference LEDs since the steel column and the concrete block did not move during loading. Thus, a change in position of these reference LEDs would indicate that the position sensor had been accidentally moved.

The position of each LED defined through the time-histories of the x-, y- and z-coordinates was recorded with a 10 Hz rate. The original coordinate system depended on the orientation of the position sensor but was rotated during the post-processing of the data. In the final coordinate system the x-axis is parallel to the test unit pointing from South to North, the y-axis points up vertically and the z-axis points from the test unit to the position sensor. To synchronise the optical measurements with the hard-wired channel measurements, the Volt-signal stemming from the actuator forces was read into both data acquisition systems. However, it was found that the recording of the Volt-signal by the optical measurement system featured a lot of noise. For this reason, the rotation of the lever beams was used to synchronise the two types of measurements. The coordinate measurement data was first smoothed and then reduced to the same recording rate as the hard-wired data, i.e. to a frequency of 0.5 Hz. The positions of the LEDs were also recorded at each load step when the loading was stopped. The measurements were performed over a duration of approximately one minute and were later averaged over the recording time to obtain the deformations of the spandrel at the load steps.

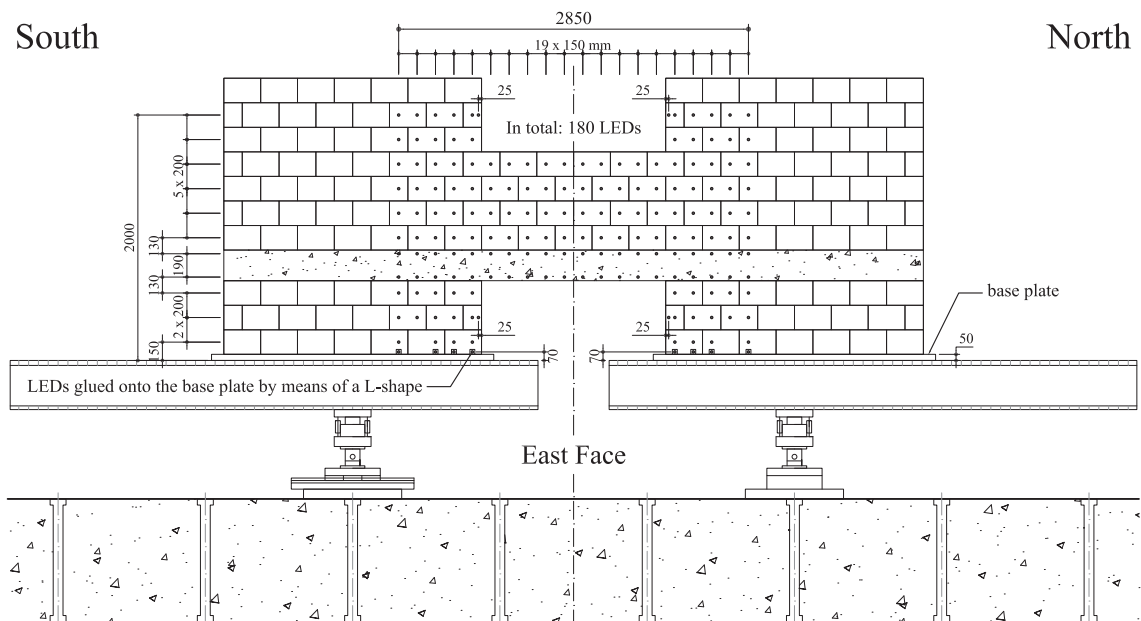


Figure 1.9: Layout of the LEDs on the East face of the test unit. All dimensions in [mm].

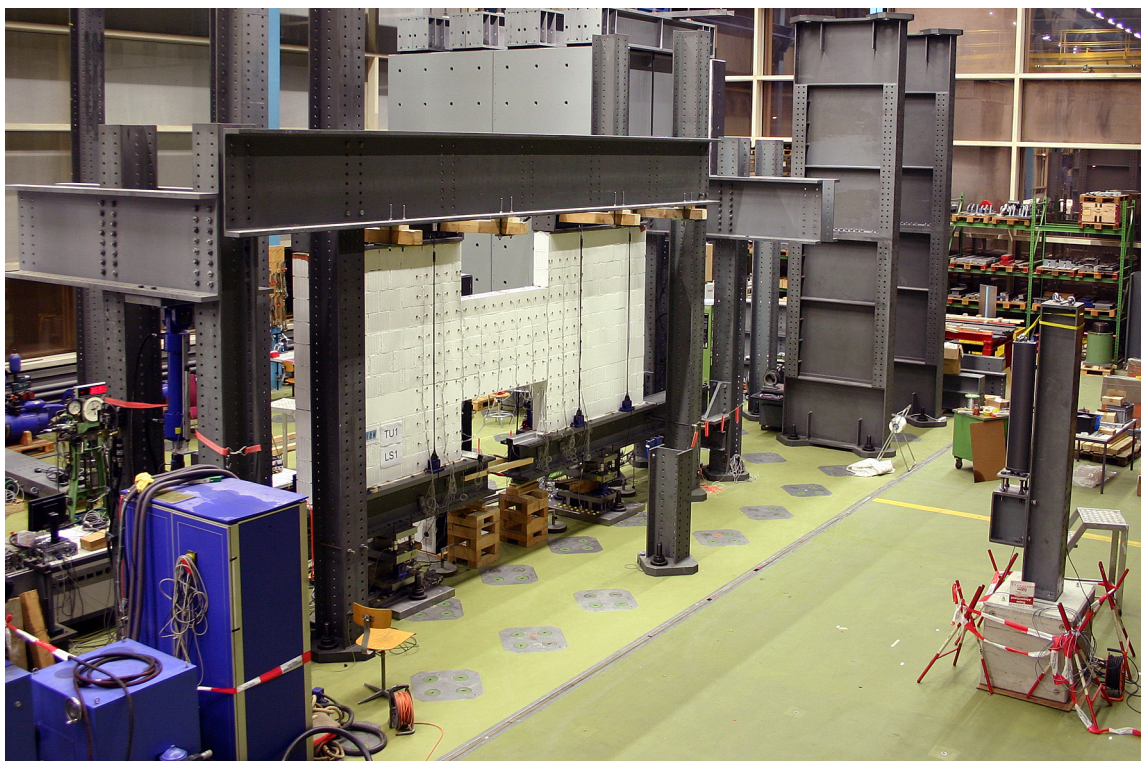


Figure 1.10: Test setup including Optotrak position sensor. View from the South-East.

1.4 Testing procedure

Testing of one test unit took between 2 and 4 days. For each test unit the testing days and the load steps covered during each day are given at the beginning of the section "test observations".

Both the monotonic and the cyclic loading scheme followed different steps of storey drifts in displacement control. Force-controlled load steps, which are often used at the beginning of quasi-static cyclic tests of RC elements, were not applied. Force-controlled load steps are typically used to determine a yield displacement which forms the basis of the step-wise increase of the displacement amplitude in the ensuing displacement-controlled cycles. Determining a yield displacement is already difficult and ambiguous for RC elements; it is even less clear for URM elements. For this reason the loading history was solely controlled by different storey drift levels and the applied storey drift levels were the same for all test units. The storey drift corresponds to the rotation of the two lever beams, which were approximately identical throughout the test. The rotation of the lever beams were determined by means of the LVDTs mounted underneath the lever beams (see Section 1.3.1).

When the monotonic loading scheme was applied the loading was stopped at the storey drift levels 0.025%, 0.05%, 0.1%, 0.2%, 0.3%, 0.4%, 0.6%, 0.8%, 1.0%, 1.5%, 2.0%, 2.5%, 3.0%, 4.0% as shown in Fig. 1.11. The same drift levels determined the amplitudes of the cyclic loading scheme. At each drift level the test unit was subjected to two loading cycles. A schematic figure of the cyclic loading scheme is shown in Fig. 1.12. Table 1.4 summarises the load step (LS) numbers for each drift level of both the monotonic and the cyclic loading history. A load step corresponds to the drift level, at which loading was stopped (monotonic loading) or to the peaks of the cyclic loading history. The numbering of the drift-controlled load steps commences with LS 2. LS 0 refers to the state before any rotations or axial forces were applied (see Section 1.1.2). First, the axial load was applied to the piers (LS 1) while the rotation of the lever beams was still zero. Next, the actuators were connected to the lever beams. To do so, the actuator pistons were driven downwards until the swivel bases were force-locked. The latter were then bolted onto the lever beams and the temporary supports below the lever beams were removed. The lever beams could now be rotated by the actuators. Table 1.4 also gives the velocities with which the actuator pistons were moved ("loading velocity"). Small values were chosen for the loading velocity in order to avoid any dynamic effects, to allow time for readjusting the axial force applied to the piers and to record sufficient data points with the hard-wired channels. The recording frequency of 0.5 Hz for the hard-wired channels was given by the capacity of the data acquisition system.

At each load step the loading was stopped, the cracks were marked with a black pen and photos were taken. Observations concerning the development of the crack pattern were noted down. Additionally, LED measurements were performed over a period of about one minute. During testing of TU2-5 the same overall picture was taken continuously at about 2 minutes intervals. At the end of a testing day, the rotation of the lever beams was reduced until the forces in the two actuators were approximately equal. The temporary supports of the lever beams were reinstalled, the swivel plates unbolted from the lever beams, the pistons of the actuators pulled-in and the latter switched off. The valves controlling the pressure in the hollow core jacks were closed and the load followers switched off, i.e the axial load acting on the piers reduced only slightly overnight due to negligible leaking of the hydraulic system.

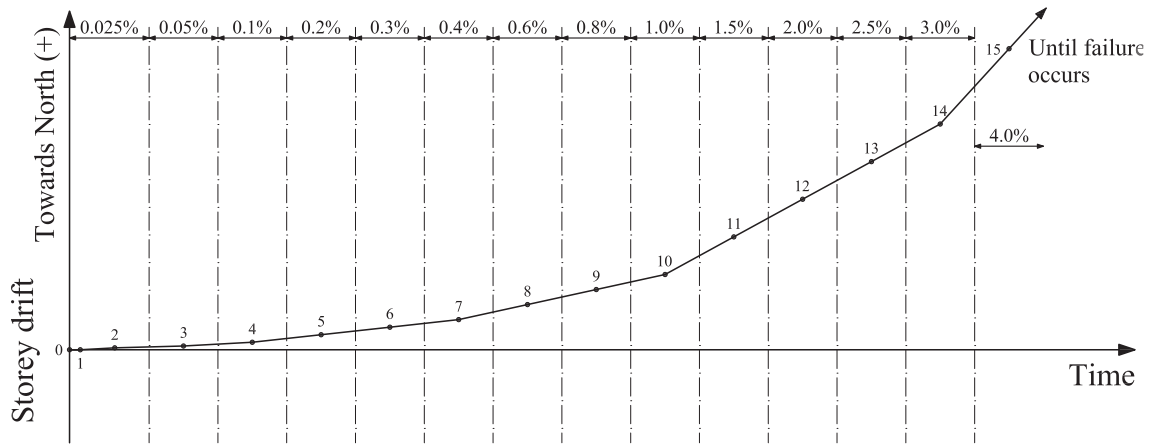


Figure 1.11: Loading history for monotonic loading.

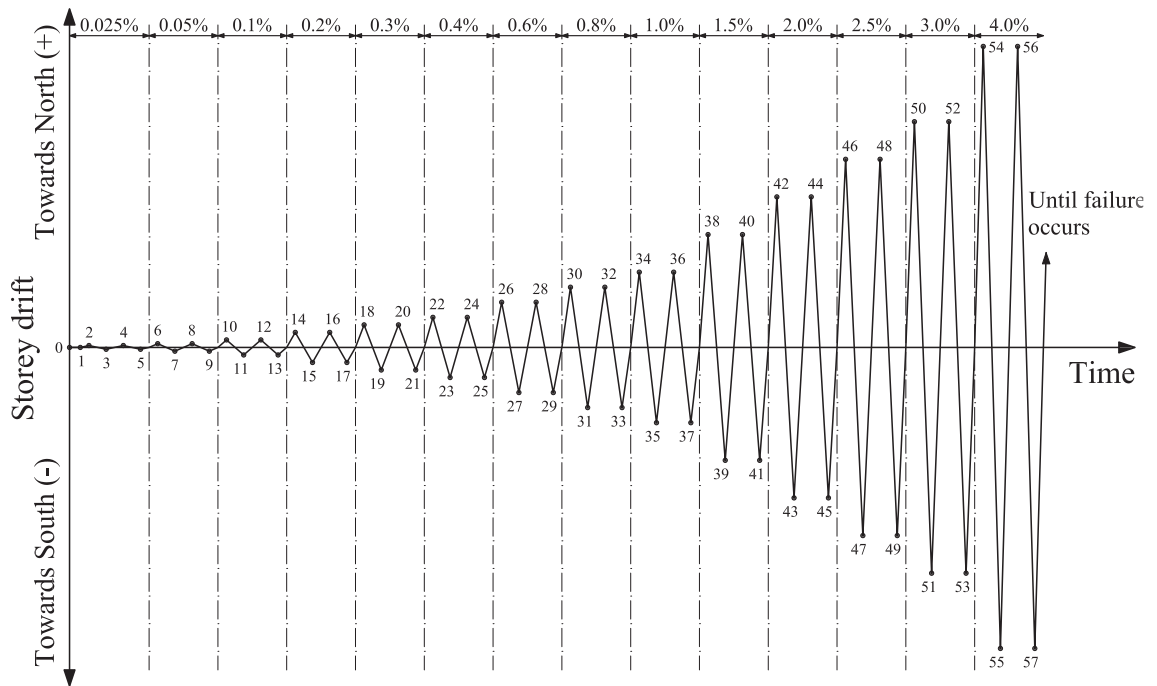


Figure 1.12: Loading history for cyclic loading.

1. Test units, test setup, instrumentation and testing procedure

Table 1.3: Hard-wired channels measured for TU1.

Channel name	Instrument type	Description of measured quantity
ACT_FORCE_N	±250 kN LC	Actuator force of North actuator
ACT_FORCE_S	±250 kN LC	Actuator force of South actuator
ACT_LVDT_N	LVDT HBM W50 ±50 mm	Vertical displ. of lever beam at the position of the North actuator
ACT_LVDT_S	LVDT HBM W50 ±50 mm	Vertical displ. of lever beam at the position of the South actuator
BEAM_N_N	LVDT Precisor TK50 ±50 mm	Vertical displ. of lever beam at the position of the North edge of the North pier
BEAM_N_S	LVDT Precisor TK50 ±50 mm	Vertical displ. of lever beam at the position of the South edge of the North pier
BEAM_S_N	LVDT Precisor TK50 ±50 mm	Vertical displ. of lever beam at the position of the North edge of the South pier
BEAM_S_S	LVDT Precisor TK50 ±50 mm	Vertical displ. of lever beam at the position of the South edge of the South pier
SLID_E	LVDT Precisor TK25 ±25 mm	Sliding displacement at support of South lever beam measured at the East rail
SLID_W	LVDT Precisor TK25 ±25 mm	Sliding displacement at support of South lever beam measured at the West rail
LC_N_KMD_C	Compression LC	Support of North lever beam, Compression LC (original name: LC_N_C)
LC_N_KMD_1	Tension LC	Support of North lever beam, Tension LC 1 (original name: LC_N_17)
LC_N_KMD_2	Tension LC	Support of North lever beam, Tension LC 2 (original name: LC_N_16)
LC_N_KMD_3	Tension LC	Support of North lever beam, Tension LC 3 (original name: LC_N_19)
LC_N_KMD_4	Tension LC	Support of North lever beam, Tension LC 4 (original name: LC_N_08)
LC_S_KMD_C	Compression LC	Support of South lever beam, Compression LC (original name: LC_S_C)
LC_S_KMD_1	Tension LC	Support of South lever beam, Tension LC 1 (original name: LC_S_15)
LC_S_KMD_2	Tension LC	Support of South lever beam, Tension LC 2 (original name: LC_S_0)
LC_S_KMD_3	Tension LC	Support of South lever beam, Tension LC 3 (original name: LC_S_24)
LC_S_KMD_4	Tension LC	Support of South lever beam, Tension LC 4 (original name: LC_S_22)
AFP_N_EN	Tension LC	Axial force on North pier, North rod on East face
AFP_N_ES	Tension LC	Axial force on North pier, South rod on East face
AFP_N_WN	Tension LC	Axial force on North pier, North rod on West face
AFP_N_WS	Tension LC	Axial force on North pier, South rod on West face
AFP_S_EN	Tension LC	Axial force on South pier, North rod on East face
AFP_S_ES	Tension LC	Axial force on South pier, South rod on East face
AFP_S_WN	Tension LC	Axial force on South pier, North rod on West face
AFP_S_WS	Tension LC	Axial force on South pier, South rod on West face
HOR_N	LVDT Precisor TK25 ±25 mm	Horizontal displacements of crosses at the top
HOR_C	LVDT Precisor TK25 ±25 mm	
HOR_S	LVDT Precisor TK25 ±25 mm	
VERT_N	LVDT Precisor TK10 ±10 mm	
VERT_NC	LVDT Precisor TK25 ±25 mm	Vertical displacements of crosses
VERT_SC	LVDT Precisor TK25 ±25 mm	
VERT_S	LVDT Precisor TK10 ±10 mm	
DIAG_N_1	LVDT Precisor TK25 ±25 mm	
DIAG_N_2	LVDT Precisor TK25 ±25 mm	Diagonal displacements of crosses
DIAG_C_1	LVDT Precisor TK25 ±25 mm	
DIAG_C_2	LVDT Precisor TK25 ±25 mm	
DIAG_S_1	LVDT Precisor TK25 ±25 mm	
DIAG_S_2	LVDT Precisor TK25 ±25 mm	Elongation of RC beam, top row (measured on the West face)
SLAB_T_1	LVDT Precisor WSF20 ±10 mm	
SLAB_T_2	LVDT Precisor WSF20 ±10 mm	
SLAB_T_3	LVDT Precisor TK10 ±10 mm	
SLAB_T_4	LVDT Precisor TK10 ±10 mm	
SLAB_T_5	LVDT Precisor TK10 ±10 mm	
SLAB_T_6	LVDT Precisor TK10 ±10 mm	
SLAB_T_7	LVDT HBM WSF20 ±10 mm	
SLAB_T_8	LVDT HBM WSF20 ±10 mm	
SLAB_T_9	LVDT HBM WSF20 ±10 mm	
SLAB_T_10	LVDT HBM WSF20 ±10 mm	
SLAB_T_11	LVDT HBM WSF20 ±10 mm	Elongation of RC beam, bottom row (measured on the West face)
SLAB_B_1	LVDT Precisor WSF20 ±10 mm	
SLAB_B_2	LVDT Precisor TK10 ±10 mm	
SLAB_B_3	LVDT Precisor TK10 ±10 mm	
SLAB_B_4	LVDT Precisor TK10 ±10 mm	
SLAB_B_5	LVDT Precisor TK10 ±10 mm	
SLAB_B_6	LVDT Precisor TK10 ±10 mm	
SLAB_B_7	LVDT HBM WSF20 ±10 mm	
SLAB_B_8	LVDT HBM WSF20 ±10 mm	
SLAB_B_9	LVDT HBM WSF20 ±10 mm	
SLAB_B_10	LVDT HBM WSF20 ±10 mm	
SLAB_B_11	LVDT HBM WSF20 ±10 mm	Displ. betw. transfer beam and base plate at the North end of the North pier (measured on the West face)
HEIGHT_N_N	LVDT Precisor TK25 ±25 mm	
HEIGHT_N_S	LVDT Precisor TK25 ±25 mm	
HEIGHT_S_N	LVDT Precisor TK25 ±25 mm	
HEIGHT_S_S	LVDT Precisor TK25 ±25 mm	Displ. betw. transfer beam and base plate at the South end of the South pier (measured on the West face)
HEIGHT_S_S	LVDT Precisor TK25 ±25 mm	
Voltage		Volt measurement. The displacement measurement of BEAM_N_N, BEAM_N_S, BEAM_S_N and BEAM_S_S is based on a voltage.

Table 1.4: Composite spandrels: Load steps of monotonic and cyclic loading histories.

Storey drift	Monotonic loading		Cyclic loading	
	LS	Loading velocity [mm/min]	LS	Loading velocity [mm/min]
0.025%	2	0.3	2-5	0.3
0.05%	3	0.3	6-9	0.6
0.1%	4	0.3	10-13	0.9
0.2%	5	0.6	14-17	1.2
0.3%	6	0.6	18-21	1.8
0.4%	7	0.6	22-25	2.4
0.6%	8	1.2	26-29	3.6
0.8%	9	1.2	30-33	4.8
1.0%	10	1.2	34-37	6.0
1.5%	11	2.4	38-41	9.0
2.0%	12	2.4	42-45	12.0
2.5%	13	2.4	46-49	15.0
3.0%	14	2.4	50-53	18.0
4.0%	15	2.4	54-57	18.0

2 Material tests for composite spandrels

Parallel to the quasi-static cyclic tests on the composite spandrel test units, material tests on reinforcement bars, concrete, mortar, bricks and masonry were carried out. The results of these tests are summarised in this chapter. Table 2.1 gives an overview on the construction and testing dates for the spandrel test units and the dates of the material tests. For the quasi-static cyclic tests on the spandrel test units the age at the Day-of-Testing (DoT) refers to the age of the test unit at the first day of testing. The first day of testing started with connecting the actuators to the lever beams. Typically the axial load on the piers was applied the day before the first testing day.

Table 2.1: Construction dates of TU1-5 and dates when spandrel test units and material samples were tested.

Element	TU1	TU2	TU3	TU4	TU5
<i>Test units</i>					
Longit. reinf.	4D12	4D12	4D12	4D16	4D10
Type of loading	monotonic	monotonic	cyclic	cyclic	cyclic
Construction	28.10.2008	20+23.03.2009	20+23.03.2009	14+15.05.2009	14+15.05.2009
Testing date	02-03.03.2009	22.04.2009	28.05-02.06.2009	15-18.06.2009	9-10.07.2009
Age at DoT [d]	125	33	69	32	56
<i>RC beams</i>					
Casting	17.09.2008	15.09.2008	17.09.2008	11.09.2008	11.09.2009
Age at DoT [d]	166	219	252	277	297
Concrete material tests	20.05.2009	20.05.2009	20.05.2009	14.07.2009	14.07.2009
Age at day of material test [d]	245	247	245	306	302
<i>Mortar</i>					
Material tests	27.05.2009	27.05.2009	27.05.2009	14.07.2009	14.07.2009
Age at day of material test [d]	211	68	68	61	61
<i>Bricks</i>					
Material tests	26.10.2009	27.10.2009			
<i>Wallettes</i>					
Compression tests, X-dir	-	see Table 2.11			
Compression tests, Y-dir	-	see Table 2.12			
Shear tests	-	see Table 2.18			

2.1 Reinforcement steel

The RC beams of Test Units 1-5 were built with reinforcement bars of 6, 10, 12 and 16 mm diameter. The 6 mm reinforcement bars were used for the shear reinforcement, the other diameters

2. Material tests for composite spandrels

were used for the longitudinal reinforcement (10 mm: TU5, 12 mm: TU1-3, 16 mm: TU4). For all longitudinal reinforcement bars a steel quality S500C was ordered. Table 2.2 summarises the strength and strain requirements for reinforcing steel of Class B and C according to Eurocode 2 [CEN03].

Table 2.2: Strength and strain requirements for reinforcement steel of Class B and C (from Table C.1 of [CEN03]).

Property	Class B	Class C	Quantile value
Characteristic yield strength f_{yk} or $f_{0.2k}$	400 – 600 MPa	400 – 600 MPa	5%
Ratio of ultimate to yield strength f_{uk}/f_{yk}	≥ 1.08	$1.15 \leq f_{uk}/f_{yk} \leq 1.35$	10%
Characteristic strain at max. force $\varepsilon_{uk} = A_{gt}$	$\geq 5.0\%$	$\geq 7.5\%$	10%

2.1.1 Testing procedure

For the monotonic tensile tests of the reinforcing steel, bars of approximately 85 cm length were cut. The cutting surfaces were ground, the bars were weighted and the exact length of the undeformed bars measured. From these two measurements the effective area of each bar was determined assuming a steel density of $\rho = 7850 \text{ kg/m}^3$. The bars were tested in a Schenk $\pm 480 \text{ kN}$ universal testing machine. The clear length L_c of the specimens in the testing machine was 600 mm. Approximately at the centre of the clear length, an extensometer of type MFI-40 was mounted on the specimen. The extensometer had a gauge length of 300 mm and a displacement range of 20 mm.

The monotonic tensile tests were performed in displacement control. At $\varepsilon = 0.005$ and $\varepsilon = 0.02$ the displacement was held constant for two minutes to allow the stress to drop to a static value. For the D16 bars the latter strain was doubled to $\varepsilon = 0.04$ since $\varepsilon = 0.02$ was still within the yield plateau. At $\varepsilon = 0.007$ the bar was unloaded to about 10% of its yield strength. All aforementioned strain values refer to measurements with the extensometer. The loading velocity was 0.03 mm/s until the end of the unloading and 0.2 mm/s afterwards. The extensometer was dismantled at $\varepsilon = 0.05$ in order to avoid any damage to the instrument. The final stress-strain curve was assembled from the extensometer measurements before dismantling and from the machine stroke after dismantling of the extensometer. The machine stroke was calibrated with the extensometer readings using the elastic branch of the stress-strain curve. The point of dismantling of the extensometer is marked with a cross on the stress-strain curves in Fig. 2.1. Except for four D12 bars, which were tested prior to testing of the spandrels on 18.12.2008, all bars were tested after completion of the test on TU5 on 21.07.2009.

The hoops manufactured of D6 bars were too small to cut specimens of 85 cm length. The hoops of a 600 mm wide RC beam, which had been manufactured together with the 200 mm wide beams but was eventually not used for this test series, were used to cut specimens of approximately 70 cm length. The hoops were straightened by hand taking care that plastic deformations occurred only at the ends of the specimens which would be clamped during the test. For the D6 bars the clear length L_c of the specimens in the testing machine was reduced to 500 mm. The specimens were not perfectly straight. For this reason the length could not be measured exactly and the effective area could not be calculated.

2.1.2 Test results

The following mechanical properties were determined from the stress-strain curves of the monotonic tensile tests on the reinforcement bars. All stress values are based on the nominal area of the bar.

D_{nom}	Nominal diameter.
D_{eff}	Effective diameter. Computed from weight and length of specimen assuming a steel density of $\rho = 7850 \text{ kg/m}^3$.
E_s	Modulus of elasticity: Computed from stress-strain points at $1/3$ and $2/3 f_{y,dyn}$ on the initial loading branch.
$f_{y,dyn}$	Dynamic yield stress: Stress at the transition from elastic behaviour to yield plateau (if present) or stress at 0.2% remaining strain (if no yield plateau present).
$f_{y,stat}$	Static yield stress: Computed as the dynamic yield stress $f_{y,dyn}$ minus the stress drop measured at $\varepsilon = 0.005$.
$f_{t,dyn}$	Dynamic tensile stress: Maximum measured stress.
$f_{t,stat}$	Static tensile stress: Computed as the dynamic tensile stress $f_{t,dyn}$ minus the stress drop measured at $\varepsilon = 0.02$ (D6, D10 and D12 bars) or $\varepsilon = 0.04$ (D16 bars).
A_{gt}	Percentage total elongation at maximum force.

The stress-strain curves of the reinforcement bars are shown in Fig. 2.1. A summary of the mean values and standard deviations of the mechanical properties listed above is given in Table 2.4.

Table 2.4: Mechanical properties of reinforcement bars used for the RC beams (mean values and standard deviations).

Property	D6 bars	D10 bars	D12 bars	D16 bars
# bars	3	6	8	5
D_{nom} [mm]	6	10	12	16
D_{eff} [mm]		10.1 ± 0.004	11.8 ± 0.011	16.0 ± 0.047
E_s [GPa]	215 ± 15.4	202 ± 6.7	187 ± 8.6	206 ± 13.3
$f_{y,dyn}$ [MPa]	586 ± 14.3	535 ± 1.9	540 ± 13.6	505 ± 2.6
$f_{t,dyn}$ [MPa]	634 ± 13.0	646 ± 2.3	630 ± 3.7	616 ± 2.2
$f_{t,dyn} / f_{y,dyn}$	1.08 ± 0.01	1.21 ± 0.01	1.17 ± 0.02	1.22 ± 0.01
$f_{y,stat}$ [MPa]	563 ± 13.6	510 ± 4.4	501 ± 10.5	485 ± 6.1
$f_{t,stat}$ [MPa]	596 ± 17.3	618 ± 2.9	576 ± 2.9	581 ± 4.9
$f_{t,stat} / f_{y,stat}$	1.06 ± 0.01	1.21 ± 0.02	1.15 ± 0.02	1.20 ± 0.02
A_{gt} [%]	4.87 ± 0.36	8.72 ± 0.59	6.83 ± 0.69	12.8 ± 0.58

2. Material tests for composite spandrels

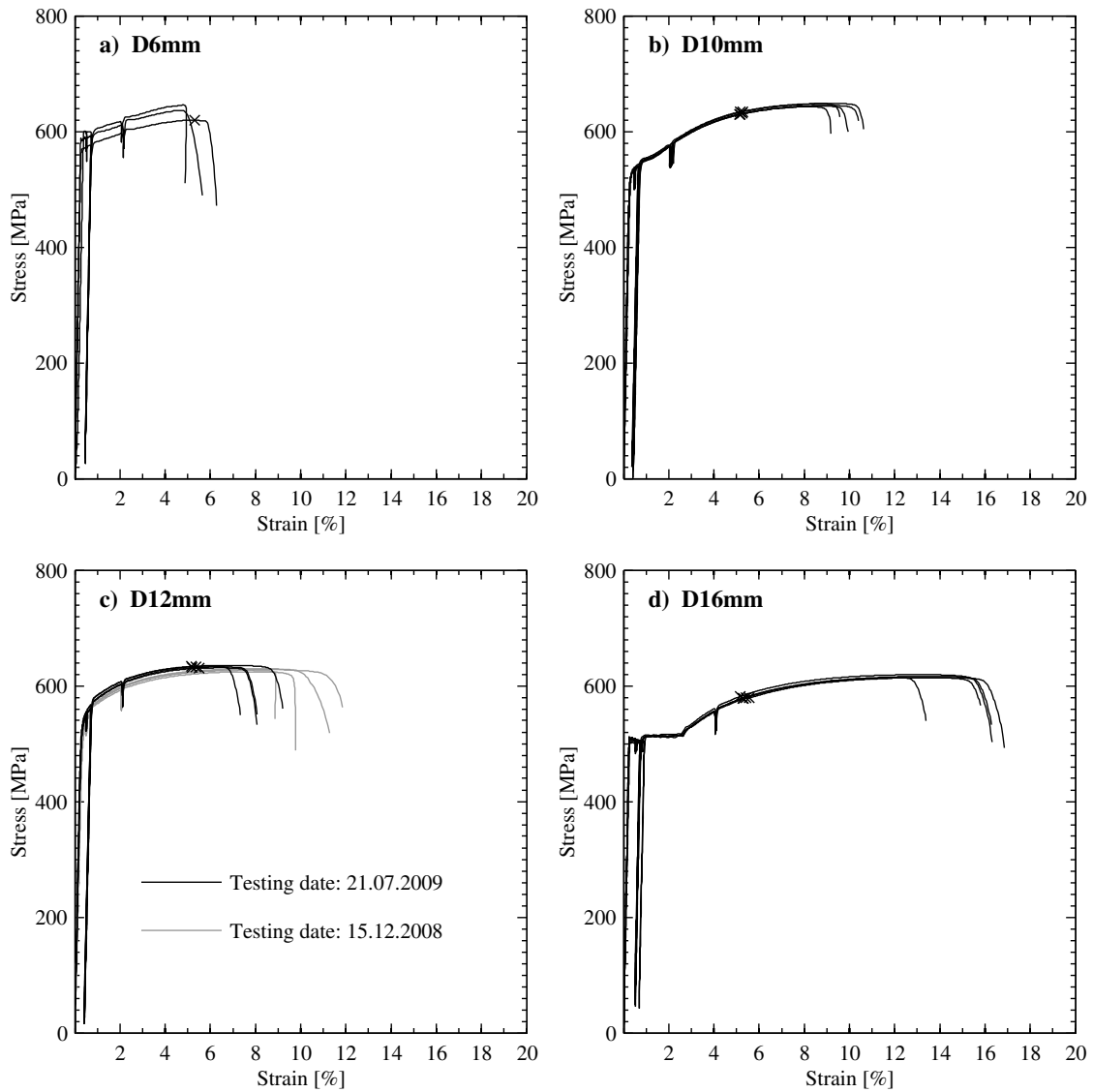


Figure 2.1: Stress-strain curves for D6, D10, D12 and D16 mm reinforcement bars.

2.2 Concrete

This section summarises the mechanical properties of the concrete that was used for the construction of the RC beams that were part of TU1-5. The RC beams were produced by the precast manufacturing company Stüssi AG in Dällikon, Switzerland. The five beams were cast at three different dates in July 2008 (see Table 2.1). The concrete mix included 325 kg/m^3 cement CEM I 42.5N and 130 l/m^3 water; no additives were used. The maximum aggregate size was 32 mm.

2.2.1 Testing procedure

Tests on the concrete specimens were only conducted close to the time of testing the spandrel test units; tests to determine the 28-day-strength were not performed. For each beam the following concrete specimens were cast:

- 4 cylinders with 150 mm diameter and 300 mm height,
- 3 cubes with dimensions of 150x150x150 mm,
- 2 prisms with dimensions of 120x120x360 mm.

For each of the specimens the density was determined. The testing sequence was as follows:

- From the three cubes an average cube compressive strength $f_{c,cube}$ was determined according to SIA162/1 [SIA95] by means of a force-controlled test with a velocity of 0.6 MPa/s.
- Three cylinder were used to determine the E-Modulus according to SIA262/1 [SIA03a], by applying three load cycles between 0 MPa and 1/3 of the mean value of $f_{c,cube}$. The deformation of the cylinder were measured by means of two potentiometers that were aligned with the cylinder axis and mounted at opposite sides of the cylinder (Figure 2.2a). The modulus of elasticity E_{cm} was determined from the third cycle.
- The same three cylinders were used to determine the cylinder compressive strength f_c .
- The remaining cylinder was cut in half and on each of these 2 cylinders with a height of 150 mm a double-punch test [Che70] for determining the tensile strength of the concrete was carried out. The test setup is shown in Figure 2.2b.
- The tensile strength of the concrete was also determined from the two prisms by means of a 3-point-bending test with a clear span of 300 mm. The test was force-controlled and conducted with a velocity of 0.05 kN/s. The tensile strength was computed as the stress at the edge of the prism assuming a linear stress profile at the peak force obtained during the test.

All tests were conducted on a Walter & Bai universal testing machine. Note that the RC beams of TU2 and TU3 were cast from the same concrete batches. For these two test units the concrete strengths were therefore assumed as identical. One of the cylinder specimens for TU5 broke in two. For this reason only one double-punch test could be performed for TU5.

2.2.2 Test results

Table 2.5 summarises the mean values and standard deviations of the density of the concrete specimens. In this table also the number of specimens evaluated for each type of test is given. The mean values and standard deviations of the concrete properties are summarised in Table 2.6. The mean ratios of $f_c/f_{c,cube}$ vary between 0.85 – 0.90 and are therefore very similar to the ratios predicted by the commonly used equation $f_c = 0.85f_{c,cube}$.

Two different tests were used to determine the tensile strength f_{ct} of the concrete, i.e. the 3-point-bending test and the double-punch test. Apart from the specimens for TU5, f_{ct} obtained from the double-punch test is always around half than f_{ct} obtained from the 3-point-bending test. In [BDP08] it was found that the double-punch test yielded a similar tensile strength as a direct

2. Material tests for composite spandrels

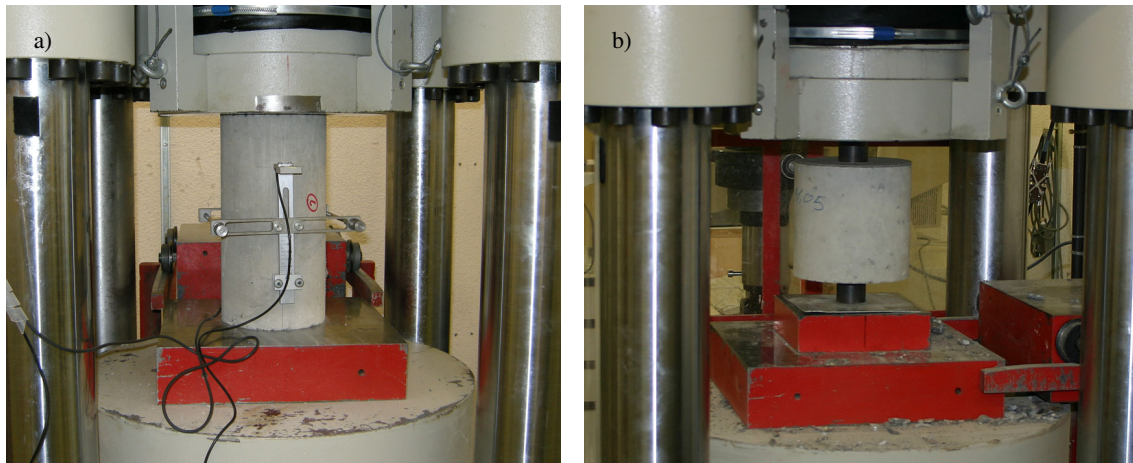


Figure 2.2: Setup for determining the E-Modulus of concrete (a) and for carrying out the double-punch test (b).

tensile test while the 3-point-bending test typically yielded higher strengths. The latter finding also applies to the concrete tensile strength tests conducted here.

Table 2.5: Concrete tests: Number of concrete specimens tested and mean values and standard deviations of the concrete density.

Specimen		TU1+3	TU2	TU4	TU5
Cubes	Density [kg/m ³]	2310 ± 12.2	2330 ± 9.3	2293 ± 7.9	2303 ± 18.1
	# specimens	6	3	3	3
Cylinders for f_c and E_{cm}	Density [kg/m ³]	2336 ± 17.6	2338 ± 14.1	2331 ± 6.0	2338 ± 14.1
	# specimens	6	3	3	3
Cylinders for double-punch test	Density [kg/m ³]	2324 ± 25.6	2312	2318	2319
	# specimens	4	2	2	1
Prisms for 3-point-bending test	Density [kg/m ³]	2343 ± 27.6	2371	2394	2396
	# specimens	4	2	2	2

Table 2.6: Concrete tests: Mechanical properties of concrete (mean values and standard deviations).

Property	TU1+3	TU2	TU4	TU5
Cube strength $f_{c,cube}$ [MPa]	39.2 ± 1.55	37.8 ± 1.13	35.6 ± 1.05	36.7 ± 1.35
Cylinder strength f_c [MPa]	35.2 ± 1.59	33.4 ± 1.62	30.2 ± 0.75	31.4 ± 0.53
Modulus of elasticity E_{cm} [GPa]	31.0 ± 1.79	30.0 ± 0.43	27.8 ± 0.56	29.1 ± 1.03
Tensile strength f_{ct} from double punch test [MPa]	3.38 ± 0.32	3.36	2.79	2.62
Tensile strength f_{ct} from 3-point bending test [MPa]	6.20 ± 0.16	6.49	5.39	7.04

2.3 Mortar

For the construction of the first test unit a different type of mortar was used than for the construction of the other tests units. For TU1 the mortar Kelit 110 was used, which is often used

for facades and which has a higher tensile strength than ordinary mortar. For TU2-5 the mortar Maxitmur 920 was used. Maxitmur 920 is one of the most frequently used mortars in Switzerland (information from HG Commerciale, a Swiss building material supplier). It is a portland cement based mortar for bearing and non-bearing standard brick, lime stone and concrete masonry. Figure 2.3a shows a photograph of a batch of fresh Maxitmur 920 mortar used for the construction of TU2 and TU3.

2.3.1 Testing procedure

During the construction of each test unit several samples of mortar were taken and steel moulds with dimensions of 40x40x160 mm filled. The mortar was compacted by lifting alternately one side of the mould by a couple of centimeters and letting it fall down. The mortar was stored in a climatized room (20°C, 95% humidity) for one day. It was then removed from the mould and stored together with the test units in the structural engineering laboratory.

For each prism the density and the tensile strength f_{ctm} were determined. The tensile strength was determined from a 3-point-bending test with a loading velocity of 0.05 kN/s and a clear span of 100 mm. The tensile strength was computed as the stress at the edge of the prism assuming a linear stress profile at the peak force obtained during the test. The prisms broke approximately in half. With the two halves, cube tests with a loading velocity of 0.6 MPa/s were performed and the cube strength f_{cm} determined. The material tests on the mortar samples were performed at about the same time as the spandrel test units and the masonry wallettes, respectively, were tested (see Table 2.1). The masonry wallettes were used for compression tests and shear tests (see Sections 2.5 and 2.6).

2.3.2 Test results

The mechanical properties of the mortar samples are summarised in Table 2.7. The field "Age" refers to the age at the day of the tests on the prisms and cubes. The Swiss Code for masonry structures SIA266 [SIA05] requires a minimum characteristic value for the compressive strength of mortar of 5.0 MPa. The smallest compressive strength that was obtained for the Maxitmur 920 mortar samples was 9.0 MPa. For the Kelit 110 mortar samples the minimum obtained compressive strength was 13.1 MPa. Figure 2.3b shows the tensile strength plotted against the compressive strength of the mortar for all prisms tested. The compressive strength was determined as the average of the two cube strengths obtained for one prism. The results show that the tensile strength can be estimated as approximately one quarter of the compressive strength.

2. Material tests for composite spandrels

Table 2.7: Mortar tests for TU1-5 and masonry wallettes: Mechanical properties of mortar (mean values and standard deviations).

Test unit / Wallette	Mortar	# prisms	# cubes	Age [d]	Density [kg/m ³]	f_{ctm} [MPa]	f_{cm} [MPa]
TU1	Kelit 110	4	8	211	1720 ± 63.5	4.64 ± 0.33	16.5 ± 3.20
TU2 + 3	Maxit 920	9	18	68	1670 ± 23.2	2.47 ± 0.68	11.4 ± 2.25
TU4	Maxit 920	6	12	61	1670 ± 20.9	3.21 ± 0.28	12.2 ± 0.88
TU5	Maxit 920	5	12	61	1660 ± 31.4	2.86 ± 0.17	12.1 ± 0.90
Wallettes TU1	Kelit 110	2	4	210	1770	4.92	19.2 ± 1.87
Wallettes TU2+3	Maxit 920	3	6	113	1640 ± 20.8	2.11 ± 0.50	9.9 ± 1.41
Wallettes TU4+5	Maxit 920	6	12	60	1680 ± 14.5	3.22 ± 0.45	13.4 ± 0.89
Wallettes shear tests	Maxit 920	3	6	82	1670 ± 10.2	2.80 ± 0.22	10.8 ± 1.81

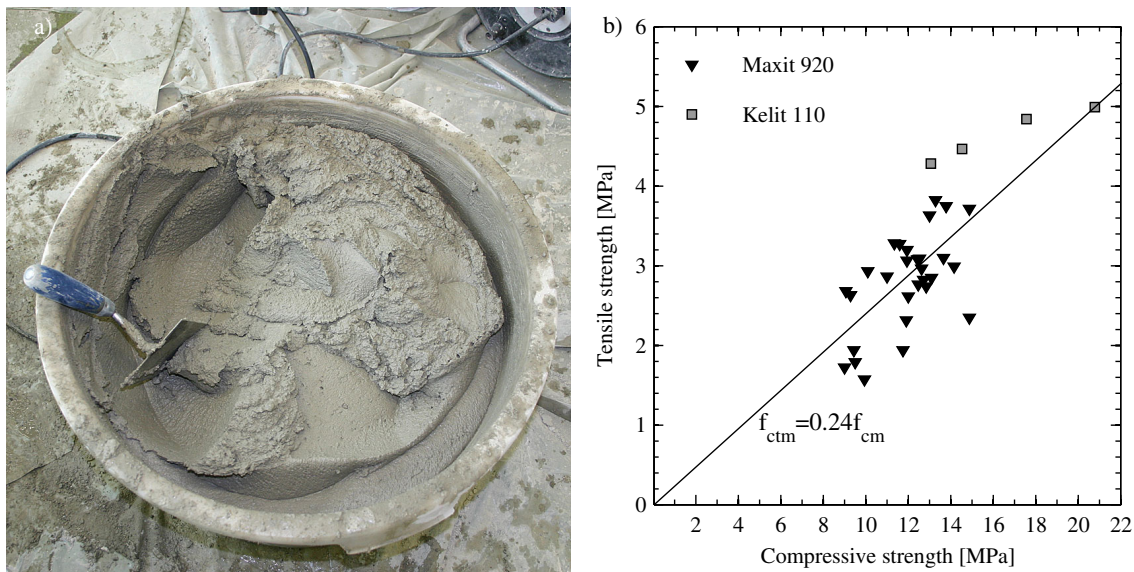


Figure 2.3: Photo of fresh Maxitmur 920 mortar (a) and relationship between compressive and tensile strength of mortar (b).

2.4 Bricks

This section summarises the mechanical properties of the brick units that were used for the construction of the test units TU1-5 and for the small wallettes, which were used to determine the masonry strengths (see Sections 2.5 and 2.6). For the construction of the first test unit TU1, a different type of bricks was used (Brick Type 1) than for the construction of the other tests units (Brick Type 2). All brick units had nominal dimensions of 290x200x190 mm. With bed and head joints of 10 mm, the layout of the masonry was 300x200x200 mm (LxHxT). Table 2.8 summarises the nominal dimensions and the effective areas for each brick. The values given in Table 2.8 were obtained by own measurements carried out on one brick per type, hence they have merely an indicative character. Photos of the bricks are shown in Fig. 2.4. The following coordinate system will be used to describe the properties of the bricks along its three axes: (i) the x -axis points upwards, i.e. it is parallel to the height of the brick, (ii) the y -axis points in the longitudinal direction of the brick and (iii) the z -axis points in its transverse direction.

The main difference between the two types of bricks concerns the hole pattern: While the hole pattern of Brick Type 1 is such that none of the inner webs in longitudinal (y) direction is continuous, all the longitudinal webs of Brick Type 2 are continuous. These webs are necessary to carry the in-plane shear force of the masonry piers and spandrels. They also affect the tensile strength of the bricks. A discussion with the brick manufacturer revealed, that the hole pattern of Brick Type 1 results in smaller thermal stresses and therefore in fewer cracks and a better preservation of the brick shape after the cooling process. In fact, it was also observed that bricks of Type 2 had considerably more initial cracks than those of Brick Type 1. These cracks were mainly vertical and occurred both in the inner and outer webs. For TU2, which was the first test unit tested with bricks of Brick Type 2, the initial cracks were marked (see Section 3.3.1). The Swiss masonry design code SIA266 [SIA05] does not regulate the form of the webs and therefore both brick types are used in Switzerland without giving it any particular consideration. On the contrary, the Italian seismic design code [OPC03] specifies explicitly that only bricks with continuous longitudinal webs may be used for seismic applications. Masonry with bricks of Type 1 would therefore not be admissible in Italy.

Table 2.8: Brick tests: Nominal dimensions, effective cross-sectional areas and web thicknesses of the bricks.

Dimensions	Brick Type 1 (TU1)	Brick Type 2 (TU2-5)	Ratio Type 2/ Type 1
Nominal length [mm]	290	290	
Nominal width [mm]	200	200	
Nominal height [mm]	190	190	
Ratio area of holes / gross area	42%	36%	0.86
Thickness of continuous webs in longit. dir. (y -dir.) [mm]	23	76	3.30
Ratio thickness of cont. webs in longit. dir. / width (200 mm)	12%	38%	
Thickness of continuous webs in transv. dir. (z -dir.) [mm]	92	106	1.15
Ratio thickness of cont. webs in transv. dir. / width (290 mm)	32%	37%	

2.4.1 Testing procedure

Compression and tension tests were carried out on the bricks. For the compression tests bricks were subjected to unidirectional loading along (i) their height (x -direction) and (ii) their longitudinal direction (y -direction). The tensile strength of the bricks was determined by means of 3-point-bending tests. In the following the testing procedures applicable to the three types of tests are described. All tests were conducted on a Walter & Bai universal testing machine.

The compressions tests in the x - and the y -direction were carried out according to EN772-1 [CEN00]. For the compression tests in the x -direction the top and bottom surface of the bricks were loaded. To ensure an even load introduction, the bed surfaces of the bricks were prepared by wet grinding. The bricks were then stored for ten days in the structural engineering laboratory to dry out. At the end of the drying period the outer dimensions and the weight of the bricks were measured. To determine the E-Modulus E_{bx} and the Poisson's ratio ν_{bx} Demec measurements were carried out at two load levels. These were: (i) for the bricks of Type 1: $1/3$ and $2/3 f_{c,bx}$ and (ii) for the bricks of Type 2: zero load and $1/3 f_{c,bx}$. The load levels were changed after testing the bricks of Type 1 because the standard method for determining the E-Modulus considers the stress and strain increments between zero load and $1/3 f_{c,bx}$; this was overseen when testing the

2. Material tests for composite spandrels

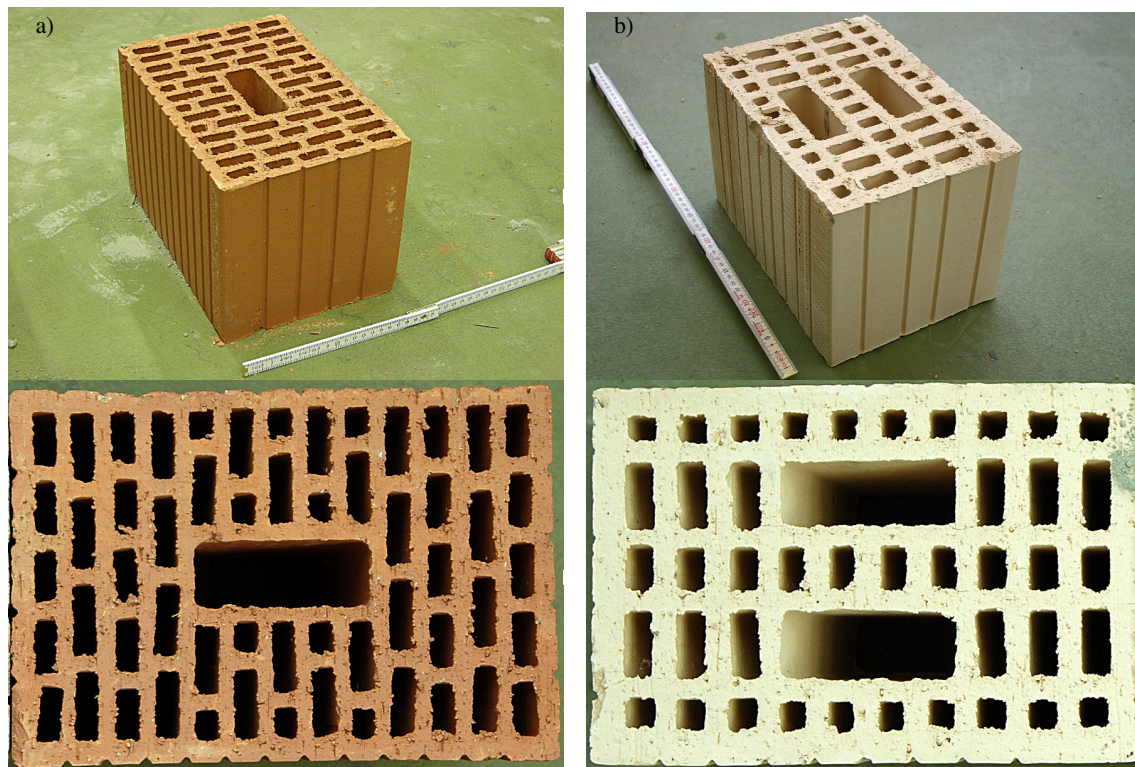


Figure 2.4: Brick types used for the composite spandrels: Brick Type 1, which was used for TU1 (a), and Brick Type 2, which was used for TU2-5 (b).

bricks of Type 1. Four Demec points were glued onto each head face of the bricks (Fig. 2.5a) in order to measure the deformation of the bricks over base lengths of 150 mm. The load was applied in displacement control with a velocity of 0.01 mm/s. At the load levels at which the Demec measurements were taken, the deformation was maintained constant and the Demec measurements were taken once a constant load level was reached. It took generally about a minute to reach a constant load after the piston of the testing machine was stopped. The compressive strength was computed as the maximum measured force divided by the nominal cross-sectional area of the loaded face of the brick. The E-Modulus was computed from the averaged vertical Demec measurements on the front and back face and the Poisson's ratio was computed from the averaged horizontal and vertical Demec measurements.

For the bricks of Type 1 (TU1) six bricks were tested in the x -direction while for the bricks of Type 2 (TU2-5) four bricks were tested in the x -direction. Demec measurements were not taken for the first brick of each group and only the compressive strength $f_{c,bx}$ was determined for this brick. This strength was then used to determine the load levels for the Demec measurements of the bricks that were subsequently tested. One other brick of Type 1 crashed while holding the load at $2/3f_{c,bx}$; this brick was therefore disregarded when computing the E-Modulus and the Poisson's ratio. The E-Modulus and the Poisson's ratio for loading in the x -direction are therefore based on four and three test results for bricks of Type 1 and 2, respectively. The compressive strength $f_{c,bx}$ is based on six and four test results for bricks of Type 1 and 2, respectively.

The compression tests in the y -direction were carried out in a similar way as the tests in the x -direction. To ensure an even load introduction the two head faces were grinded. Demec points were glued onto both sides of the bricks (Fig. 2.5b). The base lengths of the Demec measurements were again 150 mm. Since the strength of the bricks is smaller in the y -direction than in the x -direction, the loading velocity was reduced to 0.0025 mm/s. For both brick types four bricks were tested in the y -direction. For the first brick of each group no Demec measurements were taken and only the compressive strength $f_{c,by}$ was determined. This strength was then used to determine the load levels for the Demec measurements of the bricks that were subsequently tested. The E-Modulus and Poisson's ratio for loading in the y -direction are therefore based on three test results for both types of bricks.

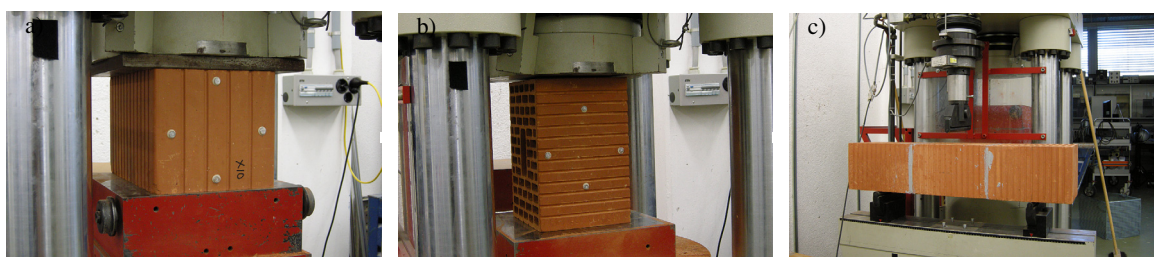


Figure 2.5: Brick tests: Setup for determining the compressive strength, E-Modulus and Poisson's ratio of bricks in the x -direction (a) and in the y -direction (b) and the setup for the 3-point-bending test (c).

The test for determining the tensile strength of the bricks is not codified. It was developed ad-hoc to gain with a simple test setup an estimate of the tensile strength of the bricks. The tensile strength of the brick units was determined by means of a 3-point-bending test with a clear span of 600 mm (Fig. 2.5c). The test specimens for this test were constructed by gluing three bricks at their head faces together. The adhesive Araldite AW2101/HW2951 was used for this purpose and proved to work well, since none of the glued surfaces failed. Before glueing the bricks together, the outer dimensions and the weight of the middle brick were determined. The tests were conducted with a loading velocity of 0.025 kN/s, which for the chosen setup corresponded to a stress rate of 0.003 MPa/s at the extreme fibres at midspan (assuming gross sectional properties when computing the stress distribution). The tensile strength was computed as the maximum bending moment divided by the section modulus W of the middle brick assuming gross sectional properties, i.e. $W = bh^2/6$.

2.4.2 Test results

Table 2.9 summarises the mean values and the standard deviations for the density of bricks as well as the number of specimens tested. The mean values and standard deviations of the brick properties are given in Table 2.10. The same table also summarises the ratios of the values obtained for the bricks of Type 1 and 2. In the following the different results for bricks of Type 1 and Type 2 are discussed.

The main difference between the bricks of Type 1 and Type 2 concerned the hole pattern (Fig. 2.4). The compressive strength for loading in the x -direction (i.e. in the direction of the height of the bricks) was in average 25% larger for bricks of Type 2 than bricks of Type 1. Part of

2. Material tests for composite spandrels

this larger strength can be attributed to the 4% larger net cross section. The main reason, however, for the larger compressive strength of Brick Type 2 is its larger tensile strength. Compression failure is typically related to a tension failure in directions orthogonal to the loading direction, i.e. in the transverse and longitudinal directions (y - and z -direction). In both directions the effective web thicknesses of Brick Type 2 are considerably larger than those of Brick Type 1. Photos of the failure mode of bricks tested in the x -direction are shown in Fig. 2.6. The effect of the continuous webs is even more apparent when considering the longitudinal direction of loading (y -direction): For this direction of loading, the strength of Brick Type 2 was approximately 2.5 times as large as the strength of Brick Type 1. Bricks of Type 1 carried the load mainly through their outer webs. Due to their honeycomb forms, the inner webs were most likely considerably softer and carried therefore only very little load. Photos of the failure modes when loading in the longitudinal direction are shown in Fig. 2.7. Figure 2.8 shows the correlation of E-Modulus and compressive strength for the two directions of loading. The trend lines were obtained as best fit lines with zero intercept. For both types of bricks the obtained correlation coefficients for the two directions of loading that were tested are relatively similar.

Table 2.9: Brick tests: Number of bricks tested and mean values and standard deviations of the density of the bricks.

Specimen		Brick Type 1 (TU1)	Brick Type 2 (TU2-5)
Bricks tested in the x -direction	Density [kg/m ³]	926 ± 4.8	940 ± 19.9
	# specimens	7	4
Bricks tested in the y -direction	Density [kg/m ³]	916 ± 7.5	932 ± 5.6
	# specimens	6	4
Bricks tested in bending	Density [kg/m ³]	930 ± 4.9	948 ± 15.4
	# specimens	4	3

Table 2.10: Brick tests: Mechanical properties of Brick Type 1 and Brick Type 2 (mean values and standard deviations).

Property	Brick Type 1 (TU1)	Brick Type 2 (TU2-5)	Ratio Type 2/ Type 1
Tests in the x -direction			
Compressive strength $f_{c,bx}$ [MPa]	24.7 ± 3.2	30.9 ± 3.1	1.25
E-Modulus E_{bx} [GPa]	8.38 ± 1.16	14.0 ± 3.80	1.91
Poisson's ratio ν_{bx} [-]	0.20 ± 0.05	0.09 ± 0.05	0.45
Tests in the y -direction			
Compressive strength $f_{c,by}$ [MPa]	3.45 ± 0.24	8.92 ± 1.23	2.58
E-Modulus E_{by} [GPa]	2.13 ± 0.48	6.12 ± 1.86	2.87
Poisson's ratio ν_{by} [-]	0.10 ± 0.07	0.26 ± 0.18	2.60
3-point-bending tests			
Tensile strength f_{tb} [MPa]	0.72 ± 0.03	1.39 ± 0.29	1.92

The tensile strength of the bricks of Type 2 is in average about 1.9 times as large as the tensile strength of bricks of Type 1. This can again be attributed to the difference in continuous web thicknesses of the two types of bricks. It is, however, interesting to note that although the width of the continuous webs of Brick Type 2 is 3.3 times as large as those of Brick Type 1, the tensile strength is only 1.9 times as large. Reasons for this observations could be: (i) The non-continuous webs of Brick Type 1 contribute to some extent to the tensile strength of the brick. A small

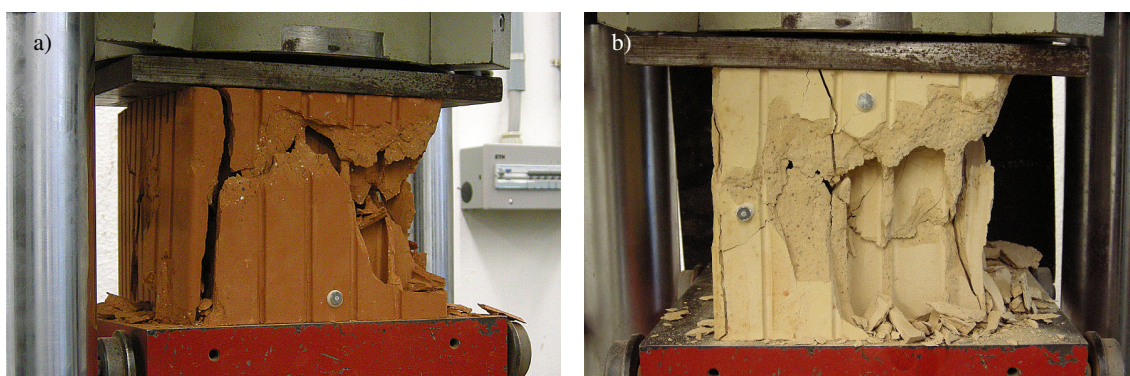


Figure 2.6: Failure modes of bricks tested in the x -direction for Brick Type 1 (a) and Brick Type 2 (b).

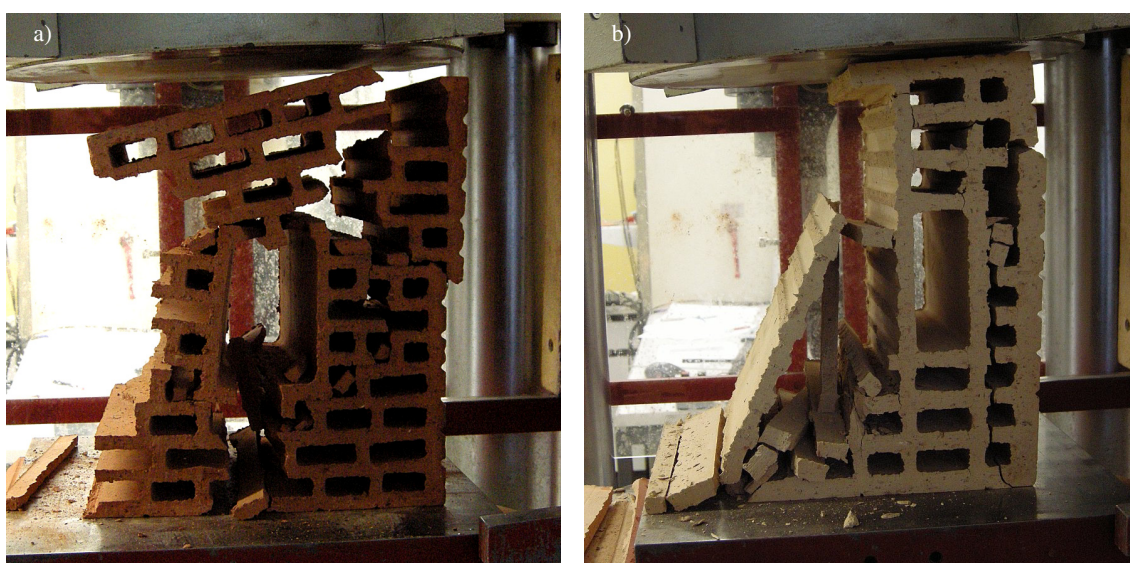


Figure 2.7: Failure modes of bricks tested in the y -direction for Brick Type 1 (a) and Brick Type 2 (b).

contribution of these webs was also observed for the compressive strength in the y -direction. (ii) The initial vertical cracks in bricks of Type 2 that were caused by the stresses generated during the cooling process seemed to influence the failure of the bricks in the 3-point bending tests. The specimens tested with bricks of Type 1 failed always approximately at mid span by a vertical crack (Figs. 2.9a and b) while the specimens with bricks of Type 2 failed not exactly at midspan but at the location of the initial crack nearest to the midspan. This is shown in Figs. 2.9c and d. One can therefore assume that the initial cracks reduced the tensile strength of the bricks of Type 2.

2. Material tests for composite spandrels

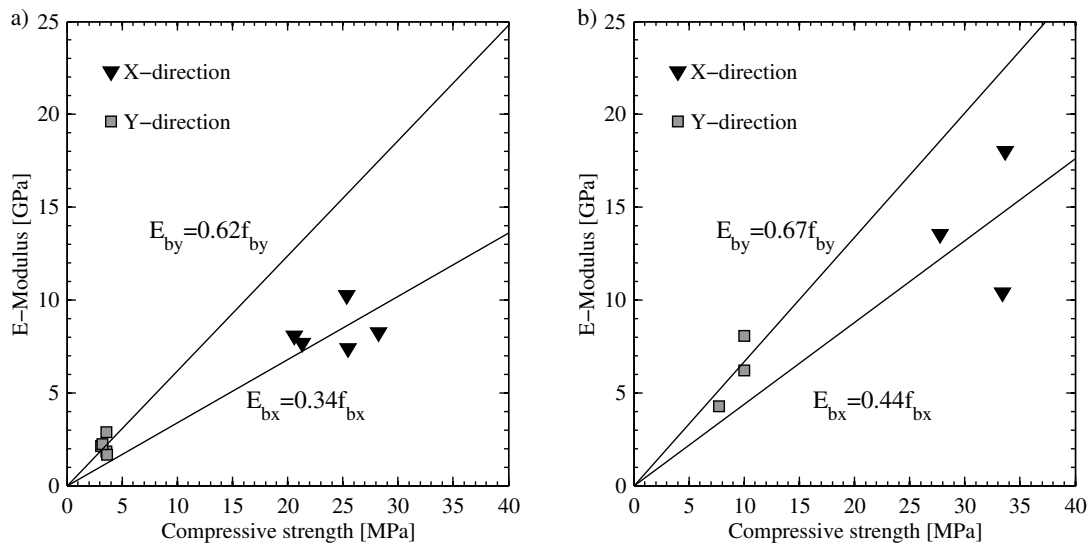


Figure 2.8: Correlation between E-Modulus and compressive strength for Brick Type 1 (a) and Brick Type 2 (b).

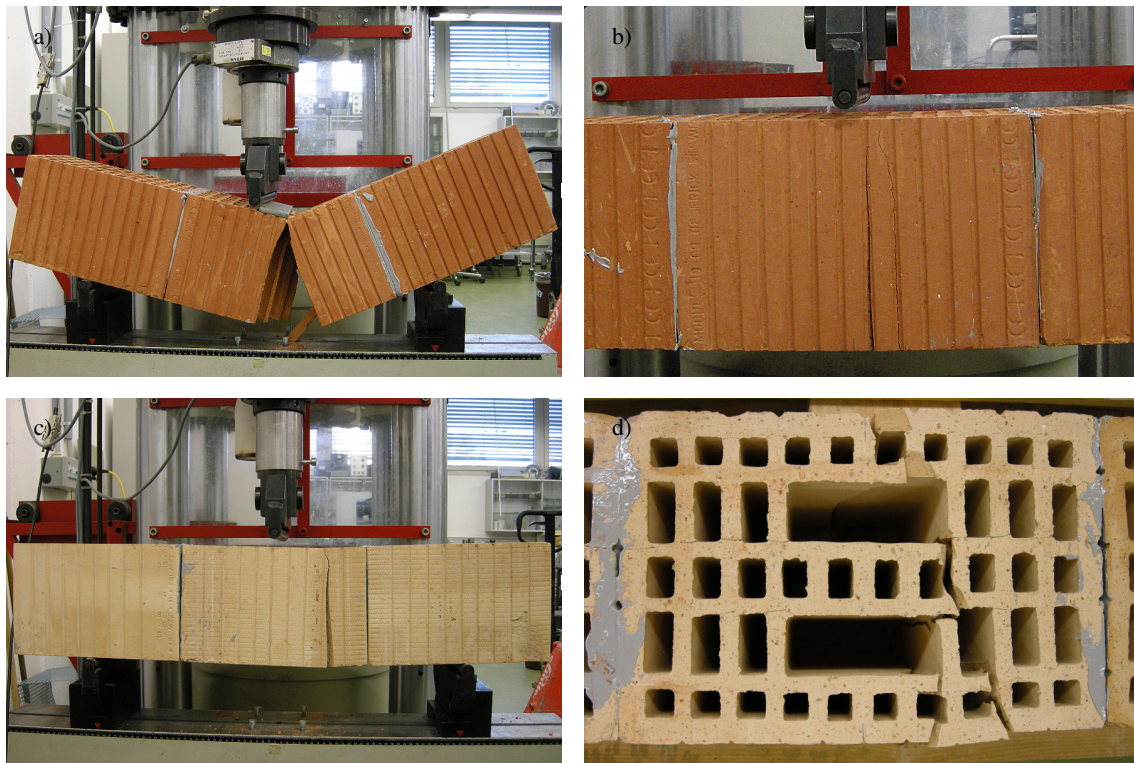


Figure 2.9: Composite spandrels: Failure modes of bricks tested under 3-point bending for Brick Type 1 (a and b) and Brick Type 2 (c and d).

2.5 Compression tests on masonry wallettes

To determine the properties of the masonry, three different types of tests were carried out on small masonry wallettes. These were: (i) compression tests with loading orthogonal to the bed joints, (ii) compression tests with loading parallel to the bed joints and (iii) shear tests. This section presents the test setup, instrumentation, testing procedure and results for the first two types of tests; the shear tests are presented in Section 2.6. The composite spandrel test units were constructed in three groups. First, TU1 was constructed. TU2 and TU3 were constructed at the same time and also TU4 and TU5 were constructed together. At the end of each of these three construction periods, the masonry wallettes for the compression tests were built using the same type of bricks and mortar that had been used for the spandrel test units.

Compression tests were carried out orthogonal to the bed joints (x -direction) and parallel to the bed joints (y -direction). The tests in the x -direction were carried out according to EN1052-1 [CEN98]. The European Standards do not include tests parallel to the bed joints. For this reason, these tests were carried out according to SIA266/1 [SIA03b]. The test setup, the testing procedure and the instrumentation were, however, for both tests similar. Apart from the loading direction, the tests differed only regarding the size of the wallettes and the baselengths of the LVDT measurements. Note that SIA266/1 allows for the compression tests parallel to the bed joints the application of a horizontal precompression of 10% of the characteristic strength in the x -direction. The application of this horizontal precompression is not mandatory but is admissible. The idea of this precompression originated from the stress situation in piers where an axial load is always present. However, in spandrels this assumption does not hold and for this reason the precompression was not applied.

Figure 2.10 shows the nominal dimensions of the masonry wallettes constructed for the two types of tests. Both types of wallettes were of course constructed with the bed joints parallel to the floor. The wallettes for the tests in the y -direction were turned when installing them on the test stand. The wallettes used for the compression tests in the x -direction consisted of five courses of masonry in running bond. The wallettes used for the compression tests in the y -direction consisted of four courses of masonry laid in running bond. Tables 2.11 and 2.12 summarise the construction dates of the wallettes used for the compression tests and the test programme, respectively. A total of 17 compression tests were conducted. One test unit (MX103) broke during transportation.

Table 2.11: Dates of construction and testing of masonry wallettes tested orthogonal to the bed joints (x -direction).

Test unit	Walette	Construction date	Testing date	Age [d]
TU1	MX101	29.10.2008	06.07.2009	248
	MX102	29.10.2008	07.07.2009	249
	MX103	29.10.2008	Broken	-
TU2+3	MX201	23.03.2009	29.06.2009	97
	MX202	23.03.2009	30.06.2009	98
	MX203	23.03.2009	02.07.2009	101
TU4+5	MX301	15.05.2009	09.07.2009	48
	MX302	15.05.2009	14.07.2009	53
	MX303	15.05.2009	15.07.2009	54

2. Material tests for composite spandrels

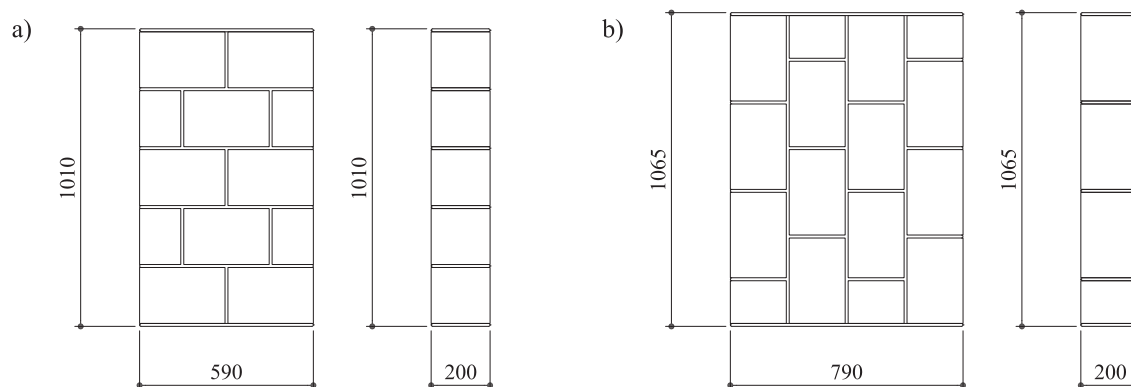


Figure 2.10: Nominal dimensions of masonry wallettes for compression tests orthogonal to the bed joints (*x*-direction, a) and parallel to the bed joints (*y*-direction, b).

Table 2.12: Dates of construction and testing of masonry wallettes tested parallel to the bed joints (*y*-direction).

Test unit	Wallette	Construction date	Testing date	Age [d]
TU1	MY101	29.10.2008	18.07.2009	260
	MY102	29.10.2008	22.07.2009	264
	MY103	29.10.2008	28.07.2009	270
TU2+3	MY201	23.03.2009	29.07.2009	127
	MY202	23.03.2009	30.07.2009	128
	MY203	23.03.2009	04.08.2009	133
TU4+5	MY301	15.05.2009	05.08.2009	74
	MY302	15.05.2009	06.08.2009	75
	MY303	15.05.2009	07.08.2009	76

2.5.1 Test setup, testing procedure and instrumentation

Figures 2.11 and 2.12 show the setup for the compression tests. The axial load was applied by means of a flat jack that was placed between two transfer beams. The test units were placed between the lower transfer beam and the strong floor. For two test units (MX201 and MX202) the test setup was slightly modified and two flat jacks were placed next to each other between the two transfer beams. This modification had been performed because some slight bending of the test units had been observed during the first two tests (MX101 and MX102). The bending had manifested itself in unequal measurements of the four linear variable differential transformers (LVDTs) that recorded the axial deformation (Fig. 2.13). However, it was found that the modified test setup did not improve the obtained results and for this reason the initial test setup with one flat jack was used again from test MX203 onwards.

In order to monitor the behaviour of the test units during testing, the following instrumentation was used:

- Six LVDTs to measure the vertical and horizontal deformations of the test unit. On each face of the wallette two LVDTs were mounted to measure the vertical deformation and one LVDT to measure the horizontal deformation.
- One compression load cell to measure the axial force applied to the test unit.
- One pressure meter to measure the oil pressure induced by the hand pump during the test. It was used as a redundant measurement of the compression force applied to the test unit.

A list of all the employed instruments is given in Table 2.13. Drawings of the instrumentation layouts for the compression tests in the x - and in the y -direction are shown in Fig. 2.13.

Table 2.13: Compression tests on masonry wallettes: List of hard-wired channels.

Channel name	Instrument type	Description of measured quantity
EN	LVDT ± 10 mm	Vertical deformation, North LVDT on East face
ES	LVDT ± 10 mm	Vertical deformation, South LVDT on East face
WN	LVDT ± 10 mm	Vertical deformation, North LVDT on West face
WS	LVDT ± 10 mm	Vertical deformation, South LVDT on West face
HE	LVDT ± 10 mm	Horizontal deformation on East face
HW	LVDT ± 10 mm	Horizontal deformation on West face
FORCE	Load cell	Compression load cell between transfer beams
PRESSURE	Pressure metre	Pressure metre to monitor pressure in hydraulic system

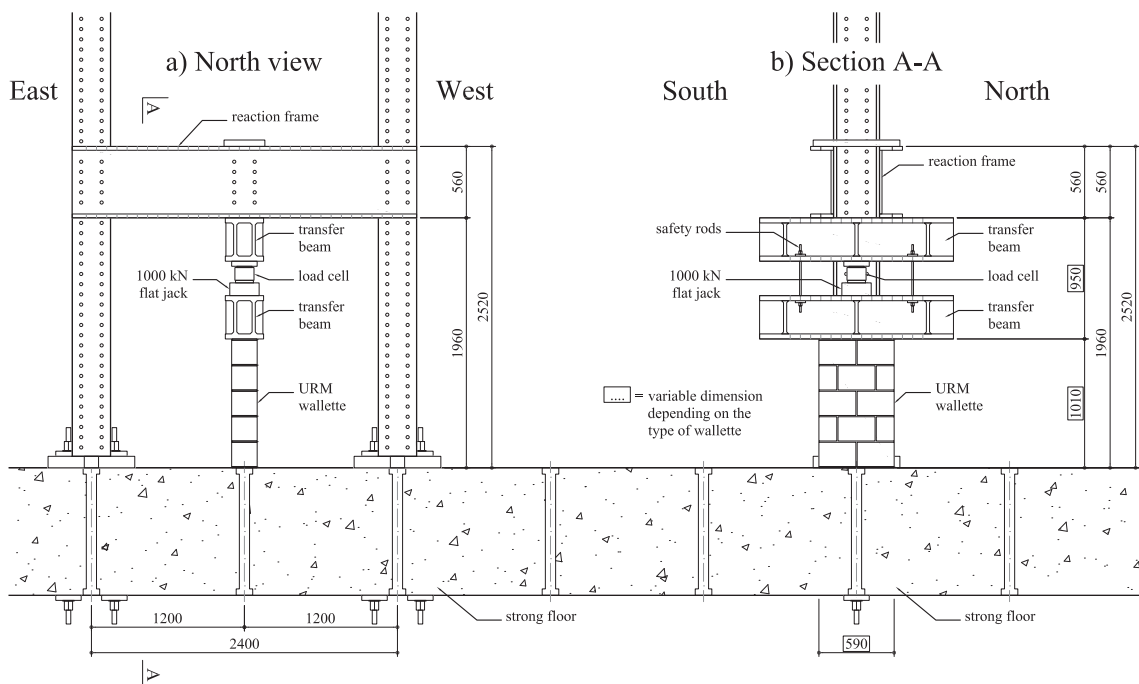


Figure 2.11: Drawing of the test setup for the compression tests on the masonry wallettes.

The procedure for the compression tests was as follows:

- The test unit was placed in the correct position under the reaction frame. The top and bottom surfaces of the unit were levelled using a mortar layer with a thickness of a few millimetres to

2. Material tests for composite spandrels

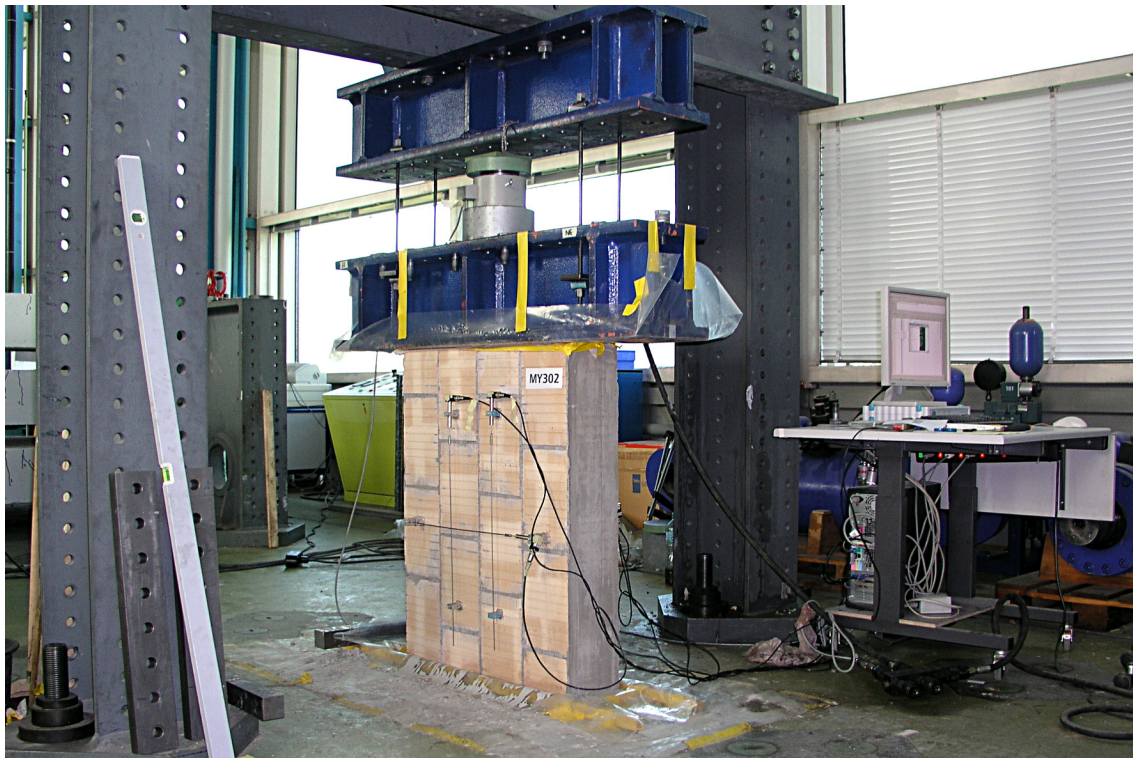
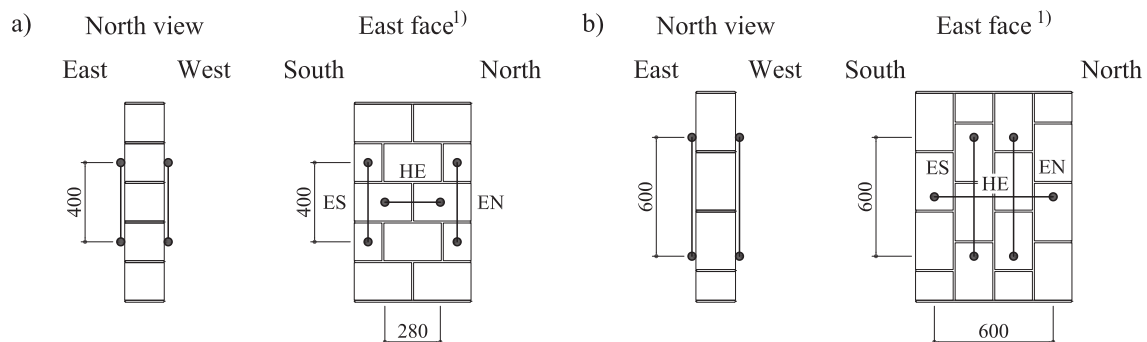


Figure 2.12: Photo of the test setup for the compression tests on the masonry wallettes.



¹⁾ Devices WS, WN and HW mounted analogously on the West face of both types of wallettes

Figure 2.13: Instrumentation for the compression tests on the masonry wallettes for tests in the x -direction (a) and tests in the y -direction (b).

ensure a better bearing surface for the lower transfer beam and for the strong floor. Particular attention was paid to the alignment of the wallette with the transfer beams.

- The LVDTs were mounted on each face of the test unit and the hard-wired measuring system was set up. All hard-wired instruments were set to zero.
- The axial force was applied using a hand-pump at an average rate of approximately 0.01 MPa per second (average axial stress acting on the wallette). The test unit was continuously loaded until failure.

2.5.2 Failure modes

Figures 2.14 and 2.15 show photos of the failure modes of the wallettes tested in compression. Failure initiated typically with the formation of vertical cracks in the bricks and mortar joints. For both directions of loading, the wallettes failed due to crushing of the outer brick shell. For loading orthogonal to the bed joints (x -direction), crushing was typically concentrated in the top half of the wallette. Photos of the failure modes of all wallettes except MX202, for which no photo was taken, are shown in Fig. 2.14. There were no significant differences in the behaviour of the wallettes constructed with bricks of Type 1 (MX101-103) and the wallettes constructed with bricks of Type 2 (MX201-203, MX301-303).

For loading parallel to the bed joints (Fig. 2.15) failure occurred often at the very top of the wallette, just underneath the load transfer beam. For test units MY101-103, which were built with bricks of Type 1, vertical cracks were dominant, which then also led to horizontal cracks. The wallettes MY201-203 and MY301-303 failed due to the formation of horizontal and diagonal cracks in the outer masonry shells, cracking along vertical mortar joints and at ultimate load due to crushing of the brick units that were in contact with the transfer beam.

2.5.3 Test results

This section summarises the results obtained from the hard-wired instruments. Before the results are presented for the compression tests in the x - and the y -direction, the post-processed quantities are defined.

The compressive strength of a test unit (f_{mx} and f_{my}) was defined as the maximum force divided by the nominal area. For the tests in the x - and the y -direction the nominal area is 590x200 mm and 790x200 mm, respectively. The measurements obtained from the load cell were considered as the more accurate readings and for this reason they are used in all the subsequent plots. To confirm the measurements obtained by means of the load cell, the maximum strength was also computed from the pressure metre readings. These quantities are annotated with f'_{mx} and f'_{my} in Tables 2.14 and 2.16, respectively. The hydraulic flat jack had a capacity of 1000 kN at 505 bar. Based on the pressure readings the force in [kN] applied to the wallette was therefore computed as the measured pressure times 1000/505.

The axial strain was computed as the average strain obtained from the four instruments measuring the vertical deformation (EN, ES, WN and WS, see Fig. 2.13) and the lateral strain as the average strain computed from the two instruments measuring the horizontal deformation (HE and HW). Only the data points up to the point when the maximum stress was reached are considered; all subsequent recordings were omitted. The E-Modulus and the Poisson's ratio were computed as the secant values when the test unit reached one third of its strength.

The left columns of Figs. 2.17 and 2.18 show the axial stress vs. axial strain curves for the tests in the x - and y -direction, respectively. The right columns show the relationship between horizontal and axial strains. Small markers in both types of plots indicate which points of the loading history correspond to one third of the strength of the wallette and were therefore used to compute the E-Modulus and Poisson's ratio. The strength, E-Modulus and Poisson's ratio are summarised for

2. Material tests for composite spandrels



Figure 2.14: Failure modes of masonry wallets tested under compression orthogonal to the bed joints.

2.5. Compression tests on masonry wallettes



Figure 2.15: Failure modes of masonry wallettes tested under compression parallel to the bed joints.

2. Material tests for composite spandrels

the two directions of loading in Tables 2.14 and 2.16, respectively. Mean values and standard deviations of the masonry properties are reported in Tables 2.15 and 2.17.

The wallette groups MX1 and MX3 had similar strengths when tested in the x -direction while the strength of MX2 was considerably lower. MX1 had been built with bricks of Type 1 and the mortar Kelit 110. The compressive strengths of these two materials were $f_{cm} = 19.2$ MPa (Table 2.7) and $f_{c,bx} = 24.7$ MPa (Table 2.10), respectively. MX2 and MX3 had been constructed with bricks of Type 2 and the mortar Maxitmur 920. The compressive strength of the bricks for loading in the x -direction was $f_{c,bx} = 30.9$ MPa. Although the same type of mortar had been used, the compressive strengths were rather different. The compressive strength of the mortar used for the wallette group MX2 was with $f_{cm} = 9.9$ MPa considerably smaller than that of wallette group MX3, which had a mortar strength of $f_{cm} = 13.4$ MPa. The ratio of the masonry strengths of MX2 and MX3 is $3.96/6.38 = 0.62$ and the ratio of the mortar strengths is $9.9/13.4 = 0.74$. Assuming the bricks of these wallettes had the same strengths, the results of MX2 and MX3 therefore suggest that the masonry strength is more or less directly proportional to the mortar strength.

MX1 and MX3 had similar masonry strengths for loading in the x -direction. However, the properties of the mortar and brick were very different. The mortar of MX1 was considerably stronger than the mortar of MX3, the ratio of the two strengths was $19.2/13.4 = 1.43$. Concerning the brick strength the situation was opposite since the bricks of Type 2 were stronger than the bricks of Type 1 ($24.7/30.9 = 0.80$). Combining the stronger mortar with the weaker bricks and the weaker mortar with the stronger bricks led to similar masonry strengths.

Figure 2.16a shows for the tests in the x -direction the correlation between the masonry strength and the E-Modulus. For all three groups of masonry wallettes the E-Modulus could be estimated as $E_{mx} = 1200f_{mx}$. This is 20% larger than the relationship given in SIA266 [SIA05] for the characteristic strength level ($E_{mx} = 1000f_{mx}$). The plots in the right column of Fig. 2.17 indicate that there were two distinct phases concerning the horizontal (lateral) strain: In an initial phase, the lateral strain grew less than the axial strain. From a certain point onwards, the lateral strain grew much faster than the axial strain indicating that vertical cracks formed, which split the wallette. Although, for all wallettes the points corresponding to one third of the compressive strength, i.e. the points used to compute the Poisson's ratio, belonged to the initial phase, the Poisson's ratios determined for the wallettes tested in the x -direction varied rather widely (Table 2.14).

Table 2.14: Mechanical properties of the masonry wallettes subjected to compression orthogonal to the bed joints (x -direction).

Wallette	f_{mx} [MPa]	f_{mx}^t [MPa]	f_{mx}^t/f_{mx} [-]	E_{mx} [GPa]	E_{mx}/f_{mx} [-]	$\nu_{m,x}$ [-]
MX101	6.13	7.01	1.14	7.09	1160	0.29
MX102	7.15	6.87	0.96	9.84	1380	0.32
MX201	3.91	3.85	0.98	4.26	1090	—
MX202	3.51	—	—	6.15	1750	0.10
MX203	4.47	4.73	1.06	5.37	1200	0.02
MX301	6.91	6.67	0.97	6.78	980	0.25
MX302	6.24	6.01	0.96	8.30	1330	0.26
MX303	6.00	5.77	0.96	5.97	990	0.18

Table 2.15: Mean values and standard deviations of the mechanical properties of the masonry material subjected to compression orthogonal to the bed joints (x -direction). Note that standard deviations are only computed if three values were available.

Property	TU1 (MX1)	TU2+3 (MX2)	TU4+5 (MX3)
Compressive strength f_{mx} [MPa]	6.64	3.96 ± 0.48	6.38 ± 0.47
E-Modulus E_{mx} [GPa]	8.47	5.26 ± 0.95	7.02 ± 1.19
Ratio E_{mx}/f_{mx} [-]	1270	1350 ± 360	1100 ± 20
Poisson's ratio ν_{mx} [-]	0.30	0.06 ± 0.02	0.23 ± 0.04

For loading in the y -direction (parallel to the bed joints), the influence of mortar and brick strengths on the masonry strength was less clear. Although the strengths of the bricks of Type 1 and 2 for loading in the y -direction were very different ($f_{c,by} = 3.45$ MPa and $f_{c,by} = 8.92$ MPa, respectively, see Table 2.10), the resulting strengths in the y -direction of all three wallette groups were very similar (Table 2.17). Hence, the ratios of strengths in the y - and x -direction were smaller for the groups 1 and 3 and larger for the group 2. The latter is with $f_{my}/f_{mx} = 0.32$ very similar to the strength ratio of 0.3 for standard clay brick masonry given in [SIA05]. While the strength of the three groups of masonry wallettes was very similar, their stiffness was rather different. For this reason, no clear relationship between strength and E-Modulus could be established for the tests in the y -direction (Fig. 2.16b). The markers in the right plots of Fig. 2.18 indicate that for loading in the y -direction the points corresponding to one third of the wallette strength were already part of the branch where the horizontal (lateral) strain increased faster than the axial strain. It does not seem reasonable to determine the Poisson's ratio, which is an elastic material property, for this part of the curve. For this reason, the Poisson's ratio is not evaluated for the tests in the y -direction.

Table 2.16: Mechanical properties of the masonry wallettes subjected to compression parallel to the bed joints (y -direction).

Wallette	f_{my} [MPa]	f'_{my} [MPa]	f'_{my}/f_{my} [-]	E_{my} [GPa]	E_{my}/f_{my} [-]
MY101	1.20	1.15	0.96	2.78	2310
MY102	1.30	1.25	0.96	3.27	2510
MY103	1.25	1.19	0.95	2.78	2230
MY201	1.44	1.38	0.96	2.09	1450
MY202	1.19	1.22	1.02	1.19	1000
MY203	1.18	1.13	0.96	2.23	1890
MY301	1.17	1.11	0.95	1.46	1250
MY302	1.41	1.35	0.96	0.76	540
MY303	1.53	1.45	0.95	1.41	930

Table 2.17: Mean values and standard deviations of the mechanical properties of the masonry material subjected to compression parallel to the bed joints (y -direction).

Property	TU1 (MY1)	TU2+3 (MY2)	TU4+5 (MY3)
Compressive strength f_{my} [MPa]	1.25 ± 0.05	1.27 ± 0.15	1.37 ± 0.18
E-Modulus E_{my} [GPa]	2.94 ± 0.29	1.84 ± 0.56	1.21 ± 0.39
Ratio E_{my}/f_{my} [-]	2350 ± 150	1450 ± 450	910 ± 360
Ratio f_{my}/f_{mx} [-]	0.19	0.32	0.21

2. Material tests for composite spandrels

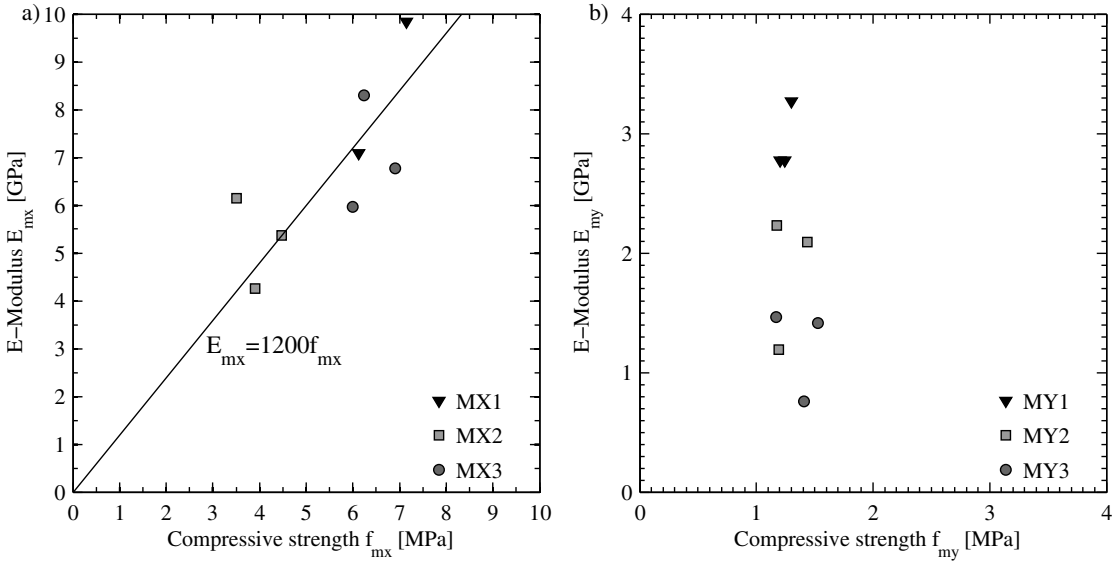


Figure 2.16: Compression tests on masonry wallettes: Correlation between E-Modulus and compressive strength for loading in the x- (a) and the y-direction (b).

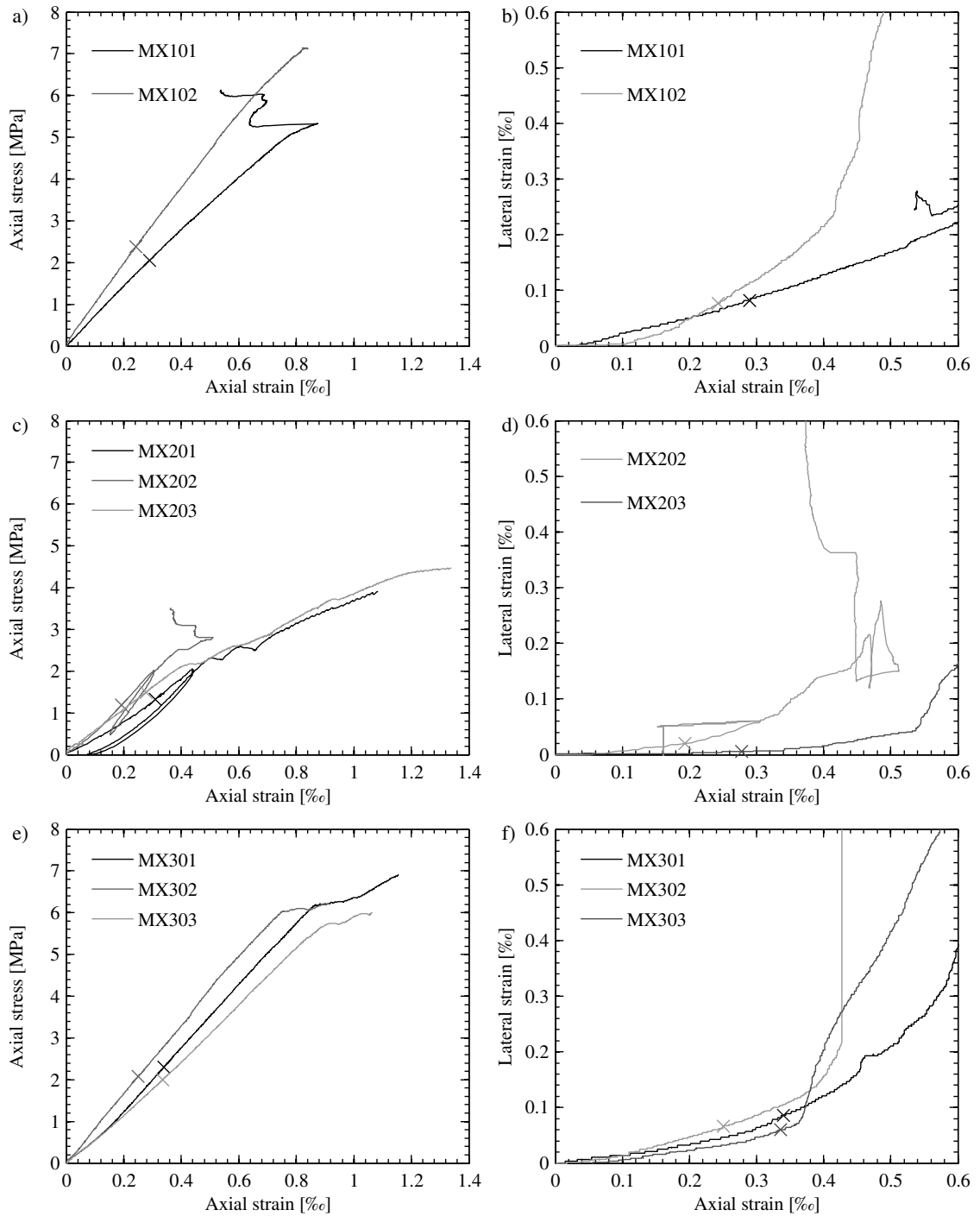


Figure 2.17: Compression tests on masonry wallettes in the x -direction: Axial stress vs. axial strain relationships (a,c,e) and lateral strain vs. axial strain relationships (b,d,f).

2. Material tests for composite spandrels

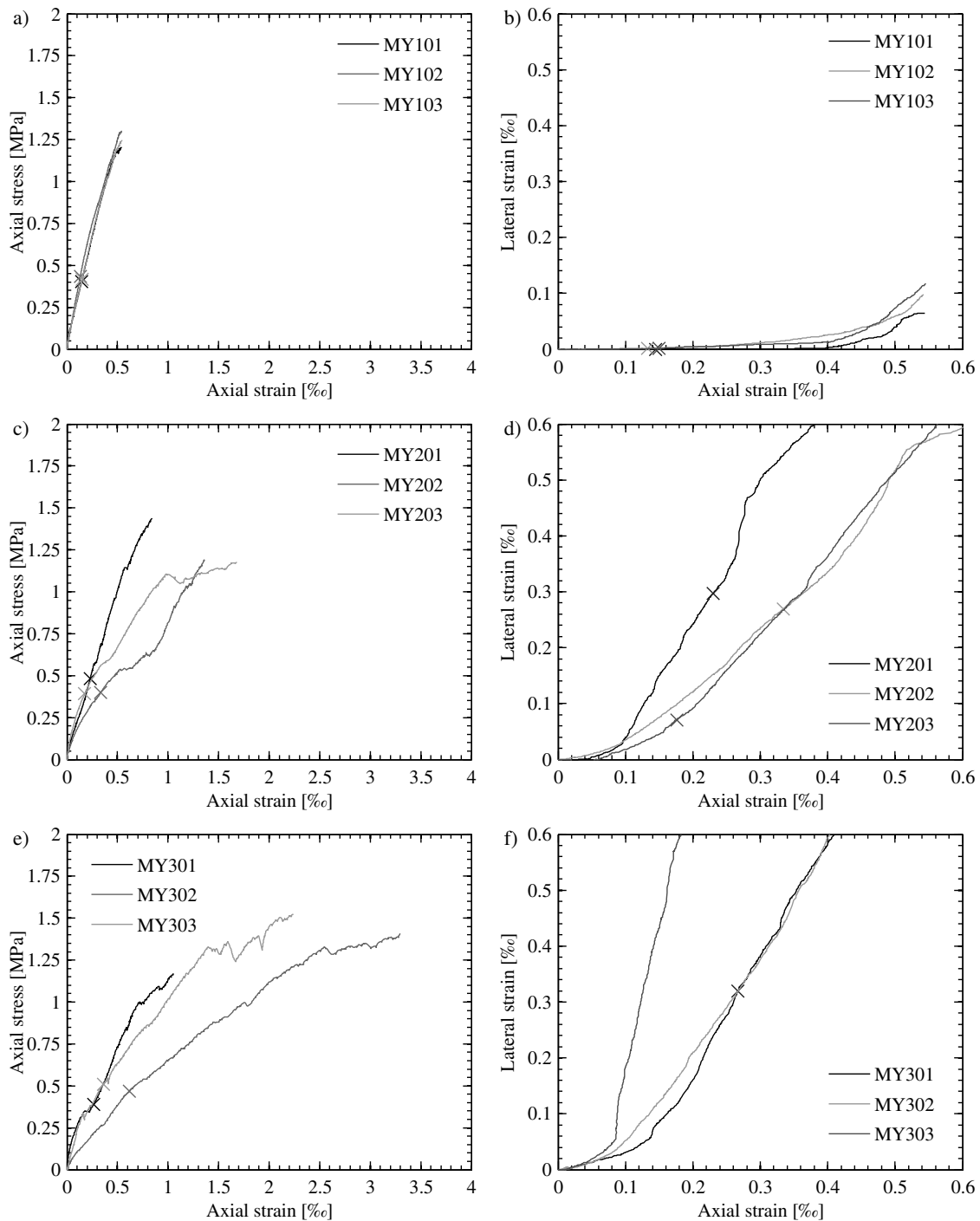


Figure 2.18: Compression tests on masonry wallettes in the y -direction: Axial stress vs. axial strain relationships (a,c,e) and lateral strain vs. axial strain relationships (b,d,f).

2.6 Shear tests on masonry wallettes

To determine the shear strength of the mortar joints, masonry wallettes consisting of three bricks and two mortar joints were tested according to EN1052-3 [CEN02b]. The masonry wallettes for the shear tests were constructed at a later stage than the spandrel test units using the same type of bricks and mortar as for TU2-5. The twelve wallettes were constructed on 19.08.2009. One of the wallettes broke before the test and one other failed due to local brick failure (for a normal stress of 1.0 MPa, see comment in Section 2.6.1) so that in total ten tests were conducted for three different levels of stress normal to the bed joints.

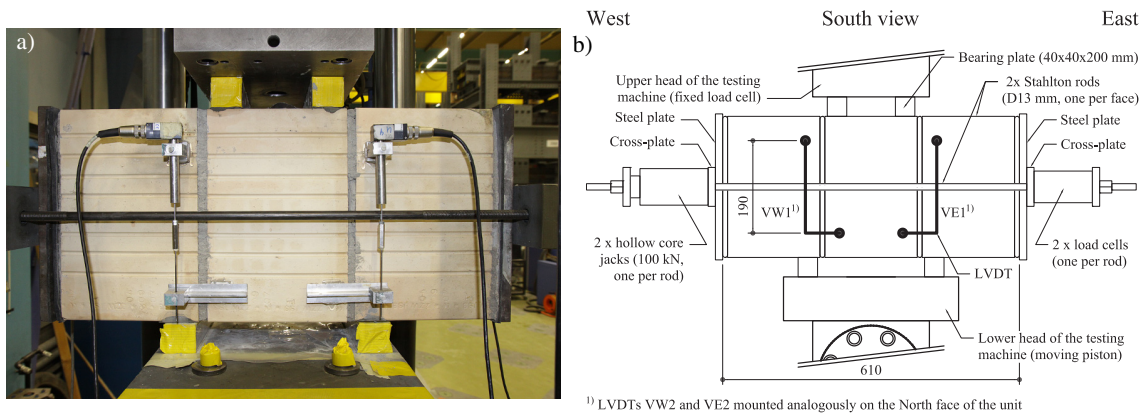


Figure 2.19: Shear tests: Photo of the test setup (a) and drawing of the test setup including instrumentation of the wallette (b).

Table 2.18: Dates of construction and testing of masonry wallettes tested in shear. The wallettes represent the test units TU2-5.

Wallette	Construction date	Testing date	Age [d]
MS20-1	19.08.2009	Nov. 2009 ¹⁾	~ 80
MS20-2	19.08.2009	Nov. 2009 ¹⁾	~ 80
MS20-3	19.08.2009	Nov. 2009 ¹⁾	~ 80
MS40-1	19.08.2009	Nov. 2009 ¹⁾	~ 80
MS40-2	19.08.2009	Nov. 2009 ¹⁾	~ 80
MS40-3	19.08.2009	Nov. 2009 ¹⁾	~ 80
MS40-4	19.08.2009	Nov. 2009 ¹⁾	~ 80
MS65-1	19.08.2009	Nov. 2009 ¹⁾	~ 80
MS65-2	19.08.2009	Nov. 2009 ¹⁾	~ 80
MS65-3	19.08.2009	Nov. 2009 ¹⁾	~ 80

¹⁾ All shear tests were performed in November 2009. The exact days of the tests were not noted down and since the date of the computer recording the measurements was not set correctly they could unfortunately not be reconstructed.

2.6.1 Test setup, testing procedure and instrumentation

The tests were performed on an universal testing machine Schenk ± 480 kN (Fig. 2.19a). Fig. 2.19b shows the support conditions of the wallette within the testing machine: At the base the wallette

2. Material tests for composite spandrels

was supported at the inner edge of the outer bricks on two 4 cm wide aluminium blocks, which had the same length as the bricks (20 cm). At the top, two 4 cm wide aluminium blocks introduced the reaction force of the testing machine at the outer edges of the middle brick. Four LVDTs – two on each face – measured during the test the relative displacements between the outer and middle bricks (Fig. 2.19b, Table 2.19).

The shear tests were conducted at three different normal stress levels where normal refers to the direction perpendicular to the mortar joints. EN1052-3 [CEN02b] requires for bricks with a compressive strength larger than 10 MPa stress levels of 0.2 MPa, 0.6 MPa and 1.0 MPa. The compressive strength in the x -direction of the bricks is considerably larger than 10 MPa (see Table 2.10). In the y -direction, however, which is the relevant strength for the application of the shear force in this specific test, the compressive strength of the bricks is slightly smaller than 10 MPa. Although a thin mortar layer between the bricks and aluminium blocks ensured a smooth load introduction, local brick failure occurred at the location where the shear force was applied to the walette when the applied normal stress was 1.0 MPa. For this reason this test was disregarded and the further ten shear tests were conducted at normal stress levels of $\sigma = 0.2$ MPa, 0.4 MPa and 0.65 MPa. For these normal stress levels the shear forces were small enough to avoid local failure of the bricks at the location where the shear force was applied. Out of the ten tests, three were tested at a normal stress level of 0.2 MPa (walleets 2.1 to 2.3), four at a normal stress level of 0.4 MPa (walleets 4.1 to 4.4) and three at a normal stress level of 0.65 MPa (walleets 6.1 to 6.3).

The normal forces were applied by means of two D13 mm steel rods and measured by two compression load cells (see Fig. 2.19). For the first five tests, which were the walleets 2.1, 4.1, 6.1 to 6.3, the steel rods were prestressed by hand and then locked-in. For this reason, the axial force varied during the test. To reduce this variation in axial force, the test setup was modified. For the final five tests (walleets 2.1, 2.2, 4.2 to 4.4) a load follower and two small hollow core jacks ensured that the axial force remained approximately constant throughout the test.

Table 2.19: Shear tests: Hard-wired channels.

Channel name	Instrument type	Description of measured quantity
VE1	LVDT ± 10 mm	Sliding deformation, North LVDT on East face
VE2	LVDT ± 10 mm	Sliding deformation, South LVDT on East face
VW1	LVDT ± 10 mm	Sliding deformation, North LVDT on West face
VW2	LVDT ± 10 mm	Sliding deformation, South LVDT on West face
FORCE_1	Load cell	Compression load cell with a capacity of 150 kN
FORCE_2	Load cell	Compression load cell with a capacity of 150 kN
SHEAR_FORCE	Load cell	Force in the piston of the testing machine

The procedure for preparing and conducting the shear tests on the walleets was as follows:

- The top and bottom faces of the walette were levelled using a mortar layer with a thickness of a few millimetres to ensure a better bearing surface for the steel plates which were used to apply the forces normal to the bed joints.
- Load cells and steel rods were mounted and axial forces inducing the normal stress on the bed joints were applied by means of the two steel rods.

- The test unit was turned by 90 degrees and was then placed on the linear supports with a width of 40 mm and a length of 200 mm (i.e. equal to the width of the brick). To achieve a introduction of the shear force with as little stress concentrations as possible, a cement paste was used to level the test unit on top of these bearing plates.
- Cement paste was applied to the top face of the central brick and the two supports with a width of 40 mm and a length of 200 mm were placed. A small initial load was applied by the universal testing machine, in order to ensure that the top supports were parallel to the loading plate of the machine. In this way a uniform stress introduction could be achieved once the cement paste was hardened.
- Two LVDTs were mounted on each face of the test unit and the hard-wired measuring system was set up. All hard-wired measuring devices were set to zero.
- For the five final tests the two hollow core jacks were connected to a load follower, which kept the axial load approximately constant over the duration of the test.
- The shear force was applied moving the bottom plate of the universal testing machine upwards. The tests were performed in displacement control. The initial rate of loading was 0.3 mm/min. This loading rate was maintained until the peak shear strength had been passed. The loading rate was then increased to 1.00 mm/min. The test was terminated at average shear displacements between 10 to 15 mm.

2.6.2 Failure modes

All the observed failures occurred at the interface of mortar and brick and not within the mortar joint itself. The peak shear strength of the brick-mortar interface was reached at very small shear displacements of typically some tenths of a millimetre. As the shear deformation increased, the shear resistance decreased gradually. Cracks at the mortar-brick interfaces formed. During the construction of the masonry, part of the mortar that formed the bed joints penetrated into the holes of the bricks. These small mortar pillars were sheared off during the testing exerting forces on the surrounding brick. As a consequence, some of the webs of the brick fractured. A constant residual shear strength was typically reached for shear displacements greater than 6 mm. Example photos taken at the end of the test are shown in Fig. 2.20.

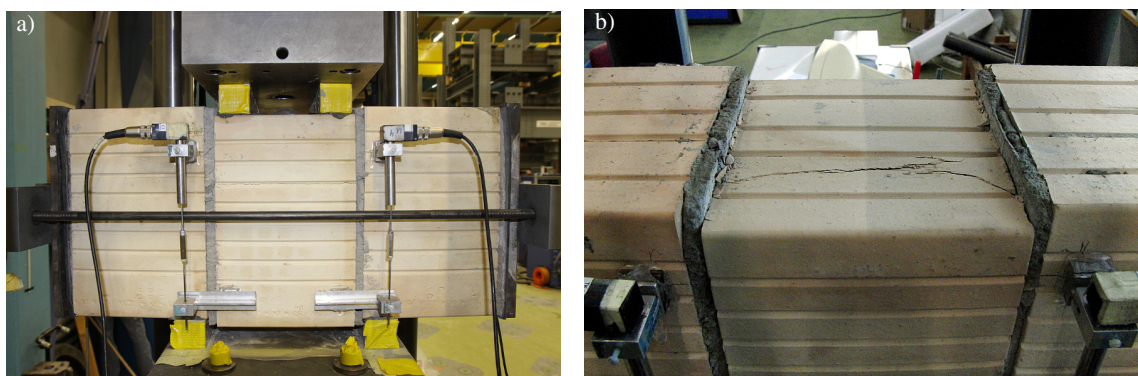


Figure 2.20: Failure of wallettes tested in shear: Global failure (a) and local brick failure due to shearing off of the mortar pillars (b).

2.6.3 Test results

For all tests the peak and residual shear stress were determined. The shear stress was defined as the shear force divided by the gross cross section area of the two mortar beds (290x200 mm). The residual shear stress was defined as the shear stress when the average shear displacement (i.e., the average measurement of the four LVDTs) reached 10 mm. In two cases the test was finished before reaching an average shear displacement of 10 mm. For these tests the residual shear stress was taken as the shear stress at the maximum imposed shear displacement. This definition of the residual strength is somewhat arbitrary. However, once the cracks between mortar and bricks had formed and all mortar pillars within the bricks had sheared off, the shear stress remained in most cases fairly constant. Figure 2.22 shows the shear stress vs. shear displacement relationships for all wallettes. The plots show that for those tests for which the axial stress was not controlled by a load follower, the normal stress acting on the bed joints varied over the duration of the test. For $\sigma = 0.2$ MPa and $\sigma = 0.4$ MPa the stress increased as the imposed shear displacement increased (wallettes 2.1 and 4.1), for $\sigma = 0.6$ MPa it decreased (wallettes 6.1 to 6.3).

The peak and residual shear stress vs. normal stress couples are plotted in Fig. 2.21. The plots also include the best-fit Mohr-Coulomb relationships, for which the numerical values are summarised in Table 2.20. For the residual stress values two best-fit lines were determined, i.e. one with and one without a cohesion term. The following observations can be made:

- The peak values show a significantly larger scatter than the residual values. This is also reflected in the correlation coefficients of the best-fit Mohr-Coulomb relationships.
- Assuming that the friction coefficients at the peak and residual stress levels are relatively similar, the results suggest that a small cohesion was also present at the residual stress level. If one assumes that the cohesion at the residual stress level is zero, the friction coefficient describing the residual behaviour is larger than the friction coefficient describing the peak behaviour.

Table 2.20: Shear tests: Friction coefficient μ , cohesion c and correlation coefficient R^2 for peak and residual shear stress.

Mohr-Coulomb relationship	μ [-]	c [MPa]	R^2 [-]
Peak stress: $\tau_{max} = \mu_{max} \cdot \sigma + c_{max}$	0.71	0.25	0.78
Residual stress: $\tau_{res} = \mu_{res,1} \cdot \sigma + c_{res}$	0.70	0.03	0.97
Residual stress: $\tau_{res} = \mu_{res,2} \cdot \sigma$	0.77	0	0.96

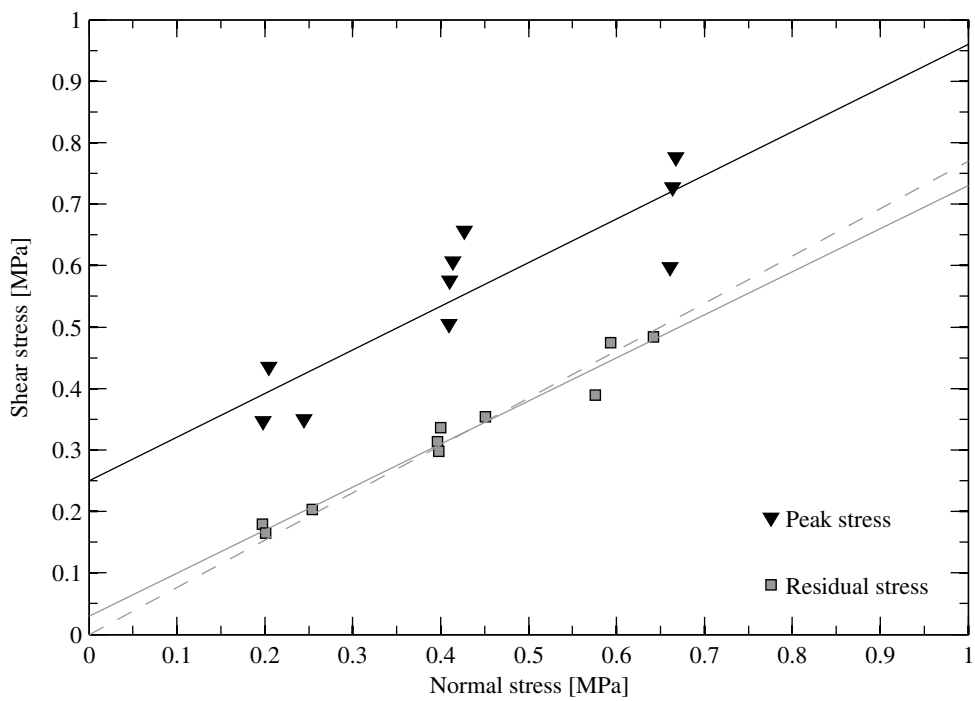


Figure 2.21: Shear tests: Peak and residual stress values in function of the applied normal stress and corresponding regression lines.

2. Material tests for composite spandrels

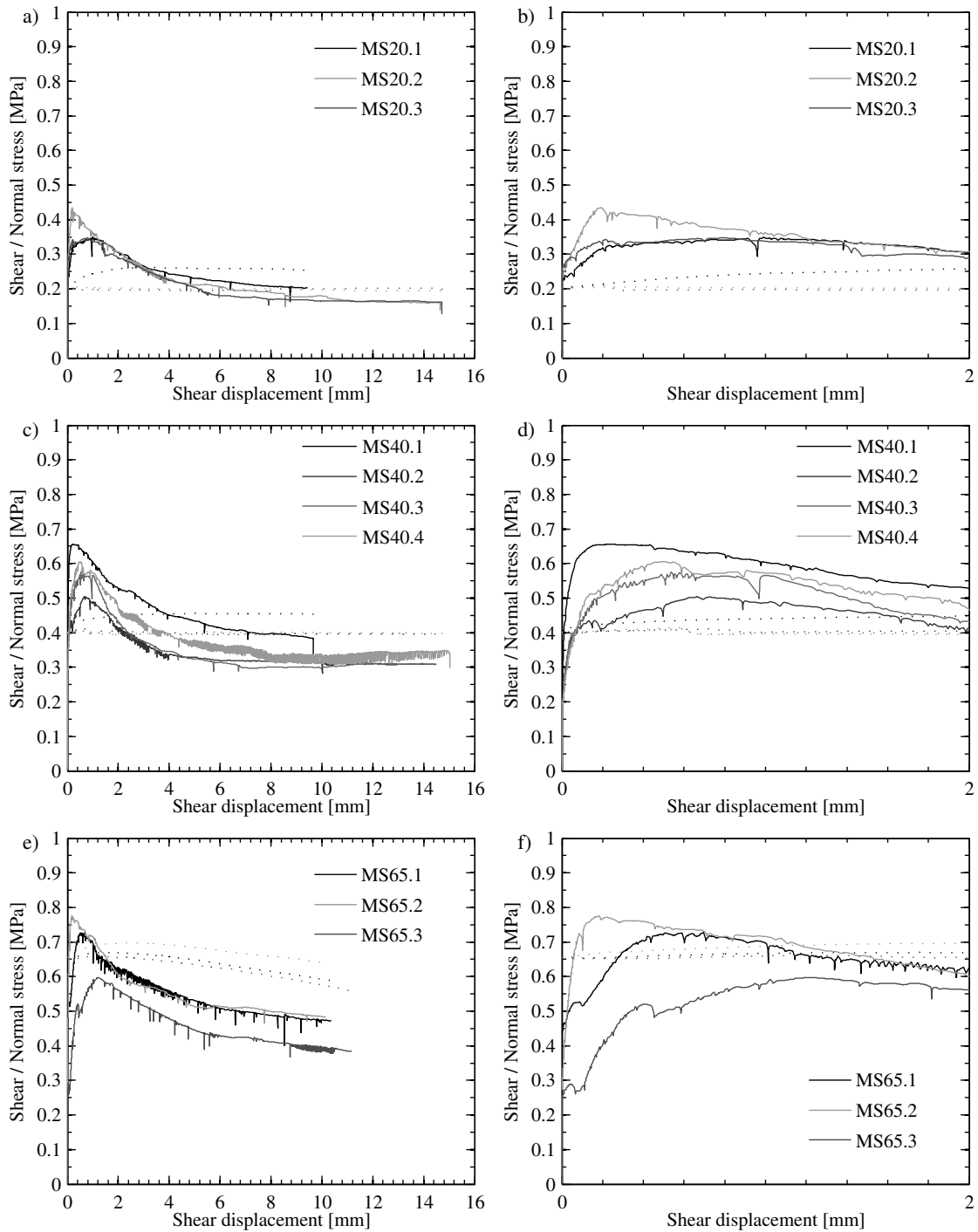


Figure 2.22: Shear tests for wallettes: Shear stress (solid lines) and normal stress (dotted lines) plotted against shear displacement. Full shear displacement range (a, c, e) and close-up of the displacement range between 0 and 2 mm (b, d, f).

3 Test results for composite spandrels

This chapter summarises the test results for the composite spandrels. For each spandrel the test observations and the most important graphs showing the results from the measurements with the hard-wired and optical instruments are given. The quantities computed from these measurements, such as for example the shear force in the spandrel and the rotation of the lever beams, are defined in Section 3.1.

During the discussion of the test observations and of the test results, reference to the loading direction is often made. The positive direction of loading is defined for a drift of the piers towards North while the negative direction of loading implies a drift of the piers towards South. The definition of the directions of loading is schematically depicted in Fig. 3.1. It shows the view of the East face on which the cracks were marked with a black pen and which is also the face shown on most photos.

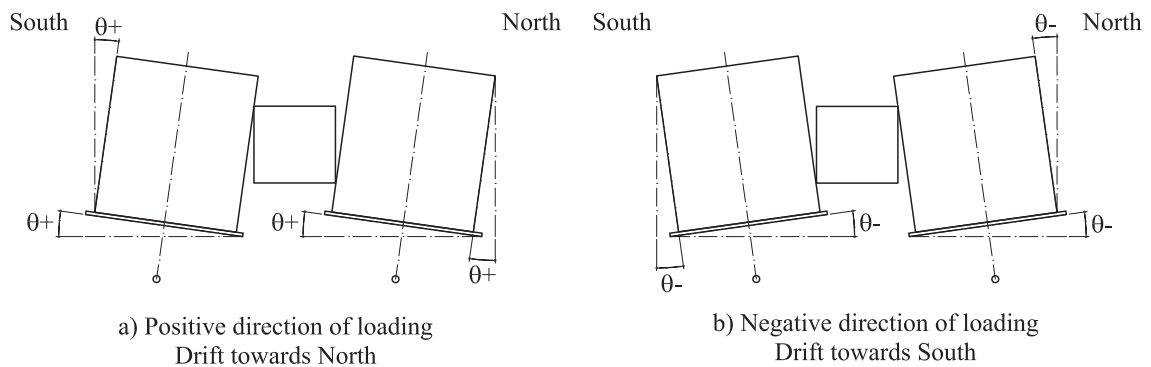


Figure 3.1: Positive (a) and negative (b) direction of loading. View from the East.

3.1 Definition of force and deformation quantities

This section defines the quantities used in the graphs showing the basic results from the hard-wired instruments. The standard graphs shown for each test unit are defined in Section 3.1.

Reaction forces at the supports

The reaction forces at the supports were measured by one compression load cell and four tension load cells (see Section 1.2). The total reaction force was computed as the sum of the five forces. Hence, for the North and South support, respectively, the reaction forces were computed as:

$$R_N = LC_{N_C} + LC_{N_17} + LC_{N_16} + LC_{N_19} + LC_{N_08} \quad (3.1)$$

$$R_S = LC_{S_C} + LC_{S_15} + LC_{S_0} + LC_{S_24} + LC_{S_22} \quad (3.2)$$

The reaction forces were set to zero before the test unit was lifted on the test stand.

3. Test results for composite spandrels

Weight of the spandrel

The weight of the spandrel was computed as the sum of the two actuator forces and the two reaction forces:

$$W_{sp} = ACT_FORCE_N + R_N + ACT_FORCE_S + R_S \quad (3.3)$$

The weight of the spandrel includes the weight of all base steel plates and of the load transfer beams that were mounted with the test unit on the test stand as well as the portion of the weight of the lever beams carried by their outer supports before the test unit was lifted onto the test stand. The actuator forces were set to zero before the actuators were connected with the lever beams. Due to measurement errors of the load cells W_{sp} varied slightly over the duration of the test. For the computation of the shear force in the spandrel an average value of W_{sp} was defined and was kept constant for the entire duration of the test.

Shear force of the spandrel

The shear force of the spandrel was computed once based on the North actuator force and the North reaction force and once from the South actuator force and the South reaction force. To obtain the shear force in the spandrel half the weight of the spandrel has to be subtracted:

$$V_N = ACT_FORCE_N + R_N - W_{sp}/2 \quad (3.4)$$

$$V_S = ACT_FORCE_S + R_S - W_{sp}/2 \quad (3.5)$$

Some unevenness of the base plates or slight misalignment of the lever beams could cause internal stresses in the test unit when placing the test unit on the test stand. These stresses correspond to an initial shear force, which Eqs. 3.4 and 3.5 can capture. Small differences between V_N and V_S result from (i) measurement errors and (ii) deviation of the actuator forces from the vertical axis at larger rotations. The final shear force is computed as the average of V_N and V_S :

$$V = (V_N + V_S)/2 \quad (3.6)$$

Axial force on piers

The axial force acting on each pier was computed from the forces in the four rods that pretensioned the load transfer beam against the base plate:

$$AFP_N = AFP_N_EN + AFP_N_ES + AFP_N_WN + AFP_N_WS \quad (3.7)$$

$$AFP_S = AFP_S_EN + AFP_S_ES + AFP_S_WN + AFP_S_WS \quad (3.8)$$

The nominal cross section of a pier was 0.2x2.1 m, which corresponds to 0.42 m². The nominal axial force on the piers was, apart from the end of the test on TU4, 4x40 kN, which corresponds – excluding the weight of the load transfer beam and the selfweight of the pier – to 0.38 MPa. The weight of the load transfer beam on top of the pier was approximately 4.4 kN and the weight of the pier down to midheight 4.1 kN. The total axial force acting on the piers at midheight of the spandrel is therefore 168.5 kN, which corresponds to 0.40 MPa.

Rotation of piers

The deformation demand on the spandrel is quantified in terms of the drift of the piers that are supported by the lever beams. The rotation of the lever beams is measured by the LVDTs mounted

underneath the lever beams. For each lever beam the rotation is computed as follows:

$$\theta_N = (BEAM_N_S - BEAM_N_N)/l_{pier} \quad (3.9)$$

$$\theta_S = (BEAM_S_S - BEAM_S_N)/l_{pier} \quad (3.10)$$

The horizontal distance between the LVDTs corresponded to the length of the pier, i.e. $l_{pier} = 2100$ mm (see Figs. 1.7 and 1.8). The drift is defined as positive when the piers are displaced towards North (see Fig. 3.1), i.e. for a positive rotation about an axis pointing from East to West. Since the velocity of the actuators was controlled via the displacement transducers mounted on the actuators themselves, the actual drifts of the two lever beams could differ slightly. This was mainly due to some small backlash within the actuators' hinges. The final drift was computed as the average of the rotation of the North and South lever beams:

$$\theta = (\theta_N + \theta_S)/2 \quad (3.11)$$

Spandrel displacement

The demand on the spandrel does not only depend on the pier rotations but also on the length of the spandrel. A "spandrel displacement" is computed as

$$\Delta_{sp} = \theta \cdot (l_{sp} + l_p) \quad (3.12)$$

where l_{sp} is the length of the spandrel ($l_{sp} = 1500$ mm) and l_p the length of the piers ($l_p = 2100$ mm) (see Fig. 1.1).

Deformation of the RC beam

The deformations of the RC beam were measured by two chains of LVDTs running along the top and bottom edges of the West face of the RC beam. The measurements were recorded in units of [mm]. The base length of all LVDTs was 300 mm. The distance between the top and bottom chains of LVDTs was 190 mm (see Figs. 1.7 and 1.8). For each pair of LVDTs an average curvature and an average axial elongation are computed as:

$$\varphi_i = (SLAB_B_i - SLAB_T_i)/300 \text{ mm}/0.19 \text{ m} \quad (3.13)$$

$$\varepsilon_i = (SLAB_T_i + SLAB_B_i)/300 \text{ mm}/2 \quad (3.14)$$

The unit of curvature is [1/m] while the mean axial strain is unitless. A curvature is defined as positive, when the strains at the bottom of the RC beam are larger than the strains at the top. The axial elongation is defined as positive, when the average strain is larger than zero.

Standard plots

Based on the just defined quantities, the following standard plots were generated for all test units:

- Force-deformation hysteresis: Shear force V plotted against the drift θ . This graph is plotted for all cycles and for cycles with amplitudes up to $\pm 0.8\%$. For TU1 and TU2, which were tested under monotonic loading, the force-deformation curve is once plotted for the entire range of imposed drifts and once for drifts up to 1%.

3. Test results for composite spandrels

- Force-deformation hysteresis for North and South quantities: The quantities necessary to determine the shear force of the spandrel were overdetermined: The shear force in the spandrel could be computed based on the North actuator force and the North support force or based on the South actuator force and the South support force. As an overall measure the average shear force V was used. To judge the quality of the measurements the two computed shear forces are plotted separately as $V_N - \theta_N$ and $V_S - \theta_S$ curves.
- Axial force on piers: The axial force on the piers was supposed to remain constant. This was achieved by means of load followers. However, some variations occurred, which are shown in a graph plotting the total axial force on the North (AFP_N) and South (AFP_S) pier, respectively, against the rotation θ .
- Curvature distribution along the RC beam: From the two LVDT chains mounted on the West face of the RC beam the curvature distribution φ_i along the RC beam was computed. It was plotted for four selected drift levels, i.e. 0.4%, 0.8%, 1% and 2%. For cyclic loading separate plots for the negative and positive direction of loading are provided.
- Axial strain distribution along the RC beam: Similar to the curvature distribution, the axial strain distribution ε_i is computed from the two LVDT chains mounted on the West face of the RC beam and is plotted for four selected drift levels, i.e. 0.4%, 0.8%, 1% and 2%. For cyclic loading separate plots for the negative and positive direction of loading are provided.

In addition to the results obtained from the hard-wired instruments, the data obtained from the optical measurements (see Section 1.3.2) was used to plot the deformed shape of the test unit for selected rotation demands. The data was obtained from the optical measurements over a duration of approximately one minute at each load step. The measurements were averaged over the recording time to obtain the deformations of the test unit at the load steps. Plots of the deformed shape of the test units are provided for the following nominal rotation levels: 0.1%, 0.2%, 0.4% and 0.8%. For the test units subjected to cyclic loading (TU3 to TU5) plots for the first positive as well as the first negative peak of the cycles corresponding to the nominal rotation level are provided. For TU2, which was subjected to monotonic loading, the deformed shape was plotted for the positive direction of loading only. The data of TU1 was not managed properly and unfortunately no results are available for LS 2 to LS 8. For this reason only the deformed shape corresponding to $\theta_{nom} = 0.8\%$ could be provided.

3.2 Composite spandrel TU1

3.2.1 Test observations

When bolting the test unit onto the lever beams, small cracks above the first row of bricks occurred. The cracks were located at the inner pier ends and extended over the length of approximately one brick. At LS 0 the forces in the eight vertical rods were zero. As a first load step, each rod was prestressed to a force of approximately 40 kN. The four outer rods were prestressed by hand and then locked-in, the inner rods were prestressed by means of four hollow core jacks that were controlled by two load followers, i.e. the two hollow core jacks on one pier were connected to the same load follower. The vertical forces were applied on 26.02.2009. The test unit was tested on 02.03 and 03.03.2009; an overview on the load steps covered during each testing day is given in Table 3.1.

Table 3.1: TU1: Testing days and corresponding load steps.

Testing day	Load step carried out
26.02.2009	LS 1
02.03.2009	LS 2 - LS 10
03.03.2009	LS 11 - LS 16

The first cracks due to the imposed loading occurred at LS 4 ($\theta_{nom} = 0.1\%$). One crack followed the bottom surface of the RC beam. It extended 40 cm from the South end of the spandrel into the South pier. The second crack was a vertical flexural crack at the North end of the spandrel, which passed through the bricks. The crack initiated at the top North corner of the spandrel and reached as far as 8 cm into the RC beam. This flexural crack led to a distinct drop in the shear force of the spandrel. At the next load step LS 5 ($\theta_{nom} = 0.2\%$) the masonry spandrel detached from the RC beam over almost the entire length of the spandrel. At the spandrel's South end the crack reached about 40 cm into the South pier. Further cracks occurred in the RC beam indicating the onset of the formation of plastic hinges. At the North end of the spandrel the plastic hinge formed at the South edge of the North pier. The bending moment in the slab at this location was negative and therefore the cracks were open at the top of the RC beam. All cracks were located very close to the edge of the pier. At the South end of the spandrel the picture was different: The three cracks that formed in the RC beam were distributed over about 45 cm reaching equally into the spandrel and pier. Since the bending moment at this location was positive, the cracks were open at the bottom of the beam. In comparison to the cracks at the North end of the spandrel, the widths of the cracks of the South plastic hinge were smaller. In addition a vertical flexural crack at the South end of the masonry spandrel formed. This flexural crack reached over the lower two and a half brick rows.

Over the course of the following load steps the crack pattern did not change significantly. The flexural cracks in the masonry spandrel and RC beam grew in width and length. At some locations additional parallel cracks formed. In particular in the positive plastic hinge of the RC beam cracks formed at the locations of the stirrups, which were spaced at 150 mm intervals. At LS 7 ($\theta_{nom} = 0.4\%$) the cracks extended 53 cm into the spandrel and 37 cm into the South pier (Fig 3.2). At the same load step the top South brick of the spandrel failed. Fig. 3.3 shows that the outer layer of the brick sheared off the inner core of the brick. Since for this type of brick (Brick Type 1, see

3. Test results for composite spandrels

Section 1.1.1) the outer layers are the only layers which are continuous over the brick length, the brick lost a significant part of its load carrying capacity.

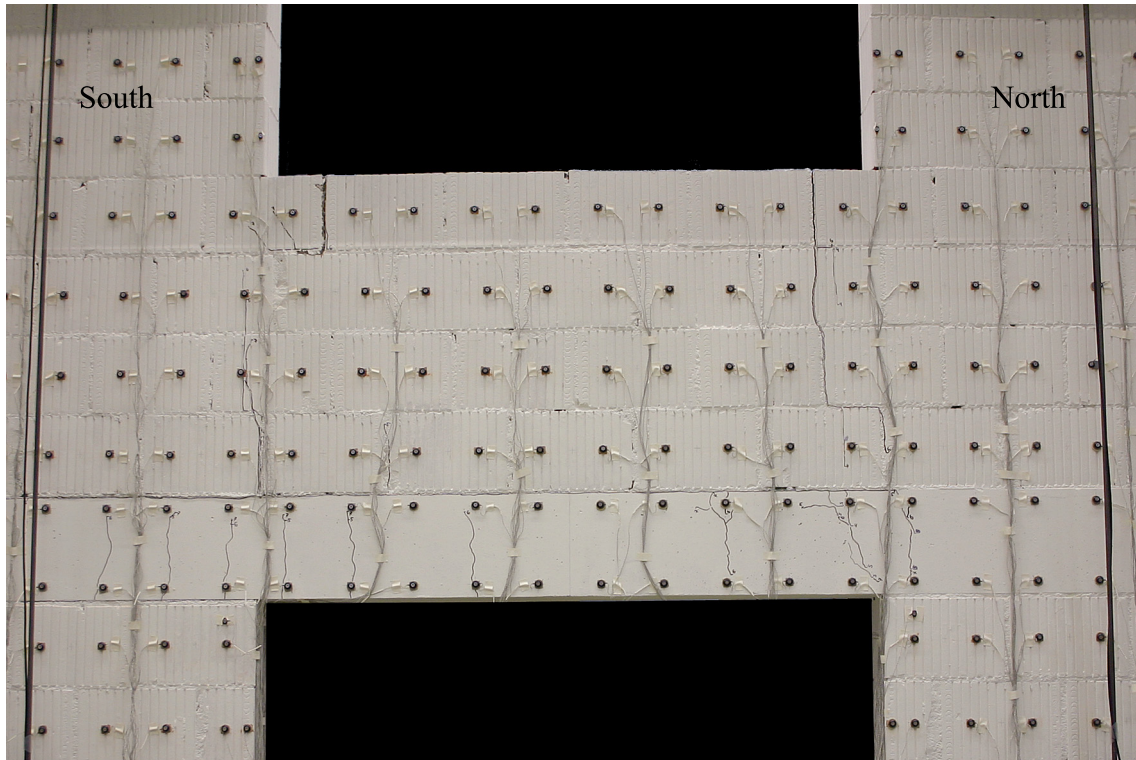


Figure 3.2: TUI: Crack pattern of spandrel at LS 7. Drift towards North with $\theta_{nom} = 0.4\%$.

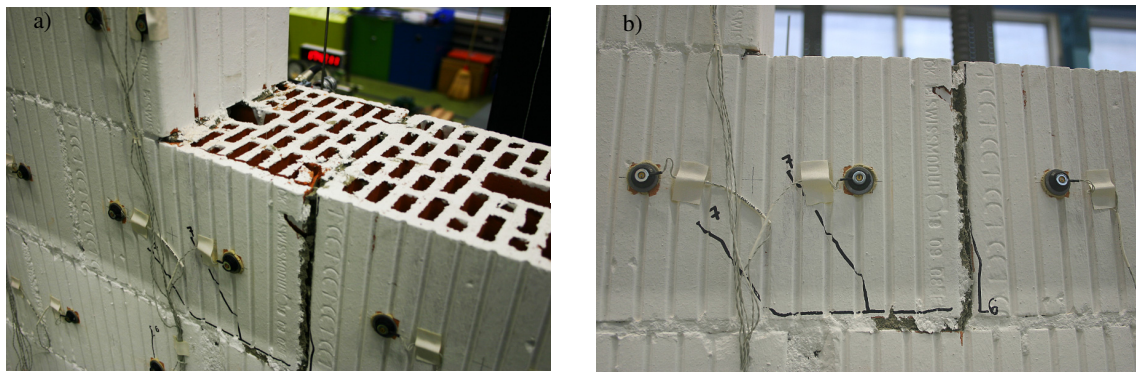


Figure 3.3: TUI: Top South brick of spandrel: The outer layer of the brick sheared off at LS 7. Drift towards North with $\theta_{nom} = 0.4\%$.

At LS 8 ($\theta_{nom} = 0.6\%$) the outer layer of the top South brick that had sheared off at LS 7 fell off. In addition inclined cracks formed running through the bricks following the compression strut that reached from the top South corner of the spandrel into the spandrel. At LS 9 ($\theta_{nom} = 0.8\%$) also part of the outer layer of the brick laying underneath the top South brick of the spandrel sheared and fell off (Fig. 3.4). LS 10 ($\theta_{nom} = 1\%$) marked the end of the first testing day. After unloading, the cracks of the South hinge in the RC beam had almost closed completely (crack widths smaller than 0.2 mm), while some of the residual crack widths of the North plastic hinge were as large as

0.8 mm. This finding corresponds to the observed crack pattern, which shows that the South plastic hinge was spread over a far greater length than the North plastic hinge, which was concentrated at the location of the South edge of the North pier. As a consequence, the curvature demand on the RC beam and hence also the plastic strains of the longitudinal reinforcement bars were larger in the North plastic hinge than in the South plastic hinge. Note that some of the LVDTs on the West face of the RC beam had to be removed because the curvatures were too large or because they fell off when a crack crossed their support.

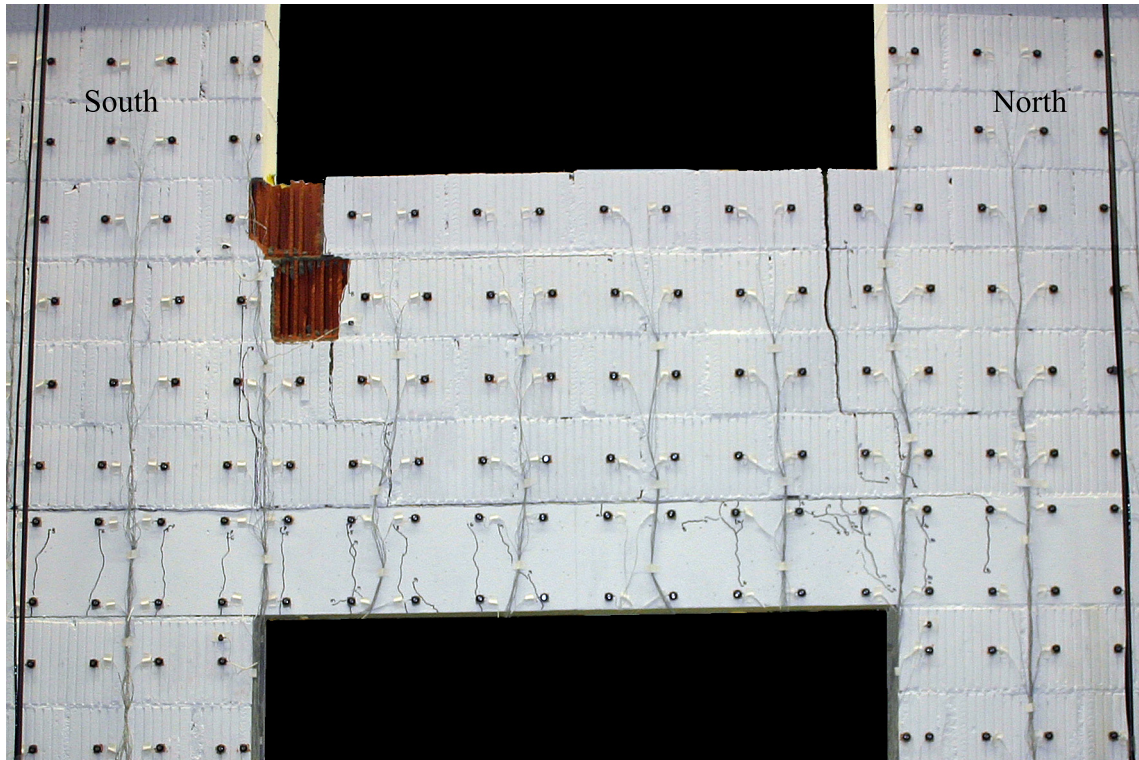


Figure 3.4: TUI: Crack pattern of spandrel at LS 9. Drift towards North with $\theta_{nom} = 0.8\%$.

Figure 3.5 shows the crack pattern of the spandrel at LS 12 ($\theta_{nom} = 2\%$). The photo illustrates well the mechanism that developed: The bending moment introduced by the South pier generated a compression strut which reached from the top South corner of the spandrel into the spandrel. Since the shear and compression capacity of the bricks was rather small, the bricks through which the compression strut passed failed. The bricks at the top failed first because at this location the width of the compression strut was limited and the stresses therefore the greatest. Further down the strut became wider and for this reason, the stresses were smaller and failure occurred later. As the top bricks failed the strut could no longer pass through these bricks and therefore moved to the South causing a reduction in shear force carried by the spandrel. The inclined compression strut that reached into the spandrel caused basically a reduction in effective span of the spandrel leading to an increased shear capacity. As the strut moved to the South, the effective span became longer and the shear capacity of the spandrel reduced. Over the effective span of the spandrel, the flexural capacity was solely provided by the RC beam. At its South end the plastic hinge was rather long. At its North end the plastic hinge was concentrated at the South edge of the North pier over which the RC beam was bent. The flexural crack at the North end of the spandrel extended over the entire

3. Test results for composite spandrels

height of the masonry spandrel indicating that at this end of the spandrel the masonry contributed very little to nothing to the capacity of the spandrel.

Apart from their lengths, the North and South plastic hinges in the RC beam differed also with regard to their crack pattern: In the South plastic hinge only flexural cracks formed. It is likely that at this location large part of the shear force – at least at the beginning of the test – was carried by the compression strut in the masonry spandrel. The cracks that belonged to the North plastic hinge and were located within the free span of the spandrel, were strongly inclined and were therefore shear-flexural cracks. At this location the masonry spandrel contributed close to nothing neither to the flexural nor to the shear capacity of the spandrel as a whole.



Figure 3.5: TU1: Crack pattern of spandrel at LS 12. Drift towards North with $\theta_{nom} = 2\%$.

As loading continued the compression strut in the masonry continued to fail leading to a South shift of the South plastic hinge in the RC beam. In the North plastic hinge the large curvatures caused the concrete cover above the top reinforcement bars to spall off. After LS 15 ($\theta_{nom} = 4\%$) it was decided to continue loading until failure. Failure occurred shortly later when several longitudinal bars ruptured (Fig. 3.5). The rupture sequence was most likely: (i) East bottom bar of South hinge, (ii) East top bar of North hinge, and (iii) West bottom bar of South hinge. Although the curvature demand on the North hinge was significantly larger than the curvature demand on the South hinge, bar rupture initiated in the South hinge. Likely reasons are the missing cover concrete in the North hinge, which allowed a more even spreading of the plastic strains along the longitudinal bars, while towards the end of the test the plastic strains in the South hinge concentrated in one single crack.

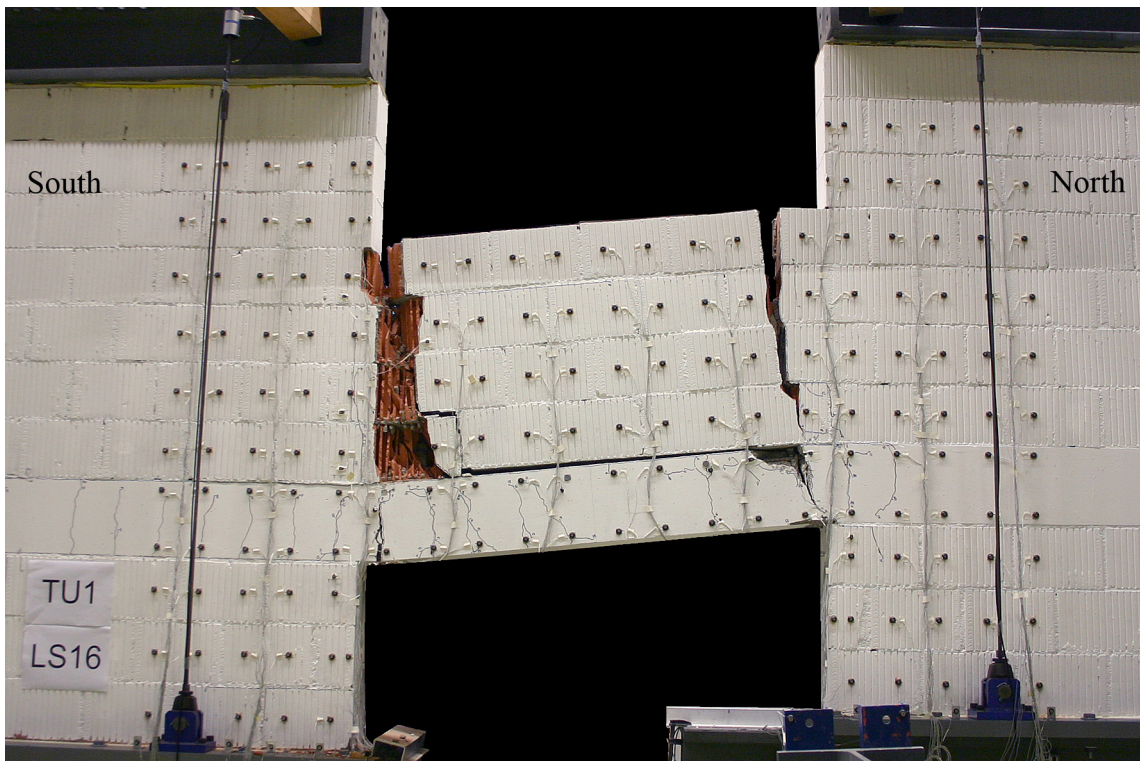


Figure 3.6: TU1: Crack pattern of spandrel at LS 16. Drift towards North with $\theta = 5.3\%$ (failure of TU1).

3.2.2 Test results

The following figures show the standard graphs derived from the hard-wired measurements that have been defined in Section 3.1. The hysteretic behaviour of the test unit in terms of spandrel shear force vs. average rotation is presented first. Then, the variation of the axial load on the piers is shown and finally the deformations of the RC beam are discussed in terms of local curvatures and axial elongations. At the end of the section a plot of the deformed shape of the test unit at $\theta_{nom} = 0.8\%$ is provided. This plot was derived from the optical measurement data.

Force-rotation behaviour of TU1

The global shear force vs. rotation relationship of TU1 is shown in Figs. 3.7 and 3.8. These two figures show the averaged quantities V and θ , which were defined in Section 3.1. In Fig. 3.9 the non-averaged quantities computed from quantities measured at the North and South pier, respectively, are plotted. The shear force shows some small differences which can be attributed to measurement errors and for larger drift demands also to the inclination of the actuators, which introduced small error, since all measured forces are assumed to act vertically. The formation of flexural cracks in the masonry spandrel was largely completed when reaching $\theta_{nom} = 0.2\%$. The rounding off of the force-rotation curve was most likely associated with the onset of yielding in the North plastic hinge in the RC beam. At the end of the first testing day residual crack widths in the North plastic hinge proved that the top reinforcement bars must have undergone inelastic strains while the South hinge behaved still largely elastic. The drop in shear force capacity for drift demands greater than 1.5% is related to the crushing of the compression diagonal in the masonry

3. Test results for composite spandrels

spandrel. The final drops in force for drifts larger than 4.5% are associated with the rupture of three longitudinal reinforcement bars.

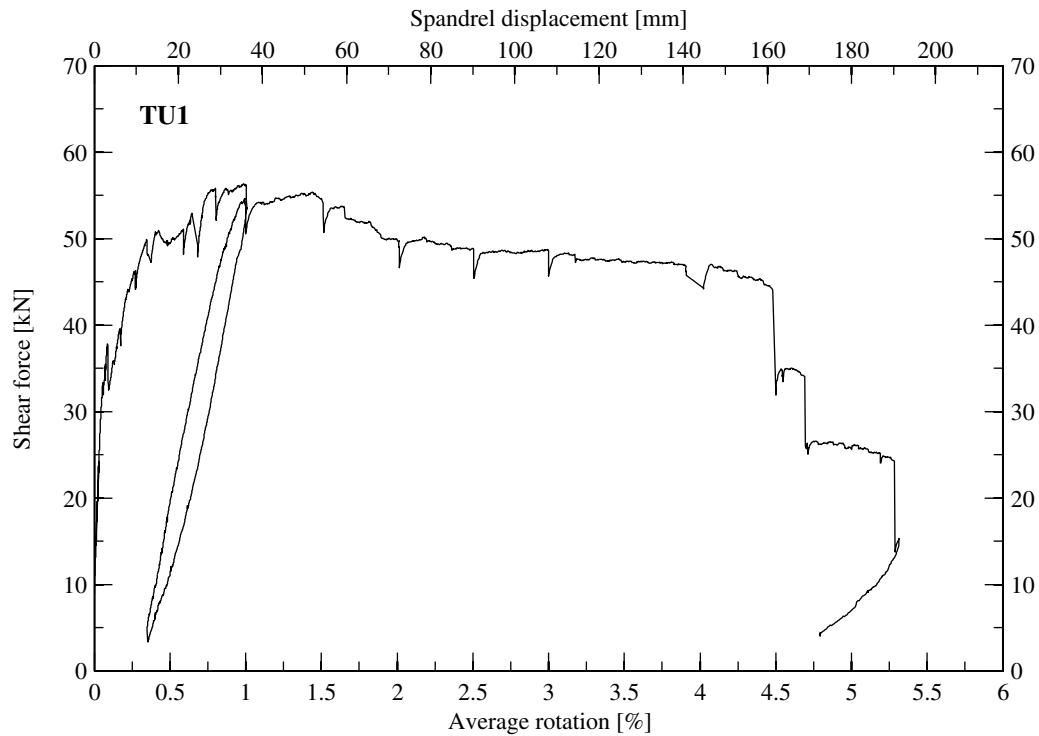


Figure 3.7: TU1: Force-rotation relationship.

Variation of the axial loads on the piers

The control of the axial forces worked well and the variation of the axial force over the course of the test was therefore rather small (Fig. 3.10).

Local deformations of the RC beam of TU1

Figures 3.11 and 3.12 show the deformation demand on the RC beam in terms of curvature and axial strain distributions along the beam, respectively. Both quantities are plotted for four load steps corresponding to nominal drift demands of 0.4%, 0.8%, 1.0% and 2.0%. Figure 3.11 confirms the observation made during testing: The South plastic hinge, which was subjected to positive bending, was for the first three plotted load steps (LS 7, 9 and 10 corresponding to $\theta_{nom} = 0.4\%$, 0.8% and 1.0%) distributed over a much larger length than the North plastic hinge, which was subjected to negative bending. As a consequence, the curvature demand on the South plastic hinge was smaller than on the North plastic hinge. As the compression strut in the masonry spandrel failed, the picture changed ($\theta_{nom} = 2\%$): Most of the deformation demand on the South plastic hinge concentrated in a single crack close to the South edge of the spandrel resulting in large curvatures which eventually led to rupture of two longitudinal bars at this location. At the North plastic hinge, the distribution of curvatures did not change significantly over the course of loading, but remained always concentrated around the edge of the spandrel.

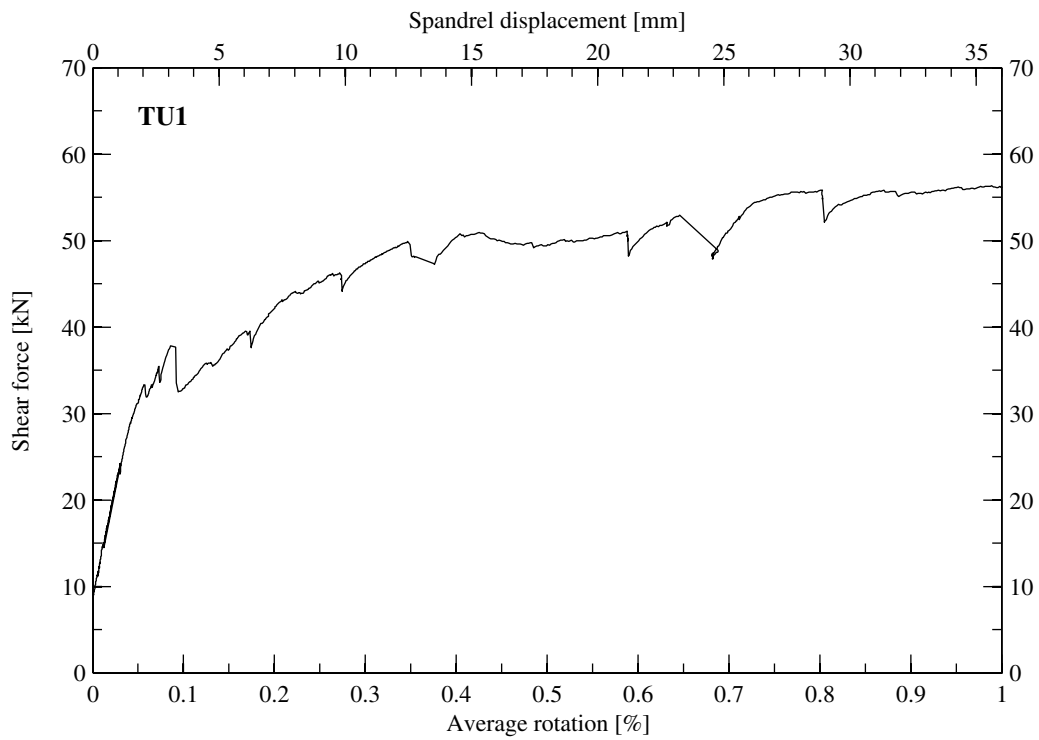


Figure 3.8: TU1: Force-rotation relationship up to a maximum drift of 1%.

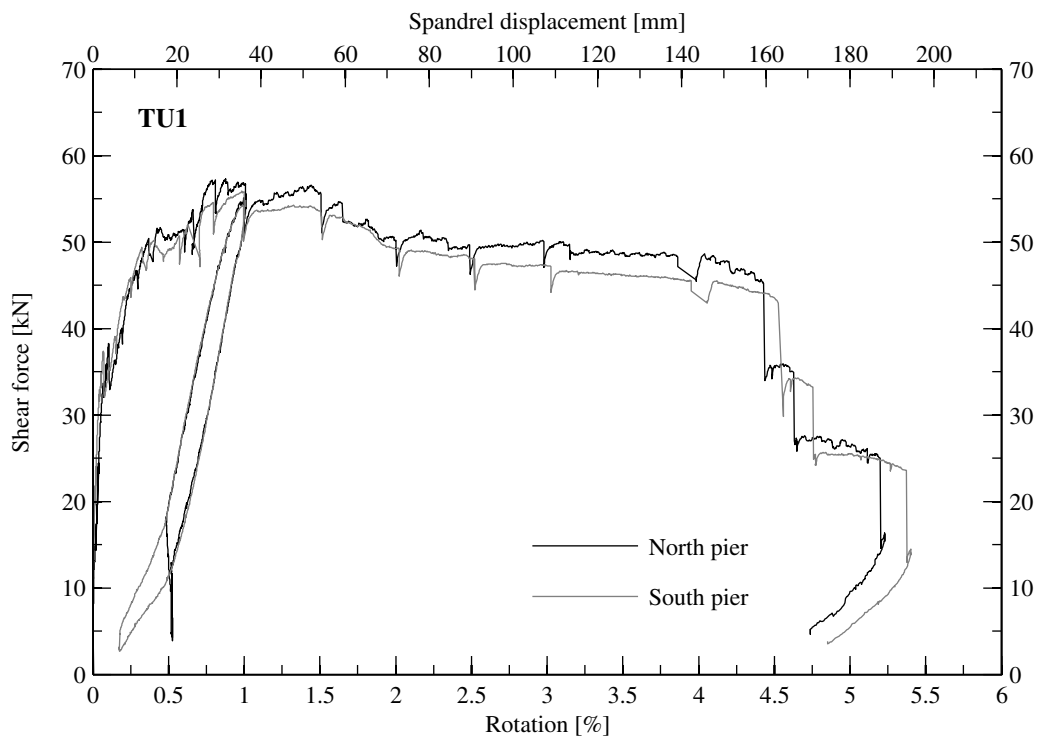


Figure 3.9: TU1: Force-rotation relationship for all cycles showing the non-averaged pier rotations and shear forces.

3. Test results for composite spandrels

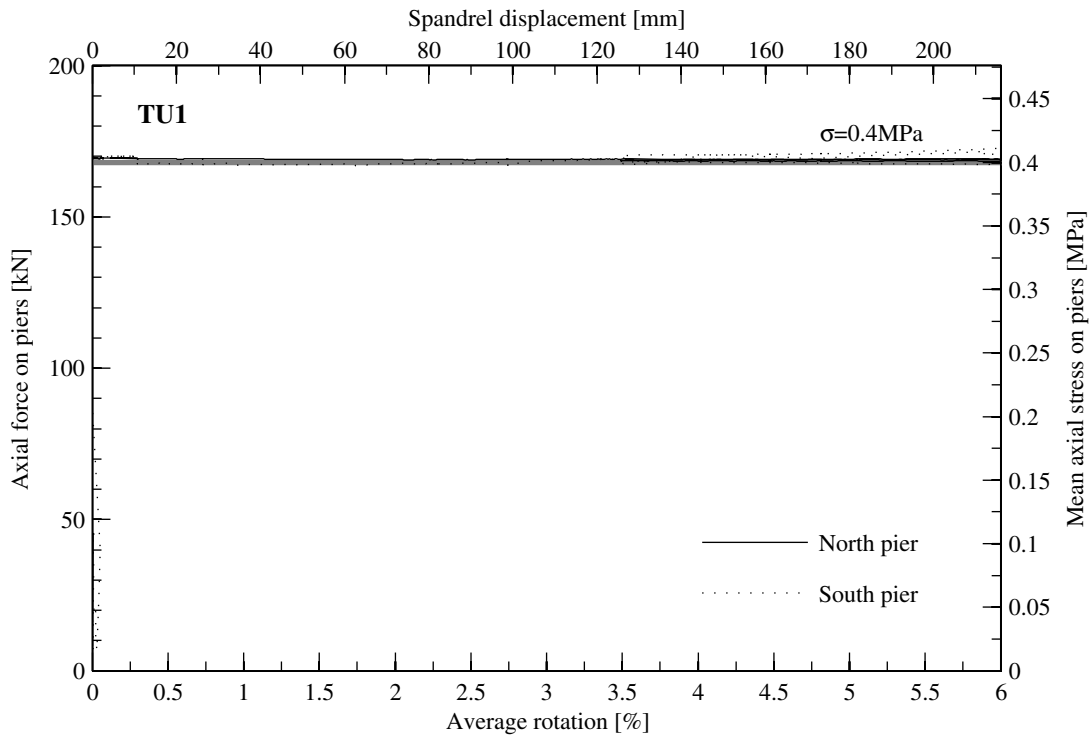


Figure 3.10: TU1: Axial force on piers - rotation relationship for all cycles.

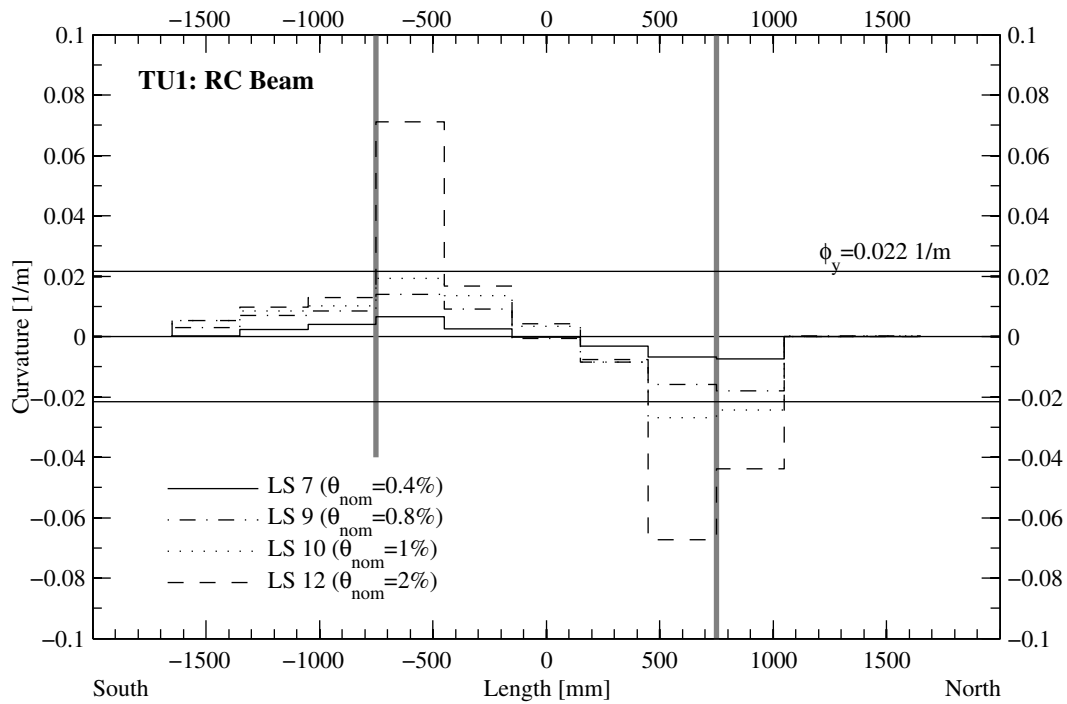


Figure 3.11: TU1: Curvature distribution along the RC beam. The thick grey lines symbolise the edges of the piers.

Since the test setup did not restrain the elongation of the test unit, the composite spandrel grew in length as the loading progressed. Figure 3.12 shows that the axial strains were distributed similarly to the curvatures in the RC beam.

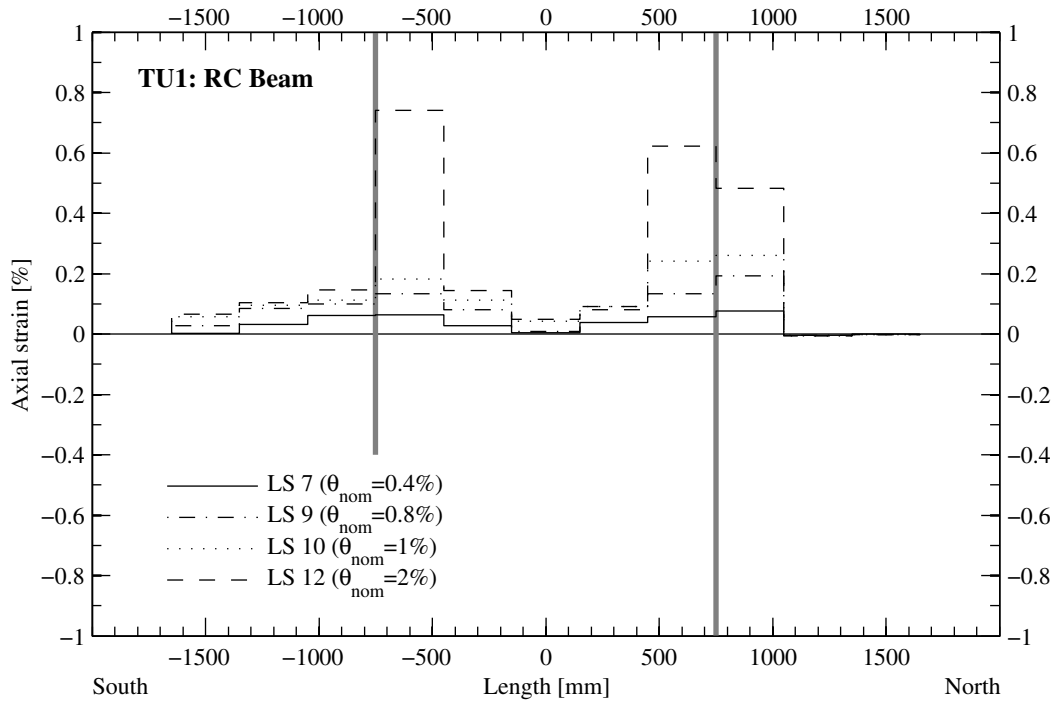


Figure 3.12: TU1: Axial strain distribution along the RC beam. The thick grey lines symbolise the edges of the piers.

3.2.3 Deformation plot

Figure 3.13 shows the deformed shape of TU1 at LS 9 ($\theta_{nom} = 0.8\%$). With respect to the dimensions of the test unit, the deformations are amplified by a factor of 20. Shown with thin lines is the undeformed state of the test unit at LS 0. The LED points of the North pier that are missing were temporarily hidden by the rod applying AFP_N_ES. The LED point at the top South corner of the spandrel is missing since the outer shell of the brick had fallen off (see Fig. 3.4). The plot confirms that the major part of the deformation of the masonry spandrel was absorbed by the flexural crack at its North end.

3. Test results for composite spandrels

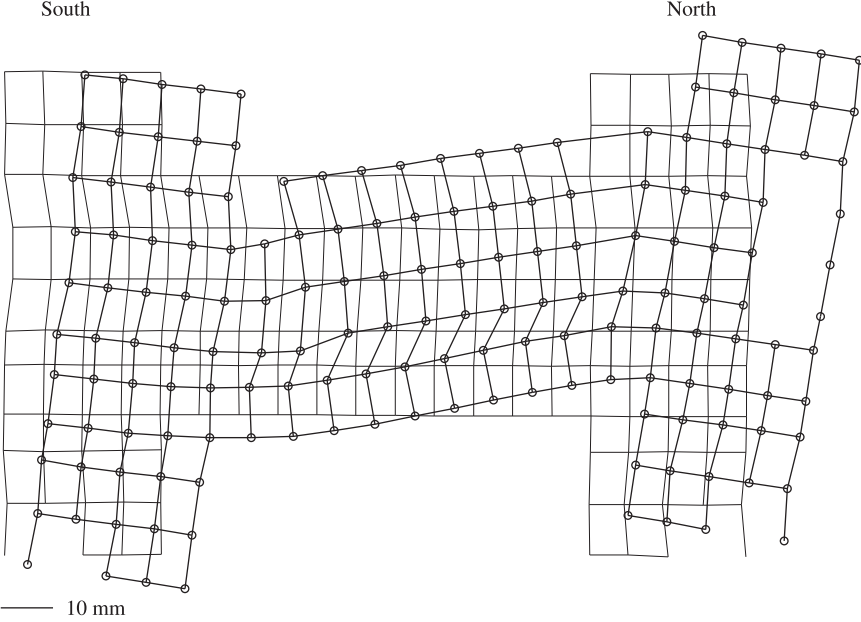


Figure 3.13: TU1: Deformed grid obtained from optical measurements at LS 9 ($\theta_{nom} = 0.8\%$).

3.3 Composite spandrel TU2

3.3.1 Test observations

Test unit TU2 was built with bricks of Type 2 (see Section 1.1). These bricks featured a number of vertical cracks which resulted from residual stresses generated during the production process. These cracks were marked at LS 0 in order to follow whether they were the origin of cracking during the loading process. At LS 0 the forces in the eight vertical rods were zero. As a first load step, each rod was prestressed to a force of approximately 40 kN. The four outer rods were prestressed by hand and then locked-in, the inner rods were prestressed by means of four hollow core jacks that were controlled by two load followers, i.e. the two hollow core jacks on one pier were connected to the same load follower. The vertical forces were applied on 22.03.2009. The test unit was tested on 23.03.2009.

The first cracks appeared when loading to LS 4 ($\theta_{nom} = 0.1\%$, Fig. 3.14). In the masonry spandrel two stair-stepped cracks formed. Further cracks of one brick height formed at the North top end of the spandrel. A crack in the RC beam formed 37 cm away from the South edge of the spandrel, i.e. approximately where the centre line of the compression strut in the masonry was supported by the RC beam. Further cracks in the RC beam formed at the North end of the spandrel.

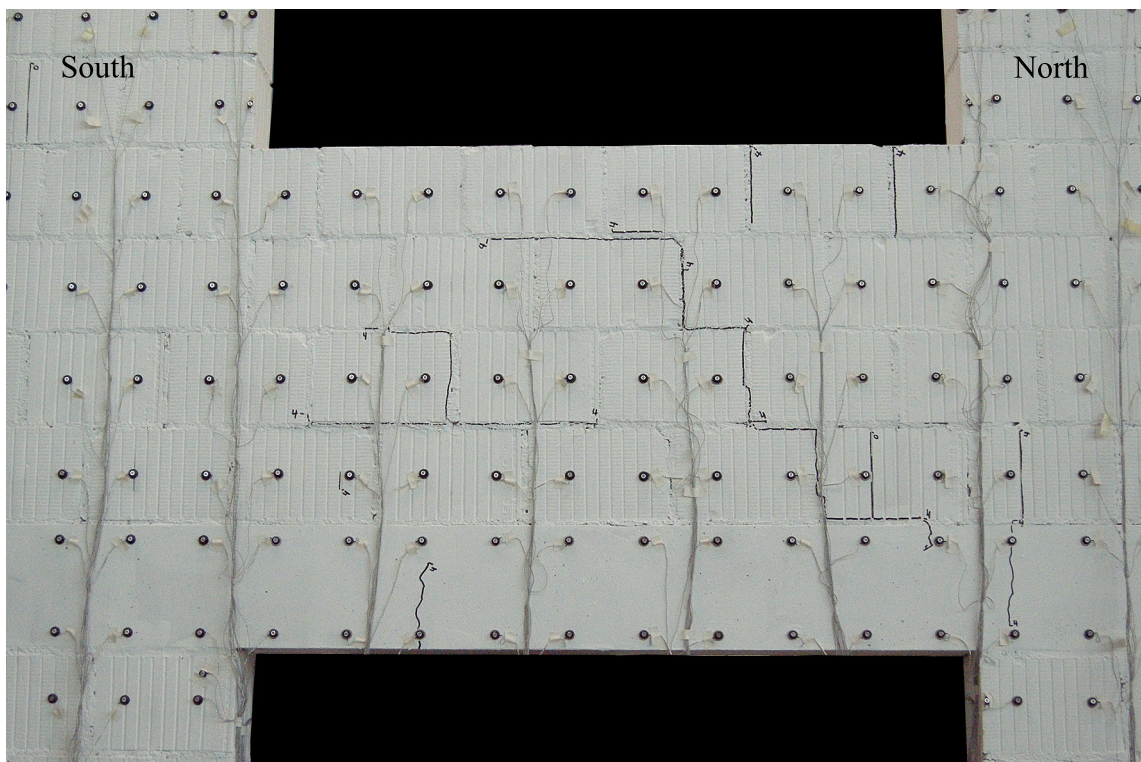


Figure 3.14: TU2: Crack pattern of spandrel at LS 4 when first cracks appeared. Drift towards North with $\theta_{nom} = 0.1\%$.

Figure 3.15 shows the crack pattern of TU2 at LS 7 ($\theta_{nom} = 0.4\%$). Most of the additional stair-stepped cracks in the masonry had formed when loading from LS 4 to LS 5. As loading continued,

3. Test results for composite spandrels

the deformation of the masonry spandrel concentrated in the stair-stepped crack originating close to the top South corner of the spandrel. At the top South brick a small chip sheared off when loading to LS 6 (Fig. 3.16). However, compared to the same brick of TU1, this brick was still in a fairly good condition. Also the crack pattern of the masonry spandrel as a whole suggested that the tensile and shear strength of the bricks of Type 2 had to be considerably higher than those of bricks of Type 1; this was confirmed by the results obtained from material tests of the bricks (Section 2.4). Nevertheless, one inclined crack running through a brick above the RC beam showed that the compression diagonal caused a high demand on the bricks. While the crack pattern of the masonry spandrel of TU2 was very different to that of TU1, the crack patterns of their RC beams were relatively similar: In both cases the South plastic hinge was spread out over a significantly larger length than the North plastic hinge, which was concentrated at the South edge of the North pier. In quantitative terms, however, differences can be identified: In TU2 the South plastic hinge spread for greater drift demands over a larger length than in TU1 since the compression diagonal in the masonry spandrel of TU2 failed significantly later in terms of drifts than the compression diagonal of TU1.

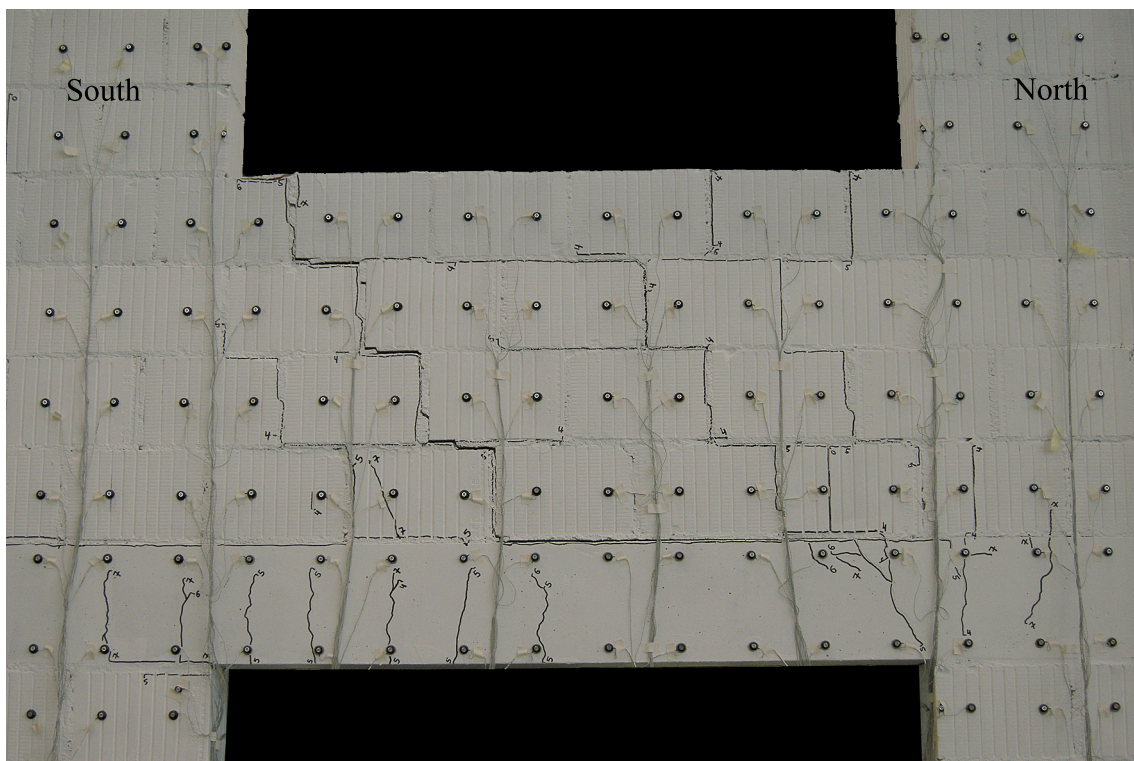


Figure 3.15: TU2: Crack pattern of spandrel at LS 7. Drift towards North with $\theta_{nom} = 0.4\%$.

The main crack pattern remained in the following fairly stable. Figure 3.17 shows the crack pattern at LS 9 ($\theta_{nom} = 0.8\%$). The figure shows clearly how the masonry spandrel North of the large stair-stepped crack lifted up and was therefore almost stressless. Some shear stresses in this part of the spandrel were caused by the shear stresses that were transmitted in the head joints of the large stair-stepped crack. These shear stresses were generated by the clamping stresses that originated from geometrical compatibility requirements. As the drift demand increased, the mortar in the head joints was increasingly compressed and at some point crushed. This led to a drop in the shear force that was transmitted through the stair-stepped crack and therefore also to a drop in the

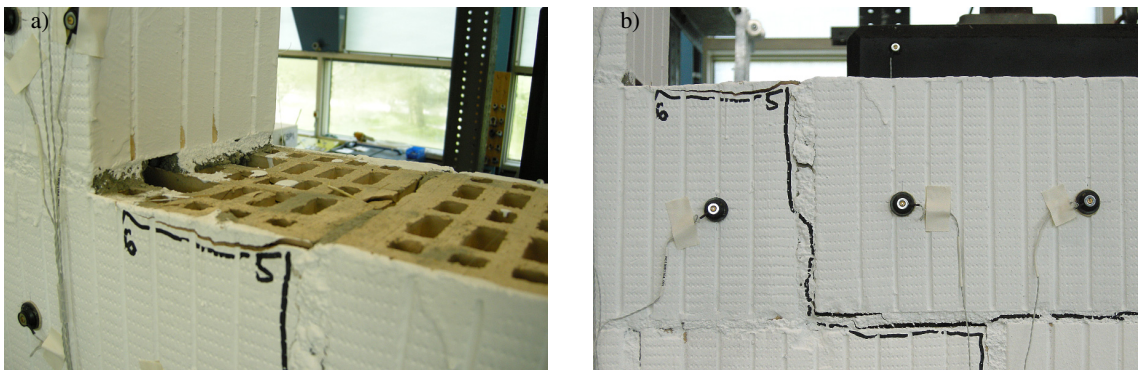


Figure 3.16: TU2: Top South brick of spandrel: A chip sheared off at the top of the brick at LS 6. Drift towards North with $\theta_{nom} = 0.3\%$.

overall spandrel shear force. The strain in the compression diagonal is strongly related to the drift of the piers, the stiffness of the RC beam and the stiffness of the compression diagonal. However, although a similar maximum drift as in the case of TU1 was reached, the compression diagonal did not fail. Cracks within the compression diagonal suggested that the latter was subjected to large stresses. The different brick geometry (see Section 2.4), however, permitted the bricks to accommodate these stresses. Failure occurred when loading to LS 15 ($\theta_{nom} = 4\%$) as in the case of TU1 due to rupture of longitudinal bars in the RC beam. The most likely order of rupture was (i) East top bar of North hinge, and (ii) one bottom bar of South hinge.

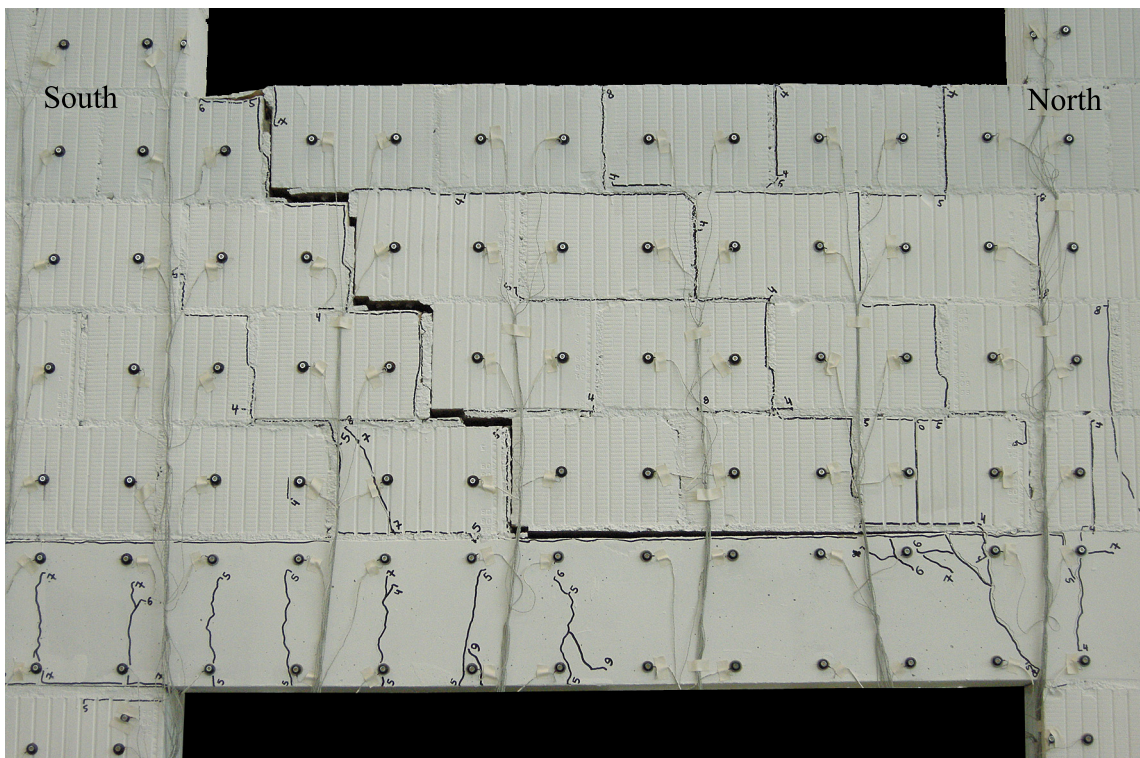


Figure 3.17: TU2: Crack pattern of spandrel at LS 9. Drift towards North with $\theta_{nom} = 0.8\%$.

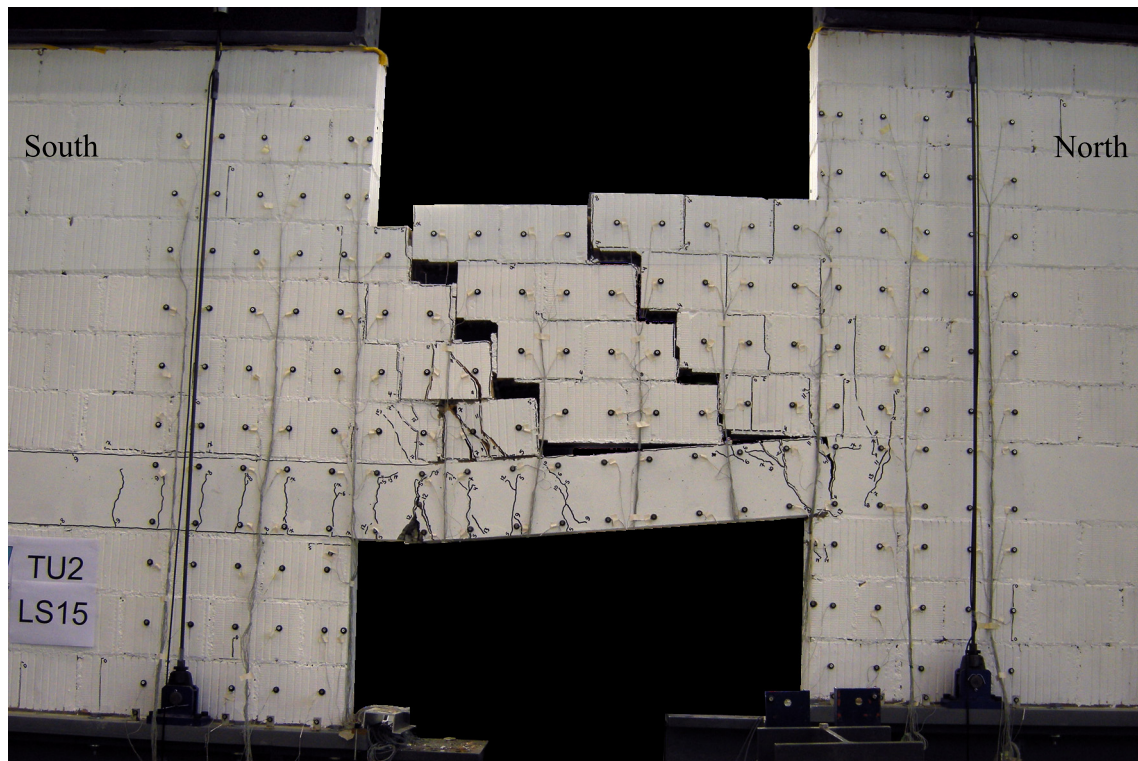


Figure 3.18: TU2: Crack pattern of spandrel at LS 15. Drift towards North with $\theta_{nom} = 4\%$ (failure of TU2).

3.3.2 Test results

The following figures show the standard graphs derived from the hard-wired measurements that have been defined in Section 3.1. The hysteretic behaviour of the test unit in terms of spandrel shear force vs. average rotation is presented first. Then, the variation of the axial load on the piers is shown and finally the deformations of the RC beam are discussed in terms of local curvatures and axial elongations. At the end of the section plots of the deformed shape of the test unit at selected load steps are presented. These plots were derived from the optical measurement data.

Force-rotation behaviour of TU2

Figures 3.19 and 3.20 show the force-rotation relationship for TU2. Although the behaviour of the masonry spandrels of TU1 and TU2 were rather different, the resulting pushover curve is similar. The sharp drops in shear force for rotations smaller than 0.25% are associated with the formation of diagonal stair-stepped cracks in the spandrel. The final drops in shear force, which constituted the failure of the test unit, are associated with the rupture of three longitudinal bars.

Variation of the axial load on the piers

The control of the axial forces worked well and the variation of the axial force over the course of the entire test was therefore rather small (Fig. 3.22).

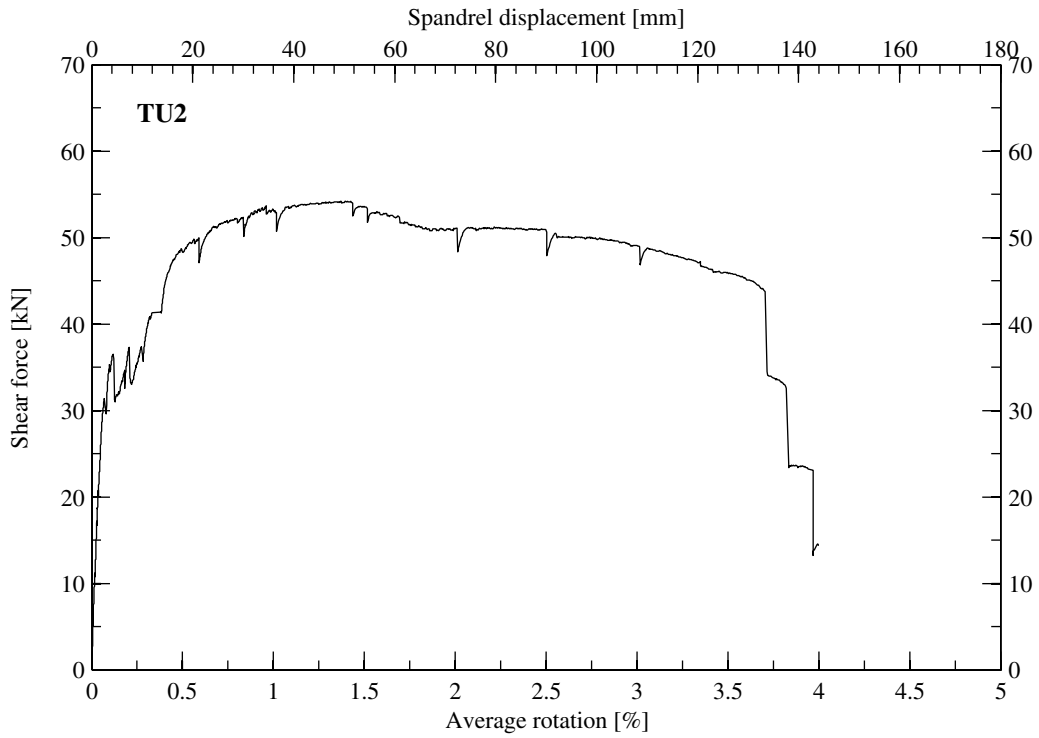


Figure 3.19: TU2: Force-rotation relationship.

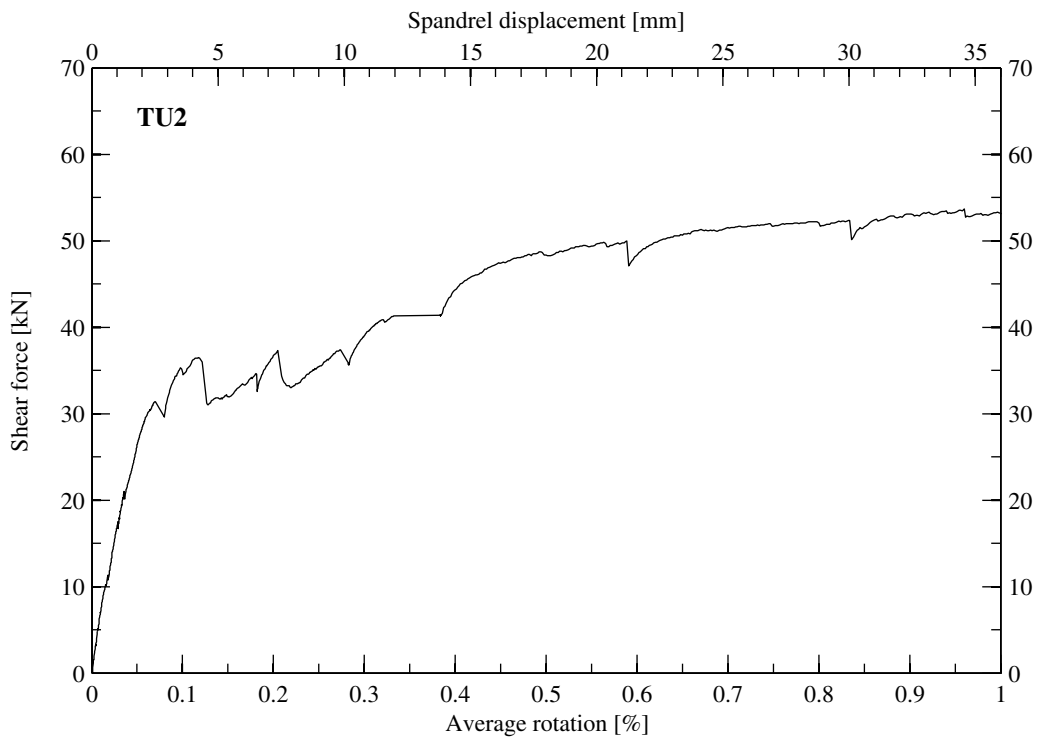


Figure 3.20: TU2: Force-rotation relationship up to a maximum drift of 1%.

3. Test results for composite spandrels

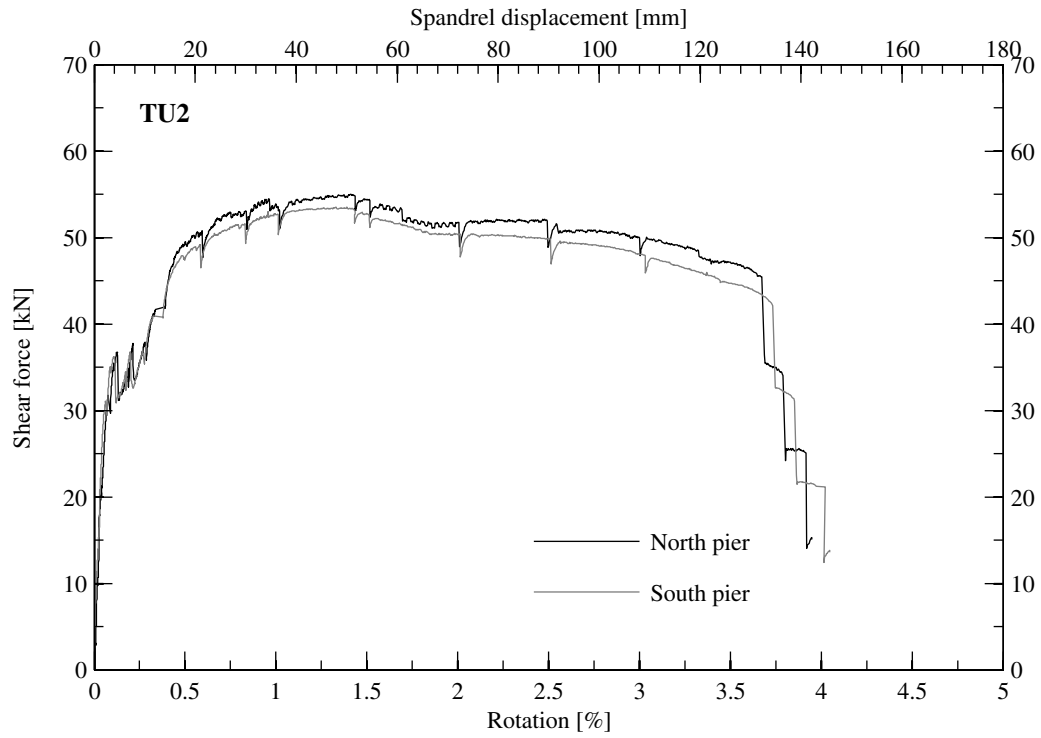


Figure 3.21: TU2: Force-rotation relationship showing the non-averaged pier rotations and shear forces.

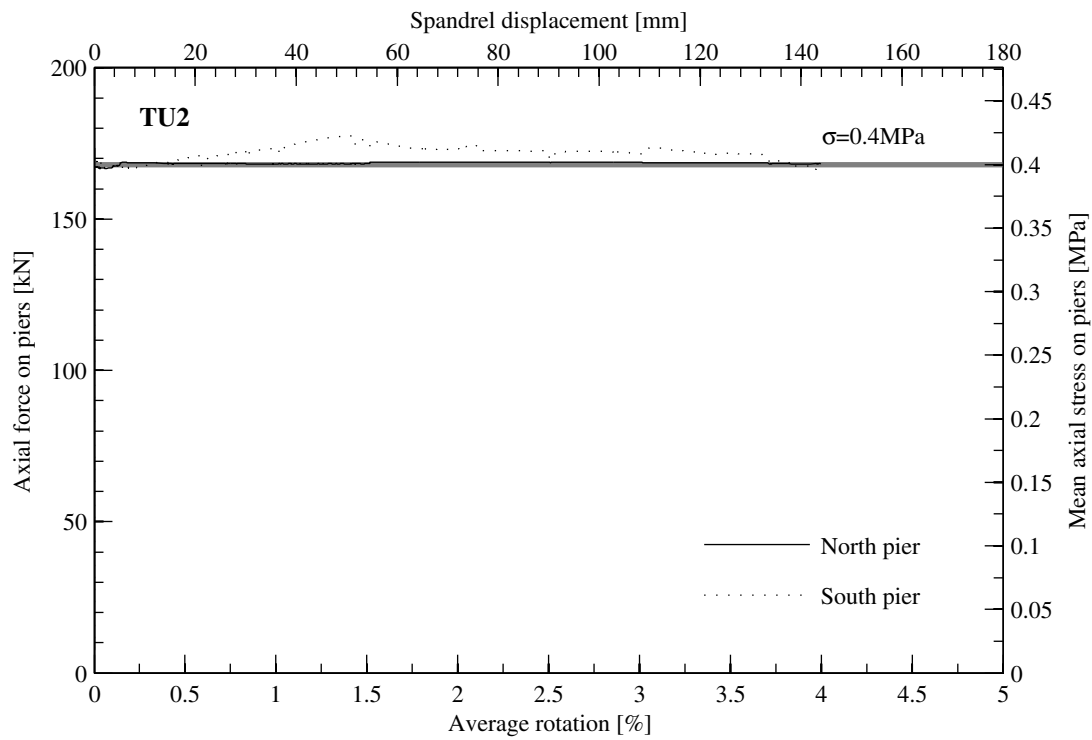


Figure 3.22: TU2: Axial force on piers - rotation relationship for all cycles.

Local deformation of the RC beam of TU2

Figures 3.23 and 3.24 show the deformation demand on the RC beam for different load steps in terms of curvature and axial strain distributions along the beam, respectively. The behaviour in general is very similar to TU1. The largest recognisable difference takes place at LS 12 ($\theta_{nom} = 2\%$), which for both test units corresponds to the load level at onset of crushing of the compression diagonal. At this load step, for TU2 the curvature demand on the South hinge is shifted more towards the centre of the span than for TU1. In addition, the curvature demand is larger for TU2 than for TU1. These two observations indicate that at this stage of loading the compression diagonal of TU2 was stronger and stiffer than the compression diagonal of TU1, forcing hence the RC beam to deform more than in the case of TU1.

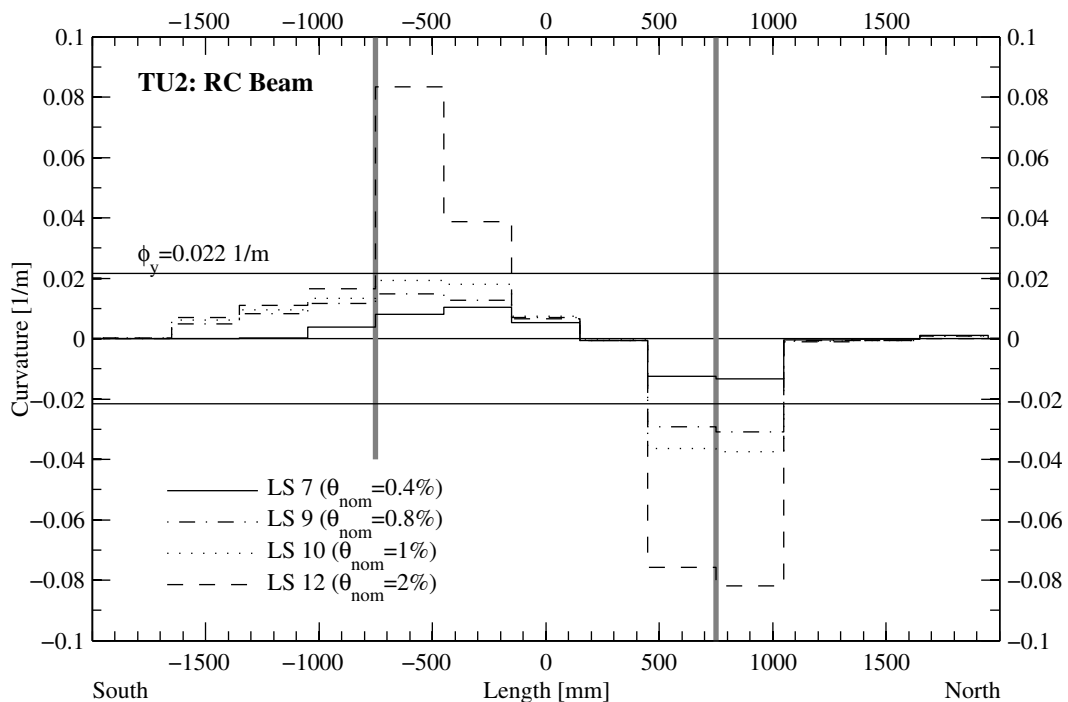


Figure 3.23: TU2: Curvature distribution along the RC beam. The thick grey lines symbolise the edges of the piers.

3.3.3 Deformation plots

Figure 3.25 shows the deformed shape of TU2 at LS 4 ($\theta_{nom} = 0.1\%$), LS 5 ($\theta_{nom} = 0.2\%$), LS 7 ($\theta_{nom} = 0.4\%$) and LS 9 ($\theta_{nom} = 0.8\%$). With respect to the dimensions of the test unit, the deformations are amplified by factors ranging between 20 and 160 so that the magnitude of the plotted deformations is for all load steps approximately equal. Shown with thin lines is the undeformed state of the test unit at LS 0. The plots show particularly well the evolution of the shear deformations of the masonry spandrel with increasing rotation demand. At LS 4 a shear crack had just formed at the North end of the spandrel (Fig. 3.25a). It was, however, only a very fine crack. When loading was continued a larger shear crack opened up at the South end of the spandrel, which became the dominant shear crack and the main mechanism of the spandrel for accommodating the

3. Test results for composite spandrels

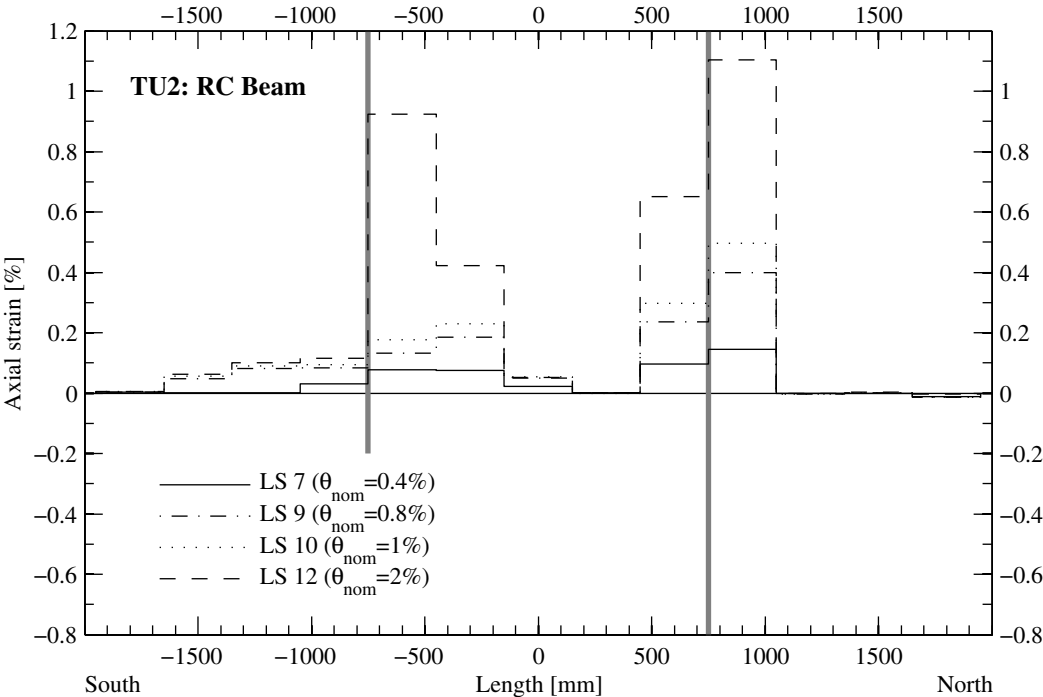


Figure 3.24: TU2: Axial strain distribution along the RC beam. The thick grey lines symbolise the edges of the piers.

deformation demand (Fig. 3.25b-d). As this shear crack became wider, bending of the masonry spandrel reduced and the North part of the masonry spandrel moved basically as a rigid body.

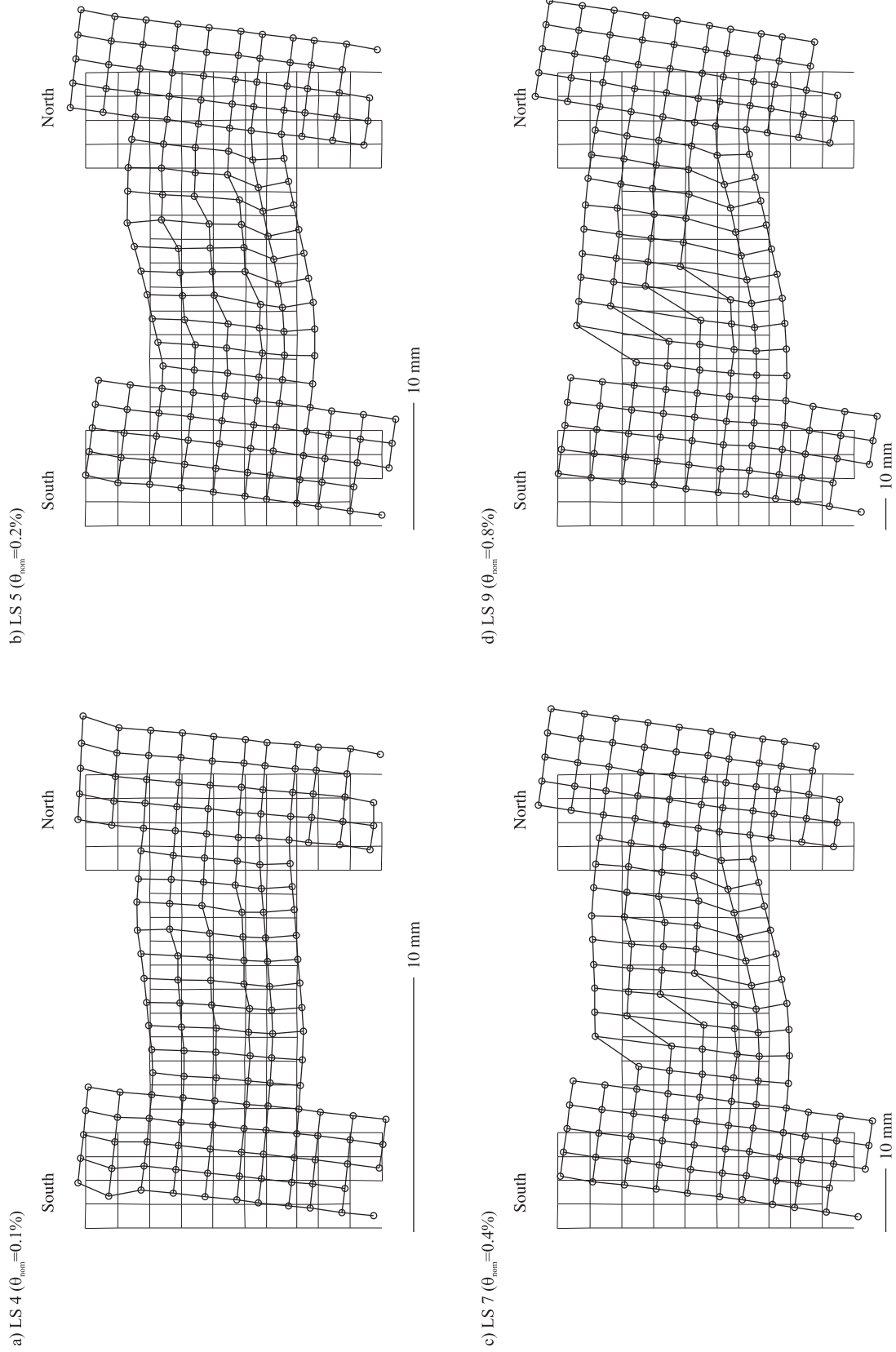


Figure 3.25: TU2: Deformed grid obtained from optical measurements at nominal rotation demands of $\theta_{nom} = 0.1\%$, 0.2% , 0.4% and 0.8% .

3.4 Composite spandrel TU3

3.4.1 Test observations

Test unit TU3 was the first spandrel tested under cyclic loading. It had the same general properties as TU2, i.e. the same type of bricks were used and the RC beam had the same longitudinal reinforcement. Although the bricks had again some initial vertical cracks, which resulted from residual stresses, these were not marked. TU2 had shown that these cracks did not influence significantly the crack pattern that formed under loading. Since only the latter is of interest here, the initial cracks were no longer marked. At LS 0 the forces in the eight vertical rods were zero. As a first load step, each rod was prestressed to a force of approximately 40 kN. The four outer rods were prestressed by hand and then locked-in, the inner rods were prestressed by means of four hollow core jacks that were controlled by two load followers, i.e. the two hollow core jacks on one pier were connected to the same load follower. The vertical forces were applied on 27.05.2009. The test unit was tested on 28.05, 29.05 and 02.06.2009; an overview on the load steps covered during each testing day is given in Table 3.2.

Table 3.2: TU3: Testing days and corresponding load steps.

Testing day	Load steps carried out
27.05.2009	LS 1
28.05.2009	LS 2 - LS 27
29.05.2009	LS 28 - LS 46
02.06.2009	LS 47 - LS 50

The first cracks appeared at LS 10 ($\theta_{nom} = 0.1\%$). These cracks were: (i) a small stair-stepped crack at about midlength of the spandrel just above the RC beam and (ii) a crack between the bottom face of the RC beam and the South pier, which reached about 15 cm into the pier. More cracks developed when the loading direction was reversed. For this direction of loading several stair-stepped cracks extended over almost the entire height of the spandrel and two small cracks formed at the South hinge, which for this direction of loading was the negative hinge. The resulting crack pattern was therefore not symmetric (Fig. 3.26). The likely reason is a slight initial rotation of the North lever beam, which was created to minimise the gap between base plates of the test unit and the lever beams when lifting the test unit on the test stand. However, the evaluation of the results suggests that this must have caused initial stresses in the test unit.

During the cycles with amplitudes of $\theta_{nom} = \pm 0.2\%$ the crack pattern became more symmetric and most of the bed and head joints of the masonry spandrel were cracked. In addition, positive flexural cracks had formed at the position of almost all stirrups within the free span of the RC beam and the innermost stirrups within the piers. Negative flexural cracks had formed close to the inner edges of the South and North piers. When loading to the first peak of the cycles with amplitudes of $\theta_{nom} = \pm 0.3\%$ (LS 18) a drop in shear force in the spandrel was associated with the shearing off of a chip at the South top edge of the spandrel, similar to what happened in the case of TU2. For the negative direction of loading (LS 19) a first inclined crack through a brick within the compression diagonal formed at the North top edge of the spandrel. Figure 3.27 shows the crack pattern at the second peak of the cycles with amplitudes of $\theta_{nom} = 0.4\%$ (LS 23). At this instant, the crack

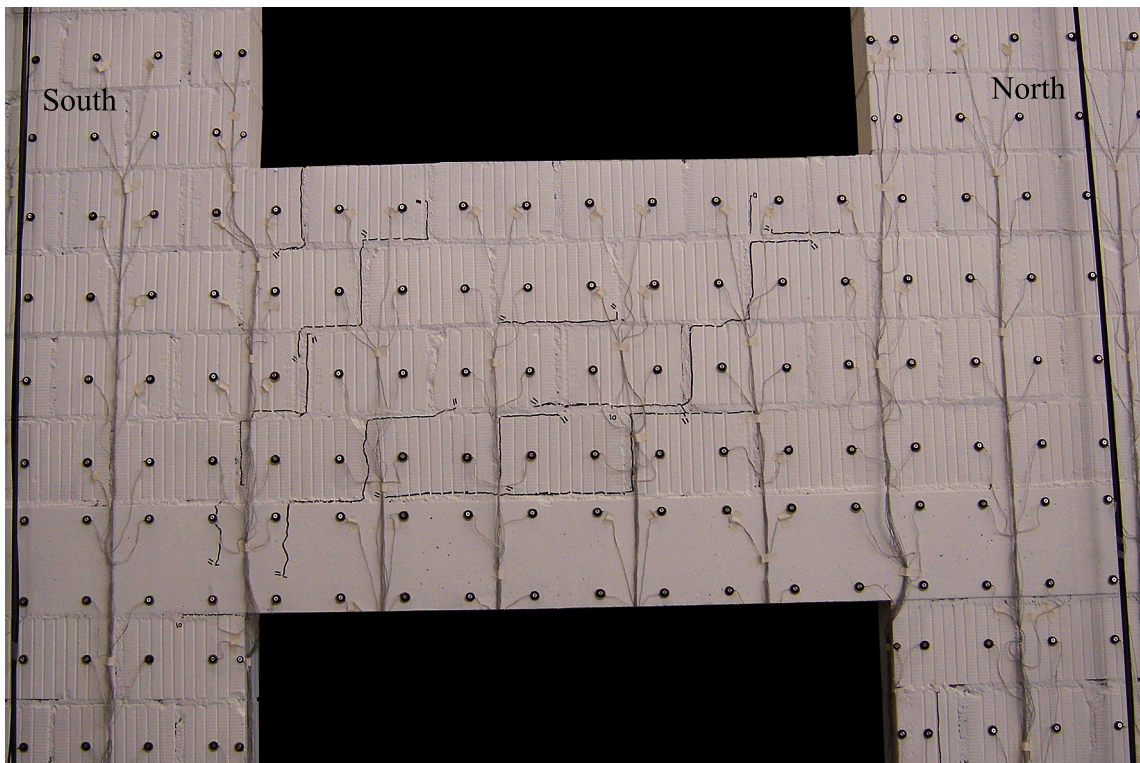


Figure 3.26: TU3: Crack pattern of spandrel at LS 11. Drift towards South with $\theta_{nom} = -0.1\%$.

pattern in the masonry spandrel and the RC beam was almost completely developed. Further cracks occurred mainly within the crushing compression diagonals in the masonry spandrel.

LS 27 ($\theta_{nom} = -0.6\%$) marked the end of the first testing day. After unloading, all the positive flexural cracks were closed. The negative flexural cracks left and right of the pier edges had residual crack widths of about 0.1 mm. The stair-stepped cracks in the masonry remained open with residual crack widths of up to 0.8 – 1.2 mm. Figures 3.28 and 3.29 show the test unit at the first and second peak with amplitudes of $\theta_{nom} = \pm 0.8\%$, respectively. The figures show that for the positive direction of loading (LS 30, Fig. 3.28) the bulk deformation in the masonry spandrel was concentrated in one single stair-stepped crack while for the negative direction of loading (LS 31, Fig. 3.29) the deformation was distributed over two cracks with almost equal crack widths.

As loading continued, splitting of the compression diagonals in the masonry spandrel continued. The cracks in the RC beam, in particular the inclined shear cracks, which were part of the negative plastic hinges, branched out. The mortar bed beneath the RC slab started to crush at the inner edges of the piers. At LS 39 ($\theta_{nom} = -1.5\%$) the shear force dropped slightly. This drop in force was most likely associated with the formation of a new shear crack in the RC beam. This new crack formed about 56 cm away from the South pier. When compared to the monotonic loading, it seems that the cyclic loading was beneficial for the masonry, in the sense that all bricks were disjunct and the deformations more equally distributed over the spandrel. As a result, the stresses in single bricks were likely to be smaller in the case of cyclic loading. For the RC beam the opposite was the case: As a result of the cyclic loading, the elongation of the beam was larger than in the case of

3. Test results for composite spandrels

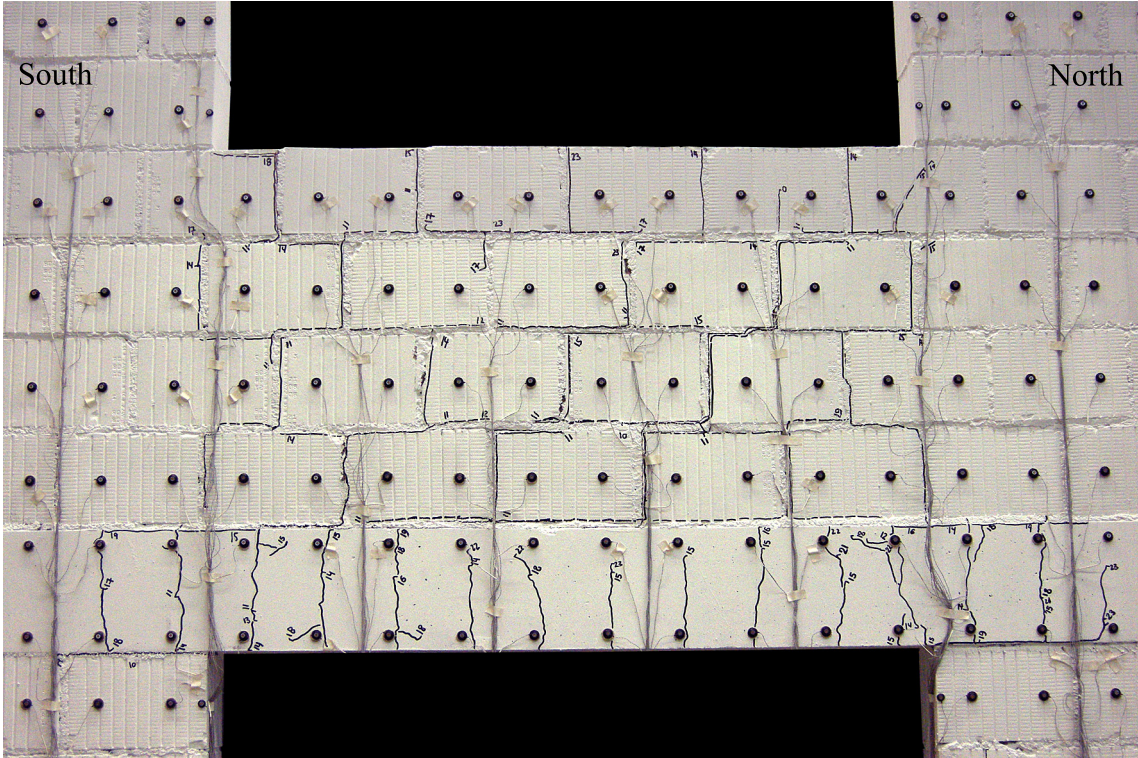


Figure 3.27: TU3: Crack pattern of spandrel at LS 23. Drift towards South with $\theta_{nom} = -0.4\%$.

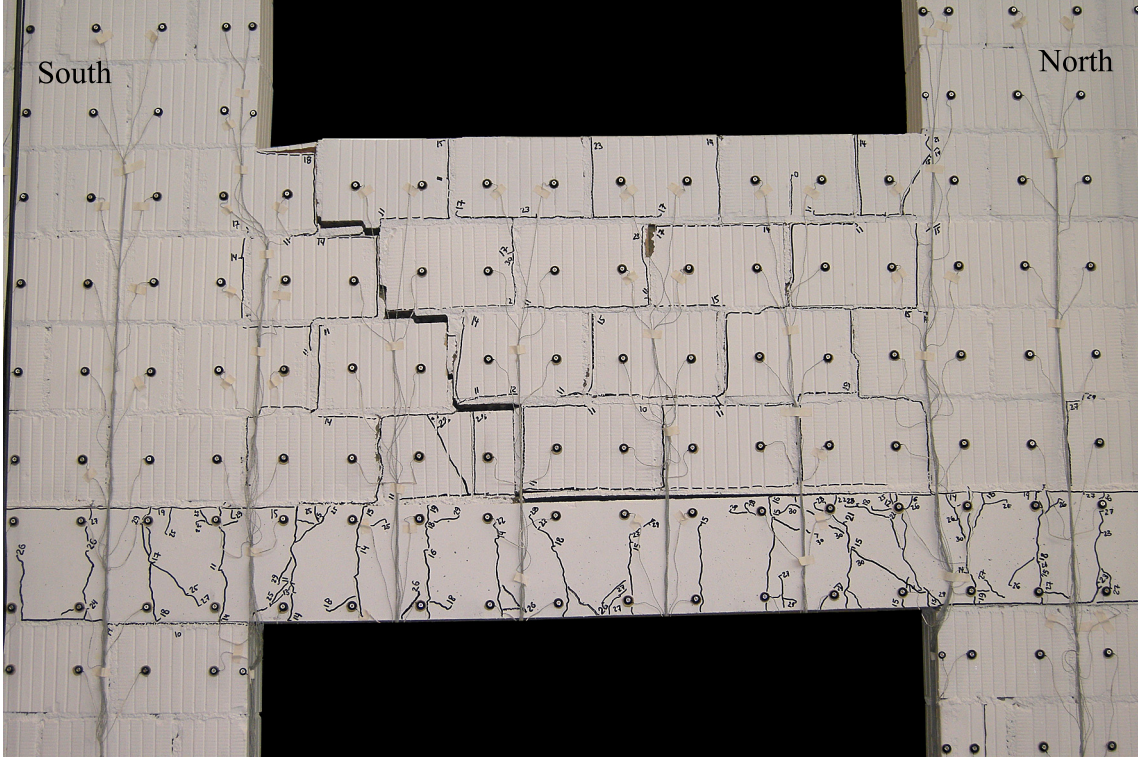


Figure 3.28: TU3: Crack pattern of spandrel at LS 30. Drift towards North with $\theta_{nom} = 0.8\%$.

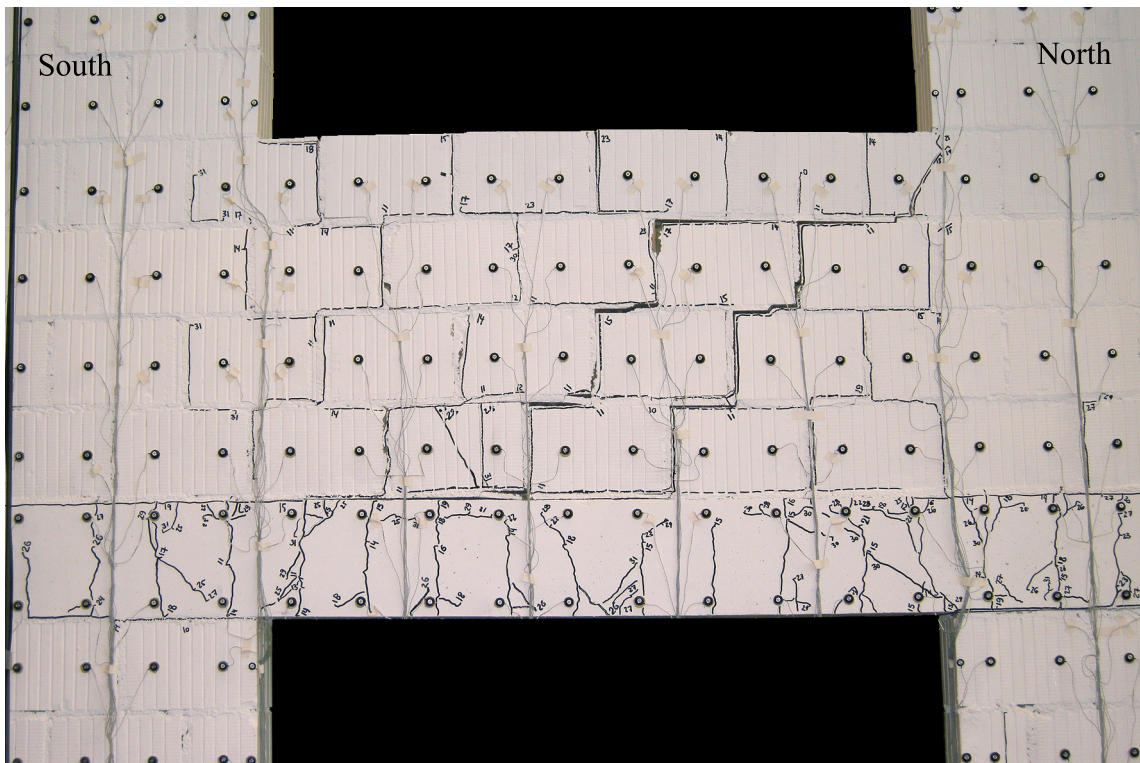


Figure 3.29: TU3: Crack pattern of spandrel at LS 31. Drift towards South with $\theta_{nom} = -0.8\%$.

monotonic loading. Hence, the crack widths in the RC beam were also larger, reducing the shear force that could be carried by aggregate interlock of the concrete.

When loading to the first peak of the cycles with amplitudes of $\theta_{nom} = \pm 2.0\%$ (LS 42) the compression diagonal strut reaching from the top South corner into the spandrel failed. Part of the outer shell of a brick within the compression diagonal fell off and revealed that also the inner part of the brick was crushed. For the negative direction of loading, the compression diagonal was in much better shape. First cracks through bricks (apart from the top brick) appeared only when loading to LS 45 ($\theta_{nom} = -2.0\%$). Spalling of the cover concrete of the RC beam started when loading to LS 43 and continued over the next load steps. When loading to LS 49 (last peak of the cycles with amplitudes of $\theta_{nom} = \pm 2.5\%$), the stirrup 54 cm away from the South end of the spandrel fractured. The stirrup did not open up since it was closed by 135° hooks. At this instant no longitudinal bars had ruptured. Loading was then reversed and the spandrel taken to a mean drift of $\theta_{nom} = 3.0\%$ (LS 50). Just before reaching this peak drift, the top West bar fractured about 5 cm northwards from the North end of the spandrel (i.e. slightly inside the North pier). This load step marked the end of the test and it is shown in Fig. 3.30.

3.4.2 Test results

The following figures show the standard graphs derived from the hard-wired measurements that have been defined in Section 3.1. The hysteretic behaviour of the test unit in terms of spandrel shear force vs. average rotation is presented first. Then, the variation of the axial load on the piers

3. Test results for composite spandrels

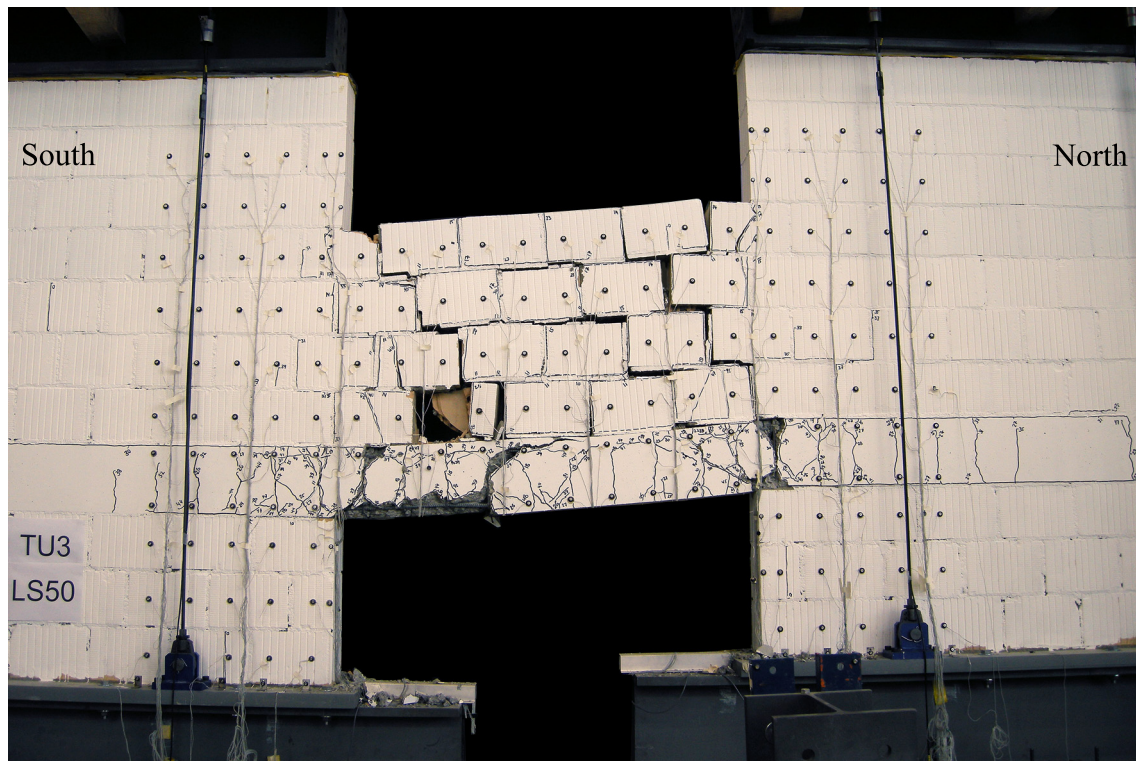


Figure 3.30: TU3: Crack pattern of spandrel at LS 50. Drift towards North with $\theta_{nom} = 3\%$ (failure of TU3).

is shown and finally the deformations of the RC beam are discussed in terms of local curvatures and axial elongations. At the end of the section plots of the deformed shape of the test unit at selected load steps are presented. These plots were derived from the optical measurement data.

Hysteretic behaviour of TU3

The global hysteretic behaviour of TU3 is shown in Figs. 3.31 and 3.32. The latter shows the cycles up to a maximum amplitude of $\theta_{nom} = \pm 0.8\%$. For this range of loading the behaviour of the test unit was still largely elastic. The hysteresis loops are narrow and the energy dissipation was limited. A significant drop in shear force capacity was observed during the second cycle with $\theta_{nom} = 1.5\%$ (LS 40, Fig. 3.31). This was – as for TU1 and TU2 – most likely associated with the onset of crushing of the compression diagonal in the masonry spandrel. The same phenomenon is reflected in the drops of shear force during the next cycle, i.e. the first cycle with $\theta_{nom} = 2.0\%$ (LS 42). Failure occurred during the first cycle with $\theta_{nom} = \pm 3.0\%$: During loading in the positive direction a stirrup of the shear reinforcement fractured, while during the ensuing loading in the negative direction a longitudinal reinforcement bar fractured. Both fractures are reflected by distinctive drops in shear capacity of the spandrel.

Figure 3.33 shows the individual shear forces and pier rotations. The difference between the quantities computed for the North and South piers is rather small and the measurements seem therefore reliable.

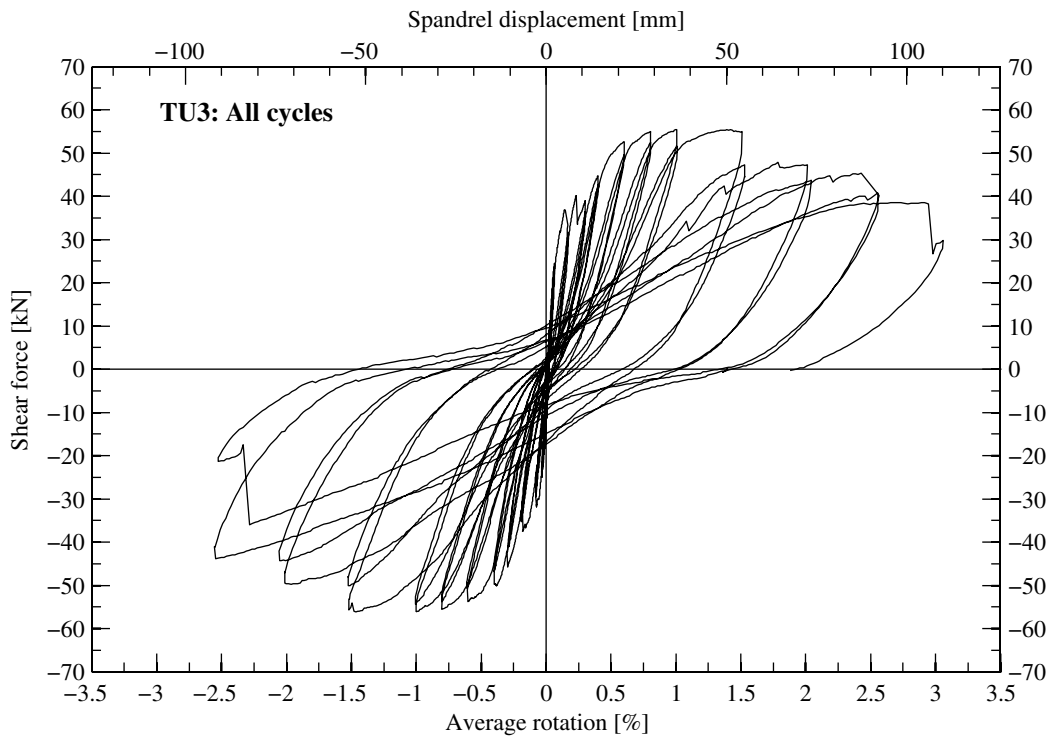


Figure 3.31: TU3: Force-rotation relationship for all cycles.

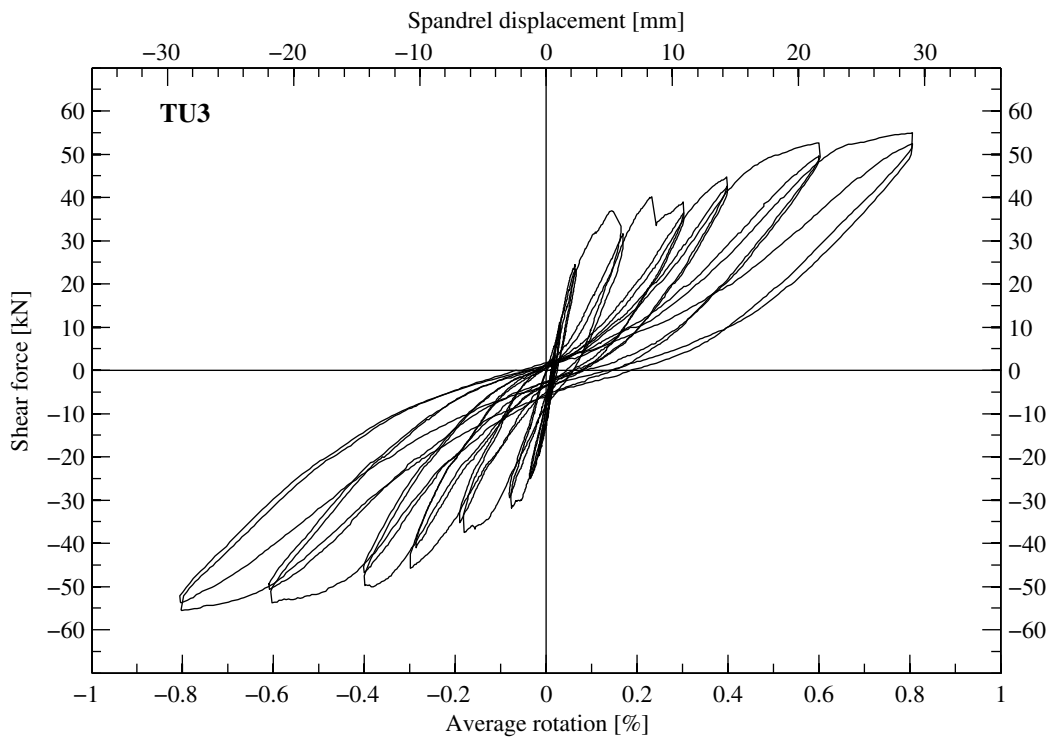


Figure 3.32: TU3: Force-rotation relationship for the cycles up to $\theta_{nom} = \pm 0.8\%$ (LS 1-33).

3. Test results for composite spandrels

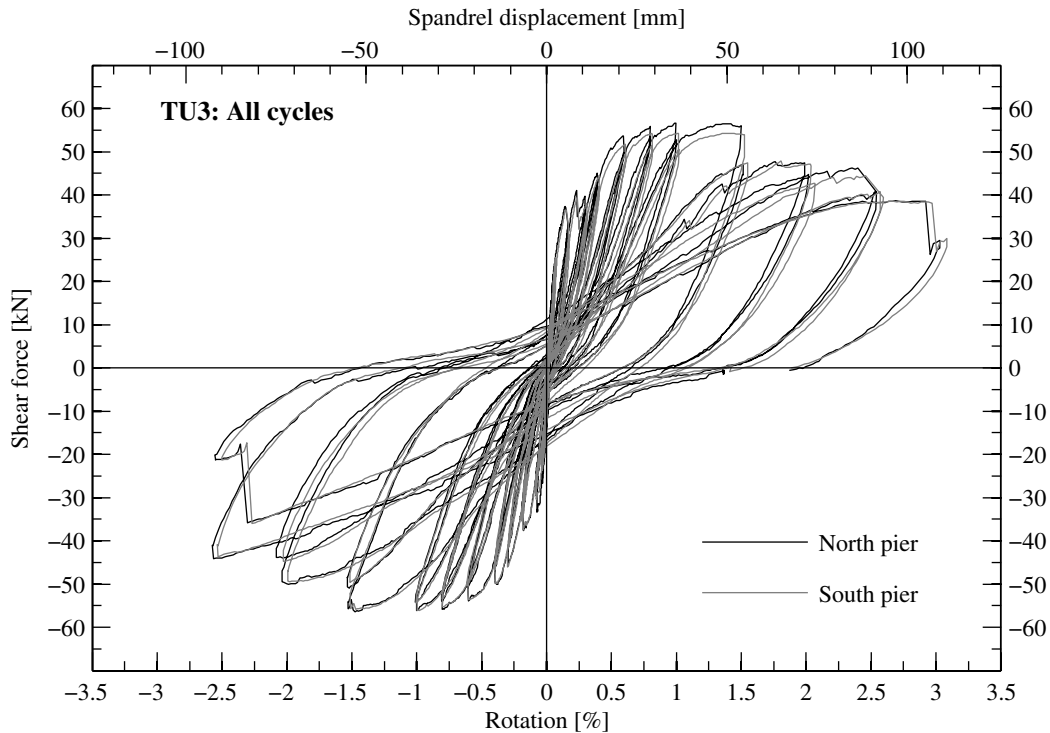


Figure 3.33: TU3: Force-rotation relationship for all cycles showing the non-averaged pier rotations and shear forces.

Variation of the axial load on the piers of TU3

For TU3 the variation in axial load was significantly larger than for TU1 or TU2, which were tested under monotonic loading (Fig. 3.34). Under cyclic loading the movement of the hollow core jacks, which were used in combination with the load follower to regulate the axial force, changed at each peak. These hollow core jacks, however, featured some slip stick effects, which caused during the cyclic loading a small hysteresis of the applied axial load since it required some change in pressure to reverse the movement of the pistons of the hollow core jacks.

Local deformations of the RC beam of TU3

Figures 3.35 and 3.36 show the deformation demand on the RC beam for different load steps in terms of curvature and axial strain distributions along the beam, respectively. Since the test unit was subjected to cyclic loading, the curvature and axial strain profiles are plotted for the positive and the negative direction of loading separately. Apart from the cycles with $\theta_{nom} = \pm 2.0\%$ the curvature distribution (Fig. 3.35) is rather symmetric for the positive and negative direction of loading. When comparing the curvature distribution to that of TU2, which was subjected to monotonic loading, it appears that the curvature distribution is very similar for TU2 and TU3. The axial strains, on the contrary, are larger for TU3 than for TU2, since the axial strains have the tendency to accumulate over the cyclic loading.

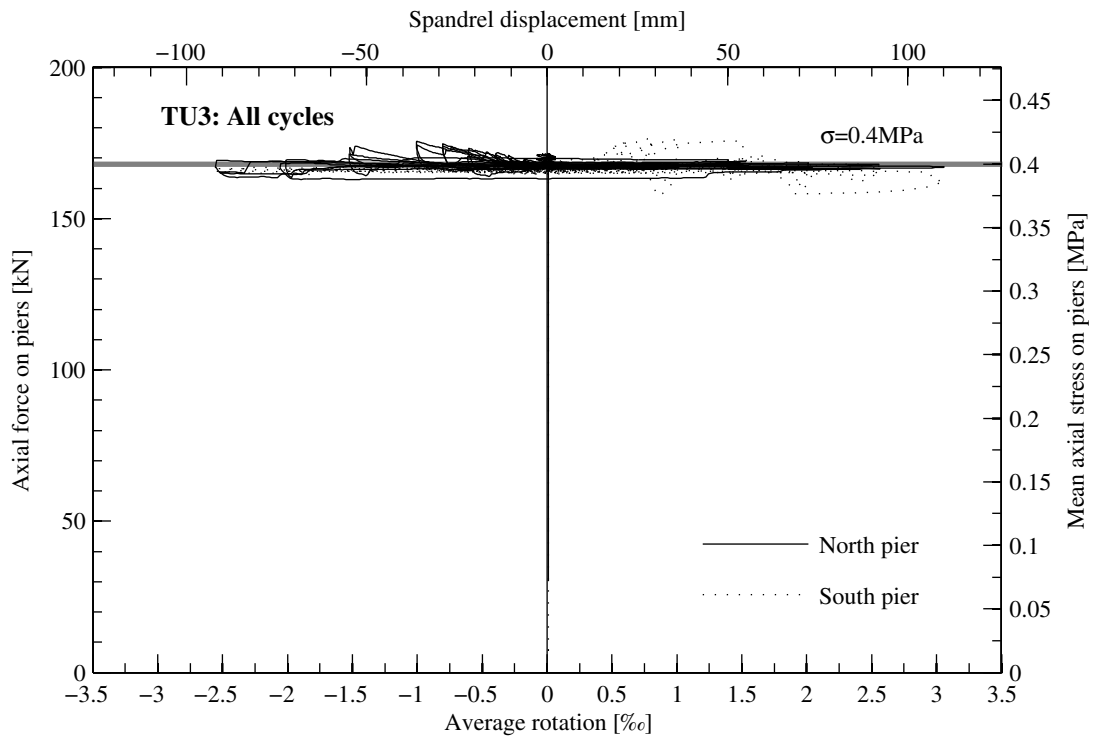


Figure 3.34: TU3: Axial force on piers - rotation relationship for all cycles.

3.4.3 Deformation plots

Figure 3.37 shows the deformed shape of TU3 at the first positive as well as the first negative peak of the cycles with amplitudes of $\theta_{nom} = \pm 0.1\%$, $\pm 0.2\%$, $\pm 0.4\%$ and $\pm 0.8\%$. With respect to the dimensions of the test unit, the deformations are amplified by factors ranging between 20 and 160 so that the magnitude of the plotted deformations is for all load steps approximately equal. Shown with thin lines is the undeformed state of the test unit at LS 0. As for TU2, the evolution of the shear deformations of the masonry spandrel with increasing rotation demand is clearly visible.

3. Test results for composite spandrels

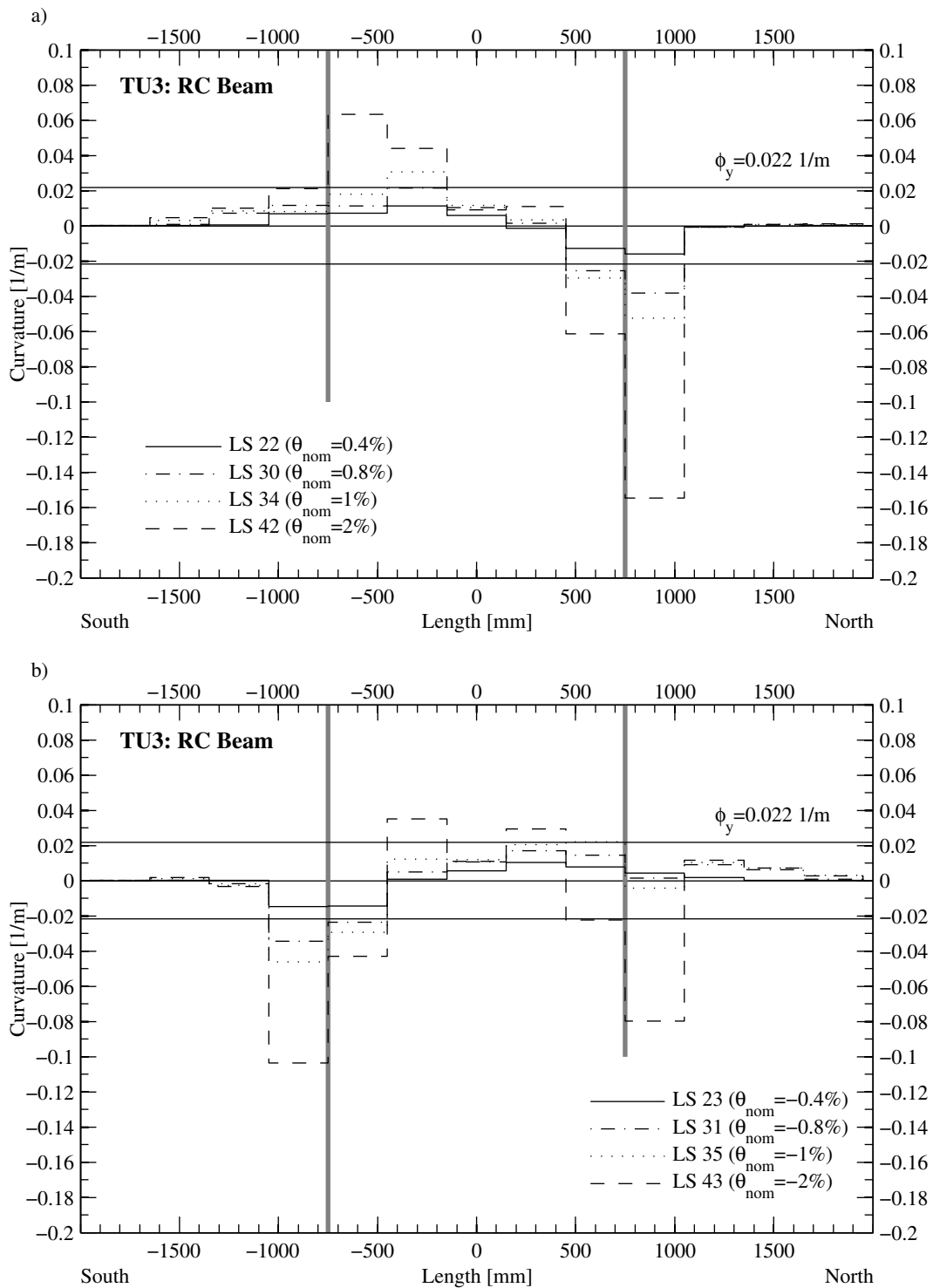


Figure 3.35: TU3: Curvature distribution along the RC beam. The thick grey lines symbolise the edges of the piers.

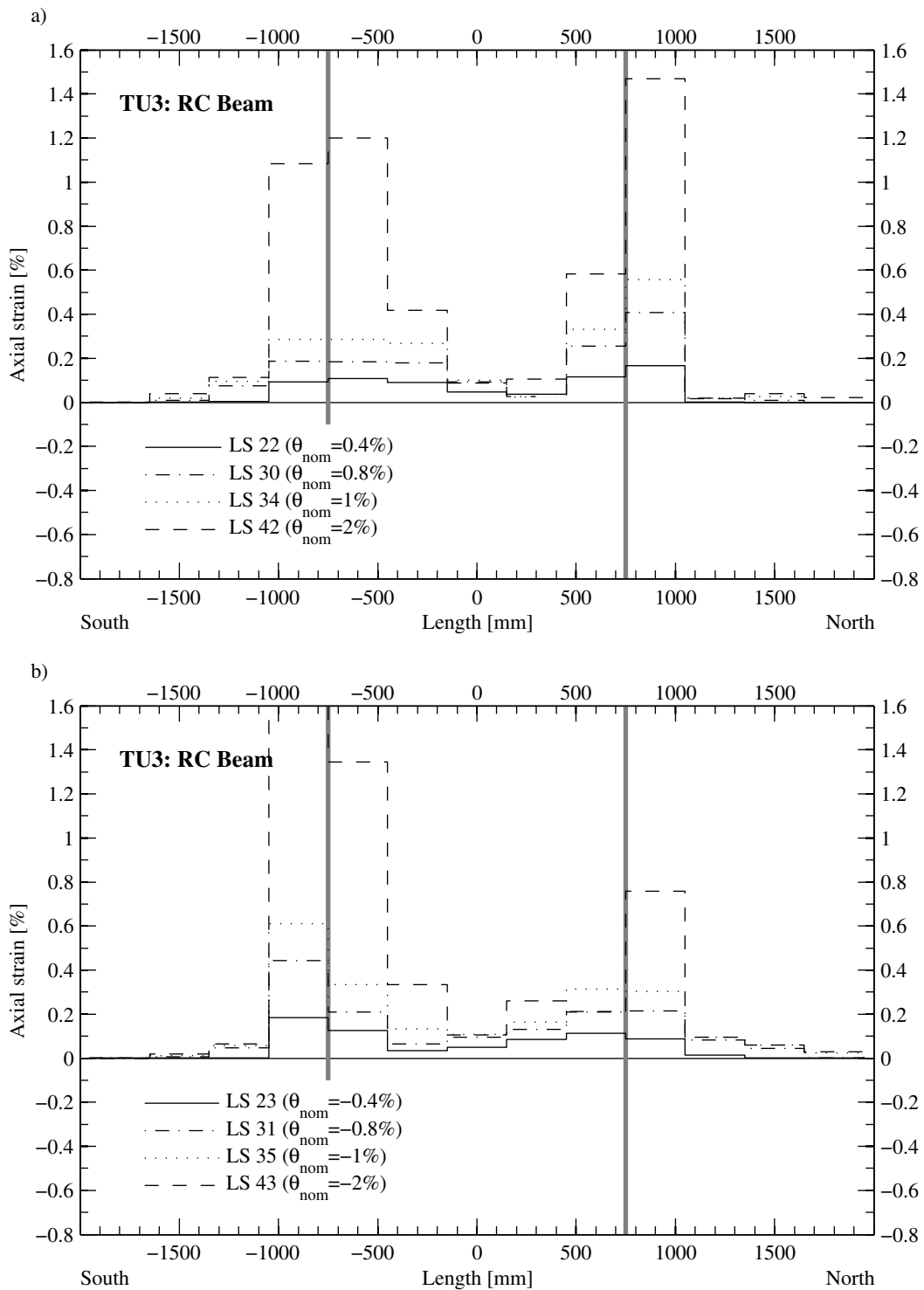
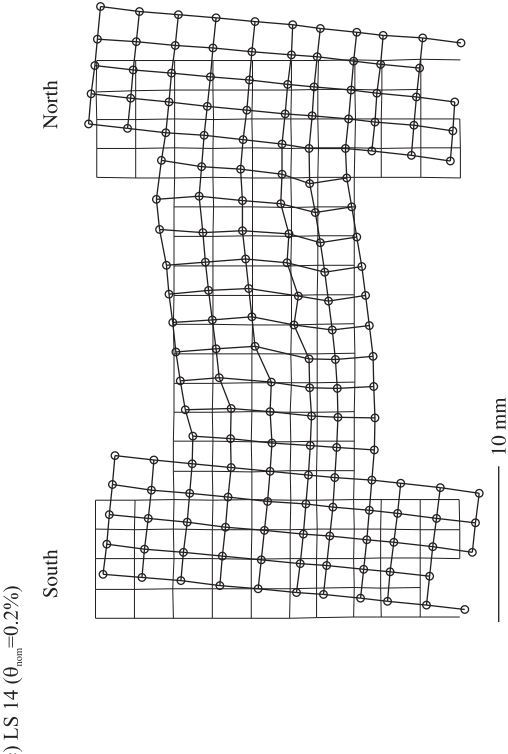
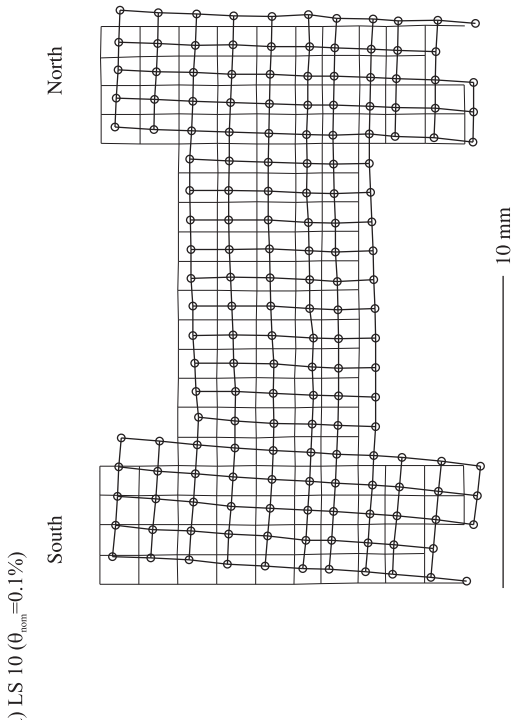
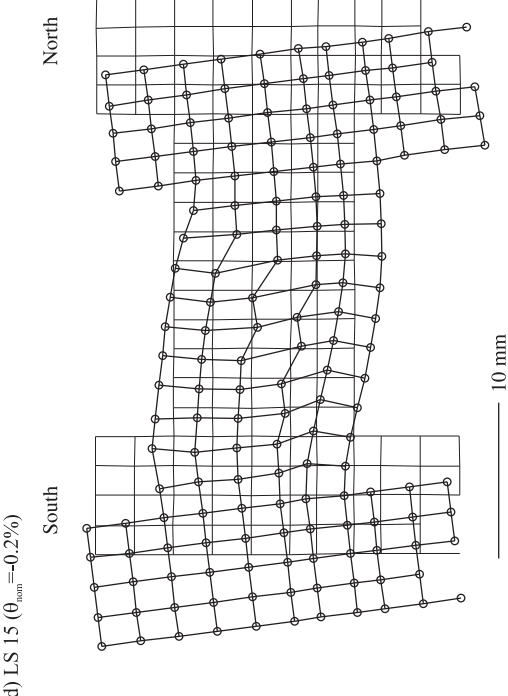
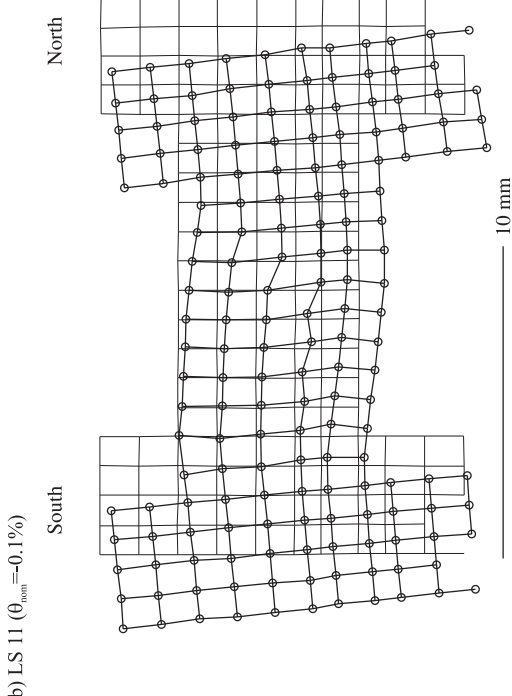


Figure 3.36: TU3: Axial strain distribution along the RC beam. The thick grey lines symbolise the edges of the piers.

3. Test results for composite spandrels



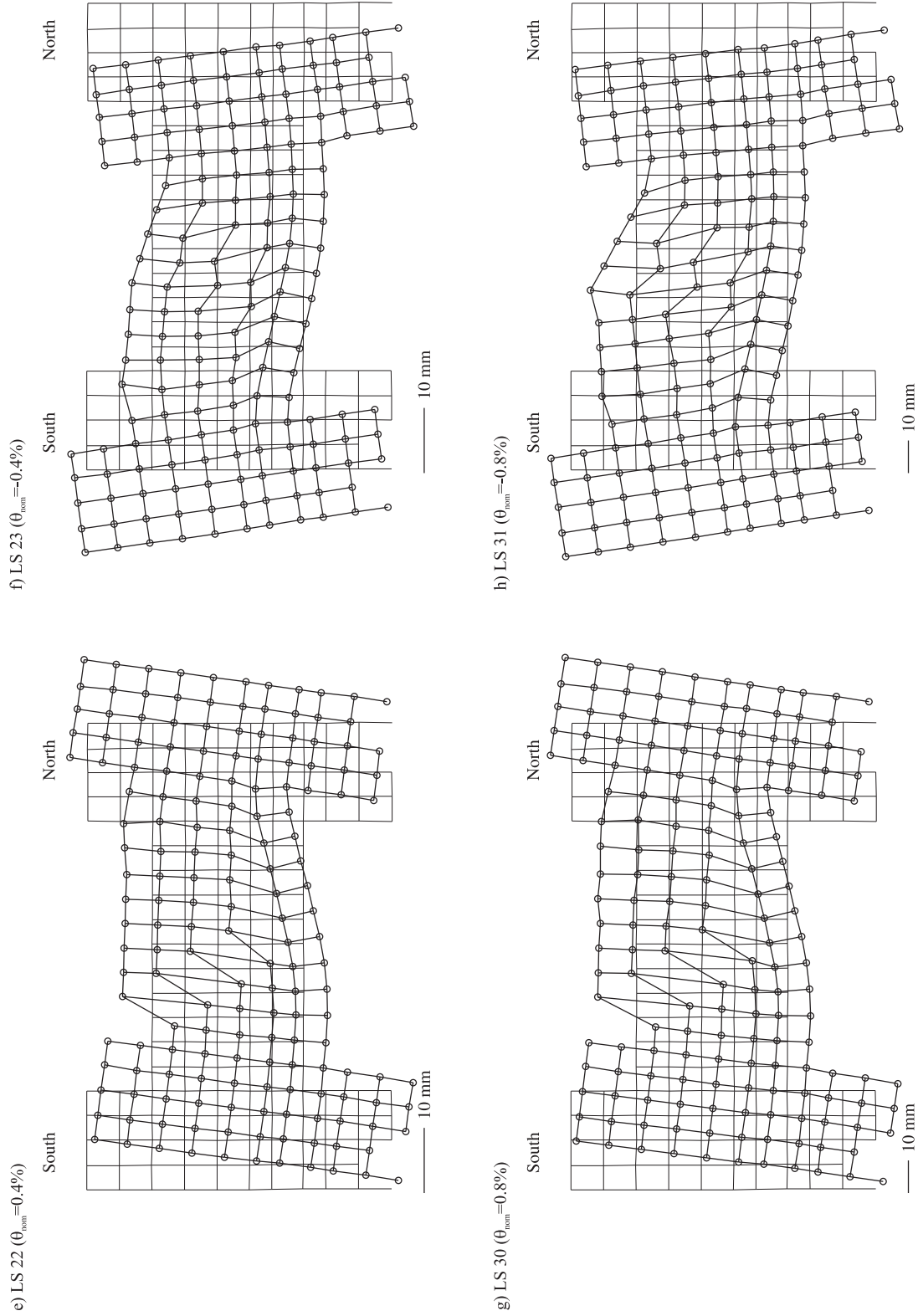


Figure 3.37: TU3: Deformed grid obtained from optical measurements at the first positive and the first negative peak of the cycles with $\theta_{nom} = \pm 0.1\%$, $\pm 0.2\%$, $\pm 0.4\%$ and $\pm 0.8\%$.

3.5 Composite spandrel TU4

3.5.1 Test observations

In comparison to the previous three test units, the RC beam of TU4 had a stronger longitudinal reinforcement, which consisted of 4 D16 mm bars instead of 4 D12 mm bars (see Table 1.1). When bolting the test unit onto the lever beams, fine cracks formed at the South end of the masonry spandrel; one crack extended into the RC beam. Normally, when bolting the test unit to the lever beams a diagonal scheme for tightening the bolts was applied and the bolts were tightened in two steps. Accidentally, for TU4, the bolts were tightened without taking such measures and it is believed that this caused the cracks in the spandrel. The cracks were marked at LS 0. However, at LS 2 further cracks were discovered, which had most likely formed when tightening the bolts. The maximum crack width in the masonry spandrel was 0.5 mm, the crack in the RC beam was a hair crack. A photo taken at LS 2 is shown in Fig. 3.38.

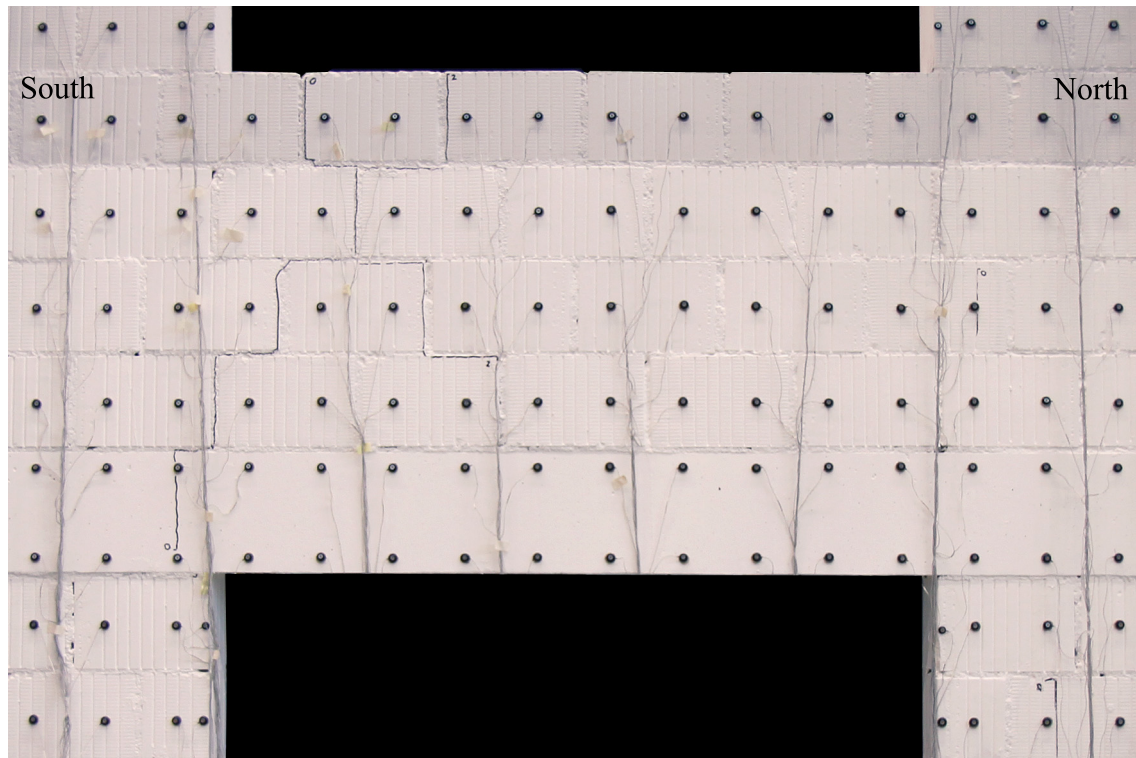


Figure 3.38: TU4: Crack pattern of spandrel at LS 2 resulting from bolting the test unit onto the lever beams.

At LS 0 the forces in the eight vertical rods were zero. As a first load step, each rod was prestressed to a force of approximately 40 kN. The four outer rods were prestressed by hand and then locked-in, the inner rods were prestressed by means of four hollow core jacks that were controlled by two load followers, i.e. the two hollow core jacks on one pier were connected to the same load follower. The vertical forces were applied on 12.06.2009. The test unit was tested on 15, 16 and 18.06.2009; an overview on the load steps covered during each testing day is given in Table 3.3.

Table 3.3: TU4: Testing days and corresponding load steps.

Testing day	Load steps carried out
12.06.2009	LS 1
15.06.2009	LS 2 - LS 27
16.06.2009	LS 28 - LS 35
18.06.2009	LS 36 - LS 47

The asymmetry in initial stresses in the spandrel resulting from the careless bolting manifested itself also in the further development of the crack pattern: During the cycles with amplitudes of $\theta_{nom} = 0.025\%$ cracking continued only for the negative direction of loading. At the first peak of the cycles with $\theta_{nom} = 0.05\%$ (LS 6), however, cracks within the masonry spandrel occurred also for the positive direction of loading. This is earlier than for the previously tested units TU1-3. A possible reason is the larger strength of the RC beam, which might have forced the masonry spandrel to deform more. Figure 3.39 shows the test unit at LS 9, i.e. the last peak of the cycles with $\theta_{nom} = 0.05\%$. At this load step TU3 was still completely uncracked. At LS 23 ($\theta_{nom} = -0.4\%$) almost all head and bed joints of the masonry spandrel were cracked (Figs. 3.40 and 3.41). This is similar to the cracking pattern of TU3 at this load step (Fig. 3.27). However, three main differences are noticeable: (i) In TU3 the first cracks within the top bricks of the compression diagonal had occurred at this load step. In TU4 the compression diagonal did not yet show any signs of crushing. (ii) The cracking pattern of the RC beam of TU3 at LS 23 was dominated by flexural cracks. For TU4, the RC beam showed clear signs of shear cracking within the negative plastic hinges. This is not surprising since the longitudinal reinforcement of the RC beam of TU4 was larger than that of TU3 while the shear reinforcement was identical. (iii) The horizontal crack between the RC beam and the top part of the pier extended in the case of TU4 over about 80% of the pier length (1.70 m), i.e. up to approximately the position of the outer vertical rods (see Fig. 3.40). In the case of TU3 this crack was much shorter and stopped about 30 cm into the pier. The different behaviour was due to the different RC beam strengths and stiffnesses: In the case of TU4 the RC beam was stronger and stiffer and had therefore the tendency to remain straight. When loading to LS 27 ($\theta_{nom} = -0.6\%$) thin stair-stepped cracks formed in the part of the North pier below the RC beam. LS 27 marked the end of the first testing day. After unloading the maximum crack width within the masonry spandrel was approximately 1.4 mm. In the RC beam all flexural crack closed completely. Only the flexure-shear cracks within both negative plastic hinges had maximum residual crack widths of 0.1 mm. This underlined the high demand in shear on the RC beam.

As the drift demand on the spandrel increased the gap between the bottom of the RC beam and the top of the bottom part of the pier became longer and wider. Figure 3.42 shows the cracking pattern at LS 31 ($\theta_{nom} = -0.8\%$). At LS 36 ($\theta_{nom} = 1.0\%$) the force in the outer rods increased significantly. Since the inner vertical rods were connected to the load follower, the crack between RC beam and pier opened up without increase in force in the inner vertical rods. The outer vertical rods were locked since it had been assumed that the crack widths at this location would be small. However, for large drift demands this was no longer applicable to TU4. For this reason, the loading was interrupted at zero drift when passing from LS 38 to LS 39 and hollow core jacks were also installed on the outer vertical bars. In this new setup, the four hollow core jacks of one pier were connected to the same load follower. At LS 42 ($\theta_{nom} = 2.0\%$) the actuator of AFP_S_EN did not have enough stroke left; this was corrected at zero drift when loading from LS 42 to LS 43 by

3. Test results for composite spandrels

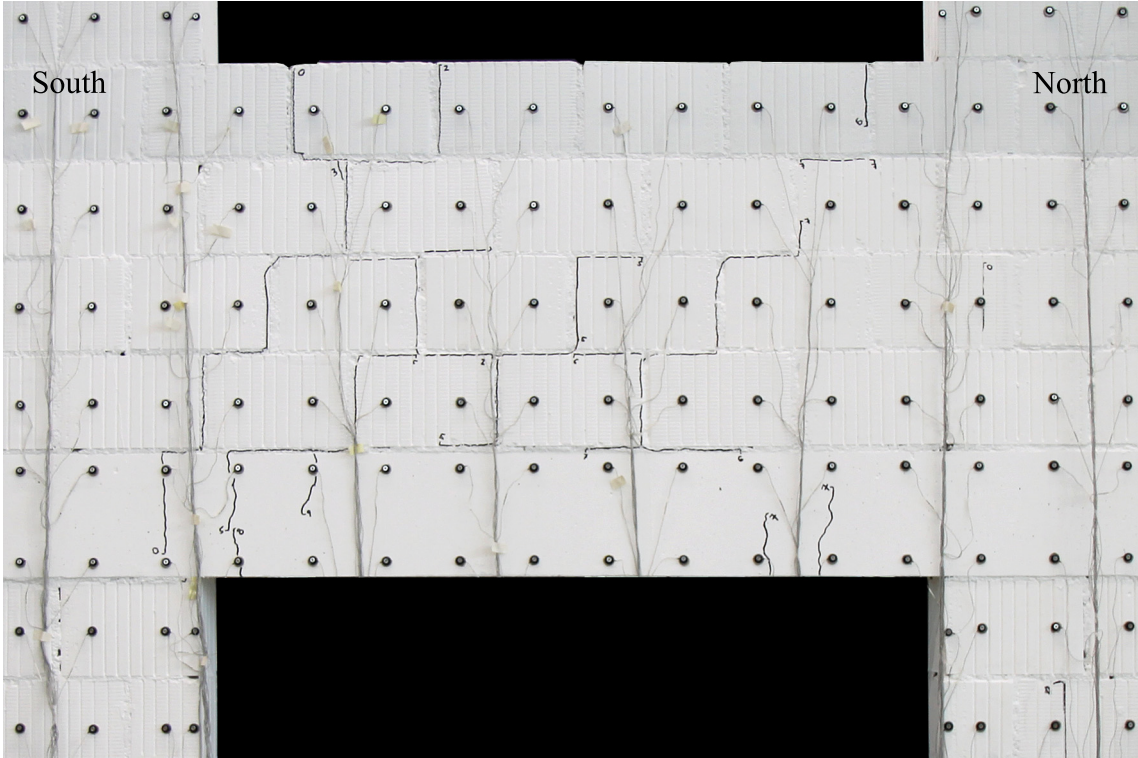


Figure 3.39: TU4: Crack pattern of spandrel at LS 9. Drift towards South with $\theta_{nom} = -0.05\%$.

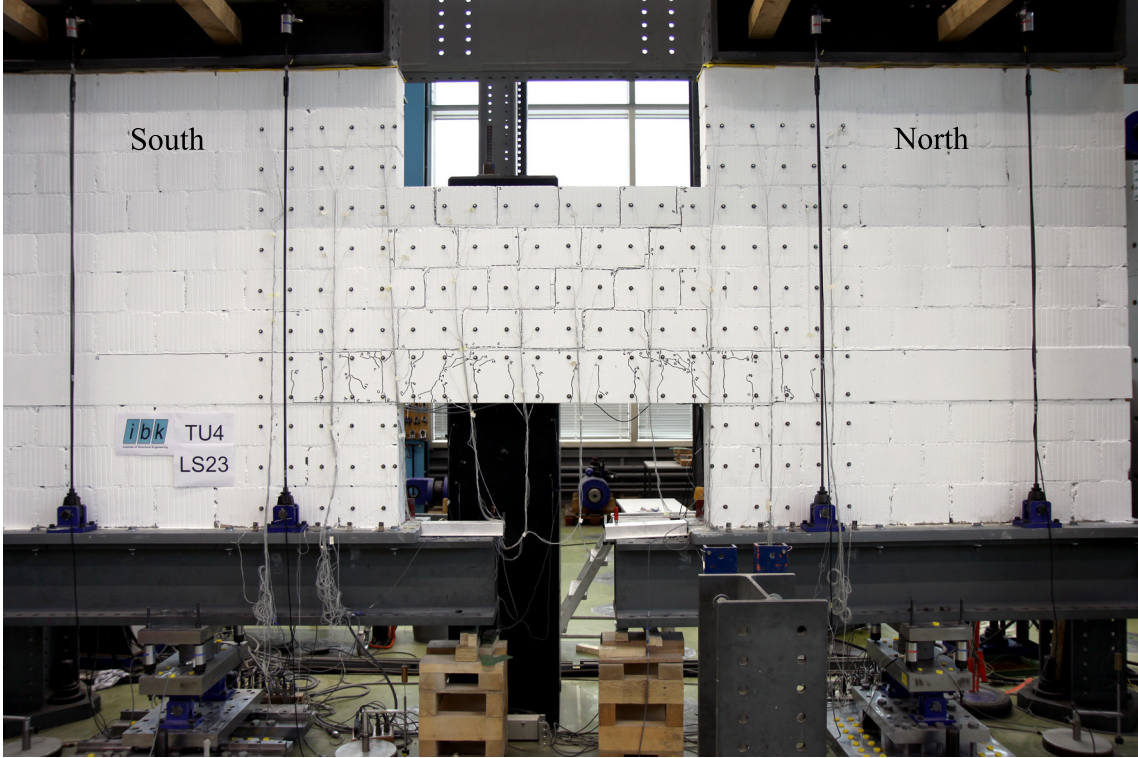


Figure 3.40: TU4: Crack pattern of entire test unit at LS 23. Drift towards South with $\theta_{nom} = -0.4\%$.

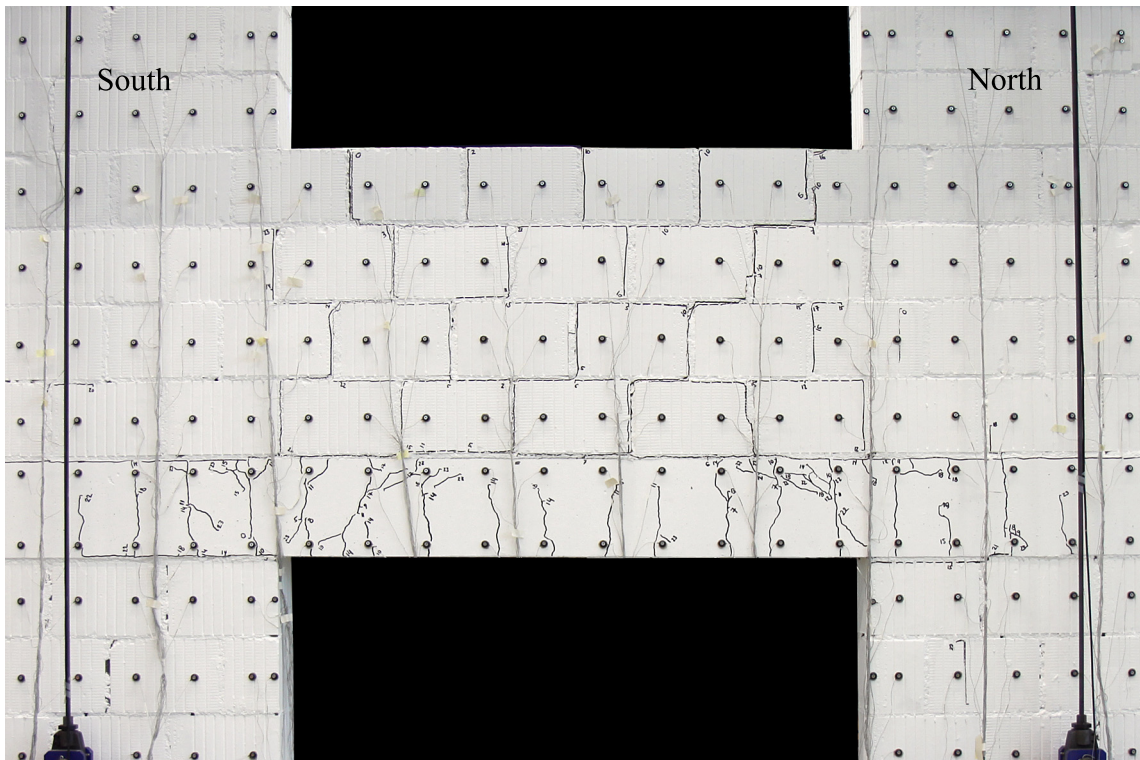


Figure 3.41: TU4: Crack pattern of spandrel at LS 23. Drift towards South with $\theta_{nom} = -0.4\%$.

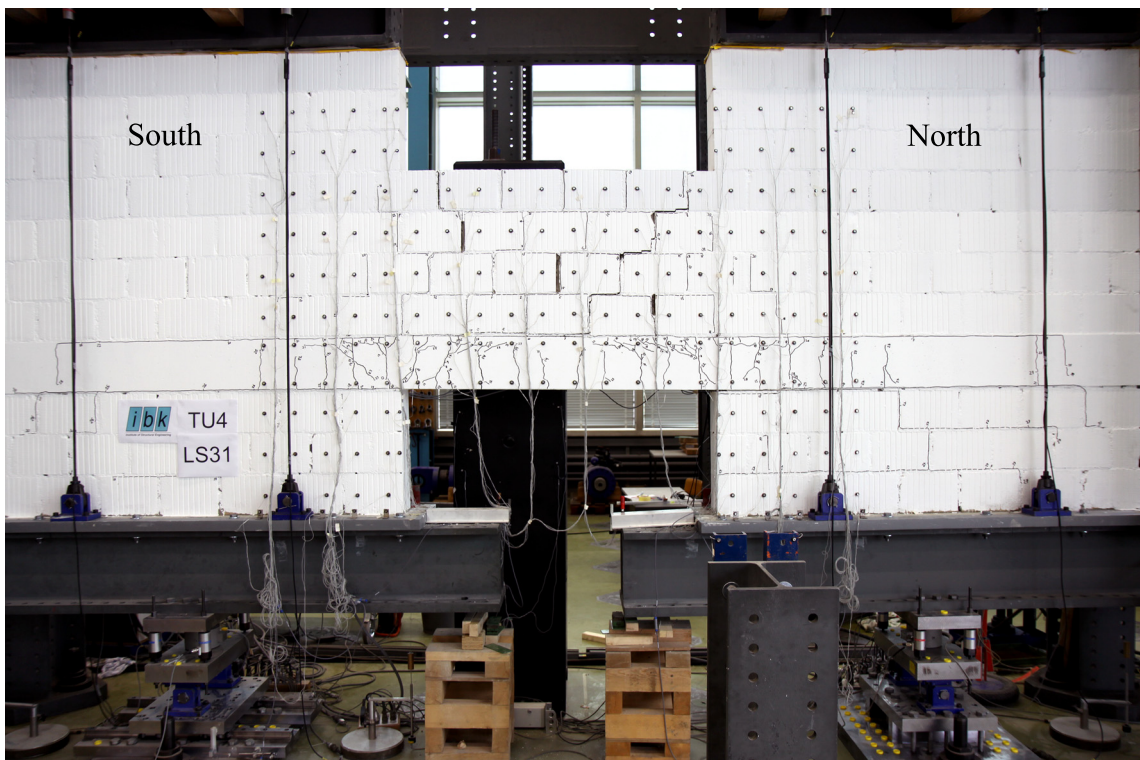


Figure 3.42: TU4: Crack pattern of spandrel at LS 31. Drift towards South with $\theta_{nom} = -0.8\%$.

3. Test results for composite spandrels

rearranging the offset of the piston. The same occurred for AFP_N_ES at LS 43 ($\theta_{nom} = -2.0\%$) and was rectified in the same manner.

The first cracks in the compression diagonal within the spandrel occurred at LS 40 ($\theta_{nom} = 1.5\%$). The largest part of the deformation demand on the spandrel was, however, absorbed by the rocking mechanism of the RC beam on the lower part of the pier. Since the top parts of the piers did not rock, the deformation demand on the spandrel was very little. Note that this might not be the case in a real building, where it is likely that the piers below and above the slab will rock. The rocking movement of the top pier would impose a strain demand on the compression diagonal of the masonry spandrel.

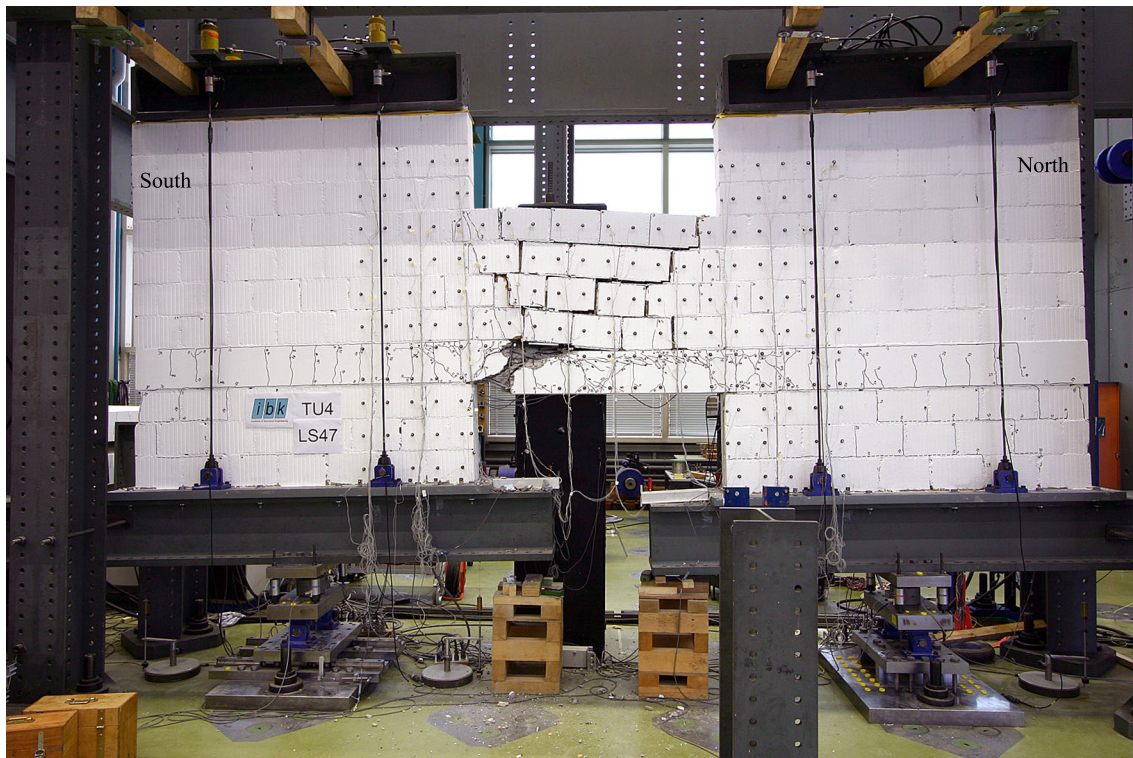


Figure 3.43: TU4: Test unit at LS 47. Drift towards South with $\theta_{nom} = -2.5\%$ (failure of TU4).

To determine the force-capacity of the spandrel, the axial load on the piers was doubled after LS 45. The last two cycles with amplitudes of $\theta_{nom} = \pm 2.0\%$ were then repeated (LS 44 and LS 45). To distinguish these from the original cycles their names were indexed with a "b". As a consequence of the increased axial load on the piers, the rocking movement of the RC beam reduced and the deformation demand on the masonry spandrel as well as the curvature demand on the RC beam increased. At already the second peak (LS 45b) the RC beam failed in shear due to fracture of the stirrup which was 24 cm away from the South end of the spandrel. Loading was nevertheless continued. The compression diagonal, which reached from the top South corner into the spandrel, crushed when loading to LS 46 ($\theta_{nom} = 2.5\%$). Many new cracks formed in the RC beam, both within the free span and within the South pier. At LS 46 the shear crack associated with the North negative plastic hinge had a maximum width of 8 mm. When loading to LS 47 "bangs" suggested that further stirrups had fractured; however, they could not be identified. When

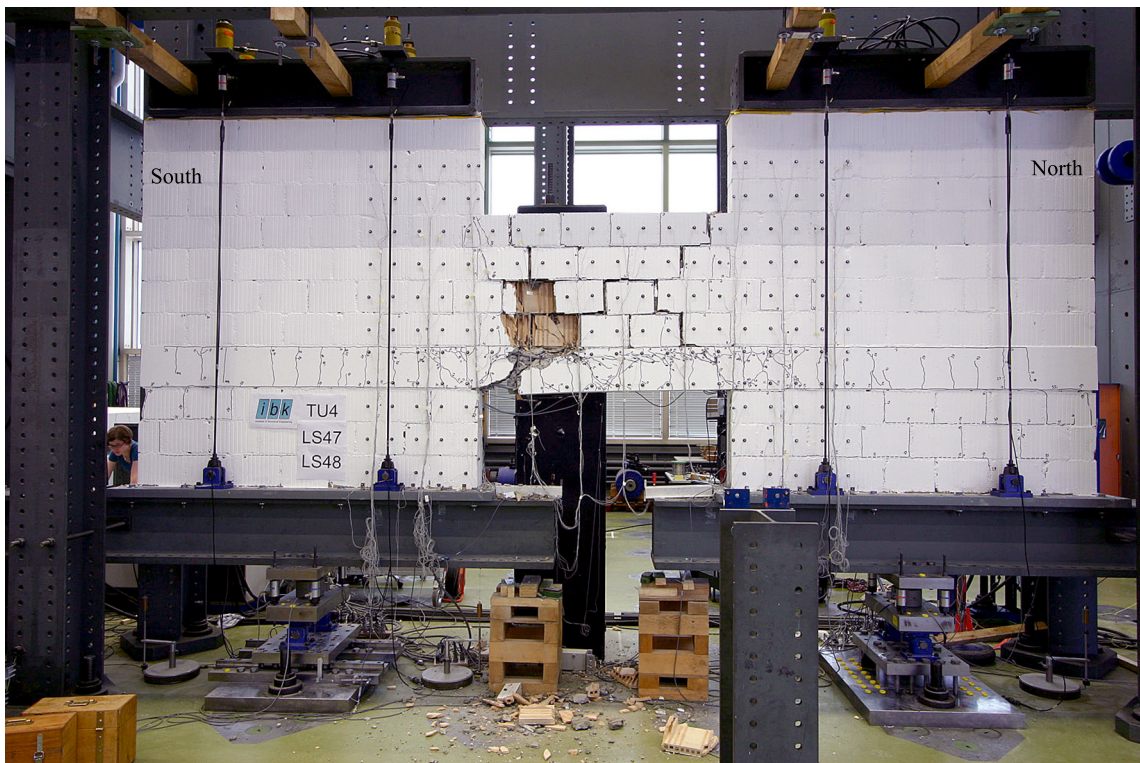


Figure 3.44: TU4: Test unit at the end of the test, i.e. after unloading from LS 47 ($\theta_{nom} = -2.5\%$).

the loading was reversed, the compression diagonal, which reached from the top South corner into the spandrel, collapsed. The test was then stopped. Figures 3.43 and 3.44 show the test unit at LS 47 and after unloading from LS 47 when the compression diagonal had collapsed.

3.5.2 Test results

The following figures show the standard graphs derived from the hard-wired measurements that have been defined in Section 3.1. The hysteretic behaviour of the test unit in terms of spandrel shear force vs. average rotation is presented first. Then, the variation of the axial load on the piers is shown and finally the deformations of the RC beam are discussed in terms of local curvatures and axial elongations.

Hysteretic behaviour of TU4

All cycles and the cycles with drift amplitudes up to $\theta_{nom} = \pm 0.8\%$ are shown in Figs. 3.45 and 3.46, respectively. The last two cycles before failure of TU4 were conducted with a higher axial force on the piers ($\sigma = 0.6$ MPa instead of $\sigma = 0.4$ MPa). The cycles that correspond to the two different axial load levels are plotted in Figs. 3.47 and 3.48, respectively.

The behaviour of the test unit with $\sigma = 0.4$ MPa was almost bilinearly elastic (Fig. 3.47: Up to a shear force of approximately 60 kN the behaviour of the test unit is linearly elastic. Then the shear force demand remains approximately constant. Although the initial branch of the loading curve is linearly elastic, its stiffness is decreasing with the number of cycles. The increasing softening

3. Test results for composite spandrels

of the test unit was due to the formation of cracks in both masonry spandrel and RC beam. The flattening of the curve for a maximum shear force of 60 kN was associated with the rocking mechanism of the RC beam on the lower parts of the piers. Up to the first peak of the cycles with amplitudes of $\theta_{nom} = \pm 1.5\%$, the force in the outer rods was not controlled by the load followers and increased as the RC beam forced the top and bottom parts of the piers apart. This is reflected in a positive stiffness of the second branch of the shear force-rotation curve. To eliminate this increase in axial force on the piers, the outer rods were connected to the load followers, too, after passing the first peak of the cycles with $\theta_{nom} = 1.5\%$. As a result the shear capacity of the test unit reduced slightly. At the peaks of the first cycle with $\theta_{nom} = \pm 2\%$ the shear force increased towards the end. This was most likely due to a slight increase in axial force in the piers. Despite the fact that by then the forces in all eight rods were controlled by the load followers, two of the hollow core jacks had initially not enough stroke left to accommodate the opening of the gaps. This was rectified during the cycles with $\theta_{nom} = 2\%$ (see Section 3.5.1).

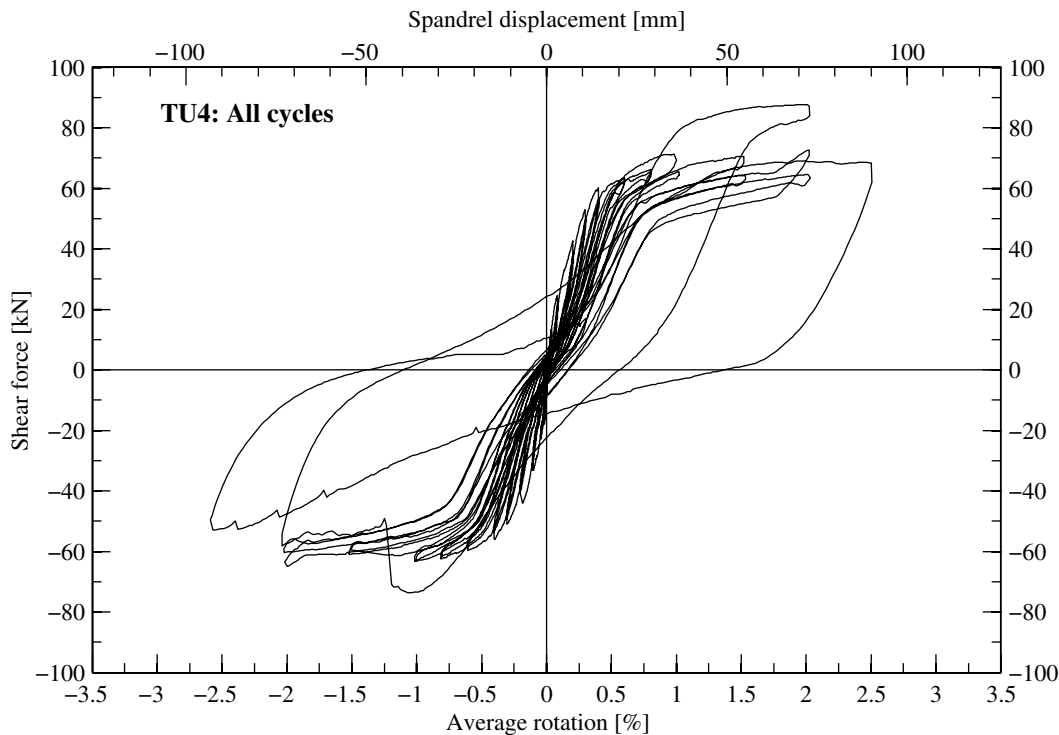


Figure 3.45: TU4: Force-rotation relationship for all cycles.

Due to the rocking mechanism of the RC beam on the lower parts of the piers, the damage in the test unit increased only slightly as the loading progressed and could have continued in an unchanged manner for larger drift demands. To gain information on how the spandrel would behave if the piers were subjected to larger axial load ratios, the axial load on the piers was increased by 50%. This increase did not subdue the rocking motion of the RC beam on the piers completely – Fig. 3.48 shows that the first half cycle of the loading history with $\sigma = 0.6$ MPa has a similar shape to the preceding cycles. However, the shear force for which the rocking motion started, had increased from about 60 kN to 90 kN. A fatter hysteresis curve indicated, however, that the RC beam and the masonry spandrel had been subjected to additional damage. When loading to the second peak, i.e. the first in the negative direction, the RC beam failed in shear at the South end

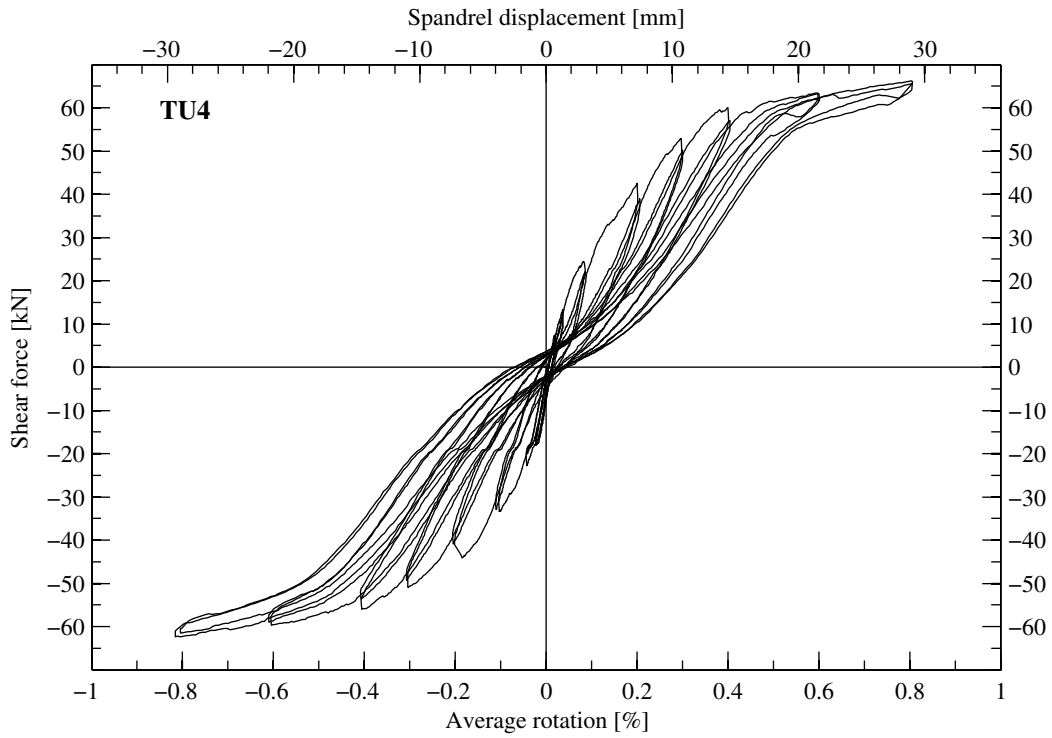


Figure 3.46: TU4: Force-rotation relationship for the cycles up to $\pm 0.8\%$ (LS 1-33).

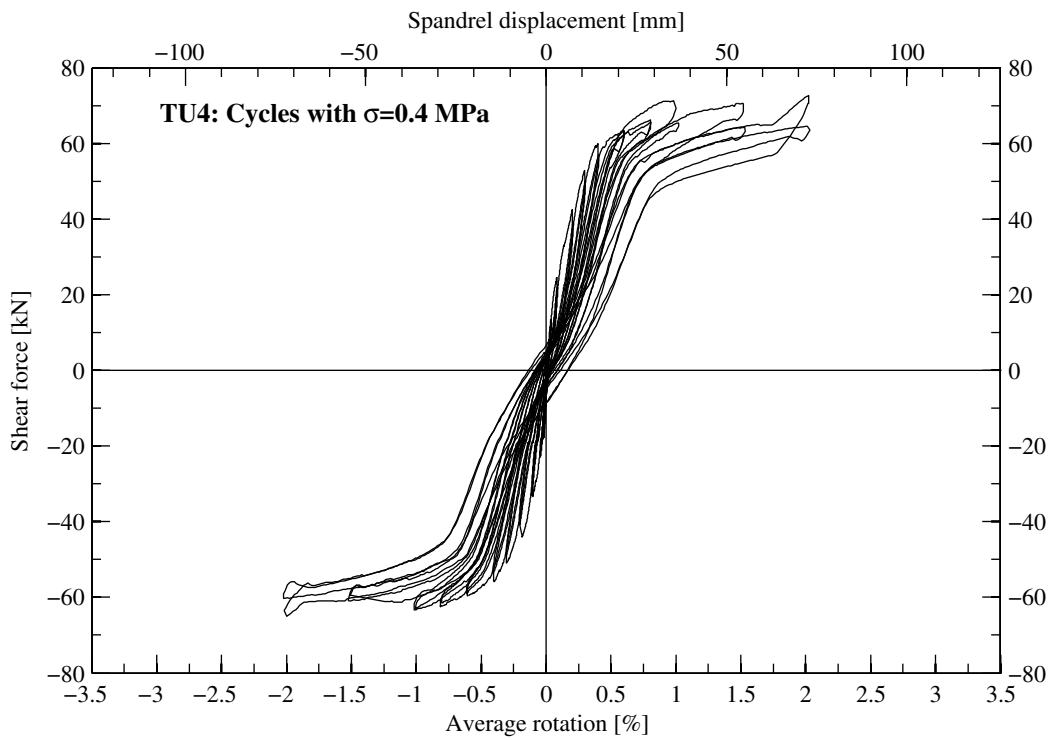


Figure 3.47: TU4: Force-rotation relationship for all cycles carried out with $\sigma = 0.4 \text{ MPa}$.

3. Test results for composite spandrels

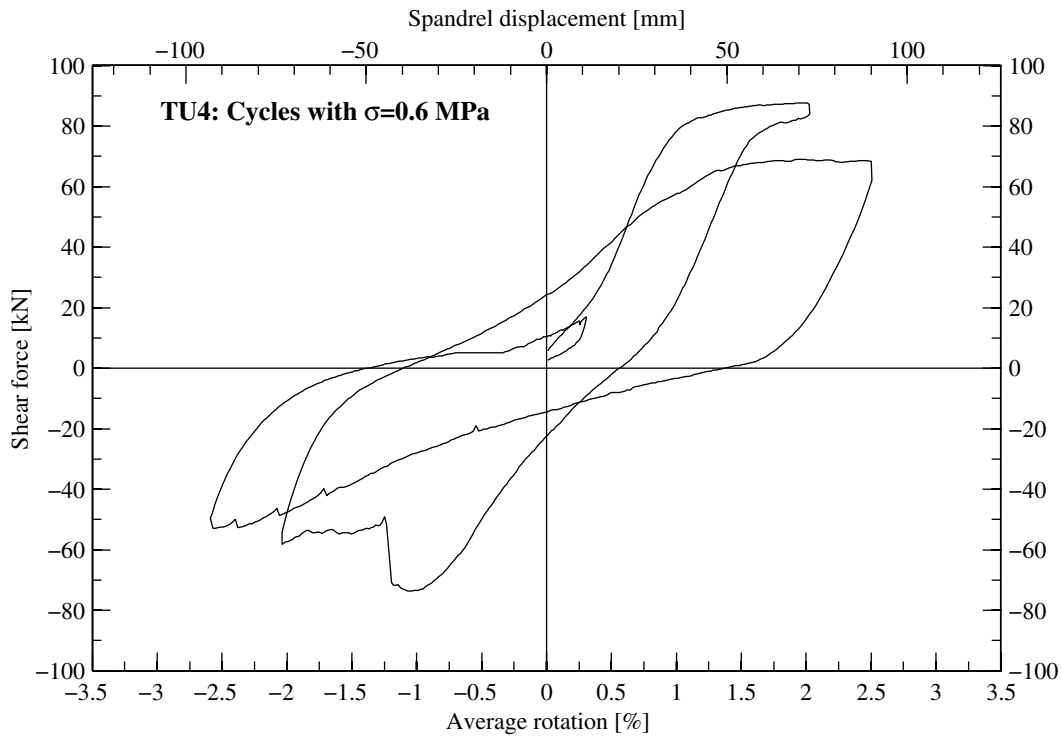


Figure 3.48: TU4: Force-rotation relationship for all cycles carried out with $\sigma = 0.6$ MPa.

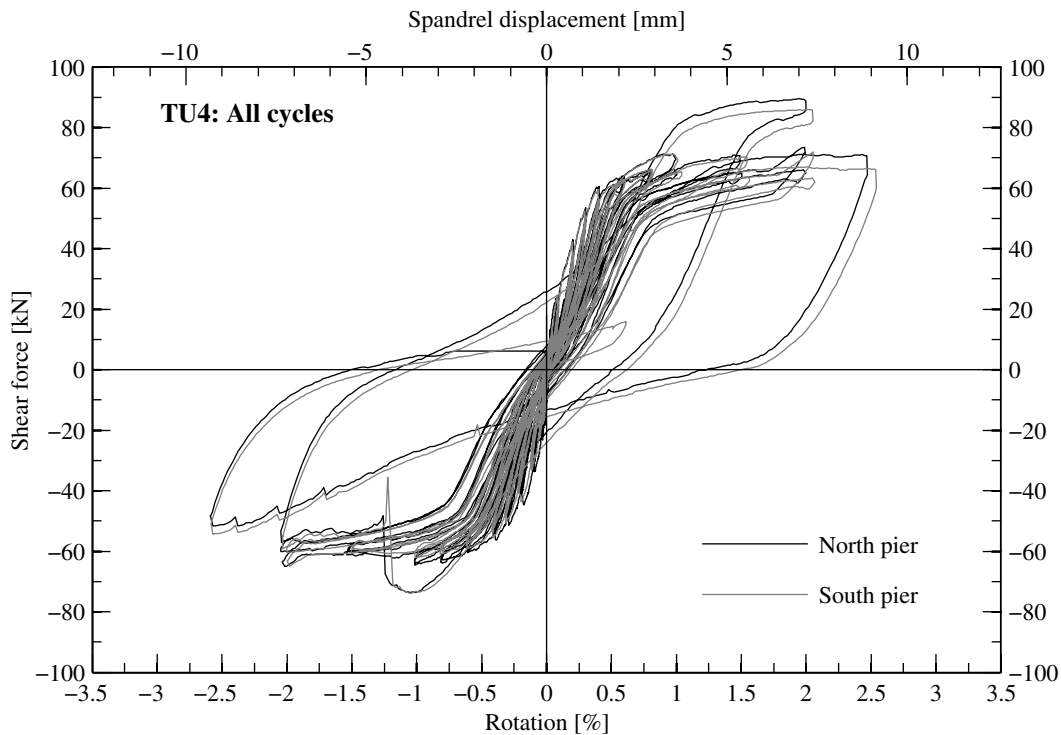


Figure 3.49: TU4: Force-rotation relationship for all cycles showing the non-averaged pier rotations and shear forces.

of the spandrel. This failure is reflected in the force-rotation curve with a distinct drop in shear capacity. Loading was continued and the final failure occurred in the cycle when the compression diagonal in the masonry spandrel crushed. This failure mode caused a continuous softening of the test unit.

Variation of the axial load on the piers of TU4

Figure 3.50 shows the axial force applied to the North and South piers. During the cycles with $\sigma = 0.4$ MPa, two groups can be distinguished: Up to the first peak of the cycles with drift amplitudes of $\theta_{nom} = \pm 1.5\%$ (LS 38), the outer axial rods were not connected to the load follower. Since the RC beam was rather strong and forced the joint between RC beam and pier to open also at the position of the outer rods, the force in the outer axial rods increased leading to an increase in total axial force on the piers. This increase was reflected in the force-rotation hysteresis of the test unit by a positive stiffness of the second branch of the curve, during which the RC beam was rocking on the lower parts of the piers. Once the axial forces in all rods were controlled by the load followers, the axial force remained rather constant. The small hysteresis of the axial force was due to some slip stick effects of the hollow core jacks. The same applies to the cycles with $\sigma = 0.6$ MPa, where the hollow core jacks had been installed from the beginning.

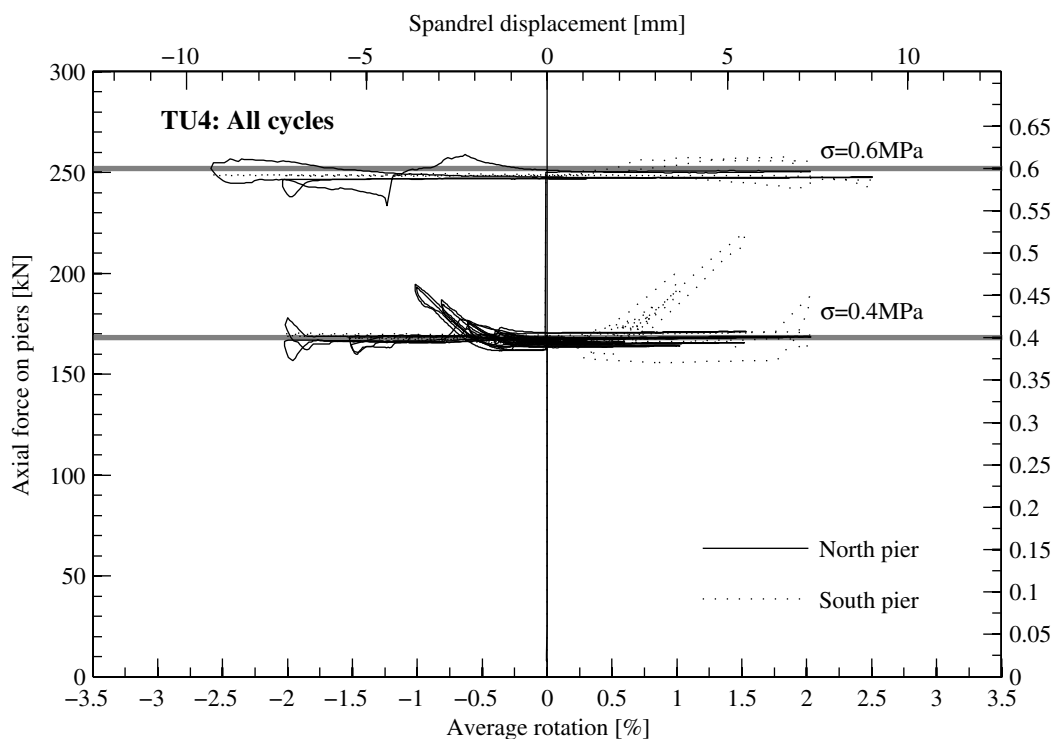


Figure 3.50: TU4: Axial force on piers - rotation relationship for all cycles.

Local deformation of the RC beam of TU4

Figures 3.51 and 3.52 show the curvature and axial strain distributions along the RC beam for various load steps. Note that for all the represented load steps the axial stress on the piers was 0.4 MPa. The results can, therefore, be directly compared to those of TU3, which was also tested with $\sigma = 0.4$ MPa. The curvature and axial strain demands on TU3 are shown in Figs. 3.35 and 3.36. Note, however, that the scale of these plots is not the same. For TU4, the curvature

3. Test results for composite spandrels

demand within the positive plastic hinge did not cause yielding of the longitudinal reinforcement bars. For TU3, on the contrary, a drift demand of 1.0% resulted in a curvature demand within the positive plastic hinge, which was larger than the yield curvature. For the negative plastic hinge the curvatures were for both test units larger than the positive curvatures. However, similar to the positive plastic hinge, the curvature demand on the RC beam of TU3 was significantly larger than the curvature demand on the RC beam of TU4. The axial strain distributions along the RC beams follow the same trends as the curvature distributions.

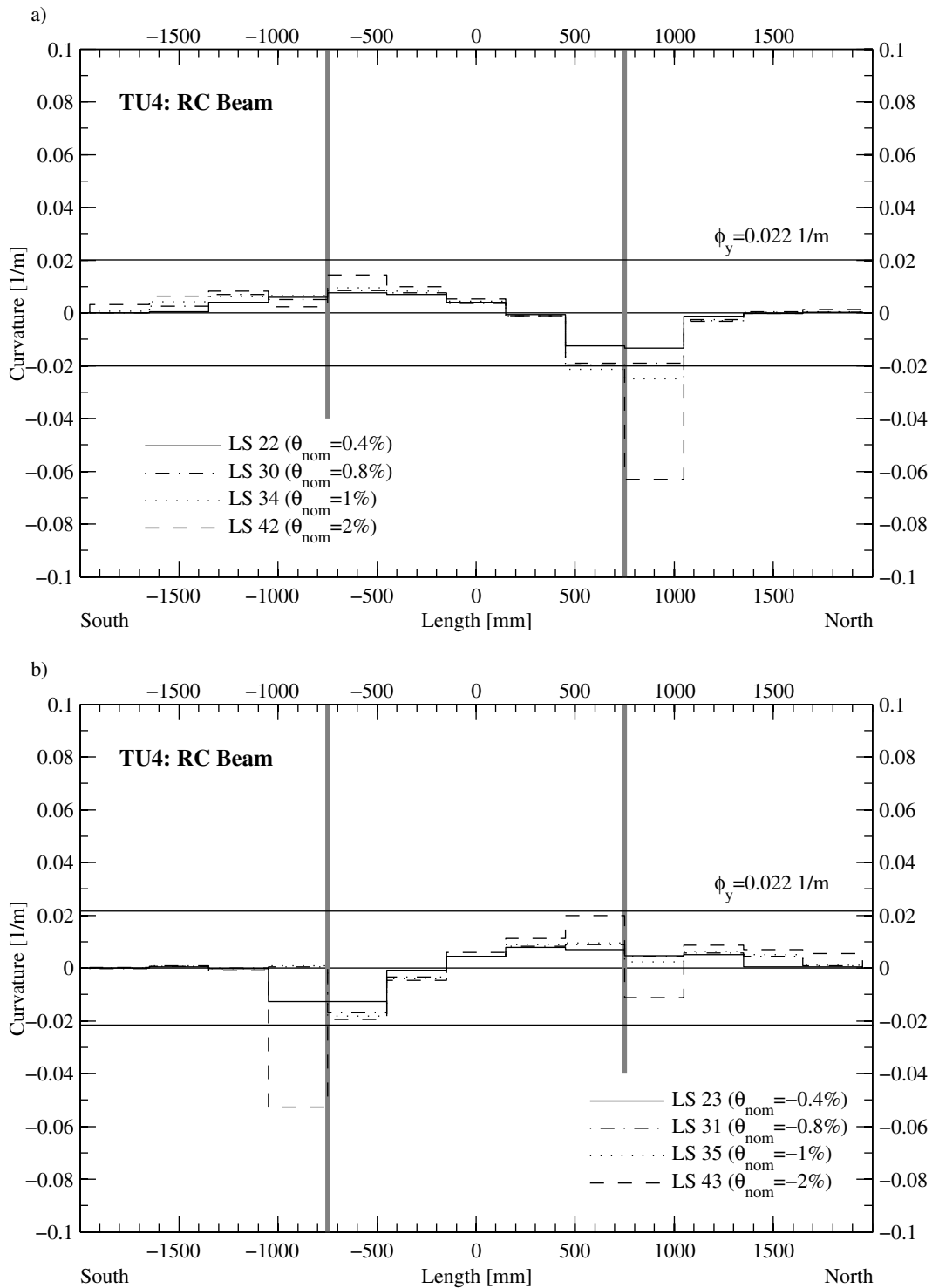


Figure 3.51: TU4: Curvature distribution along the RC beam. The thick grey lines symbolise the edges of the piers.

3. Test results for composite spandrels

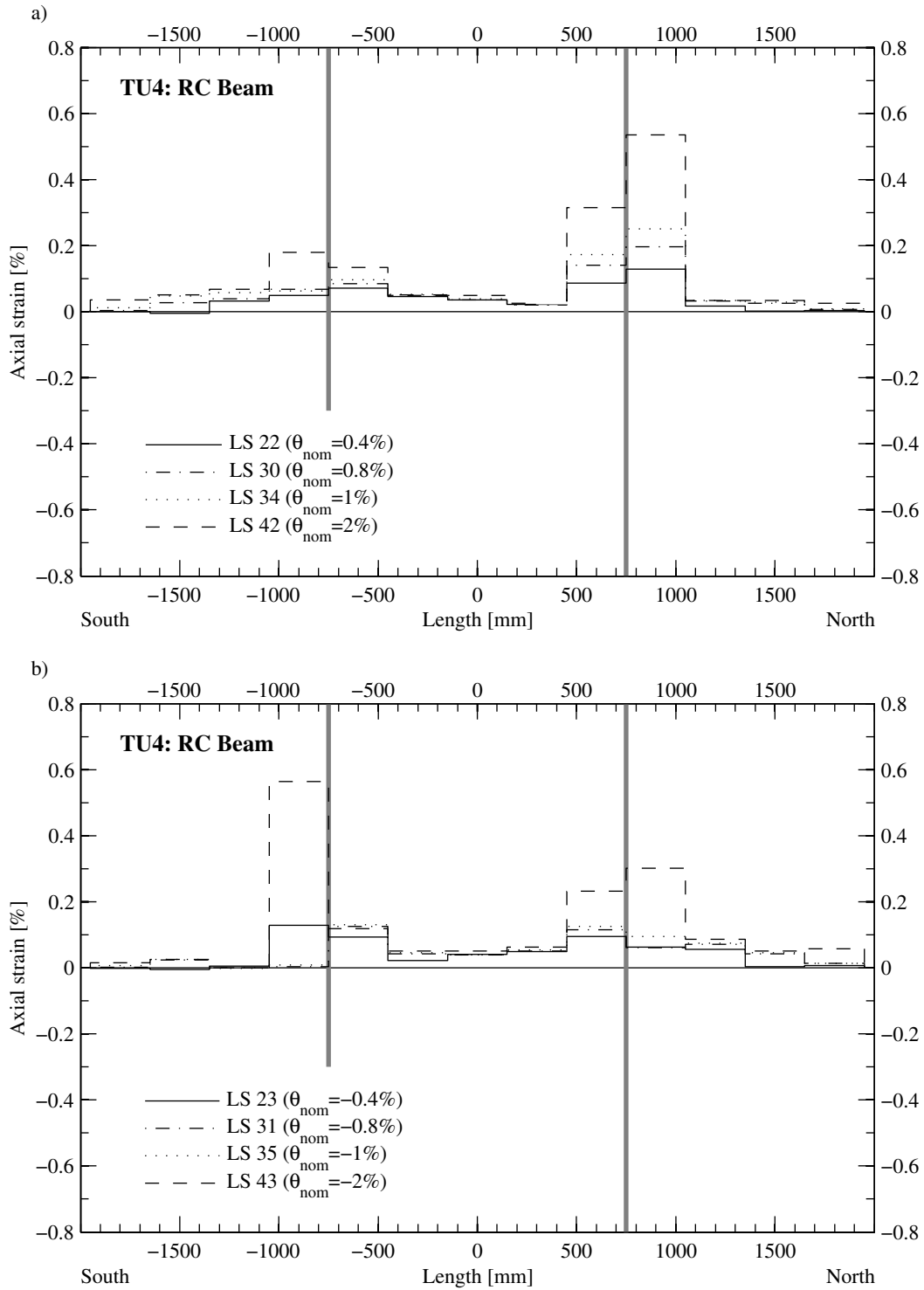
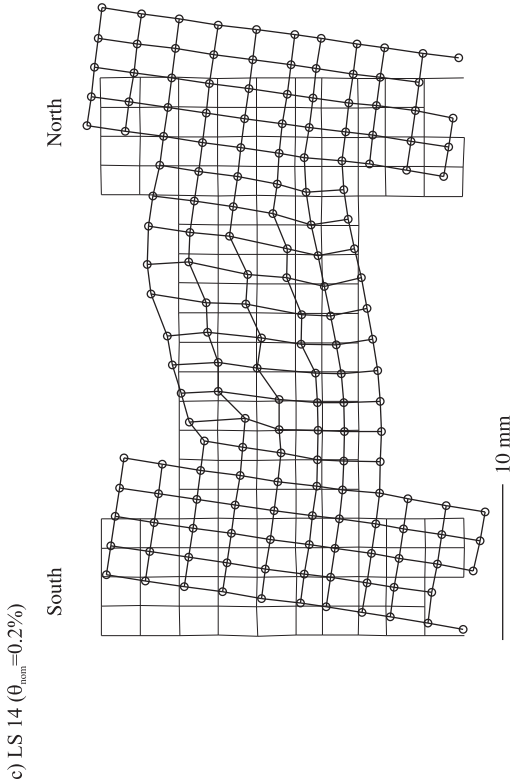
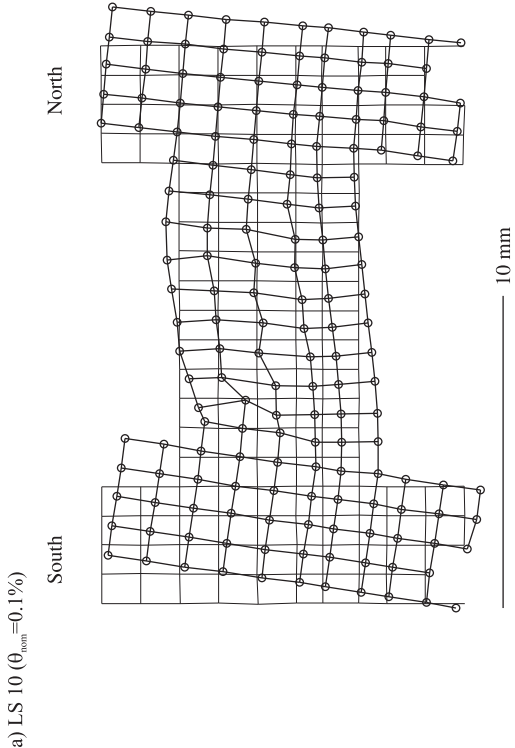
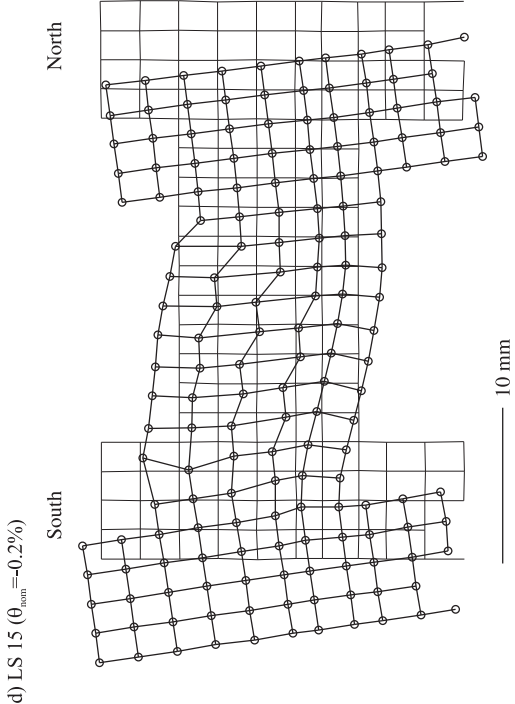
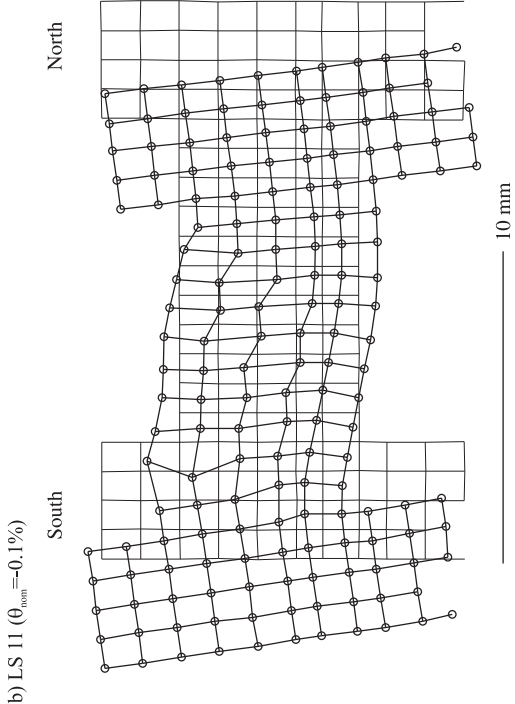


Figure 3.52: TU4: Axial strain distribution along the RC beam. The thick grey lines symbolise the edges of the piers.

3.5.3 Deformation plots

Figure 3.53 shows the deformed shape of TU4 at the first positive as well as the first negative peak of the cycles with amplitudes of $\theta_{nom} = \pm 0.1\%$, $\pm 0.2\%$, $\pm 0.4\%$ and $\pm 0.8\%$. With respect to the dimensions of the test unit, the deformations are amplified by factors ranging between 20 and 160 so that the magnitude of the plotted deformations is for all load steps approximately equal. Shown with thin lines is the undeformed state of the test unit at LS 0. When compared to TU3, the deformation sustained by the RC beam is smaller. This is particularly evident for the cycles with $\theta_{nom} = \pm 0.8\%$ for which the plots show clearly the opening of the gap between the RC beam and the lower part of the piers.

3. Test results for composite spandrels



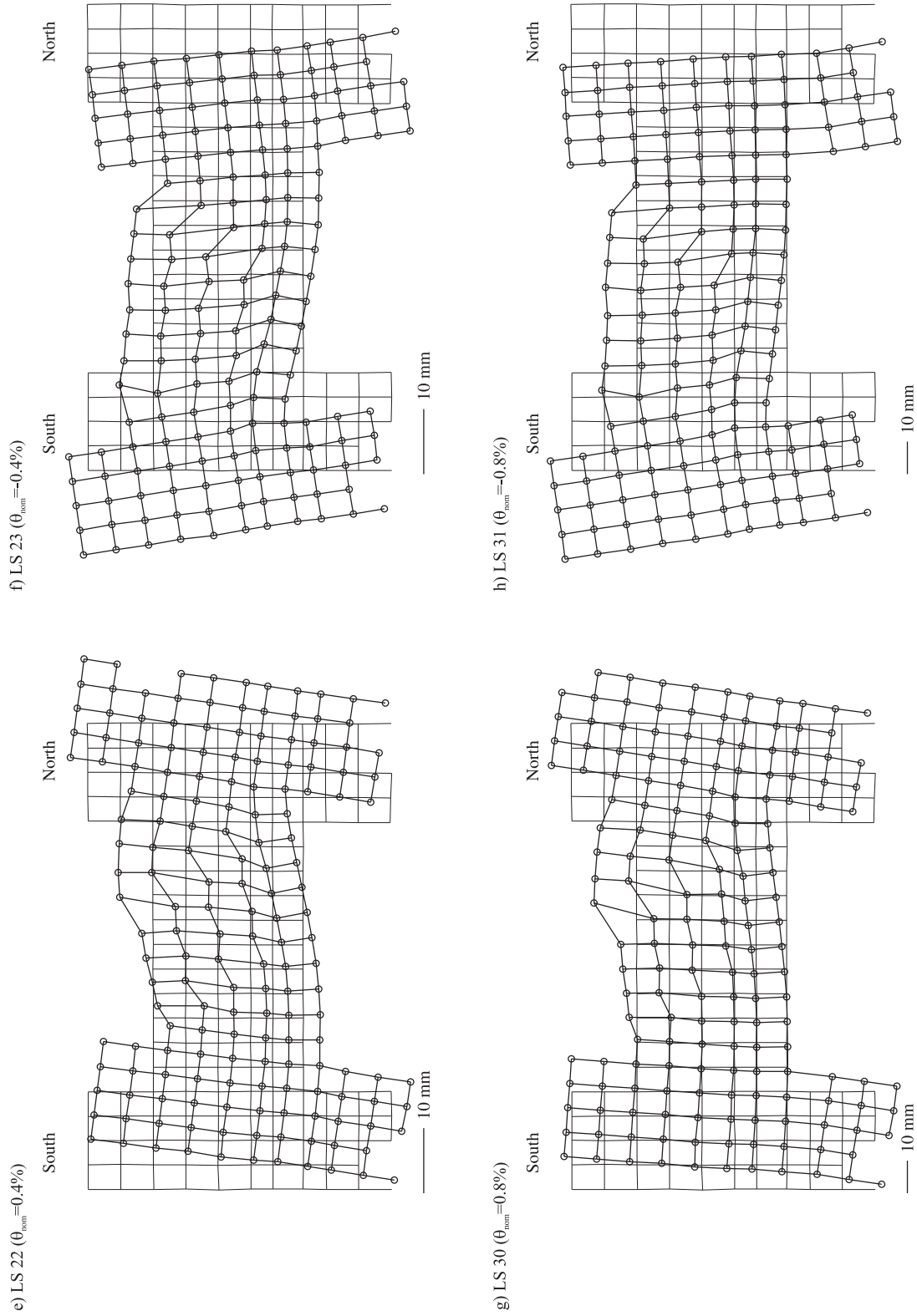


Figure 3.5.3: TU4: Deformed grid obtained from optical measurements at the first positive and the first negative peak of the cycles with $\theta_{nom} = \pm 0.1\%$, $\pm 0.2\%$, $\pm 0.4\%$ and $\pm 0.8\%$.

3.6 Composite spandrel TU5

3.6.1 Test observations

The RC beam of TU5 had a weaker longitudinal reinforcement than the first three test units and therefore also than TU4. The longitudinal reinforcement of TU5 consisted of 4 D10 mm bars instead of 4 D12 mm bars or 4 D16 mm bars for TU1-3 and TU4, respectively. At LS 0 the forces in the eight vertical rods were zero. As a first load step, each rod was prestressed to a force of approximately 40 kN. For TU5, all axial rods were pretensioned by means of hollow core jacks. The four hollow core jacks on one pier were connected to the same load follower. This was equivalent to the final setup of TU4, which had worked very well. Although large crack widths at the location of the outer rods were not expected for TU5, this setup was used since in this way the outer rods did not need to be prestressed by hand. The vertical forces were applied on 08.07.2009. The test unit was tested on 09 and 10.07.2009; an overview on the load steps covered during each testing day is given in Table 3.4.

Table 3.4: TU5: Testing days and corresponding load steps.

Testing day	Load steps carried out
08.07.2009	LS 1a
09.07.2009	LS 2 - LS 27
10.07.2009	LS 28 - LS 56

The behaviour of TU5 was on the whole similar to that of TU3. Since the longitudinal reinforcement ratio of the RC beam was smaller but the shear reinforcement ratio the same as for TU3, the shear demand on the RC beam was less for TU5 than for TU3. As a consequence only very few shear cracks developed in the RC beam. Due to the smaller flexural strength and stiffness of the RC beam, the extent of cracking of the RC beam into the piers was also reduced. As a further consequence, the test unit failed due to rupture of the longitudinal reinforcement bars of the RC beam (flexural failure) and not due to failure of the stirrups (shear failure).

At the end of the cycles with amplitudes of $\theta_{nom} = \pm 0.1\%$ (LS 13) the masonry spandrel was fully cracked. In the RC beam, however, in total only four cracks had formed: three for negative bending and a single crack for positive bending. In the following, more cracks in the beam formed. Up to LS 22 (first peak of the cycles with $\theta_{nom} = \pm 0.4\%$) all cracks in the RC beam were flexural cracks. At LS 23 a shear crack in the South plastic hinge formed under negative bending (Fig. 3.54). Since the RC beam was relatively weak, almost the entire deformation of the beam was concentrated within the free span of the beam.

At LS 26 a small chip sheared off the top North brick of the spandrel. This is similar to what has been observed for TU2 (see Fig. 3.16) and was the first crack passing through a brick. The deformation of the masonry spandrel concentrated in large stair-stepped cracks, which crossed the entire spandrel as shown in Fig. 3.55 depicting the spandrel at LS 31 ($\theta_{nom} = -0.8\%$). The bricks themselves remained until failure of the test unit in very good shape.

In the RC beam the North and South hinges for negative bending behaved differently. In the latter, the shear crack close to the South end opened up significantly. This crack did not cross a

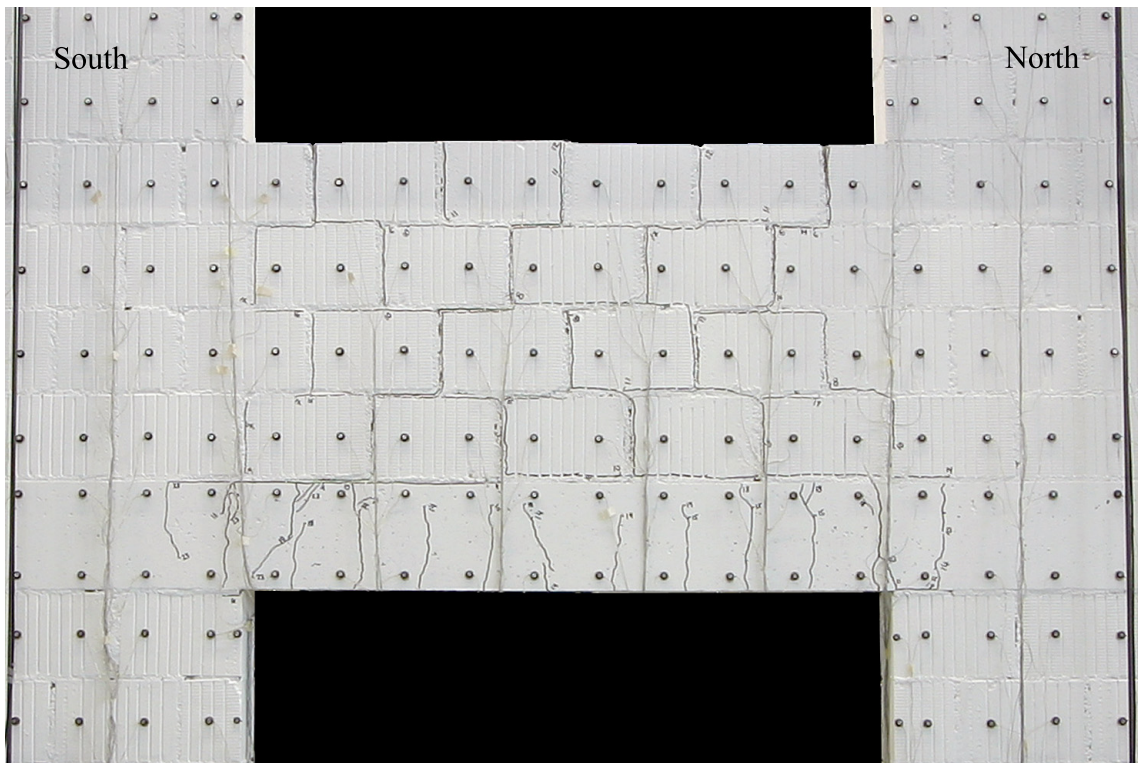


Figure 3.54: TU5: Crack pattern of spandrel at LS 23. Drift towards South with $\theta_{nom} = -0.4\%$.

stirrup and therefore all the shear force had to be transmitted via aggregate interlock and dowel action, which became increasingly critical as the deformation demand increased. Shear failure, however, did not occur, but the force-displacement hysteresis obtained a pinched shape: The resistance of the spandrel only increased, once the shear crack was closed and shear stresses could again be transmitted. In the North hinge, no shear crack had formed. At this location, all the deformation concentrated within one flexural crack, which became very wide. At LS 42 ($\theta_{nom} = 2\%$) the concrete cover spalled off the top longitudinal reinforcement bars at this location, which most likely reduced the maximum strain demand on these bars. Failure was eventually caused by the rupture of the two bottom bars of the South hinge. It occurred when loading to LS 56 ($\theta_{nom} = 4\%$). The bottom bars of the North hinge buckled as it is shown in Figs. 3.56 and 3.57.

3.6.2 Test results

The following figures show the standard graphs derived from the hard-wired measurements that have been defined in Section 3.1. The hysteretic behaviour of the test unit in terms of spandrel shear force vs. average rotation is presented first. Then, the variation of the axial load on the piers is shown and finally the deformations of the RC beam are discussed in terms of local curvatures and axial elongations.

Hysteretic behaviour of TU5

Figures 3.58 to 3.60 show the shear force - rotation hysteresis of TU5. Compared to the previously tested units, it is noticeable that the shape of the hysteresis loops, in particular of the second

3. Test results for composite spandrels

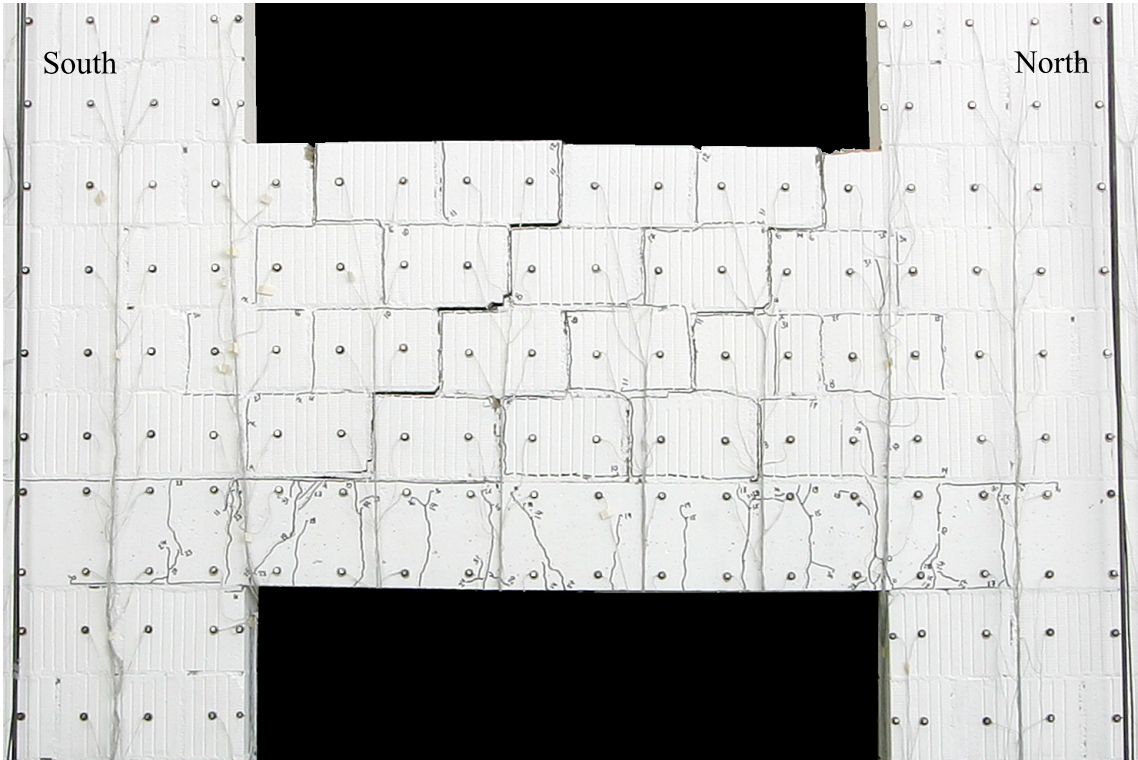


Figure 3.55: TU5: Crack pattern of spandrel at LS 31. Drift towards South with $\theta_{nom} = -0.8\%$.



Figure 3.56: TU5: Test unit at LS 56. Drift towards North with $\theta_{nom} = 4\%$ (failure of TU5).

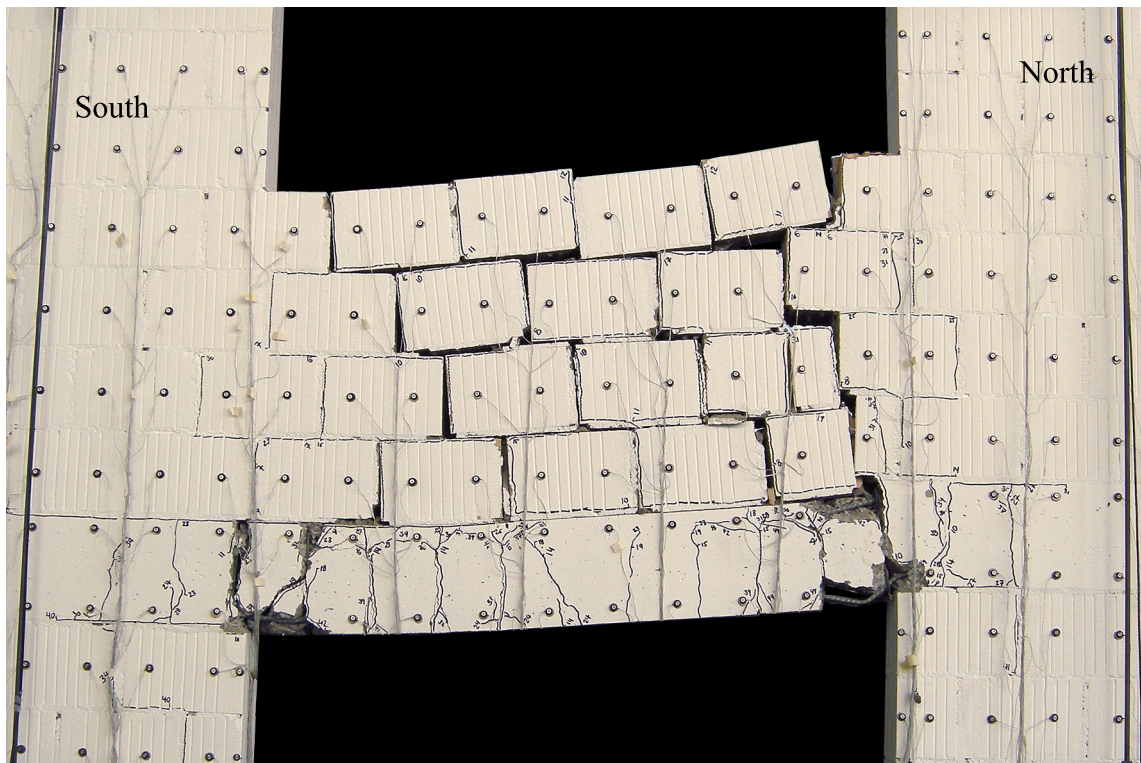


Figure 3.57: TU5: Crack pattern of spandrel at LS 56. Drift towards North with $\theta_{nom} = 4\%$ (failure of TU5).

cycles at the same drift level, are rather "pinched". Such a shape is typically associated with large shear deformations. The RC beam showed shear cracking after LS 23 (second peak of cycles with amplitudes of $\theta_{nom} = \pm 0.4\%$). Shear deformations of the RC beam became increasingly dominant, since the shear stress had to be transmitted through the cracks. Due to the cyclic loading the beam grew in length causing the aggregate interlock to deteriorate. This is most likely the main mechanism which contributed to the pinched hysteresis of the test unit. Another reason could be the larger contribution of the masonry spandrel to the total resistance of the composite spandrel.

Variation of the axial load on the piers of TU5

Since the RC beam was relatively weak, it did not force the top and bottom part of the piers apart. As a result, the hollow core jacks had only to accommodate minor movements and therefore the slip stick effects, which had been observed for earlier tests, did not play a major role. Hence, the axial load remained almost perfectly constant over the entire duration of the test as shown in Fig. 3.61.

Local deformation of the RC beam of TU5

Figures 3.62 and 3.63 show the curvature and the axial strain demand on the RC beam. The picture, on the whole, is similar to that of TU3. However, the curvature demand and axial strain demand on the RC beam is larger, since the RC beam is weaker and therefore the gap between RC beam and pier opened up less. Additionally, the lower longitudinal reinforcement content led to a reduced spread of plasticity along the length of the beam when compared to TU3. As a result,

3. Test results for composite spandrels

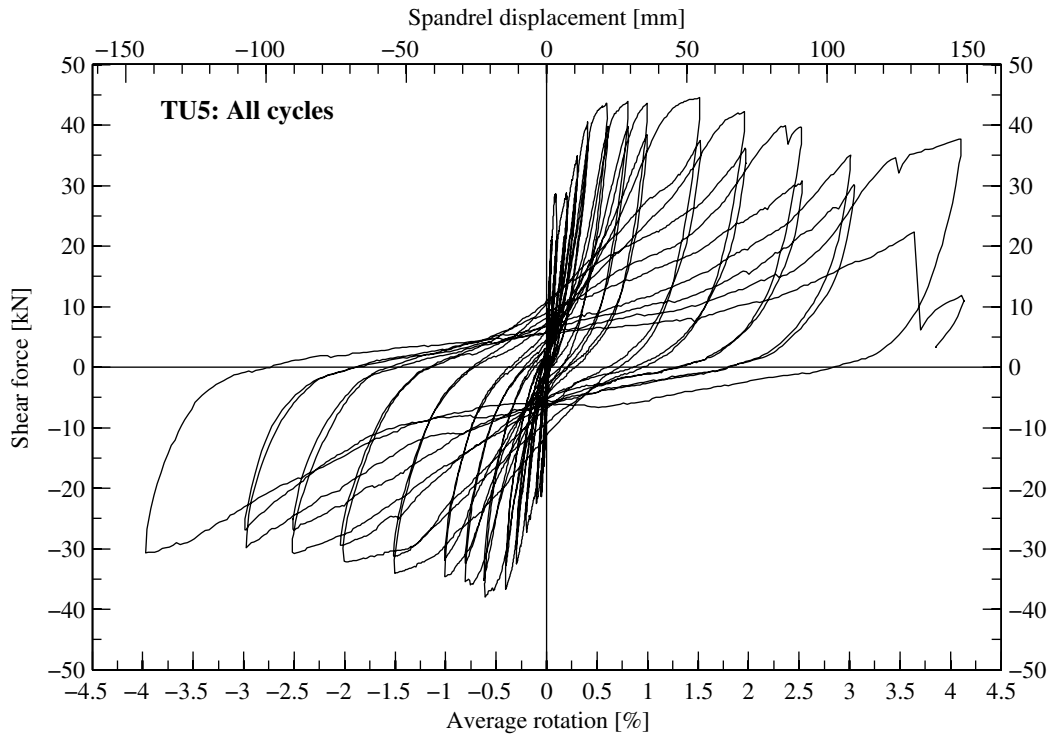


Figure 3.58: TU5: Force-rotation relationship for all cycles.

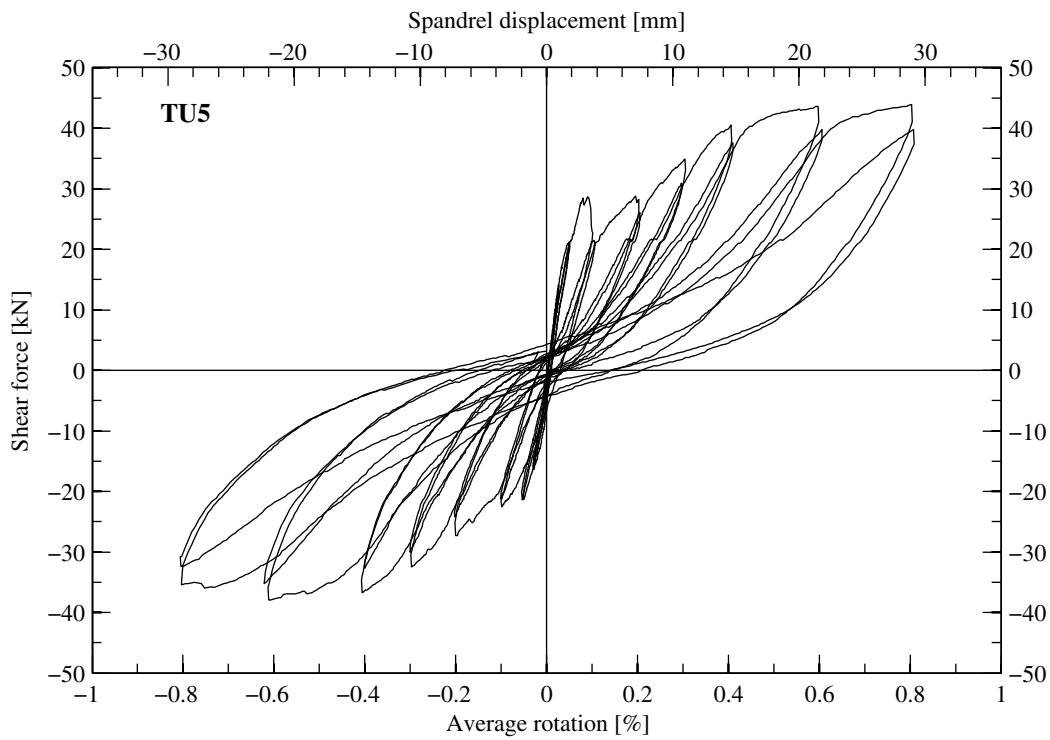


Figure 3.59: TU5: Force-rotation relationship for the cycles up to $\pm 0.8\%$ (LS 1-33).

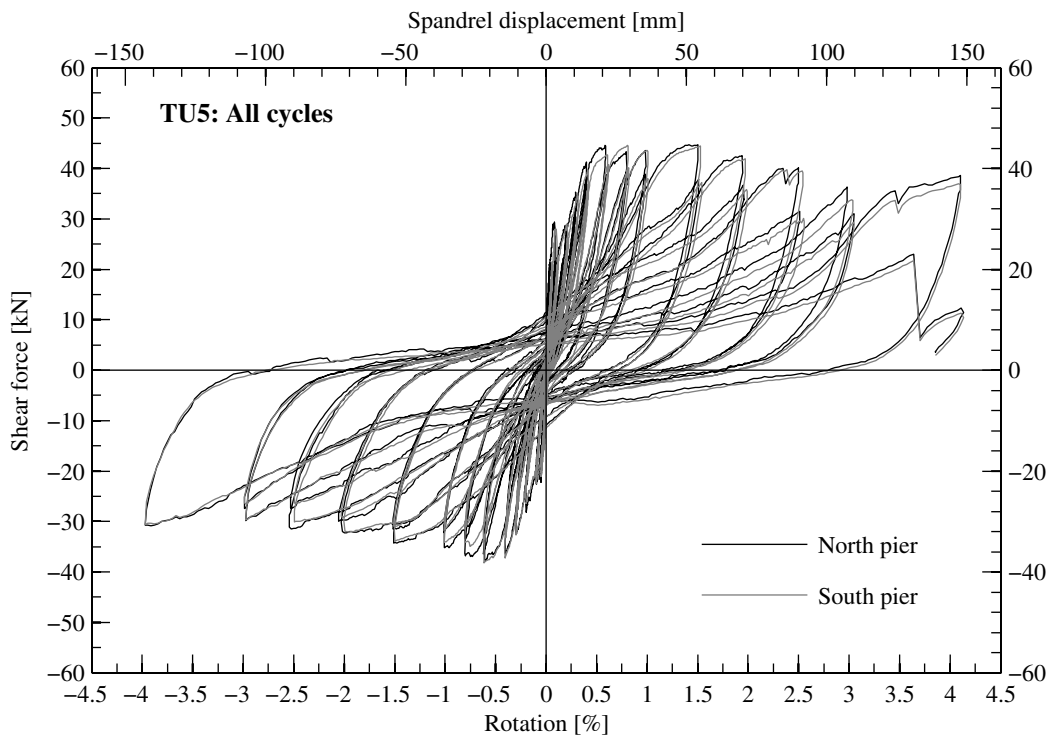


Figure 3.60: TU5: Force-rotation relationship for all cycles showing the non-averaged pier rotations and shear forces.

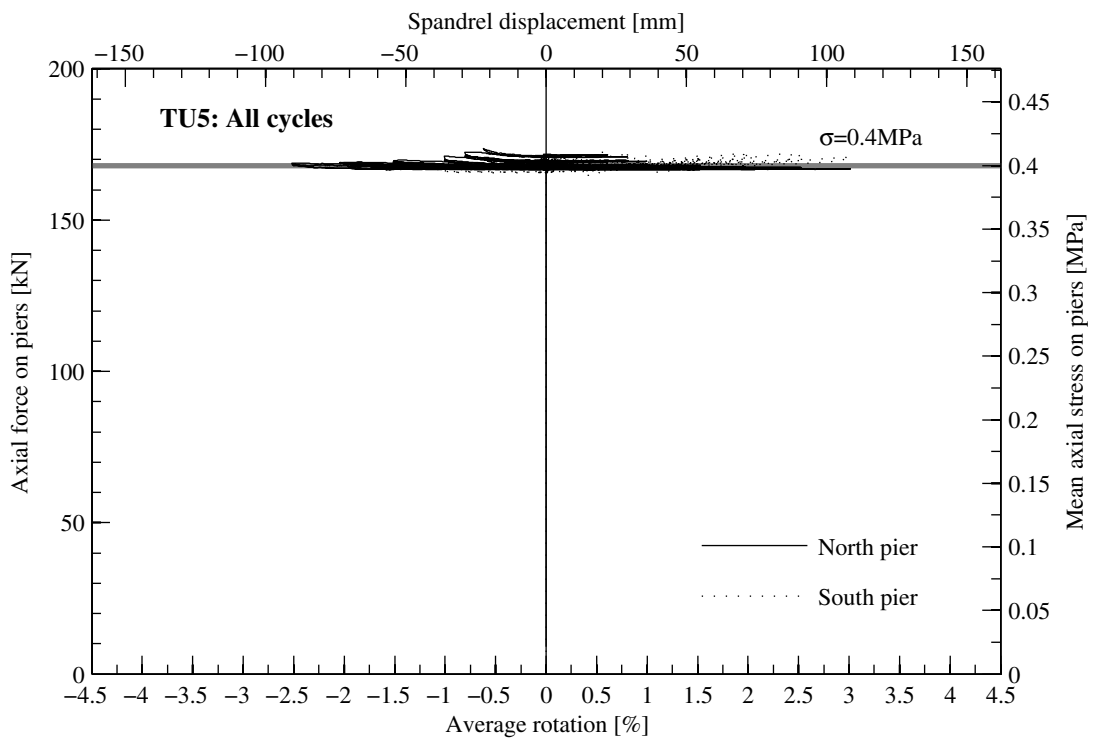


Figure 3.61: TU5: Axial force on piers - rotation relationship for all cycles.

3. Test results for composite spandrels

the RC beam of TU5 had to accommodate larger local deformations for the same nominal rotation θ_{nom} than TU3.

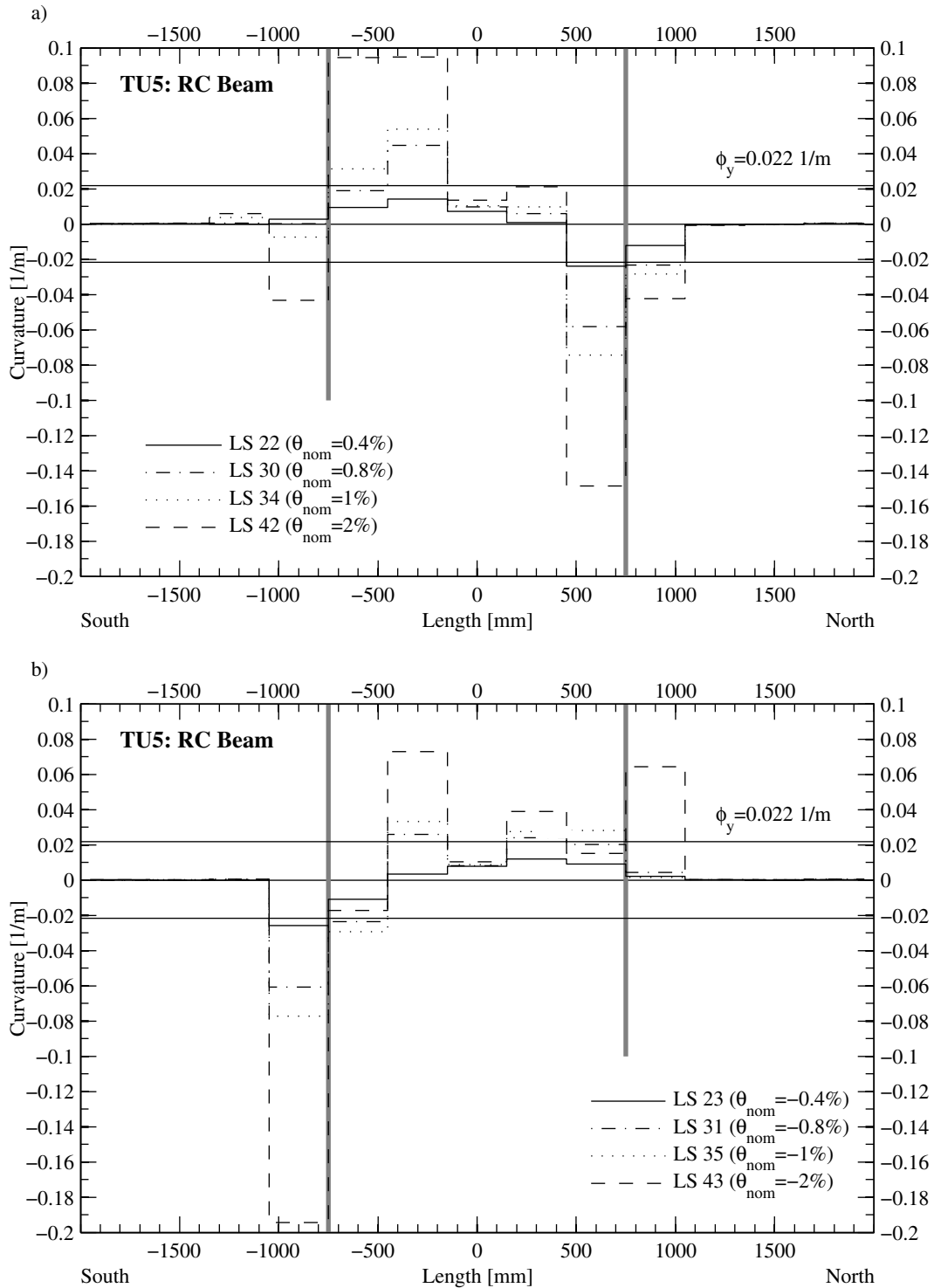


Figure 3.62: TU5: Curvature distribution along the RC beam. The thick grey lines symbolise the edges of the piers.

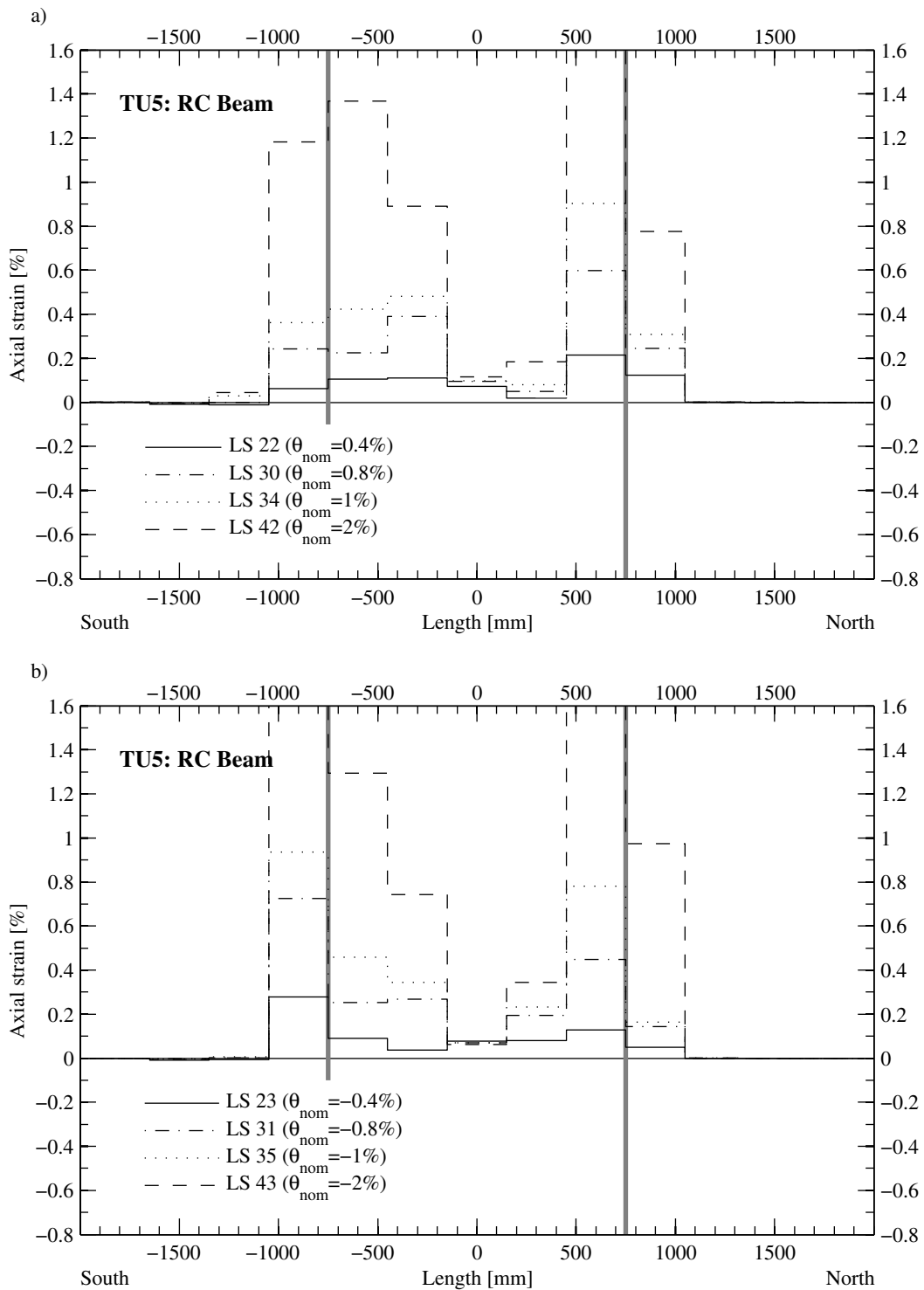
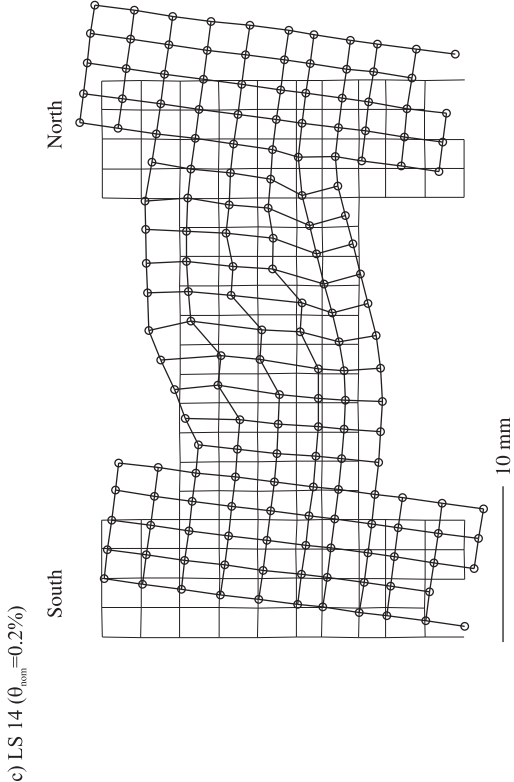
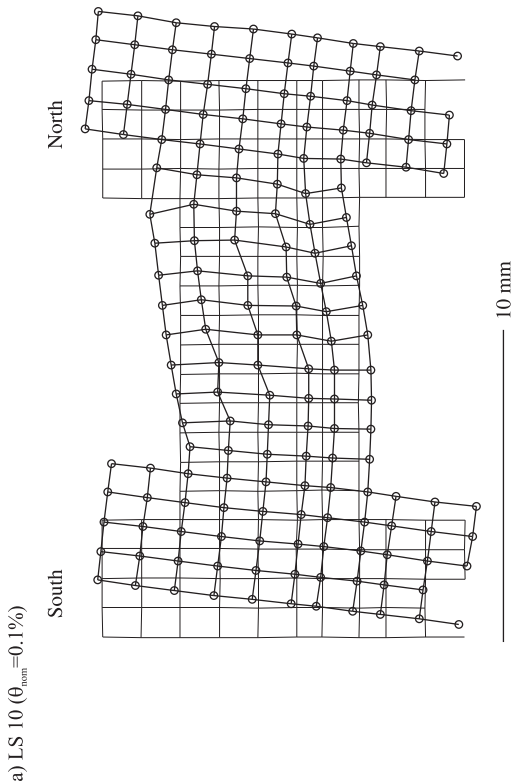
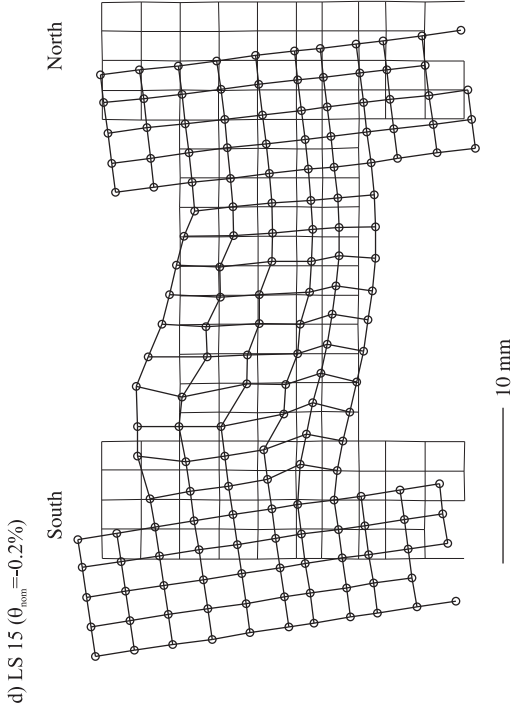
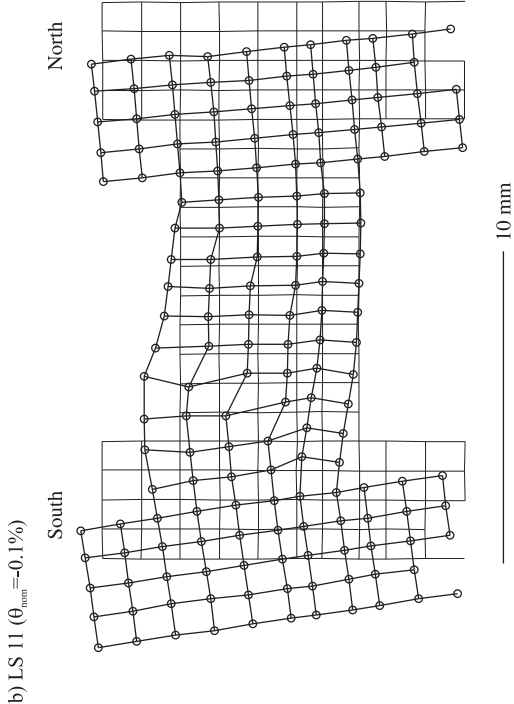


Figure 3.63: TU5: Axial strain distribution along the RC beam. The thick grey lines symbolise the edges of the piers.

3. Test results for composite spandrels



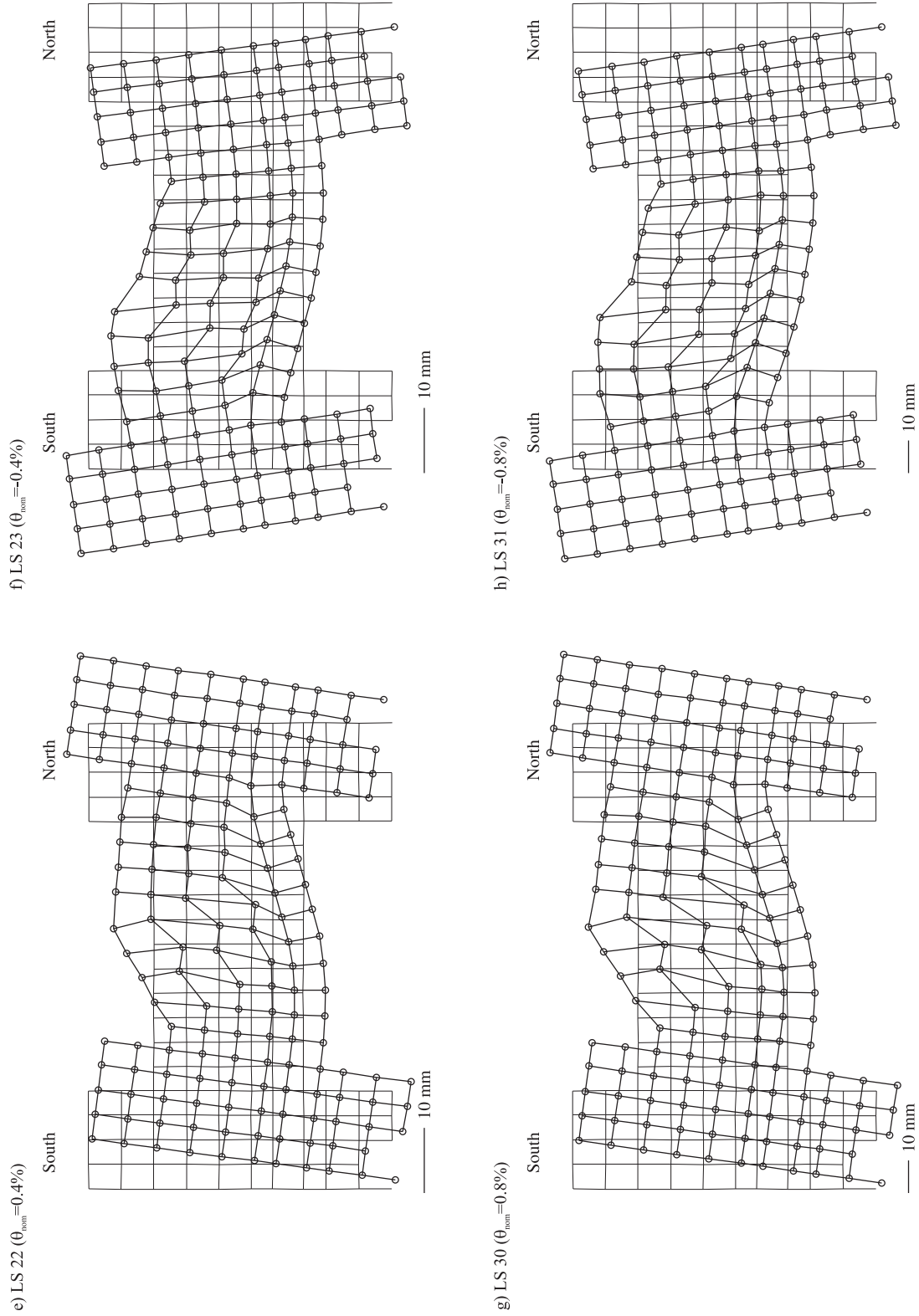


Figure 3.64: TU5: Deformed grid obtained from optical measurements at the first positive and the first negative peak of the cycles with $\theta_{nom} = \pm 0.1\%$, $\pm 0.2\%$, $\pm 0.4\%$ and $\pm 0.8\%$.

3.6.3 Deformation plots

Figure 3.64 shows the deformed shape of TU5 at the first positive as well as the first negative peak of the cycles with amplitudes of $\theta_{nom} = \pm 0.1\%$, $\pm 0.2\%$, $\pm 0.4\%$ and $\pm 0.8\%$. With respect to the dimensions of the test unit, the deformations are amplified by factors ranging between 20 and 160 so that the magnitude of the plotted deformations is for all load steps approximately equal. Shown with thin lines is the undeformed state of the test unit at LS 0. The plots show that for both directions of loading the largest stair-stepped shear crack through the masonry spandrel is in the South half of the spandrel. The point of contraflexure of the RC beam seems to be at about one third of the free span length when measuring from the end of the spandrel, at which the negative plastic hinge formed.

Part III.

Masonry spandrels

1 Test units, test setup, instrumentation and testing procedure

1.1 Test units

1.1.1 Properties of test units

In the second part of the test programme four full-scale masonry spandrels were tested. Considering the variety of spandrel shapes that can be found in older buildings two different types of spandrels were tested. The spandrels of TUA and TUB consisted of a timber lintel and a unreinforced (URM) spandrel (Fig. 1.1) while the spandrels of TUC and TUD were constructed as a URM spandrel supported by an URM arch (Fig. 1.2). The test units represent a typical spandrel that can be found in older masonry buildings built around the end of the nineteenth century. Every test unit consists basically of three parts: (i) the URM piers, (ii) the URM spandrel and (iii) the timber lintel or URM arch. In the following, the sum of the latter two parts is referred to as "spandrel". In the test units, the dimensions of the piers were smaller than the dimensions of most piers found in real buildings. The dimensions of the piers were chosen to provide realistic boundary conditions for the spandrel based on engineering judgment and taking into account the geometric constraints given by the pattern of the tie-down holes within the strong floor of the laboratory.

All masonry test units were made of solid clay bricks 25 cm long, 6 cm high and 12 cm thick. Both the bed and the head mortar joints were fully filled with an intended thickness of 1 cm. While for the head joints this specification could be met quite accurately, the bed joints turned out to be actually slightly thicker with an average thickness of about 1.4 cm. This average thickness was back-calculated from the measured total height of the test units after construction. The test units featured a solid masonry wall with an overall thickness of 38 cm. The thickness of the wall corresponded to one and a half times the length of a brick and included a 1 cm wide head joint. The bricks were laid in an English bond pattern on both faces of the masonry (see Figs. 1.1 and 1.2). The timber lintel consisted of four timber beams laid one next to the other. Each beam was 158 cm long and had a rectangular cross-section approximately 10 cm wide and 14 cm high. Hence, the total width of the timber lintel was ~ 40 cm, i.e. 2 cm wider than the masonry. The overhang of the timber lintel was 1 cm on each face of the masonry. The URM arch featured a rise of 12 cm, which corresponds to about 1/10 of the span.

Table 1.1 lists for the four test units the type of loading, the spandrel type, details about the application of the axial force in the spandrel and the construction and testing dates. It can be seen that a major difference among the test units was related to the application of the axial load in the spandrel. As it will be discussed in the following Section 1.2, the test setup was not providing any axial restraint to the spandrels and the axial load was applied by means of two steel rods running along the East and West faces of the test units as shown in Figs. 1.9 and 1.11. The rationale behind such rods was the simulation of the action provided by steel ties – often present in older

1. Test units, test setup, instrumentation and testing procedure

buildings, see e.g. [DBB⁺09] – and/or by the vertical piers constraining the axial elongation of real spandrels.

Table 1.1: Masonry spandrels: Loading scheme, spandrel type and details of the axial load application, as well as construction and testing dates for the four test units.

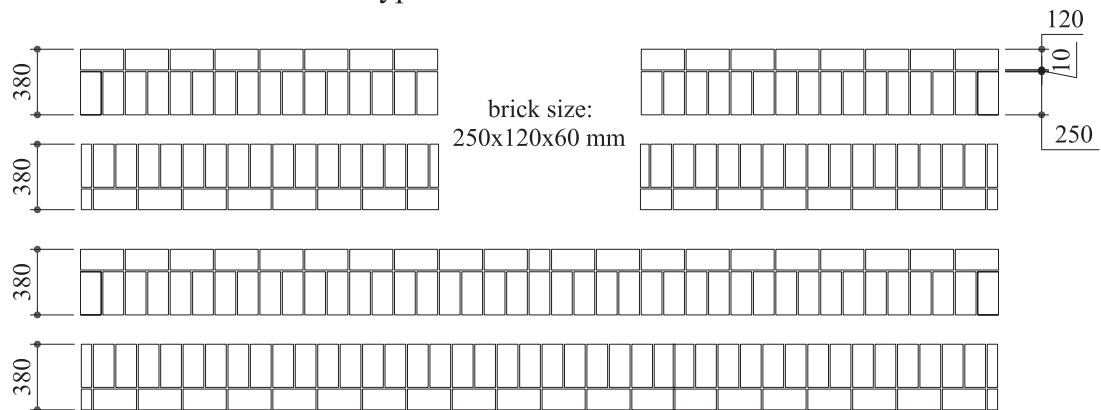
Test unit	Loading	Spandrel type	Axial force in spandrel	Construction date	Testing date
TUA	Cyclic	Timber lintel	Constant	13+14.8.2009	30.09-08.10.2009
TUB	Cyclic	Timber lintel	Variable	17+18.8.2009	04-06.11.2009
TUC	Cyclic	Arch	Constant	27-29.10.2009	21+23.12.2009
TUD	Cyclic	Arch	Variable	23-26.10.2009	13-15.1.2010

In TUA and TUC the axial load in the spandrel was provided by means of two D13 mm Stahlton rods. The rods were post-tensioned at the beginning of the test and the force in the rods was kept constant during the test by means of hollow core jacks connected to a load follower. The intention was both for TUA and TUC to carry out the entire test with a constant total axial load of 80 kN, which corresponds to about the yield strength of a D20 mm mild steel tie ($F_y = 314 \text{ mm}^2 \times 0.235 \text{ kN/mm}^2 = 74 \text{ kN}$). However, after few loading cycles of TUA it was realised that such a large post-tensioning would lead to an unrealistic failure mechanism of the test unit since large cracks opened up at the base of the piers. Hence, the axial load in the spandrel was reduced to 40 kN. The exact axial load history applied to the spandrel of TUA is extensively discussed in Section 3.2. On the contrary, TUC was tested according to the original plan and a constant total axial load of 80 kN was provided throughout the entire test.

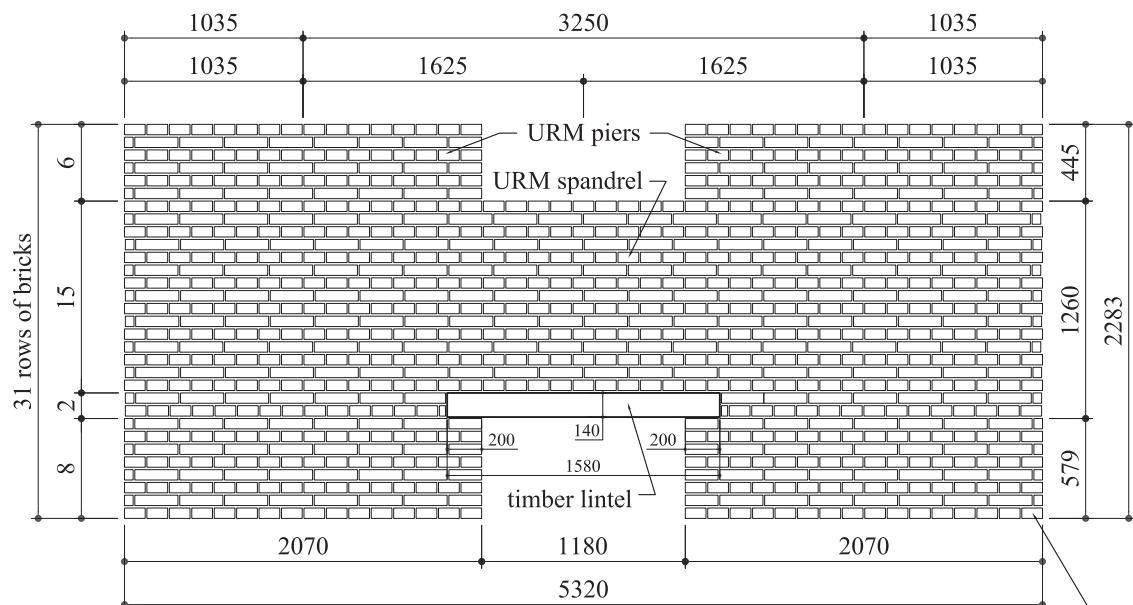
In TUB the axial load in the spandrel was provided by means of two D10 mm threaded rods. The rods were slightly post-tensioned at the beginning of the test and locked-in. Fixing the length of the rods implied an axial force increase upon axial elongation of the spandrel. The total area of the rods ($2 \times 78.5 \text{ mm}^2 = 157 \text{ mm}^2$) was chosen to simulate the axial stiffness of a D20 mild steel tie (314 mm^2) having a free length twice as the free length of the rods used in the test. The initial post-tensioning of the rods was about 2.5 kN yielding a total axial load of about 5 kN. The axial stiffness of the rods was about 6 kN/mm. Details about the axial load acting on the spandrel of TUB are given in Section 3.3.

Only in few buildings the main axial restraint on spandrel elements results from horizontal rods that are present. In most buildings a substantial axial restraint, at least for small storey drifts, is provided by the vertical piers. If the piers are long, the axial restraint is large, leading to large axial forces in the spandrel. As a consequence, shear failures tend to be the typical failure mode of spandrels in buildings with strong piers (see Fig. 1.6). Flexural failure is typically only observed when the spandrel is framed by very slender piers (see Fig. 1.7). To simulate boundary conditions on the spandrel that are similar to those found in buildings with strong piers, the axial load in the spandrel of TUD was provided by means of two D32 mm Dywidag rods. At the beginning of the test, the rods were post-tensioned to about 10 kN each and locked-in afterwards. The axial stiffness of the rods was about 59 kN/mm. The rods were chosen because they were considerably stiffer than the D10 mm rods used for TUB and because load cells for measuring the forces in the D32 mm rods were already available. Details about the axial load acting on the spandrel of TUD are given in Section 3.5.

Plan view of the typical bond of the rows of TUA and TUB



Front view (East face) of TUA and TUB



The bottom row of bricks features a special bond, laid to accommodate the block-outs for the bolts needed to fix the base plate to the lever beams

Figure 1.1: Dimensions and typical bond pattern of masonry spandrel type I featuring a timber lintel.

The goal of the tests was to provide high quality experimental evidence as a valuable benchmark for the validation and calibration of numerical and analytical models for URM spandrels with timber lintels and masonry arches. For this reason it is important to note that both the dimensions of the test units and the application of the axial load on the spandrels were not meant to represent the exact loading conditions of a spandrel in a real building but were rather chosen to allow the repetition of behaviour patterns observed during real earthquakes applying clearly defined boundary conditions.

1. Test units, test setup, instrumentation and testing procedure

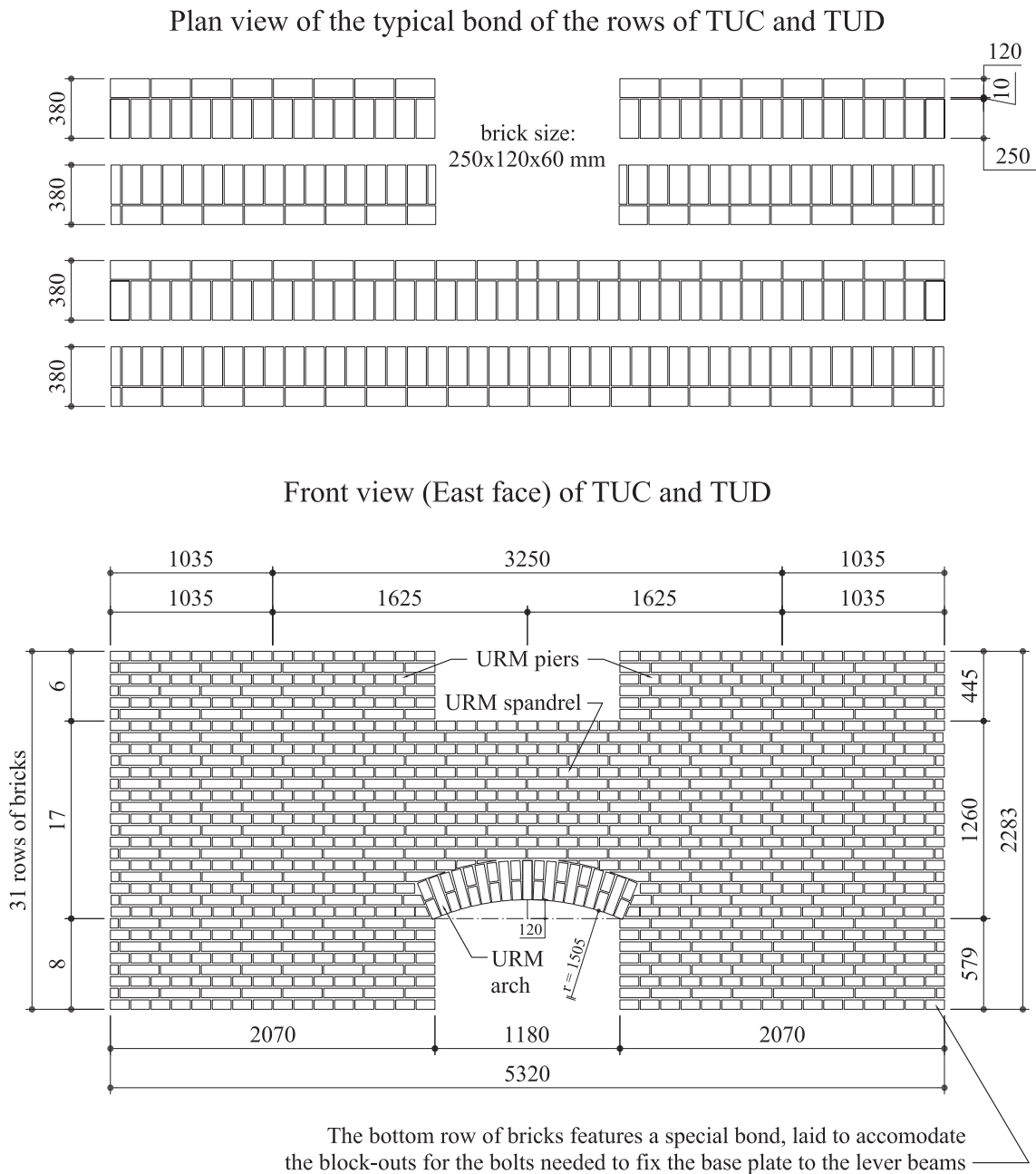


Figure 1.2: Dimensions and typical bond pattern of masonry spandrel type II featuring a URM arch.

1.1.2 Construction of test units

All masonry test units were built according to the same procedure. However, some variations in the construction procedure arose because of the different configuration of the spandrel among the test units. Selected pictures of the construction of TUA and TUB featuring the timber lintel are presented in Fig. 1.3 while the construction of TUC and TUD featuring the URM arch as support for the URM spandrel is summarised in Fig. 1.4. In the following, the construction of the test units is briefly discussed pointing out the differences occurring in the two configurations.

The test units were not constructed directly on the test stand but on the laboratory floor. In this way two test units could be built at the same time (see Table 1.1). For the construction of each test unit, two base plates were aligned on the floor (see Figs. 1.3a and 1.4a). An epoxy mortar was applied on the base plates where the piers were to be constructed. The construction of the piers started with a mortar layer. Particular attention was paid to the distance between the piers, i.e. the length of the spandrel of 1.18 m, and the alignment of the two piers to avoid any out-of-plane loading. The masonry was laid by professional masons, the bed and the head joints were fully filled using a technique called "Doppelspatz", which represents the standard in Switzerland. The filling of the head joints obtained by means of a "Doppelspatz" is shown in Fig. 1.3b: i.e. two strips of mortar are laid on the brick close to the edges and when the brick is put in place the mortar fills approximately 2/3 of the joint. In Switzerland this is considered as a "fully filled" joint.

After laying the first eight rows of bricks of each pier, paying attention that the same elevation was reached on both piers, the construction of the support of the masonry spandrel started. In the case of the timber lintel, four timber beams were laid onto the piers spanning the opening between them with a support of 20 cm on both sides. This detail of the construction is shown in Figs. 1.3a and 1.3b. In the case of the URM arch, a plywood scaffolding was built to support the bricks of the arch during construction. Figure 1.4b shows the dry staking on the scaffolding of the first row of headers of the arch. The dry stacking was carried out to check if all the bricks would fit in correctly. Then, the bricks were removed and laid again one after the other, this time filling the joints with mortar. The completed arch is shown in Fig. 1.4c where it is also clearly visible that rows 9 to 11 of the piers form the abutment of the arch.

Subsequently, the remaining of the test unit was built. The URM spandrel of the test units with timber lintel consisted of 15 rows of bricks while in the test units with arch the height of the URM spandrel varied between 14 rows over the abutment of the arch and 12 rows over the crown. The last six rows were only constructed over the piers. After two weeks or more, the load transfer beams (see Figs. 1.9 and 1.11) were mounted on the test unit. To do so, the load transfer beams were bolted to two long steel beams. The long steel beams were needed for moving the test unit onto the test stand. Capacity-wise one beam would have been sufficient. A second beam was added for additional stiffness to ensure that the test unit would not be damaged during the lifting. A mortar bed was prepared on top of the piers. The load transfer beams were placed onto the test unit together with the long beams. By means of eight vertical rods the load transfer beams were pre-stressed against the base plates. The total pre-stressing force in the rods was $8 \times 30 \text{ kN} = 240 \text{ kN}$ and therefore larger than the weight of the test unit, which was approximately 93 kN including base plates and load transfer beams. Figure 1.5 shows TUA before lifting onto the test stand by means of one of the 10 t laboratory cranes.

On the test stand the base plates were bolted onto the lever beams (see Figs. 1.9 and 1.11) and finally the two long beams were removed. During the mounting of the test unit on the lever beams and the removing of the long beams, the channels measuring the forces at the supports and the rotations of the lever beams were continuously recorded. Once the test unit was installed on the test stand the forces in the vertical rods were released. This load condition was called LS 0 and marked the onset of the loading history.

1. Test units, test setup, instrumentation and testing procedure



Figure 1.3: Construction of masonry spandrel with timber lintel (TUA).



Figure 1.4: Construction of masonry spandrel with arch (TUC).



Figure 1.5: Test unit ready to be lifted onto the test stand.

1.1.3 True dimensions and constructive imperfections of test units

The masonry test units were all built by the same three masons. However, considering the large size of the units and the small size of the bricks, the final dimensions of the test units varied slightly and minor constructive differences regarding most notably the clamped support of the timber lintel and the layout of the arch could be observed after construction.

Figure 1.6 shows the true dimensions of test units TUA to TUD measured after construction. The vertical dimensions were measured from the bottom base plates to the top load transfer beams. Hence, they include the thickness of the mortar joint located between the base plate and the first row of bricks and the thickness of the mortar joint located between the 31st row of bricks and the load transfer beam. For this reason the average total height of the test units given in Fig. 1.6 equals 2306 ± 4 mm which is 23 mm more than the height given in Figs. 1.1 and 1.2. The latter did not include the thickness of the top and bottom mortar joints. The same observation holds for all vertical dimensions in Fig. 1.6 originating from the extremities of the test unit. All test units were built taking extreme care and the variations of the dimensions are generally quite minor with basically two exceptions: (i) The top edge of the North pier of TUD was nearly 4 cm longer than the bottom edge resulting in a bellied North vertical edge of the test unit as it can be seen e.g. in Figs. 3.46 and 3.47. However, this imperfection had no visible effect on the mechanical behaviour of the spandrel. (ii) The height of the spandrel of TUC was about 2 cm shorter than the height of the spandrel of TUD. This difference corresponds to just 1.5% of the height of the spandrel and it is likely that it had only a minor effect on the mechanical behaviour of TUC.

1. Test units, test setup, instrumentation and testing procedure

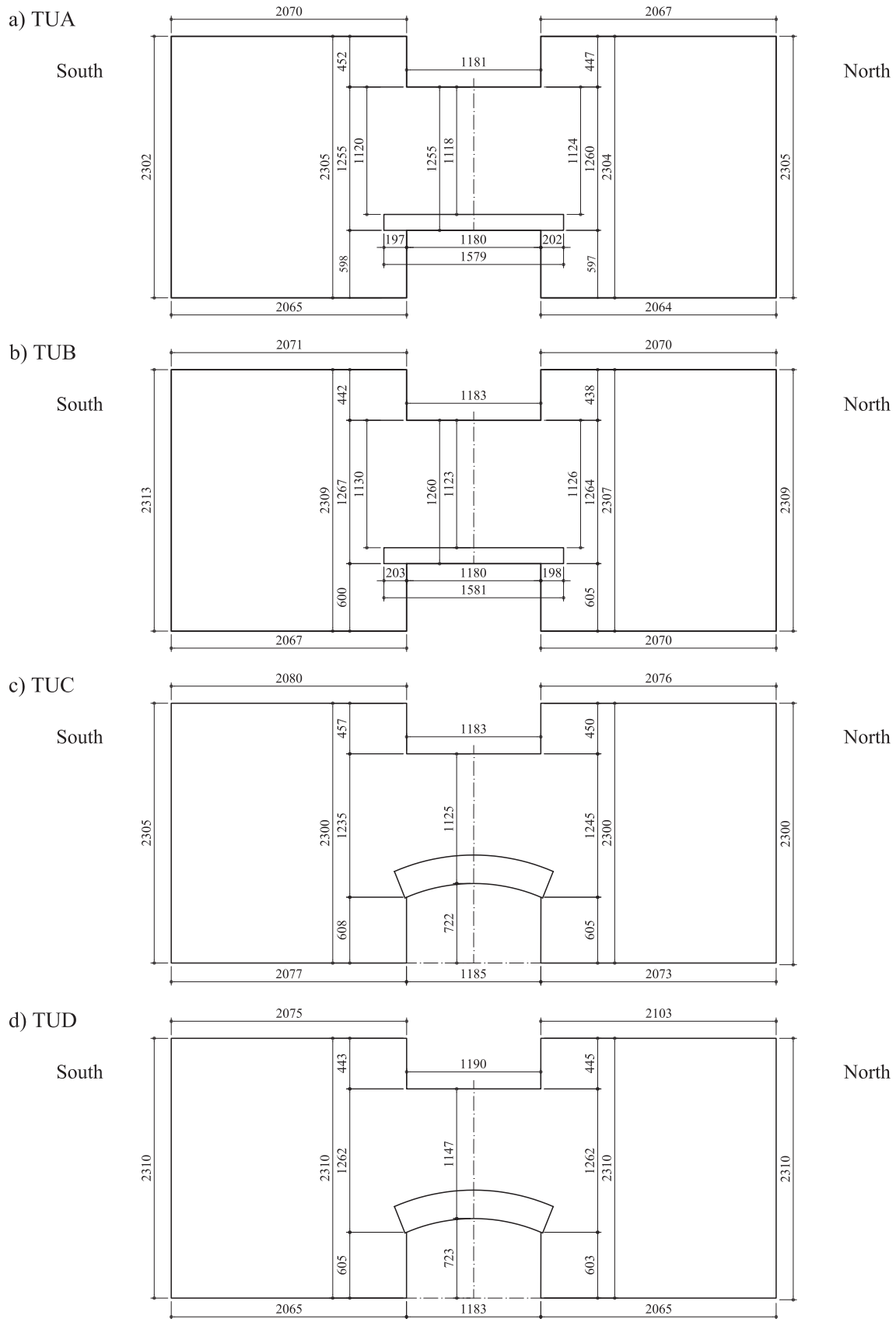


Figure 1.6: True dimensions in [mm] of test units TUA (a) to TUD (d) measured after construction.

Figure 1.7 compares the arches of TUC and TUD. In terms of construction quality there were clearly noticeable differences at the impostes of the arch and at the inclined mortar joints. In TUC the lower extremities of the North and South impostes were both located few centimetres beyond the corresponding edge of the spandrel. On the contrary, in TUD the lower extremities of the North and South impostes were basically flush with the edges of the spandrel. Before testing, based on engineering judgement it was argued that the impostes of TUC should perform significantly better due to a constructive detail that was judged as to be far superior. However, the tests showed no significant damage to the impostes of both arches making any further comment on the possible inappropriateness of TUD's impostes difficult. Comparing the inclined mortar joints within the arches of TUC and TUD comments similar to those made about the impostes are possible. Purely optically, the joints of TUC seemed to be of superior quality. All joints were neatly filled and their thickness was fairly regular along the entire arch. On the contrary, TUD's joints were quite irregular and at some locations not so well filled (at least on the visible East face). During the test, however, no significant difference between the two arches could be made out. The arches of the two test units showed a similar failure mechanism and it is difficult to ascribe possible behavioural differences to the construction quality rather than to the different axial load acting on the spandrels.

Figure 1.8 compares the constructive details of the South and the North edges of the lintel support of TUA. On the South edge the bricks were laid without head joint to the timber lintel, while on the North edge such a mortar joint was present. Based on engineering judgement alone it is difficult to formulate a hypothesis on which detail should perform better. Even after testing and despite the fact that exactly the failure of the South lintel support, albeit the part lying underneath the timber beams, caused the failure of the spandrel, it is still not possible to argue for one detail or for the other on a convincing basis.

Summarising, it can be stated that slight constructive differences could be observed among the different test units. However, no clear effect of these differences on the mechanical behaviour of the spandrels could be identified.

1.2 Test setup

The test setup for the test units with timber lintel (TUA and TUB) and URM arch (TUC and TUD) was basically the same with the only differences between the setups for the individual test units being the axial restraint and the axial load of the spandrel (see Section 1.1.1). A drawing and a photo of the test setup of TUA are shown in Figs. 1.9 and 1.10, respectively, while the pictures relevant to TUC are shown in Figs. 1.11 and 1.12.

The test setup for the test unit with masonry spandrel was in fact very similar to the setup used for test the units with composite spandrel described in Section 1.2 of Part II. The only notable differences were:

- For the masonry spandrels the distance between the supports of the lever beams was 3.28 m instead of 3.60 m as for the composite spandrels. The distance was reduced to accommodate the smaller span of the spandrel.
- For the masonry spandrels horizontal rods were installed to generate an axial load in the spandrel.

1. Test units, test setup, instrumentation and testing procedure

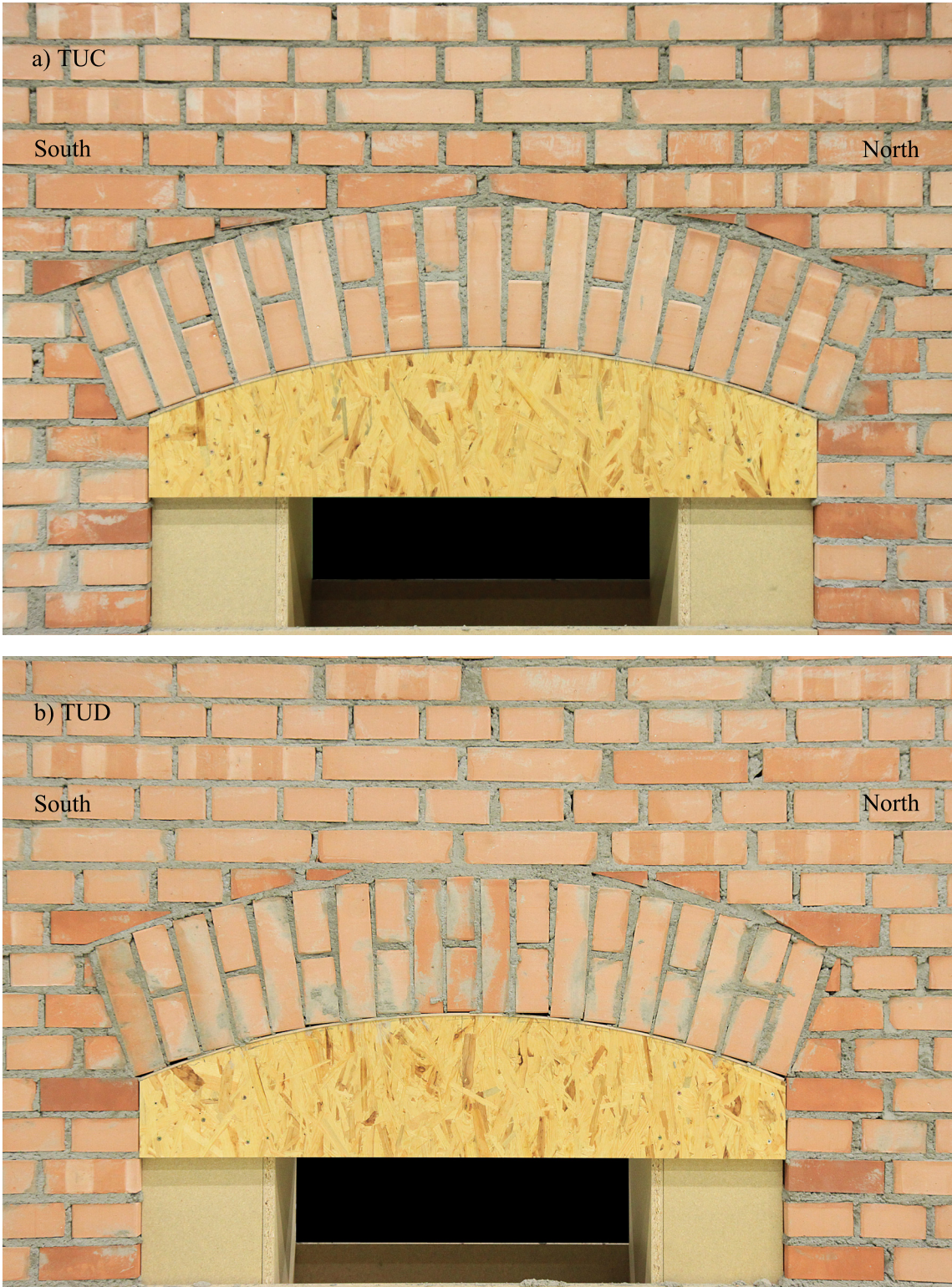


Figure 1.7: Comparison between the arch of TUC (a) and TUD (b).

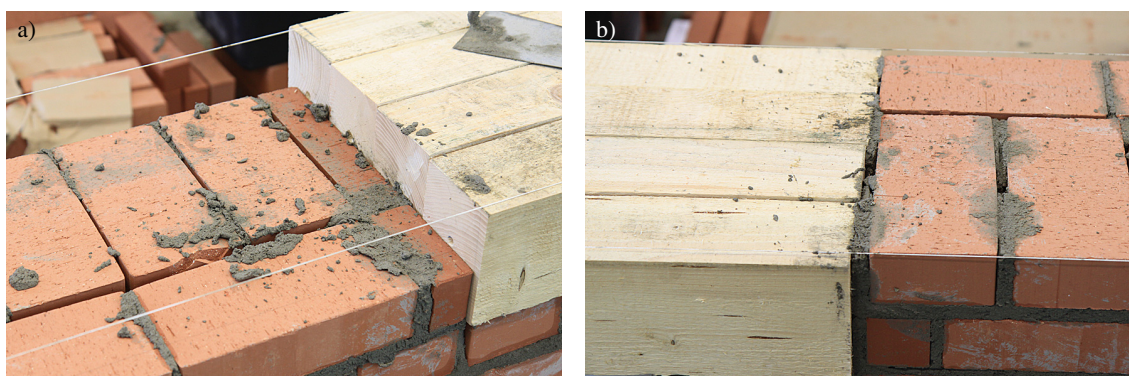


Figure 1.8: Comparison between the South (a) and the North (b) edge of the lintel support of TUA.

For the sake of completeness and despite this similarity, the setup for the masonry spandrels is presented again in the following paragraphs.

The test unit stood on two stiff steel beams (“lever beam”) that were supported on hinges at the centre line of the piers and connected to servo-hydraulic actuators at their ends. The actuators had a force capacity of ± 250 kN and a displacement capacity of ± 250 mm. Both actuators were displacement-controlled. The support of the South lever beam allowed next to a rotation also a sliding movement in the direction of the beam. Since the axial elongation of the spandrel was not restrained by the supports, the latter experienced only vertical forces. During testing the two servo-hydraulic actuators were moved with the same velocity in opposite directions. As a result, the two horizontal lever beams rotated and the piers right and left to the spandrel were subjected to the same drifts, which caused the demand on the spandrel. Note that, since the velocity of the actuators was controlled via the displacement transducers mounted on the actuators themselves, the actual drifts of the two lever beams could differ slightly. This was mainly due to some small backlash within the actuators’ hinges.

At the supports of the two lever beams the reaction forces were measured. Since the axial elongation of the spandrel was not restrained by the test setup only vertical forces developed at the supports. Within the cyclic tests, the vertical force of each support could potentially change sign (tension-compression) twice during every loading cycle. Considering that no tension-compression load cells were readily available, to measure the reaction force at each support such a load cell was assembled from one compression load cell and four tension load cells. The compression load cell was mounted between two steel plates post-tensioned together by means of four D13 mm Stahlton rods. The forces in the rods were measured by means of the four tension load cells. The total pretension force was about 200 kN and therefore larger than the expected maximum reaction force in tension. From the actuator forces and the reaction forces at the supports the shear force within the spandrel could be computed. The measured forces were redundant since the shear force in the spandrel could be once computed from the force of the North actuator and the North support and once from the force of the South actuator and the South support (see Section 3.1). This allowed a redundant measure of the shear force in the spandrel, which is a key result of the tests.

The axial load on the piers was applied by means of four D13 mm Stahlton rods per pier. Every rod was provided with a hollow core jack. All four jacks on the same pier were connected to the

1. Test units, test setup, instrumentation and testing procedure

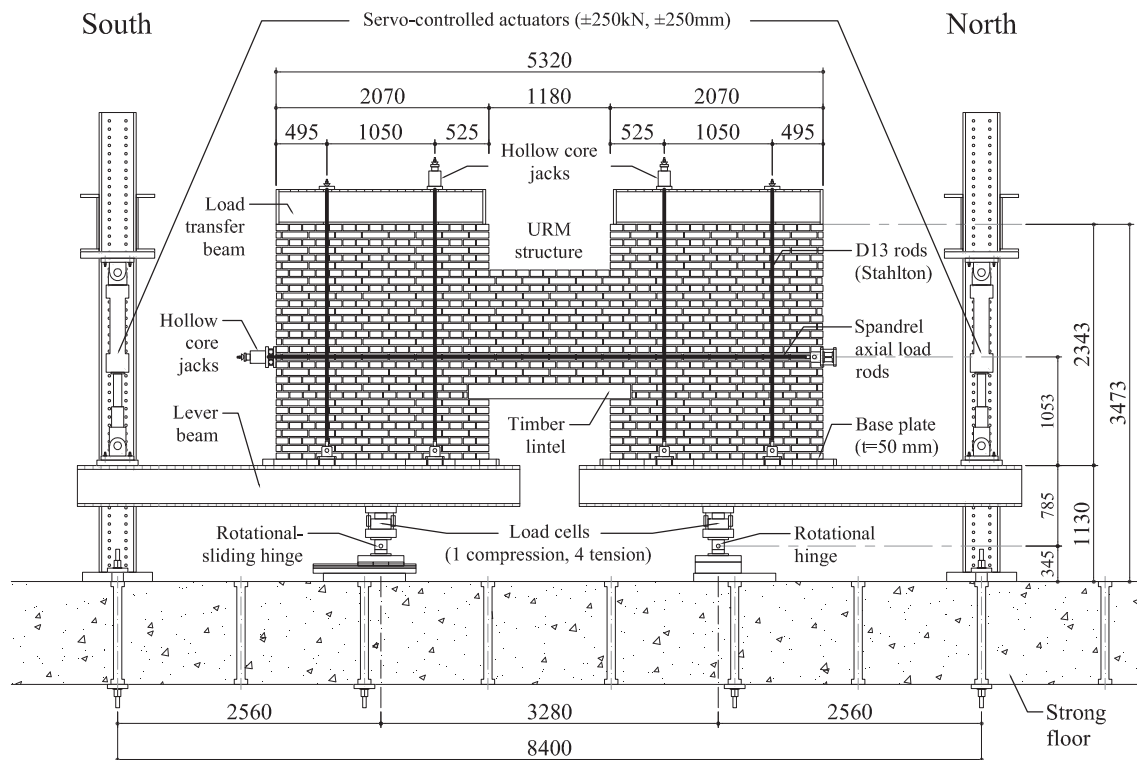


Figure 1.9: Drawing of the test setup for the masonry spandrels with timber lintel (TUA and TUB). View from the East without side restraint. All dimensions in [mm].

same hydraulic pump equipped with a load follower. The jacks were used to both post-tension the rods and to keep the forces in the rods constant during the entire test. The apparatus used to apply the axial load as well as the axial restraint of the spandrel consisted of two rods running horizontally along the East and West faces of the test unit. At the two extremities, i.e. on the South and North faces of the test unit, two cross beams introduced the force of the rods into the test unit. On the South side of the apparatus for TUA, TUB and TUC hollow core jacks were kept in place permanently to control the force in the rods according to the testing programme discussed in Section 1.1.1. In the apparatus for TUD no jacks were installed; the rods were post-tensioned by hand and locked-in immediately thereafter. The diameter of the rods and the post-tensioning force utilised for the different tests are specified in Sections 1.1.1 and 3.2 to 3.5.

To avoid out-of-plane movements of the test unit two lateral support systems were mounted: The first lateral support system restrained excessive out-of-plane movement of the lever beams. This was accomplished by steel plates that guided the web of the lever beams. The steel plates were fixed to the four inner columns shown on Figs. 1.9 and 1.11 by means of threaded bars. At the beginning of testing the clear distance between steel plates and web of the lever beams was approximately 1 cm. Checks during testing showed that the out-of-plane movement of the lever beams was rather small and therefore this lateral support system served only as a safety measure. The second lateral support system restrained the load transfer beams on top of the piers from moving out-of-plane. On each side of the test unit a steel frame consisting of two columns and a large horizontal beam were set up. Timber beams with a cross section of approximately 14x14 cm were clamped to the lower edge of the horizontal beam. Stiff plastic rollers were mounted on

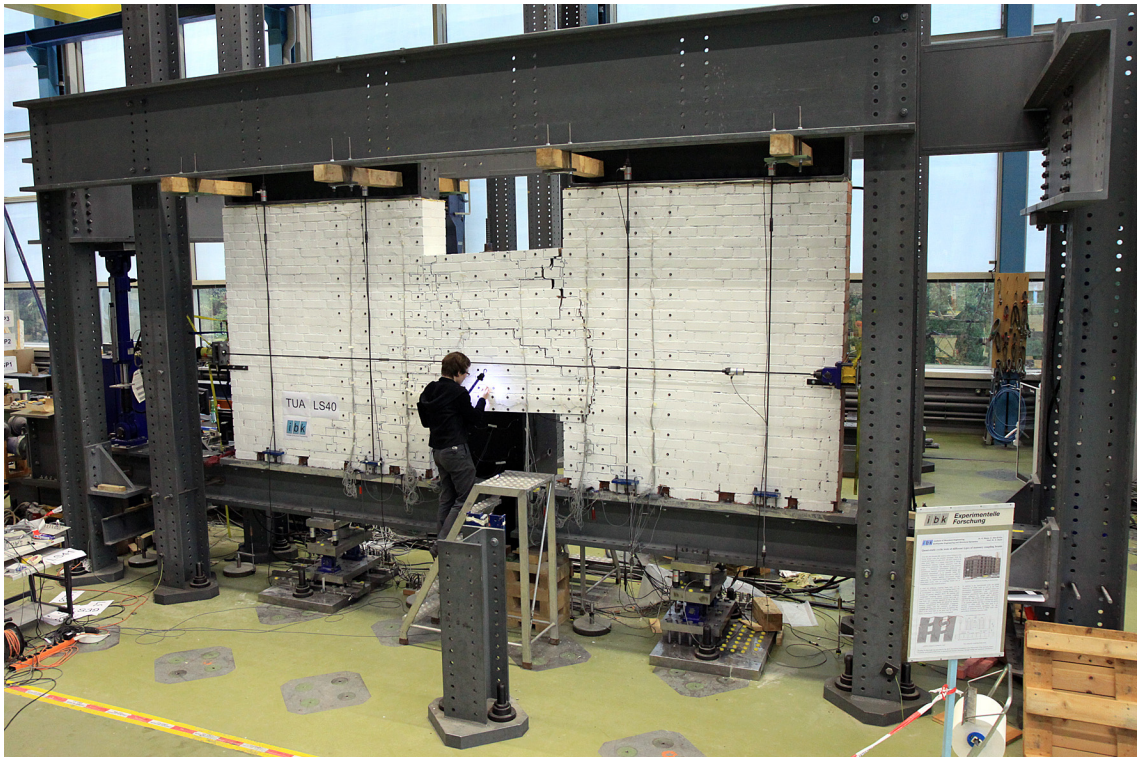


Figure 1.10: Photo of the test setup for the masonry spandrels with timber lintel (TUA and TUB). View from the East during testing of TUA.

the end cross-sections of the timber beams close to the test unit. The rollers were approximately 8 cm in diameter and are commonly used as heavy duty wheels. The axis of the rollers was vertical so that when the load transfer beam moved horizontally due to the applied pier rotation the rollers could roll on the web of the load transfer beams. Also for this lateral support system the clear distance between rollers and web of the load transfer beams at the beginning of testing was approximately 1 cm.

1.3 Instrumentation

Different global and local deformation quantities were measured during testing by means of hard-wired instruments. In addition, an optical measurement system was used to measure the coordinates of LEDs mounted on the East face of the test units. In the following, the quantities measured with the two measurement systems are described in detail.

1.3.1 Hard-wired channels

In the framework on the tests on masonry spandrels hard-wired instruments were used to measure different sets of quantities. These were:

1. Test units, test setup, instrumentation and testing procedure

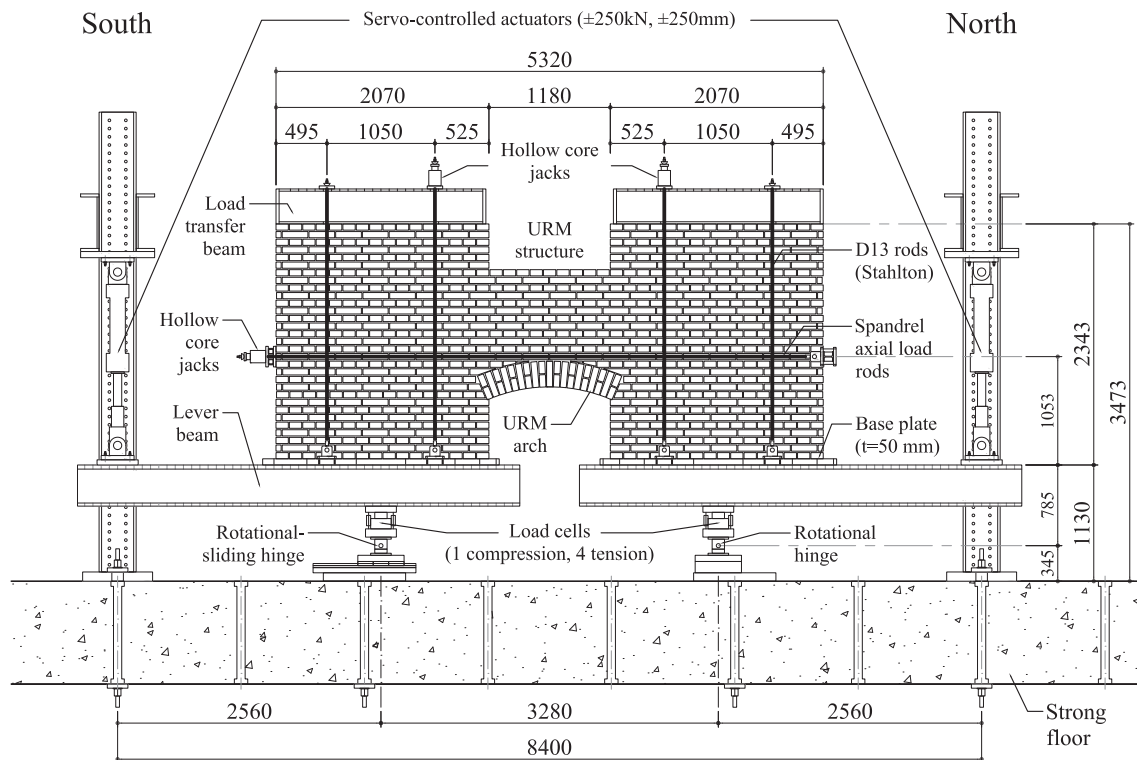


Figure 1.11: Drawing of the test setup for the masonry spandrels with arch (TUC and TUD). View from the East without side restraint. All dimensions in [mm].

- The actuator forces and the reaction forces at the supports of the lever beams (TUA, TUB, TUC and TUD).
- Global deformation quantities, i.e. the rotation of the lever beams and the movement of the sliding support of the South lever beam (TUA, TUB, TUC and TUD).
- The forces in the vertical rods generating the axial load in the piers (TUA, TUB, TUC and TUD).
- The forces in the horizontal rods generating the axial load in the spandrel (TUA, TUB, TUC and TUD).
- Local deformation of the timber lintel by means of two LVDT chains running along the top and bottom edges of the lintel West face (TUA and TUB).

In total 55 hard-wired instruments were used to monitor the behaviour of TUA and TUB: 32 displacement transducers (LVDTs), 22 load cells (LC) and 1 voltmeter. The labels and the specification of these instruments are summarised in Table 1.2 while their exact location is specified in Fig. 1.13. To monitor the behaviour of TUC and TUD 31 hard-wired instruments were used in total: 8 displacement transducers (LVDTs), 22 load cells (LC) and 1 voltmeter. The labels and the specification of these instruments are summarised in Table 1.3 while their exact location is specified in Fig. 1.14. The hard-wired instruments were recorded at 2 s intervals.



Figure 1.12: Photo of the test setup for the masonry spandrels with arch (TUC and TUD). View from the East during testing of TUD.

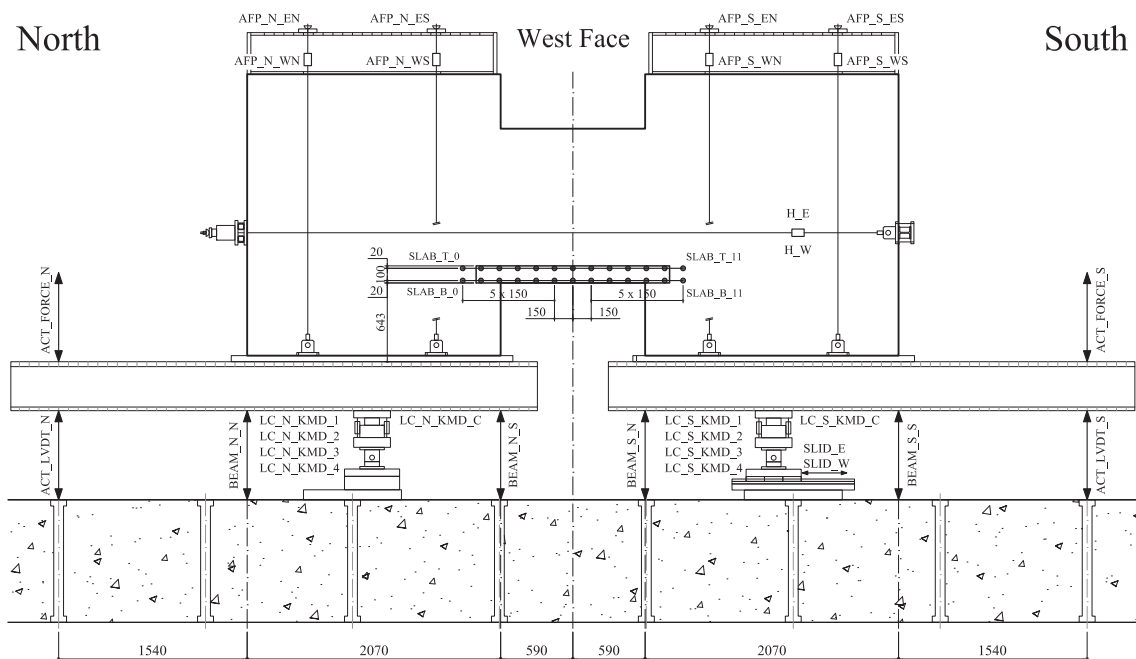


Figure 1.13: Layout of the hard-wired instruments for masonry spandrels with timber lintel (TUA and TUB). West face, all dimensions in [mm].

1. Test units, test setup, instrumentation and testing procedure

Table 1.2: Hard-wired channels measured for TUA and TUB.

Channel name	Instrument type	Description of measured quantity
ACT_FORCE_N	±250 kN LC	Actuator force of North actuator
ACT_FORCE_S	±250 kN LC	Actuator force of South actuator
ACT_LVDT_N	LVDT HBM W50 ±50 mm	Vertical displ. of lever beam at the position of the North actuator
ACT_LVDT_S	LVDT HBM W50 ±50 mm	Vertical displ. of lever beam at the position of the South actuator
BEAM_N_N	LVDT Precisor TK50 ±50 mm	Vertical displ. of lever beam at the position of the North edge of the North pier
BEAM_N_S	LVDT Precisor TK50 ±50 mm	Vertical displ. of lever beam at the position of the South edge of the North pier
BEAM_S_N	LVDT Precisor TK50 ±50 mm	Vertical displ. of lever beam at the position of the North edge of the South pier
BEAM_S_S	LVDT Precisor TK50 ±50 mm	Vertical displ. of lever beam at the position of the South edge of the South pier
SLID_E	LVDT Precisor TK25 ±25 mm	Sliding displacement at support of South lever beam measured at the East rail
SLID_W	LVDT Precisor TK25 ±25 mm	Sliding displacement at support of South lever beam measured at the West rail
LC_N_KMD_C	1 MN Compression LC	Support of North lever beam, Compression LC (original name: LC_N_C)
LC_N_KMD_1	Tension LC	Support of North lever beam, Tension LC 1 (original name: LC_N_17)
LC_N_KMD_2	Tension LC	Support of North lever beam, Tension LC 2 (original name: LC_N_16)
LC_N_KMD_3	Tension LC	Support of North lever beam, Tension LC 3 (original name: LC_N_19)
LC_N_KMD_4	Tension LC	Support of North lever beam, Tension LC 4 (original name: LC_N_08)
LC_S_KMD_C	1 MN Compression LC	Support of South lever beam, Compression LC (original name: LC_S_C)
LC_S_KMD_1	Tension LC	Support of South lever beam, Tension LC 1 (original name: LC_S_15)
LC_S_KMD_2	Tension LC	Support of South lever beam, Tension LC 2 (original name: LC_S_0)
LC_S_KMD_3	Tension LC	Support of South lever beam, Tension LC 3 (original name: LC_S_24)
LC_S_KMD_4	Tension LC	Support of South lever beam, Tension LC 4 (original name: LC_S_22)
AFP_N_EN	Tension LC	Axial force on North pier, North rod on East face
AFP_N_ES	Tension LC	Axial force on North pier, South rod on East face
AFP_N_WN	Tension LC	Axial force on North pier, North rod on West face
AFP_N_WS	Tension LC	Axial force on North pier, South rod on West face
AFP_S_EN	Tension LC	Axial force on South pier, North rod on East face
AFP_S_ES	Tension LC	Axial force on South pier, South rod on East face
AFP_S_WN	Tension LC	Axial force on South pier, North rod on West face
AFP_S_WS	Tension LC	Axial force on South pier, South rod on West face
SLAB_T_0	LVDT Precisor TK25 ±25 mm	Elongation of timber lintel, top row (measured on the West face)
SLAB_T_1	LVDT Precisor TK10 ±10 mm	
SLAB_T_2	LVDT Precisor TK10 ±10 mm	
SLAB_T_3	LVDT Precisor TK10 ±10 mm	
SLAB_T_4	LVDT Precisor TK10 ±10 mm	
SLAB_T_5	LVDT Precisor TK10 ±10 mm	
SLAB_T_6	LVDT Precisor TK10 ±10 mm	
SLAB_T_7	LVDT HBM WSF20 ±10 mm	
SLAB_T_8	LVDT HBM WSF20 ±10 mm	
SLAB_T_9	LVDT HBM WSF20 ±10 mm	
SLAB_T_10	LVDT HBM WSF20 ±10 mm	
SLAB_T_11	LVDT HBM WSF20 ±10 mm	
SLAB_B_0	LVDT Precisor TK10 ±10 mm	Elongation of timber lintel, bottom row (measured on the West face)
SLAB_B_1	LVDT Precisor TK10 ±10 mm	
SLAB_B_2	LVDT Precisor TK10 ±10 mm	
SLAB_B_3	LVDT Precisor TK10 ±10 mm	
SLAB_B_4	LVDT Precisor TK10 ±10 mm	
SLAB_B_5	LVDT Precisor TK10 ±10 mm	
SLAB_B_6	LVDT Precisor TK10 ±10 mm	
SLAB_B_7	LVDT HBM WSF20 ±10 mm	
SLAB_B_8	LVDT HBM WSF20 ±10 mm	
SLAB_B_9	LVDT HBM WSF20 ±10 mm	
SLAB_B_10	LVDT HBM WSF20 ±10 mm	
SLAB_B_11	LVDT HBM WSF20 ±10 mm	
H_E	Tension LC	Tension force in the East horizontal rod
H_W	Tension LC	Tension force in the West horizontal rod
Voltage		Volt measurement. The displacement measurement of BEAM_N_N, BEAM_N_S, BEAM_S_N and BEAM_S_S is based on a voltage.

1.3.2 Optical measurements

In addition to the hard-wired instruments, an optical measurement system (NDI Optotrak Certus HD [NDI09]) was used to measure the local deformations of the test unit. The system works with a position sensor consisting of three cameras, which measured the 3D-coordinates of LEDs glued onto the test unit and the base plates. The position sensor shown on the left of Fig. 1.17 was placed

Table 1.3: Hard-wired channels measured for TUC and TUD.

Channel name	Instrument type	Description of measured quantity
ACT_FORCE_N	±250 kN LC	Actuator force of North actuator
ACT_FORCE_S	±250 kN LC	Actuator force of South actuator
ACT_LVDT_N	LVDT HBM W50 ±50 mm	Vertical displ. of lever beam at the position of the North actuator
ACT_LVDT_S	LVDT HBM W50 ±50 mm	Vertical displ. of lever beam at the position of the South actuator
BEAM_N_N	LVDT Precisor TK50 ±50 mm	Vertical displ. of lever beam at the position of the North edge of the North pier
BEAM_N_S	LVDT Precisor TK50 ±50 mm	Vertical displ. of lever beam at the position of the South edge of the North pier
BEAM_S_N	LVDT Precisor TK50 ±50 mm	Vertical displ. of lever beam at the position of the North edge of the South pier
BEAM_S_S	LVDT Precisor TK50 ±50 mm	Vertical displ. of lever beam at the position of the South edge of the South pier
SLID_E	LVDT Precisor TK25 ±25 mm	Sliding displacement at support of South lever beam measured at the East rail
SLID_W	LVDT Precisor TK25 ±25 mm	Sliding displacement at support of South lever beam measured at the West rail
LC_N_C	1 MN Compression LC	Support of North lever beam, Compression LC (original name: LC_N_C)
LC_N_KMD_1	Tension LC	Support of North lever beam, Tension LC 1 (original name: LC_N_17)
LC_N_KMD_2	Tension LC	Support of North lever beam, Tension LC 2 (original name: LC_N_16)
LC_N_KMD_3	Tension LC	Support of North lever beam, Tension LC 3 (original name: LC_N_19)
LC_N_KMD_4	Tension LC	Support of North lever beam, Tension LC 4 (original name: LC_N_08)
LC_S_C	1 MN Compression LC	Support of South lever beam, Compression LC (original name: LC_S_C)
LC_S_KMD_1	Tension LC	Support of South lever beam, Tension LC 1 (original name: LC_S_15)
LC_S_KMD_2	Tension LC	Support of South lever beam, Tension LC 2 (original name: LC_S_0)
LC_S_KMD_3	Tension LC	Support of South lever beam, Tension LC 3 (original name: LC_S_24)
LC_S_KMD_4	Tension LC	Support of South lever beam, Tension LC 4 (original name: LC_S_22)
AFP_N_EN	Tension LC	Axial force on North pier, North rod on East face
AFP_N_ES	Tension LC	Axial force on North pier, South rod on East face
AFP_N_WN	Tension LC	Axial force on North pier, North rod on West face
AFP_N_WS	Tension LC	Axial force on North pier, South rod on West face
AFP_S_EN	Tension LC	Axial force on South pier, North rod on East face
AFP_S_ES	Tension LC	Axial force on South pier, South rod on East face
AFP_S_WN	Tension LC	Axial force on South pier, North rod on West face
AFP_S_WS	Tension LC	Axial force on South pier, South rod on West face
H_E	Tension LC	Tension force in the East horizontal rod
H_W	Tension LC	Tension force in the West horizontal rod
Voltage		Volt measurement. The displacement measurement of BEAM_N_N, BEAM_N_S, BEAM_S_N and BEAM_S_S is based on a voltage.

approximately 5.3 m away from the East face of the test unit. At this distance LEDs within an area of 3.25x2.45 m could be tracked. Figures 1.15 and 1.16 show the layout of the LEDs glued onto the test units with timber lintel and masonry arch, respectively. The lowest rows of LEDs was not glued onto the test units but onto angles (L-shapes) that were glued onto the base plates. In addition to the LEDs shown in Figs. 1.15 and 1.16, four LEDs were fixed to two short steel columns standing in front and behind of the test unit. These four LEDs were used as reference LEDs since the steel columns did not move during loading. Thus, a change in position of these reference LEDs would indicate that the position sensor had been accidentally moved.

The position of each LED defined through the time-histories of the x-, y- and z-coordinates was recorded with a 10 Hz rate. The original coordinate system depended on the orientation of the position sensor but was rotated during the post-processing of the data. In the final coordinate system the x-axis is parallel to the test unit pointing from South to North, the y-axis points up vertically and the z-axis points from the test unit to the position sensor. To synchronise the optical measurements with the hard-wired channel measurements, the Volt-signal stemming from the actuator forces was read into both data acquisition systems. However, it was found that the recording of the Volt-signal by the optical measurement system featured a lot of noise. For this reason, the rotation of the lever beams was used to synchronise the two types of measurements. The coordinate measurement data was first smoothed and then reduced to the same recording rate as the hard-wired data, i.e. to a frequency of 0.5 Hz. The positions of the LEDs were also recorded at each load step when the loading was stopped. The measurements were performed over a du-

1. Test units, test setup, instrumentation and testing procedure

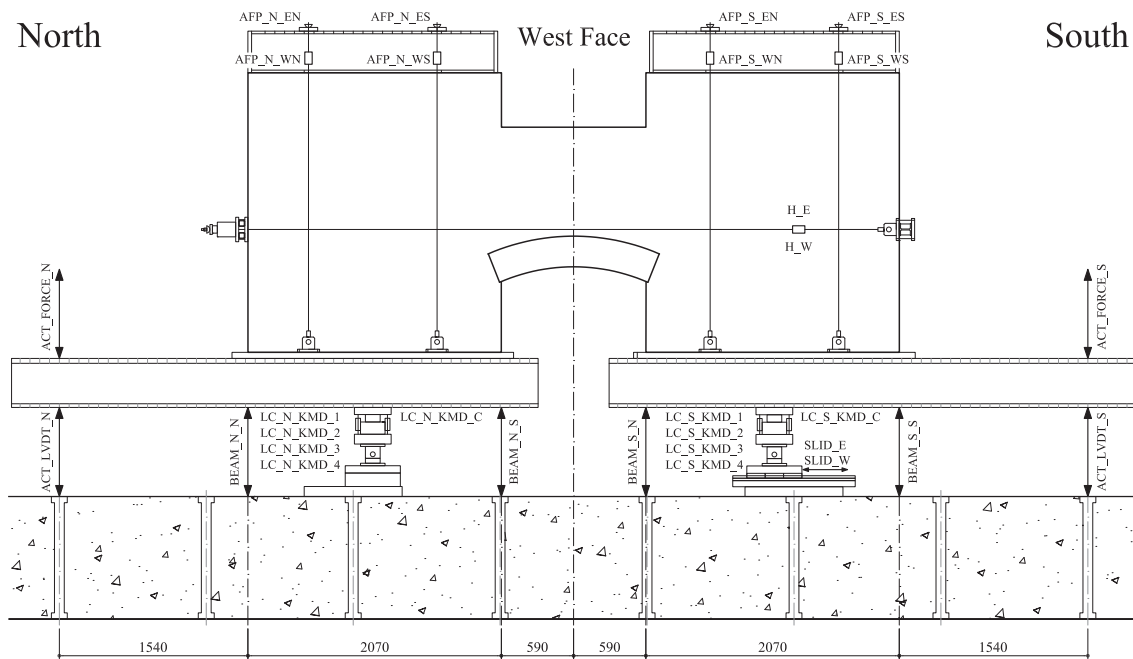


Figure 1.14: Layout of the hard-wired instruments for masonry spandrels with arch (TUC and TUD). West face, all dimensions in [mm].

ration of approximately one minute and were later averaged over the recording time to obtain the deformations of the spandrel at the load steps.

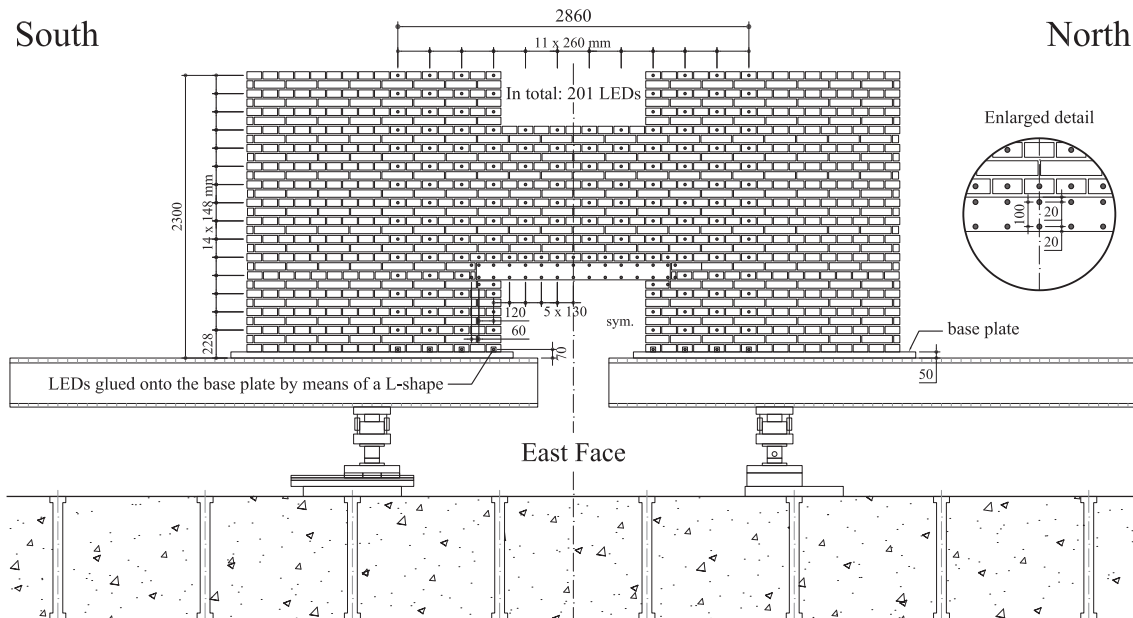


Figure 1.15: Layout of the LEDs on the East face of the test units with timber lintel (TUA and TUB). All dimensions in [mm].

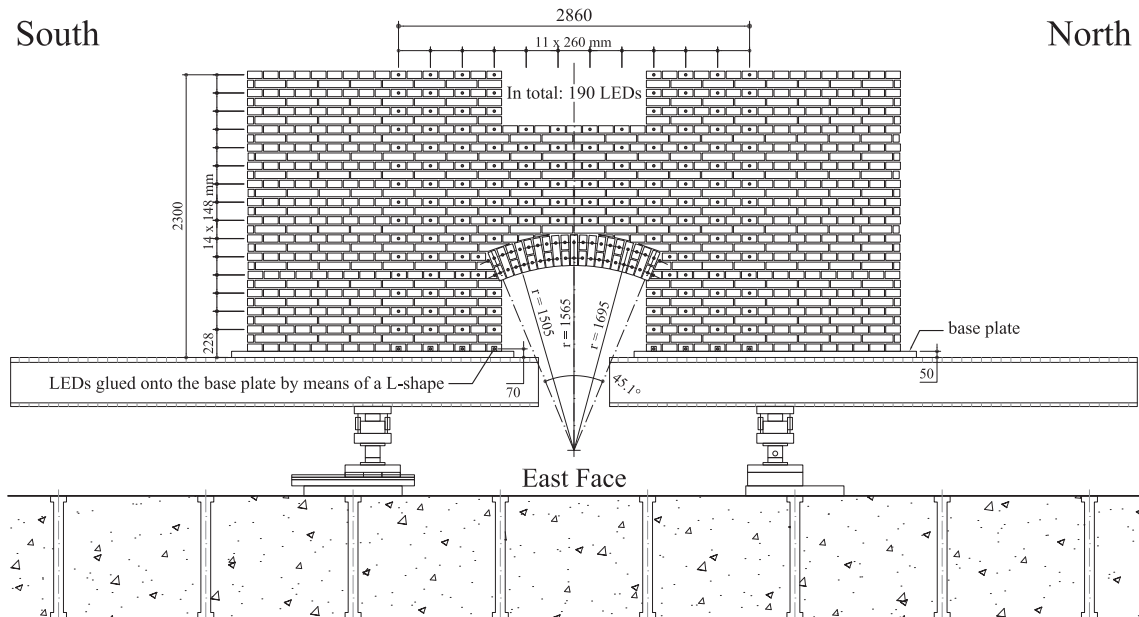


Figure 1.16: Layout of the LEDs on the East face of the test units with masonry arch (TUC and TUD). All dimensions in [mm].



Figure 1.17: Test setup including Optotrak position sensor. View from the North-East.

1.4 Testing procedure

Only cyclic tests were carried out on the masonry spandrels (see Table 1.1) and the applied loading history corresponded exactly to the loading history used to test the composite spandrels (see Section 1.4 of Part II). The only difference consisted in splitting Load Step 1 (LS 1) in two parts: During LS 1a the vertical rods applying the axial load on the piers were post-tensioned while during LS 1b the horizontal rods restraining the axial elongation of the spandrel were post-tensioned. For the sake of completeness and despite this similarity, the testing procedure for the masonry spandrels is presented again in the following paragraphs.

Testing of one test unit took between 2 and 4 days (excluding the day when the axial loads were applied). For each test unit the testing days and the load steps covered during each day are given at the beginning of the section "test observations".

The cyclic loading scheme followed different steps of storey drifts in displacement control. Force-controlled load steps, which are often used at the beginning of quasi-static cyclic tests of RC elements, were not applied. Force-controlled load steps are typically used to determine a yield displacement, which forms the basis of the step-wise increase of the displacement amplitude in the ensuing displacement-controlled cycles. Determining a yield displacement is already difficult and ambiguous for RC elements; it is even less clear for URM elements. For this reason the loading history was solely controlled by different storey drift levels and the applied storey drift levels were the same for all test units. The storey drift corresponds to the rotation of the two lever beams, which were approximately identical throughout the test. The rotation of the lever beams were determined by means of the LVDTs mounted underneath the lever beams (see Section 1.3.1).

As already mentioned, the loading scheme was cyclic and for each amplitude level two cycles were run. The considered amplitudes of the half-cycles corresponded to following storey drift levels: 0.025%, 0.05%, 0.1%, 0.2%, 0.3%, 0.4%, 0.6%, 0.8%, 1.0%, 1.5%, 2.0%, 2.5%, 3.0% and 4.0%. A schematic figure of this loading scheme is shown in Fig. 1.18 while Table 1.4 summarises the load step (LS) numbers for each drift level of the loading history. A load step corresponds to a peak of one half-cycle of the loading history. The numbering of the drift-controlled load steps commences with LS 2. LS 0 refers to the state before any rotations or axial forces were applied (see Section 1.2). Afterwards, the axial load was applied to the piers (LS 1a) and the rods restraining the axial elongation of the spandrel were post-tensioned (LS 1b). Up to LS 1b the lever beams were not rotated and hence their rotation was for any practical purpose zero. Next, the actuators were connected to the lever beams. To do so, the actuator pistons were driven downwards until the swivel bases were force-locked. The latter were then bolted onto the lever beams and the temporary supports below the lever beams were removed. The lever beams could now be rotated by the actuators. Table 1.4 also gives the velocities with which the actuator rods were moved ("loading velocity"). Small values were chosen for the loading velocity in order to avoid any dynamic effects, to allow time for re-adjusting the axial force applied to the piers and to record sufficient data points with the hard-wired channels. The recording frequency of 0.5 Hz for the hard-wired channels was given by the capacity of the data acquisition system.

At each load step the loading was stopped, the cracks were marked with a black pen and photos were taken. Observations concerning the development of the crack pattern were noted down. Additionally, LED measurements were performed over a period of about one minute. During

Table 1.4: Masonry spandrels: Load steps of cyclic loading history.

Storey drift	LS	Loading velocity [mm/min]
0.025%	2-5	0.3
0.05%	6-9	0.6
0.1%	10-13	0.9
0.2%	14-17	1.2
0.3%	18-21	1.8
0.4%	22-25	2.4
0.6%	26-29	3.6
0.8%	30-33	4.8
1.0%	34-37	6.0
1.5%	38-41	9.0
2.0%	42-45	12.0
2.5%	46-49	15.0
3.0%	50-53	18.0
4.0%	54-57	18.0

testing the same overall picture was taken continuously at about 2 minutes intervals. At the end of a testing day, the rotation of the lever beams was reduced until the forces in the two actuators were approximately equal. The temporary supports of the lever beams were reinstalled, the swivel bases unbolted from the lever beams, the actuator pistons pulled-in and the actuators switched off. The valves controlling the pressure in the hollow core jacks were closed and the load followers switched off. Overnight the axial load acting on the piers and on the spandrels reduced only slightly due to negligible leaking of the hydraulic system.

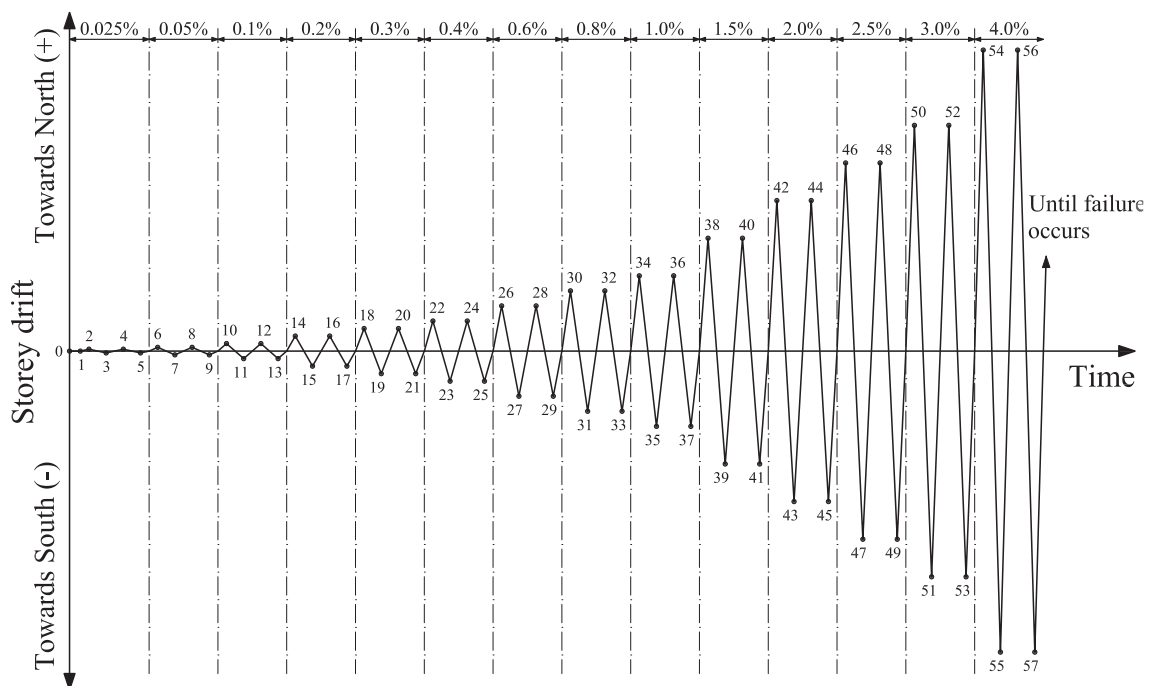


Figure 1.18: Loading history for cyclic loading.

2 Material tests for masonry spandrels

Parallel to the quasi-static tests on the four test units representing spandrels in old buildings, material tests on mortar, brick and masonry were carried out. In addition, for the test units TUA and TUB the timber beams used for the lintels was tested. For TUB also tension tests on the threaded rod, with which the horizontal restraint was applied, were carried out. Table 2.1 summarises the construction and testing dates for the four test units and the corresponding material tests. If the material tests were carried out on several days, only the date of the first day is given. For the quasi-static cyclic tests on the spandrel test units the age at the Day-of-Testing (DoT) refers to the age of the test unit at the first day of testing. The first day of testing started with connecting the actuators to the lever beams.

Table 2.1: Construction dates of TUA-TUD and dates when spandrel test units and material samples were tested.

Element	TUA	TUB	TUC	TUD
<i>Spandrel test units</i>				
Spandrel type	Timber lintel	Timber lintel	Masonry arch	Masonry arch
Type of loading	cyclic	cyclic	cyclic	cyclic
Construction	13+14.8.2009	17+18.8.2009	27-29.10.2009	23-26.10.2009
Testing	30.09-08.10.2009	04-06.11.2009	21+23.12.2009	13-15.1.2010
Age at DoT [d]	48	79	55	82
<i>Mortar</i>				
Material tests	09.10.2009	09.11.2009	15.12.2009	12.1.2010
Age at day of material test [d]	57	84	49	81
<i>Bricks</i>				
Material tests	17.11.2009	17.11.2009	17.11.2009	17.11.2009
<i>Wallettes - Compression tests</i>				
Construction	19.08.2009		29.10.2009	
Testing	12.01.2010		08.01.2010	
Age at day of material test [d]	146		71	
<i>Wallettes - Shear tests</i>				
Construction	19.08.2009		29.10.2009	
Testing	25.11.2009		02.12.2009	
Age at day of material test [d]	98		34	
<i>Timber beams</i>				
Material tests	25.01.2010	25.01.2010	-	-
<i>Threaded steel bars</i>				
Material tests	-	20.01.2010	-	-

2.1 Mortar

For the construction of the test units TUA-TUD a ready-mixed mortar was used. Fresh mortar was delivered to the structural laboratory, where the test units were built, every morning. The type

2. Material tests for masonry spandrels

of mortar was labelled as M10. The mortar contained 280 kg/m³ cement (CEM II/A-LL 42.5 N). The testing procedure used for the mortar was the same as for the first five test units on masonry spandrels with RC beams (Part II, Section 2.3.1). For completeness it is, however, repeated here.

2.1.1 Testing procedure

During the construction of each spandrel several samples of the mortar were taken and moulds with dimensions of 40x40x160 mm filled. The mortar was compacted by lifting alternately one side of the mould by a couple of centimeters and letting it fall down. The mortar was stored in a climatised room (20°C, 95% humidity) for one day and then together with the test units in the structural laboratory.

For each prism the density and the tensile strength f_{ctm} were determined. The tensile strength was determined from a 3-point-bending test with a loading velocity of 0.05 kN/s and a clear span of 100 mm. The tensile strength is computed as the stress at the edge of the prism assuming a linear stress profile at the peak strength obtained during the test. The prisms broke approximately in half. With the two halves cube tests with a loading velocity of 0.6 MPa/s were performed and the cube strength f_{cm} determined. The material tests on the mortar samples were performed at about the same time as the spandrels and the masonry wallettes, respectively, were tested (see Table 2.1).

2.1.2 Test results

The mechanical properties of the mortar samples are summarised in Table 2.2. The field "Age" refers to the age at the day of the tests on the prisms and cubes. The wallettes comprise both the wallettes used for compression tests (Section 2.3) and the wallettes used for the shear tests (Section 2.4). The mortar used for the construction of TUC and TUD had a considerably larger strength than the mortar used for TUA and TUB. When ordering the mortar, a mortar of class M10, i.e. with a characteristic strength of 10 MPa had been ordered. From the test results, however, it appeared that the mortar delivered for TUC and TUD corresponded to a mortar M15.

Table 2.2: Mortar tests for TUA-TUD and masonry wallettes: Mechanical properties of mortar (mean values and standard deviations).

Test unit / Walette	# prisms	# cubes	Age [d]	Density [kg/m ³]	f_{ctm} [MPa]	f_{cm} [MPa]
TUA	18	36	57	1650 ± 33	3.34 ± 0.25	11.2 ± 1.6
TUB	15	30	84	1650 ± 61	3.42 ± 0.55	13.0 ± 2.8
TUC	12	24	49	1710 ± 35	4.25 ± 0.34	17.9 ± 3.3
TUD	15	30	81	1720 ± 42	4.46 ± 0.37	20.3 ± 2.8
Wallettes TUA+TUB	3	6	84	1620 ± 8	3.74 ± 0.44	14.4 ± 1.9
Wallettes TUC+TUD	6	12	49	1730 ± 13	4.30 ± 0.17	16.5 ± 2.5

2.2 Bricks

For the construction of the masonry spandrels, full bricks with the standard format 120x250x60 mm were used. The bricks were manufactured by Keller Ziegeleien in Pfungen (Switzerland) and are normally used for the construction of chimneys ("Kaminsteine").

2.2.1 Testing procedure

Brick samples were taken from different pallets used for the construction of the spandrels. For each of the spandrels four sample groups of three to four bricks were taken. With these groups of three or four bricks two different types of tests were carried out:

- From each group of bricks one brick was cut down to a sample with the dimensions 40x40x160 mm, i.e. a prism with the same size as the mortar samples. On these brick prisms the same type of tests as on the mortar sample were conducted, i.e. a 3-point-bending test for determining f_{ctb} and compression tests for determining f_{cb} . Photos of the test setup are shown in Fig. 2.1.
- In addition, from each group of bricks two or three bricks were tested in their longitudinal direction taking Demec measurements at different stages of loading (Fig. 2.2). The base length of the vertical and horizontal measurements was 150 mm and 100 mm, respectively. Demec points were glued onto the front and back faces of the brick and the obtained strains averaged. From these Demec measurements the E-Modulus as well as the Poisson's ratio were determined. The brick was then loaded until failure and the compressive strength computed. To ensure an even load introduction into the brick the top and bottom faces of the bricks had been machine grinded and were therefore even and parallel.

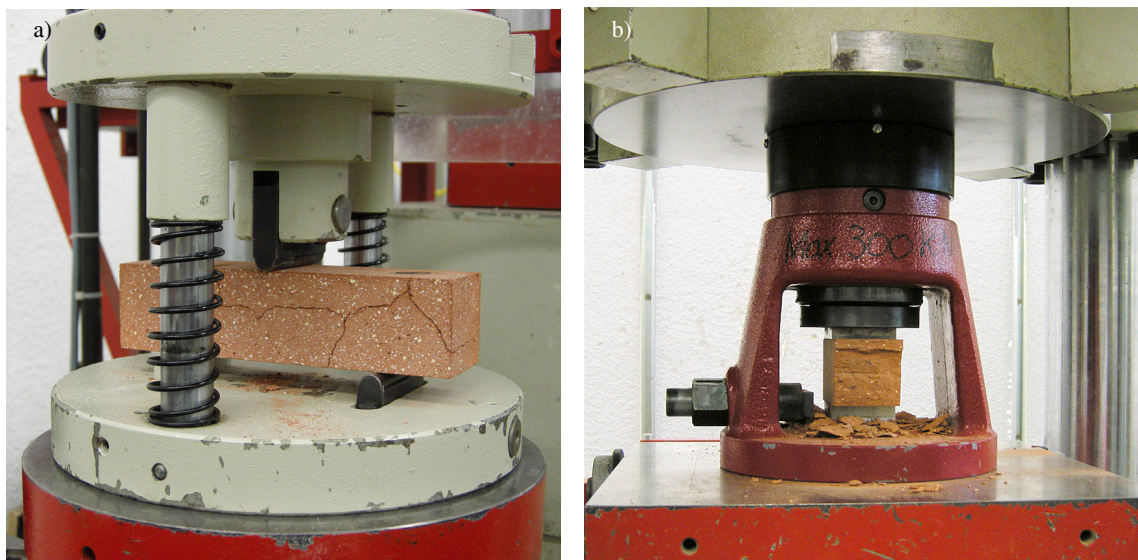


Figure 2.1: Material tests on brick prisms: 3-point-bending test (a) and cube compression test (b).

2. Material tests for masonry spandrels

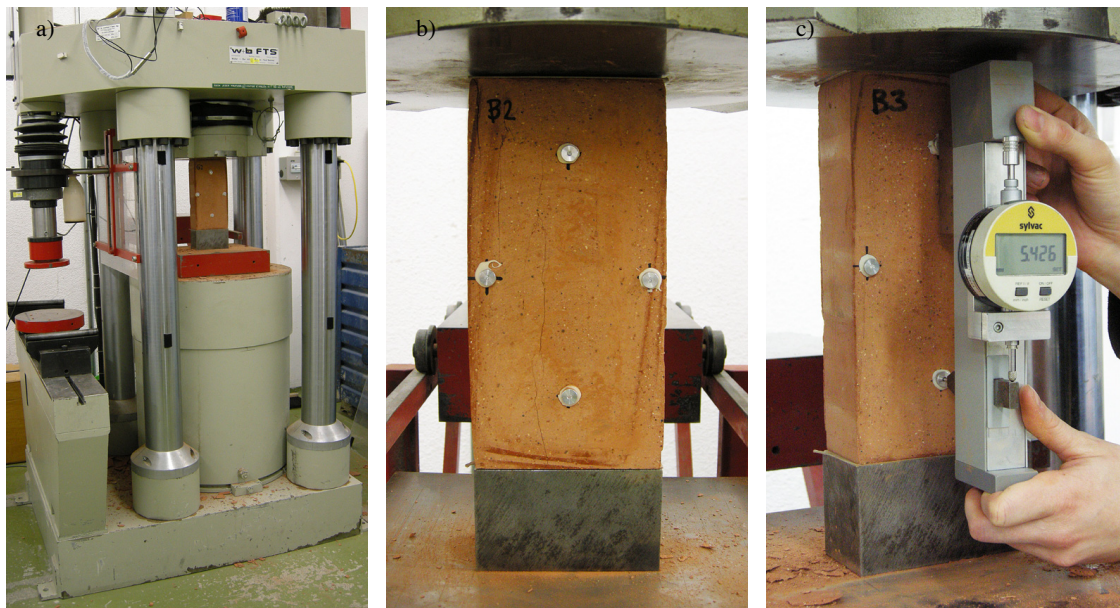


Figure 2.2: Compression tests on whole bricks: Test setup (a), brick with Demec points (b), and manual Demec measurement (c).

2.2.2 Test results

Cutting down the bricks to prisms of 40x40x160 mm revealed the internal crack pattern of the bricks. Differences were observed between the bricks used for the construction of TUA and TUB and those used for the construction of TUC and TUD. The latter tended to have more and wider cracks (Figs. 2.3 and 2.4) leading to a larger variation of obtained tensile strengths (Table 2.3). Both, density and tensile strength are smaller for TUC and TUD than for the first two test units TUA and TUB. For the compressive strength the picture is less clear, however, in average it is also larger for TUA and TUB than for TUC and TUD. These findings suggest that the quality of the bricks used for the first two test units was better than for the final two test units resulting in more homogenous and higher strength values. This is also confirmed by the histograms of the tensile and compressive strength shown in Fig. 2.5: For TUA and TUB the distribution is narrower than for TUC and TUD with a clear concentration towards the median value.

Table 2.3: Brick tests: Mechanical properties of bricks obtained from tests on prisms (median values and standard deviations).

Test unit	# prisms	# cubes	Density [kg/m ³]	f_{ctb} [MPa]	f_{cb} [MPa]
TUA	4	8	1890 ± 5	8.48 ± 0.54	78.6 ± 6.48
TUB	4	8	1890 ± 5	7.02 ± 1.58	58.5 ± 18.5
TUC	4	8	1830 ± 7	6.45 ± 3.65	38.9 ± 12.4
TUD	4	8	1840 ± 30	5.02 ± 3.36	75.3 ± 24.6

Figure 2.6 shows that the compressive and tensile strengths obtained from the brick prisms were basically uncorrelated. For this plot one compressive strength value was computed for each prisms



Figure 2.3: Brick prisms for TUA (Prisms 1-4) and TUB (Prisms 4-8).

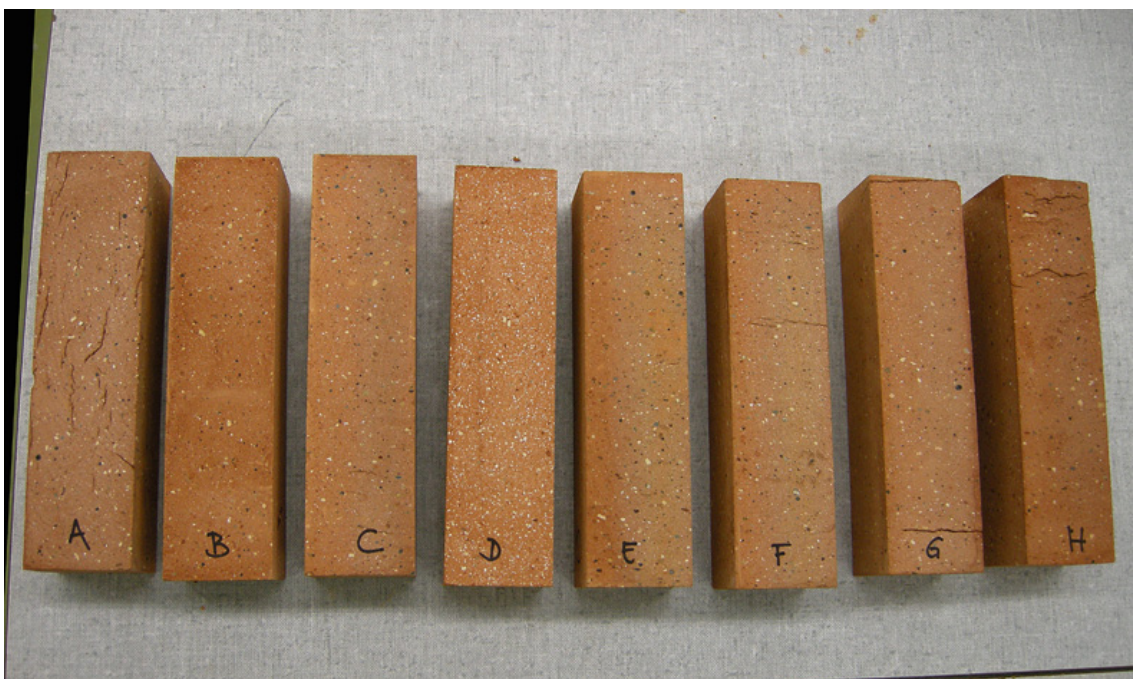


Figure 2.4: Brick prisms for TUC (Prisms E-H) and TUD (Prisms A-D).

2. Material tests for masonry spandrels

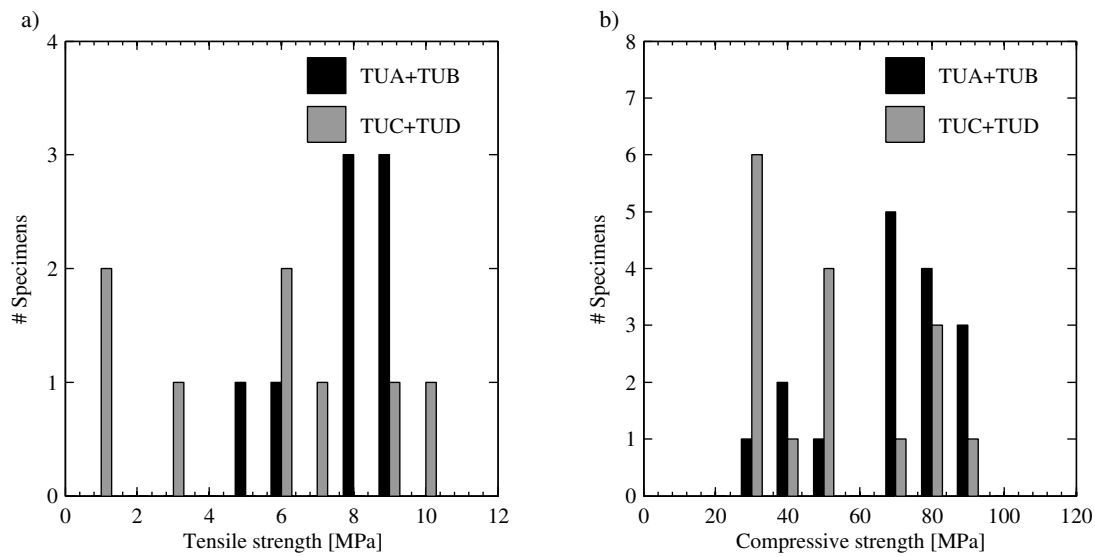


Figure 2.5: Distribution of obtained strength values for material tests on brick prisms: 3-point-bending test (a) and cube compression test (b).

by averaging the values obtained from the two cube tests. Figure 2.7 shows two examples of the 3-point-bending tests after failure of the specimen. In the first case (Fig. 2.7a) the crack pattern within the prism influenced the rupture of the brick while in the second case the prism appeared relatively homogenous leading also to a higher tensile strength (Fig. 2.7b).

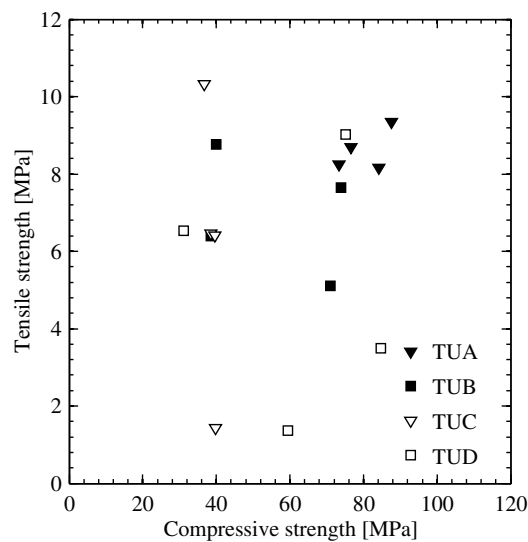


Figure 2.6: Correlation of obtained tensile and compressive strength values for material tests on brick prisms.

In the second group of tests whole bricks were subjected to monotonically increasing compression in their longitudinal direction. The loading was applied with a velocity of 0.3 MPa/s. For determining the E-Modulus and the Poisson's ratio, Demec measurements were taken once a

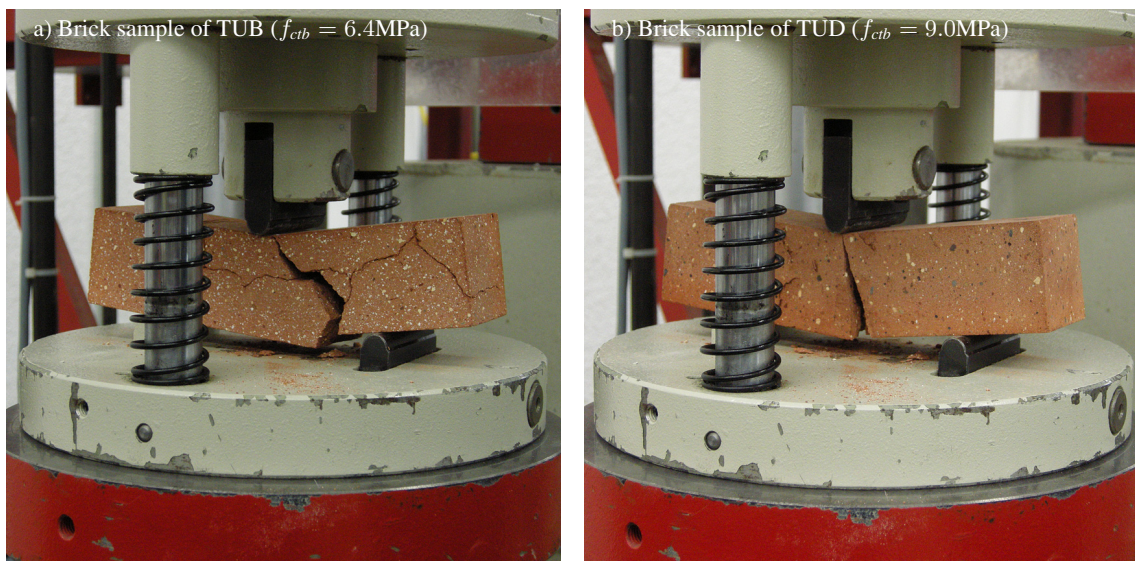


Figure 2.7: Two examples of crack patterns obtained from bending tests on brick prisms: Brick sample of TUB (a) and of TUD (b).

small precompression (approximately 3 kN) and again when a force corresponding to about 1/3 of the compressive strength were applied. To do so, the approximate compressive strength had to be determined first. For TUC and TUD three brick samples per batch were available while for TUA and TUB only two brick samples per patch were left over. For this reason, one brick of the eight batches belonging to TUC or TUD were tested first and the average compressive strength determined. For these eight samples no Demec measurements were taken. From these tests a median strength of 30.7 MPa was determined, corresponding for an average cross section area of 60x120 mm to 221 kN. In a second step, the second and third brick of each batch of TUC and TUD were tested taking Demec measurements at approximately 3 and 74 kN. Demec measurements were taken approximately half a minute after the loading was stopped to allow the brick to stabilise. After the Demec measurements at 74 kN, loading was continued until failure of the brick. A typical failure mode is shown in Fig. 2.10b. When testing the bricks belonging to TUC and TUD vertical cracks formed in some cases before a load of 74 kN was reached. This led to unrepresentative large Poisson's ratios, which were not considered when evaluating the test data. For this reason, when testing the bricks belonging to TUA and TUB, Demec measurements were also taken at approximately 30 kN, which corresponds to approximately $10\%f_{cb}$. Table 2.4 summarises the density, compressive strength, E-Modulus and Poisson's ratios obtained from the test on whole bricks. For TUA and TUB, eight bricks each were tested (two bricks from four batches). For TUC and TUD, the density and the compressive strength were determined from twelve bricks each (three bricks from four batches), while the E-Modulus and the Poisson's ratio were also determined from eight bricks (two bricks from four batches). TUA and TUB have almost identical properties. The compressive strength of TUC and TUD is slightly lower than that of TUA and TUB, while the E-Modulus of TUC is slightly above and that of TUD slightly below that of TUA and TUB.

As expected, the compressive strengths obtained from the tests on whole bricks are significantly lower than those obtained from the tests on the cubes with 40 mm side length (Fig. 2.8b). The

2. Material tests for masonry spandrels

strength values obtained from the tests on whole bricks ($f_{cb} = 30 - 36$ MPa) seem reasonable when compared with cylinder strength values of normal concrete. The E-Modulus of the bricks is, however, significantly lower than that of normal concrete.

Table 2.4: Brick tests: Mechanical properties of bricks obtained from compression tests on whole bricks (median values and standard deviations).

Test unit	Density [kg/m ³]	f_{cb} [MPa]	0 – 33% f_{cb}		0 – 10% f_{cb}	
			E_b [GPa]	ν_b [-]	E_b [GPa]	ν_b [-]
TUA	1880 ± 30	36.2 ± 5.3	10.8 ± 0.9	0.17 ± 0.06	11.7 ± 0.9	0.10 ± 0.08
TUB	1880 ± 6	35.5 ± 4.6	10.8 ± 1.6	0.14 ± 0.20	11.7 ± 2.9	0.07 ± 0.10
TUC	1840 ± 28	31.3 ± 10.0	11.1 ± 0.7	0.12 ± 0.09	-	-
TUD	1840 ± 52	30.2 ± 5.3	8.4 ± 2.5	0.28 ± 0.34	-	-

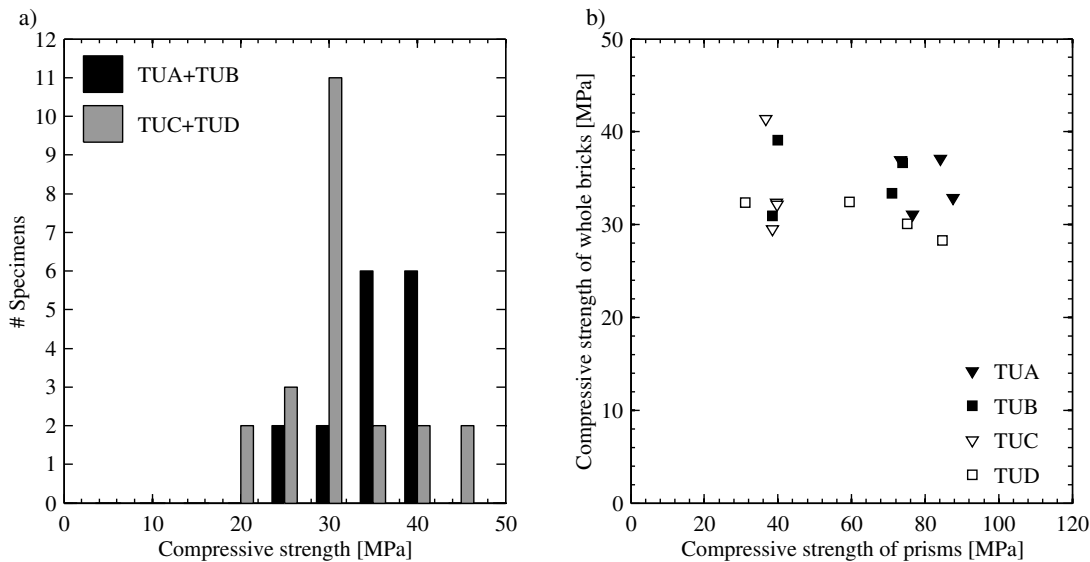


Figure 2.8: Distribution of obtained compressive strength values for material tests on whole bricks (a) and correlation of compressive strength obtained for whole bricks and brick prisms (b).

The E-Modulus determined from the Demec measurements at 3 and 30 kN (0 – 10% f_{cb}) is approximately 8% larger than the E-Modulus obtained from the Demec measurements at 3 and 74 kN (0 – 33% f_{cb}) (see Fig. 2.11a). Unexpectedly, the Poisson's ratios obtained for the lower load range vary significantly more than those obtained for the larger load range (Fig. 2.11b). The values given in Table 2.4 are median values to avoid an undue effect of outliers on E-Modulus and Poisson's ratio due to premature cracking of the bricks. For the density and the compressive strength median and mean values are very similar.

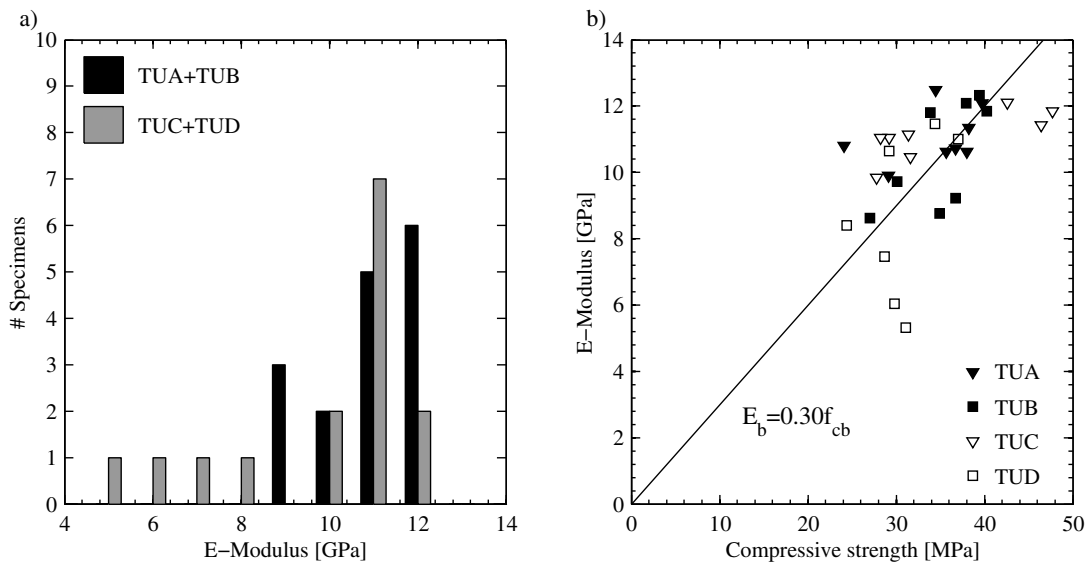


Figure 2.9: Tests on whole bricks: Distribution of obtained E-Modulus values (0 – 33% f_{cb}) (a) and correlation of compressive strength and E-Modulus (b).

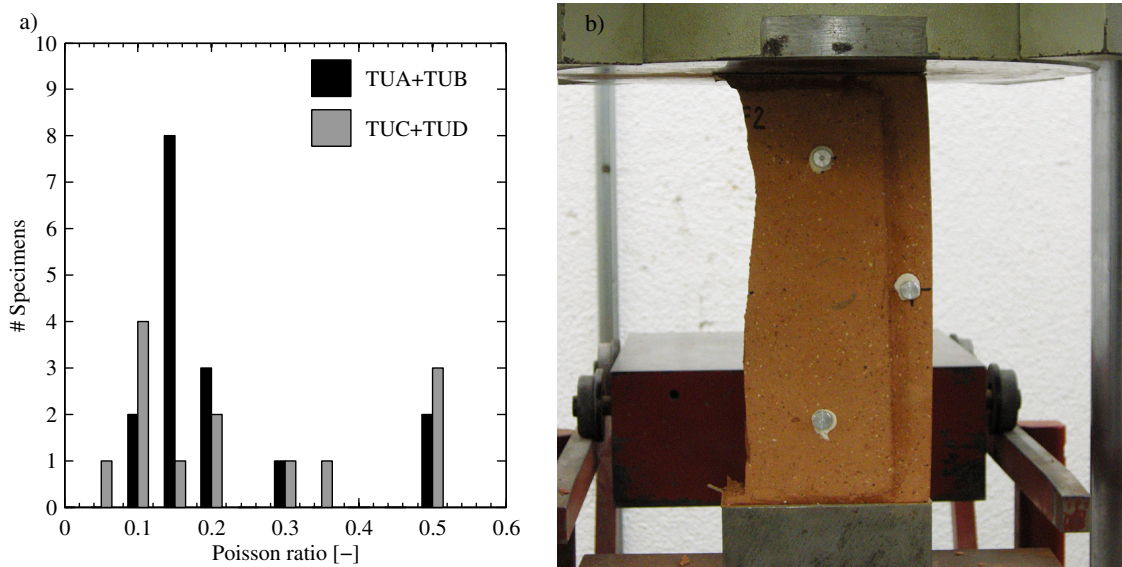


Figure 2.10: Tests on whole bricks: Distribution of obtained Poisson's ratio (0 – 33% f_{cb}) (a) and typical failure mode (b).

2. Material tests for masonry spandrels

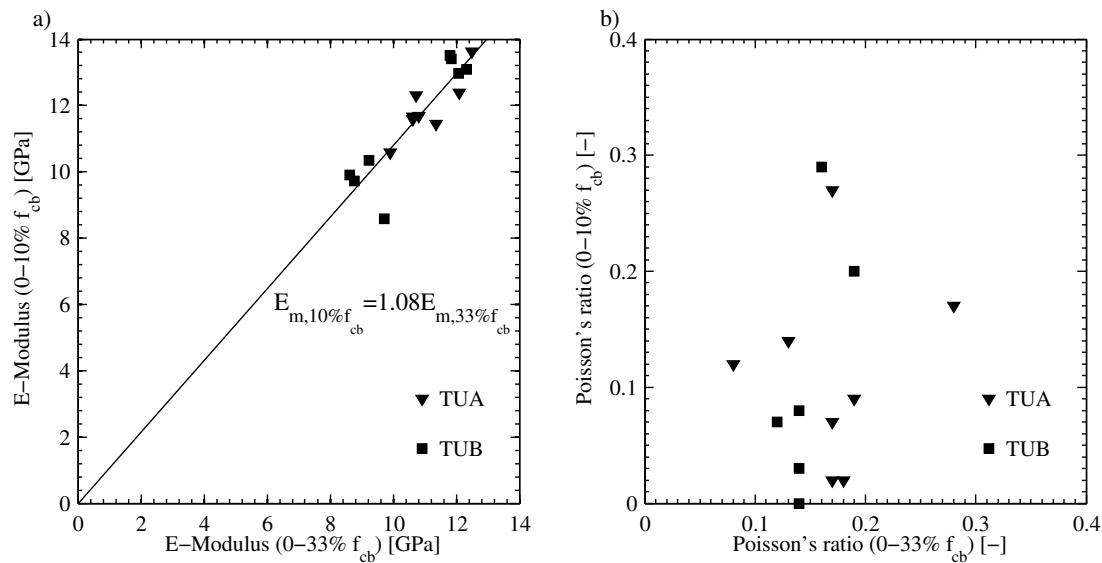


Figure 2.11: Tests on whole bricks: Correlation of E-Modulus (a) and Poisson's ratio (b) obtained as secant values between 0 – 33% f_{cb} and 0 – 10% f_{cb} .

2.3 Compression tests on masonry wallettes

In Sections 2.1 and 2.2 the strengths of mortar and bricks were determined. In this section, the compressive strength of masonry is determined by testing small wallettes. The tests were conducted according to [CEN02a]. The wallettes consisted of seven bricks and six mortar layers. The size of the test units is therefore approximately 120x250x500 mm. For TUA+TUB and TUC+TUD six wallettes each were built (i.e. twelve in total). The wallettes representing TUA+TUB and TUC+TUD were labelled CM1-6 and CMA-F, respectively.

2.3.1 Test setup and testing procedure

The tests were performed in a Schenk ± 1600 kN universal testing machine (Fig. 2.12). The top reaction plate is supported by a free spherical cap ensuring a central load application on the wallette. The base plate, which is the moving plate during the loading process, is always horizontal. The wallette is placed at the centre of the base plate. Four LVDTs, two on each side, are mounted so that they cover the central two bricks and two mortar layers. The base length of these measurements varied between 145 and 149 mm. The top and bottom faces of the wallettes of TUC+TUD had been grinded to ensure an even load introduction. For the wallettes of TUA+TUB this had not been done. Cardboard layers were used instead to avoid stress concentrations. In some cases minor spalling took place at the top and bottom bricks. However, it is believed that this did not affect the global failure of the wallette which was controlled by the central bricks and mortar layers. The load was applied in two steps: First a load of 20 kN was applied at a rate of 2.0 mm/min; then the load rate was reduced to 0.4 mm/min. From the instance when 20 kN were reached it took in average 13 minutes until failure of the unit occurred.



Figure 2.12: Compression tests on masonry wallettes: Global view of the test setup (a) and detail of a wallette with the instrumentation (b).

2.3.2 Failure modes

The onset of softening of the test unit was caused by vertical splitting cracks in the most central bricks. More cracks formed and some crushing of the mortar layers occurred until the unit failed. Failure occurred typically within the 3 – 5 central bricks. The bricks that were in contact with the testing machine did not fail and showed just in some cases spalling at the edges of the bricks when the bricks had not been ground. The central bricks, which had failed, were on the contrary fragmented in several pieces (Fig. 2.13). For all units except CM4-6 the crack patterns at the end of the test are shown in Fig. 2.14 and 2.15; for CM4-6 the photos are unfortunately out of focus.

2.3.3 Test results

From these tests the compressive strength and the E-Modulus were determined. The compressive strength was calculated as the maximum force divided by the nominal area of the wallette (250x120 mm). The E-Modulus was determined as the secant value between a stress of 1.0 MPa and $f_{cm}/3$. For two test units no E-Modulus was computed: (i) CMA was the first unit to be tested. Since such tests had not been performed before in this laboratory, no LVDTs were mounted on the wallette to avoid damage to the instruments in case of a very brittle and explosive failure mode. (ii) CM3 broke in three pieces when lifting it onto the test stand (the mortar joints including one of the two central joints failed). Despite this, the unit was tested. However, the unit was significantly softer, most likely because the position of the bricks had slightly shifted and therefore crushing of small mortar grains caused a softer behaviour (see Fig. 2.16a). The E-Modulus obtained from this tests was therefore not used.

2. Material tests for masonry spandrels

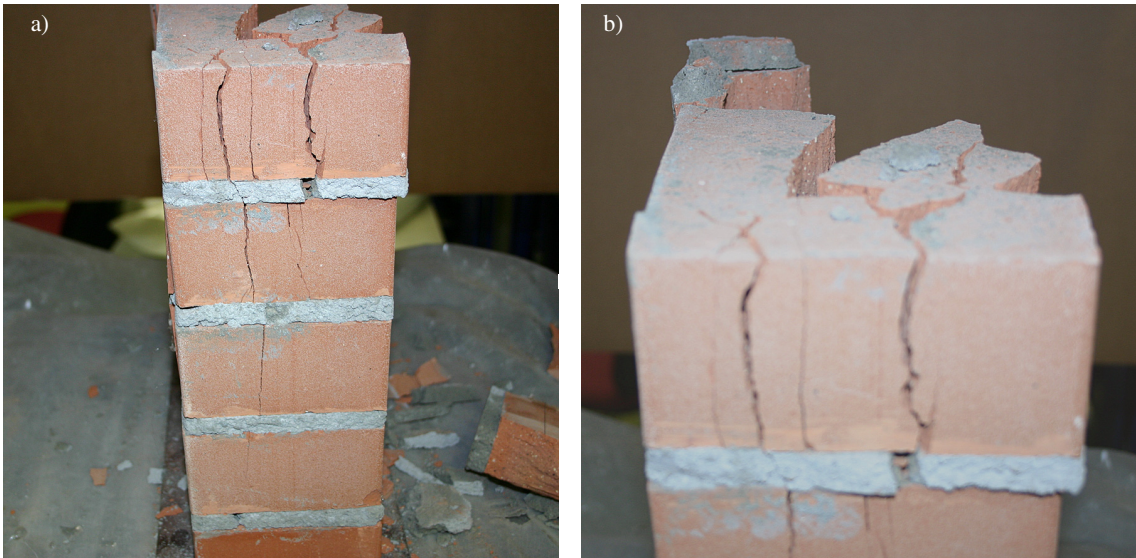


Figure 2.13: Compression tests on masonry wallettes: Fragmented bricks after failure.



Figure 2.14: Compression tests on masonry wallettes: Crack pattern after failure for units CM1-CM3.

Table 2.5 summarises the obtained compressive strength and the E-Modulus values for the individual test units. It shows that both compressive strength and E-Modulus were larger for the units representing TUA+TUB than for the units representing TUC+TUD. This is inline with the finding that the tensile strength of the bricks used for the TUC+TUD wallettes was smaller than the tensile strength of the bricks for the TUA+TUB wallettes (Table 2.3 and 2.4). The mortar strength showed an opposite tendency (the mortar of TUC/TUD wallettes was stronger than the mortar for TUA+TUB wallettes, Table 2.2). However, the observations showed that the failure was mainly associated with a tensile failure of the bricks and not with crushing of the mortar. The E-Modulus, on the other hand, seems related to the masonry strength (Fig. 2.17), though the scatter is significant.

2.3. Compression tests on masonry wallettes



Figure 2.15: Compression tests on masonry wallettes: Crack pattern after failure for units CMA-CMF.

2. Material tests for masonry spandrels

Table 2.5: Compression tests on masonry wallettes: Compressive strength f_{cm} and E-Modulus E_{cm} .

TUA+TUB	f_{cm} [MPa]	E_{cm} [GPa]	TUC+TUD	f_{cm} [MPa]	E_{cm} [GPa]
CM1	19.7	15.2	CMA	16.0	—
CM2	19.0	17.5	CMB	15.7	9.9
CM3	17.5	—	CMC	16.4	8.0
CM4	17.6	14.2	CMD	12.7	6.2
CM5	19.8	9.7	CME	10.2	13.2
CM6	14.5	9.7	CMF	16.8	7.6
Mean	18.0	13.2	Mean	14.7	8.9
Median	18.3	14.2	Median	15.9	8.0
Stdev	2.0	3.5	Stdev	2.6	2.8

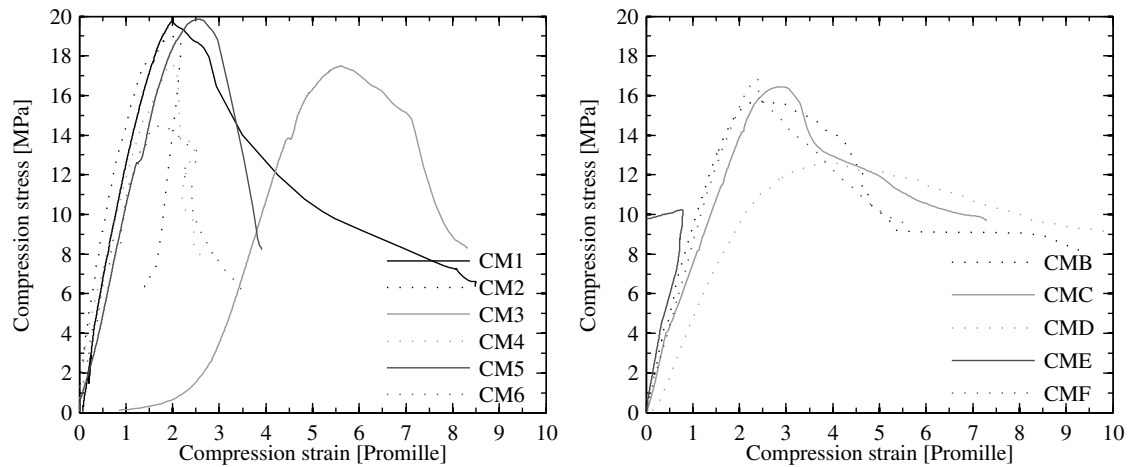


Figure 2.16: Compression tests on masonry wallettes: Stress-strain relationships for TUA and TUB (a) and TUC and TUD (b).

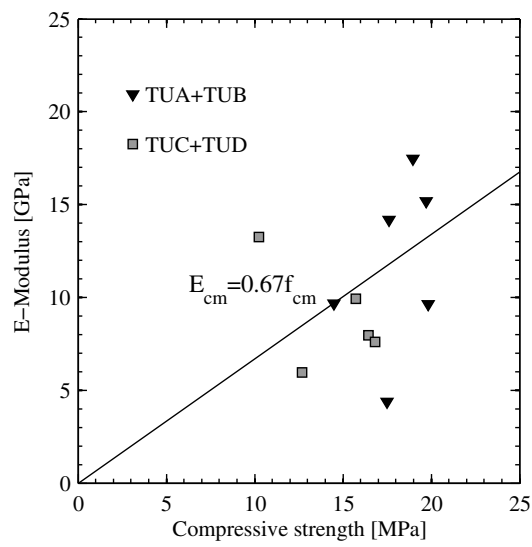


Figure 2.17: Compression tests on masonry wallettes: Relationship between compressive strength and E-Modulus.

2.4 Shear tests on masonry wallettes

To gain information on the shear resistance of the mortar joints, small masonry wallettes consisting of three bricks and two mortar joints were tested according to EN1052-3 [CEN02b]. For TUA+TUB and TUC+TUD twelve wallettes each were built. One of the wallettes for TUA+TUB and one of the wallettes for TUC+TUD were broken before the test and one other failed due to local brick failure (for a normal stress of 1.0 MPa, see comment in Section 2.4.1) so that in total $10 + 11 = 21$ wallettes were tested. The testing procedure was very similar to the procedure used for the shear tests on the large perforated bricks used for the construction of the composite spandrels (Part II, Section 2.6). For reasons of completeness it is repeated here.

2.4.1 Test setup and testing procedure

The tests were performed on a Schenk ± 480 kN universal testing machine (Fig. 2.18a). Figure 2.18b shows the support conditions of the wallette within the testing machine: At the base the wallette was supported at the inner edge of the outer bricks on two 4 cm wide aluminium blocks, which had the same length as the bricks (12 cm). At the top, two 2 cm wide aluminium blocks introduced the reaction force of the testing machine at the outer edges of the middle brick. Four LVDTs – two on each face – measured during the test the relative displacements between the outer and middle bricks (Fig. 2.18b).

The shear tests were conducted at three different normal stress levels, where normal refers to the direction perpendicular to the mortar joints. EN1052-3 [CEN02b] requires for bricks with a compressive strength larger than 10 MPa stress levels of 0.2 MPa, 0.6 MPa and 1.0 MPa. The compressive strength of the bricks is larger than 30 MPa (see Table 2.4). Although a thin mortar layer laid between the bricks and the aluminium blocks ensured a smooth load introduction, local brick failure occurred for normal stresses of 1.0 MPa. For this reason the shear tests were conducted at normal stress levels of 0.2 MPa, 0.4 MPa and 0.6 MPa, which corresponded to normal forces of 6.0 kN, 12.0 kN and 24.0 kN, respectively. The normal forces were applied by means of two D13 mm steel rods. A load follower (on the right of Fig. 2.18a) and two small hollow core jacks (on the right of Fig. 2.18b) ensured that the load remained approximately constant throughout the test. The force in the rods was monitored constantly by means of two compression load cells (on the left of Fig. 2.18b). A list of all instruments used for the shear tests is given in Table 2.6.

Table 2.6: Shear tests on masonry wallettes: List of hard-wired channels.

Channel name	Instrument type	Description of measured quantity
VE1	LVDT ± 10 mm	Vertical deformation, North LVDT on East face
VE2	LVDT ± 10 mm	Vertical deformation, South LVDT on East face
VW1	LVDT ± 10 mm	Vertical deformation, North LVDT on West face
VW2	LVDT ± 10 mm	Vertical deformation, South LVDT on West face
FORCE_1	Load cell	Compression load cell with a capacity of 150 kN
FORCE_2	Load cell	Compression load cell with a capacity of 150 kN
SHEAR_FORCE	Load cell	Force in the piston of the testing machine

The procedure for preparing the wallette and conducting the test was as follows:

- The top and bottom surface of the walette were levelled using a mortar layer with a thickness of a few millimetres to ensure a better bearing surface for the steel plates which were used to apply the forces normal to the bed joints.
- Load cells and steel rods were mounted and axial forces inducing the normal stress on the bed joints were applied by means of the two steel rods.
- The test unit was turned by 90 degrees and was then placed on the linear supports (bearing plates) with a width of 40 mm and a length of 120 mm (i.e. equal to the width of the brick). To achieve an introduction of the shear force with as little stress concentrations as possible, a cement paste was used to level the test unit on top of these bearing plates.
- Cement paste was applied to the top face of the central brick and the two supports with width of 20 mm and a length of 120 mm were placed. A small initial load was applied by the universal testing machine, in order to ensure that the top supports were parallel to the loading plate of the machine. In this way a uniform stress introduction could be achieved once the cement paste was hardened.
- Two LVDTs were mounted on each face of the test unit and the hard-wired measuring system was set up. All hard-wired measuring devices were set to zero.
- For the five final tests the two hollow core jacks were connected to a load follower, which kept the axial load approximately constant over the duration of the test.
- The shear force was applied moving the bottom head of the universal testing machine upwards. The tests were performed in displacement control. The initial rate of loading was 0.3 mm/min. This loading rate was maintained until the peak shear strength had been passed. The loading rate was then increased to 1.00 mm/min. The test was terminated at average shear displacements between 10 to 15 mm.

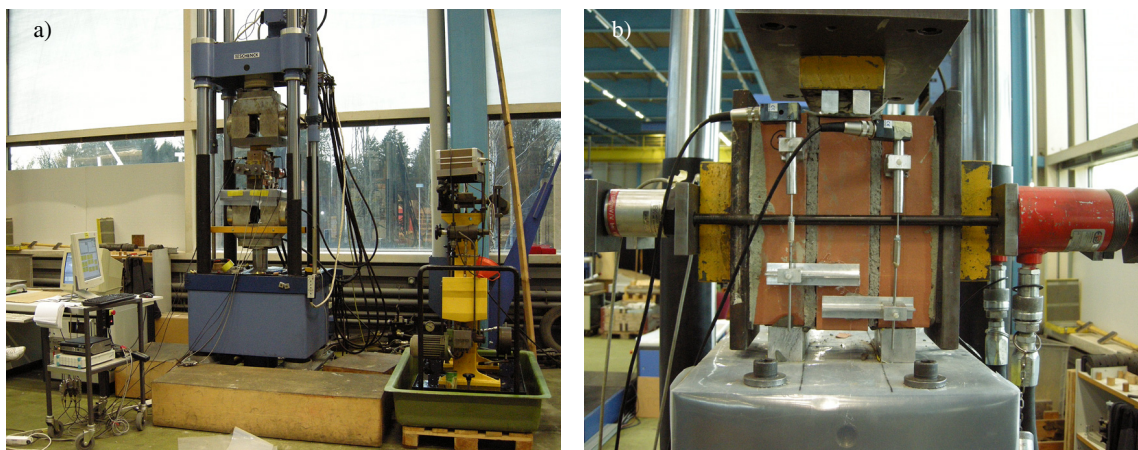


Figure 2.18: Shear tests: General test setup (a) and instrumentation of the walette (b).

2.4.2 Failure modes

At the beginning of the loading no cracks within the mortar joint were visible. Two distinct knocks indicated that the mortar joints had detached from the brick and that the initial cohesion was overcome. These knocks were accompanied by distinct drops in the shear stress and by the formation of a crack between mortar and brick. Note that the two knocks did not always occur at the same instant. For this reason two distinct drops of the shear stress were often recorded within

2. Material tests for masonry spandrels

the initial phase of the test. Deformations before these drops were typically very small and often not measured by the LVDTs. The cracks between mortar and brick were either along the inner or outer face of the mortar joint (e.g.2.19b); in some cases the crack changed along the length of the brick from one face to the other (e.g.2.19a) resulting in a nearly horizontal crack through the mortar. Cracks running entirely within the mortar joints were not observed. Once the cracks had formed the shear stress remained approximately constant and the test was ended when a shear displacement of approximately 15 mm was reached.

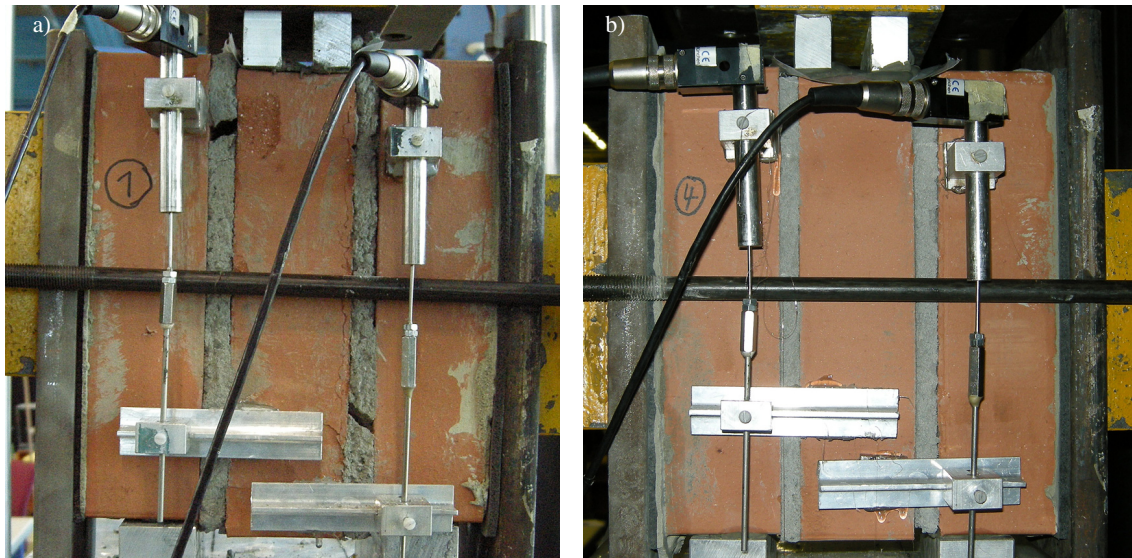


Figure 2.19: Shear tests: Two wallettes at the end of loading.

2.4.3 Test results

For all tests the peak and residual shear stress were determined. The shear stress was defined as the shear force divided by the gross cross section area of the two mortar beds (two times 250x120 mm). The peak shear stress was defined as the maximum shear stress measured while the residual shear stress was defined as the shear stress when the average shear displacement (i.e., the average measurement of the four LVDTs) reached 10 mm. The latter definition is somewhat arbitrary. However, once the cracks between mortar and bricks had formed, the shear stress remained in most cases fairly constant. Figures 2.20 and 2.21 show the stress vs. shear displacement relationships for all wallettes. The figures show that – despite the dilation of the mortar joints – the normal stress remained indeed relatively constant throughout the test. It also shows the two clear drops which are related to the formation of the cracks between mortar joints and bricks.

The peak and residual shear stress vs. normal stress couples are plotted in Fig. 2.22. The plots also include the best-fit Mohr-Coulomb relationships, for which the numerical values are summarised in Table 2.7. For the residual stress values two best-fit lines were determined, i.e. one with and one without a cohesion term. The following observations can be made:

- Both, for the wallettes of TUA+TUB and TUC+TUD, the peak values show a significantly larger scatter than the residual values. This is also reflected in the correlation coefficients of the best-fit Mohr-Coulomb relationships.
- The peak cohesion c_{max} for TUC+TUD is only about half as large as the cohesion for TUA+TUB despite the fact that tensile strength of the mortar used for the wallettes of TUC+TUD was larger than the tensile strength of the mortar used for the wallettes of TUA+TUB (Table 2.2).
- For the wallettes of TUC+TUD one peak stress at $\sigma = 0.6$ MPa is significantly larger than the peak stress obtained for three other wallettes. If this peak stress is discarded, the best-fit Mohr-Coulomb relationship changes from $\tau_{max} = 0.93\sigma + 0.12$ MPa (solid line) to $\tau_{max} = 0.73\sigma + 0.18$ MPa (dashed line).
- For the residual values the cohesion term is very small and negative; for this reason it is suggested to neglect it ($\tau_{res} = \mu_{res,2} \cdot \sigma$).
- The friction coefficients obtained for the peak and residual stress values are relatively similar.

Table 2.7: Shear tests: Friction coefficient μ , cohesion c and correlation coefficient R^2 for peak and residual shear stress.

Mohr-Coulomb relationship	μ [-]	c [MPa]	R^2 [-]
TUA + TUB			
Peak stress: $\tau_{max} = \mu_{max} \cdot \sigma + c_{max}$	0.85	0.35	0.59
Residual stress: $\tau_{res} = \mu_{res,1} \cdot \sigma + c_{res}$	0.78	-0.01	0.92
Residual stress: $\tau_{res} = \mu_{res,2} \cdot \sigma$	0.77	0	0.92
TUC + TUD			
Peak stress: $\tau_{max} = \mu_{max} \cdot \sigma + c_{max}$	0.93 (0.73) ¹⁾	0.12 (0.18)	0.73 (0.84)
Residual stress: $\tau_{res} = \mu_{res,1} \cdot \sigma + c_{res}$	0.75	-0.01	0.99
Residual stress: $\tau_{res} = \mu_{res,2} \cdot \sigma$	0.73	0	0.99

¹⁾ Test with largest peak shear stress deleted.

2. Material tests for masonry spandrels

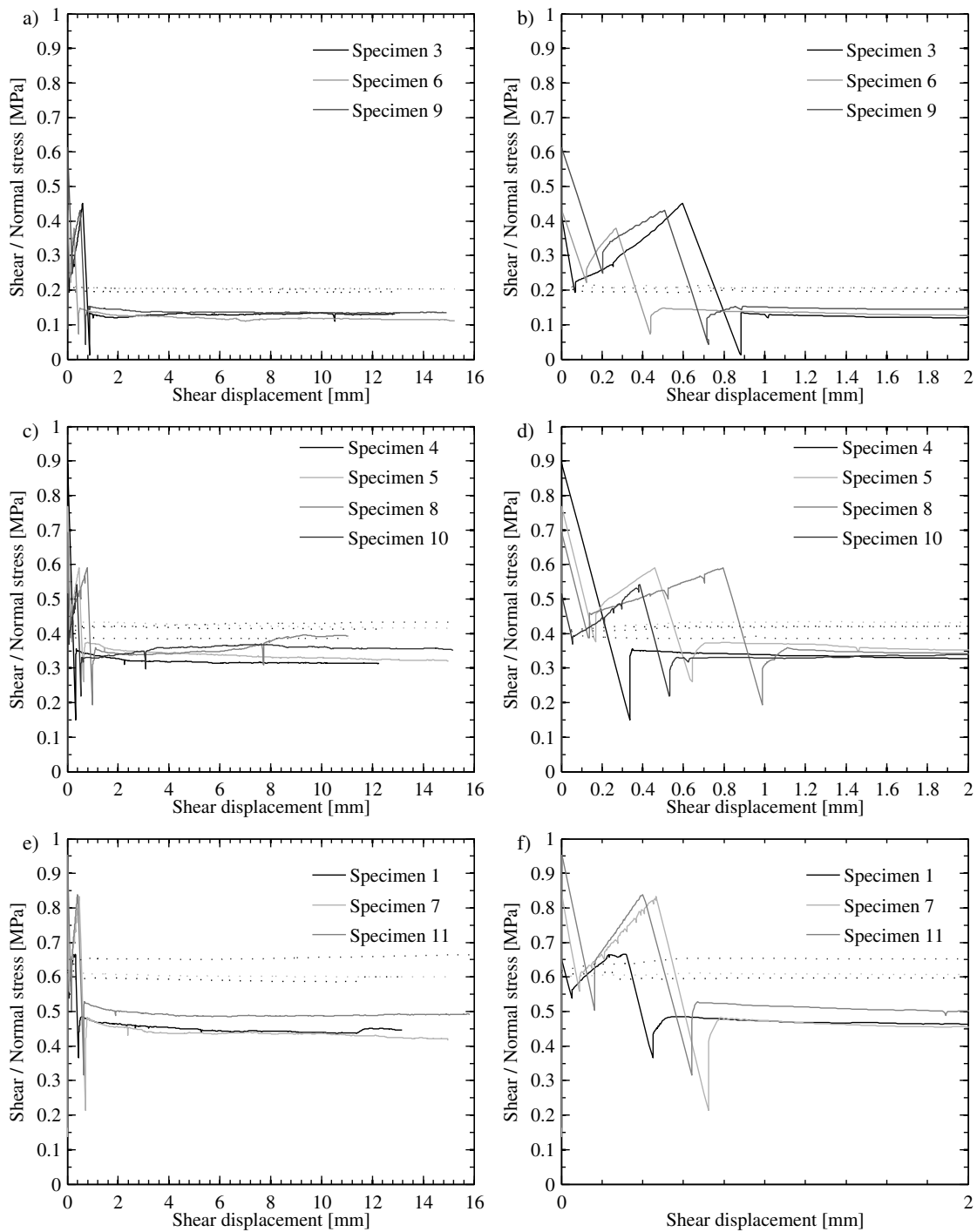


Figure 2.20: Shear tests for wallettes of TUA and TUB: Shear stress (solid lines) and normal stress (dotted lines) plotted against shear displacement. Full shear displacement range (a, c, e) and close-up of the displacement range between 0 and 2 mm (b, d, f).

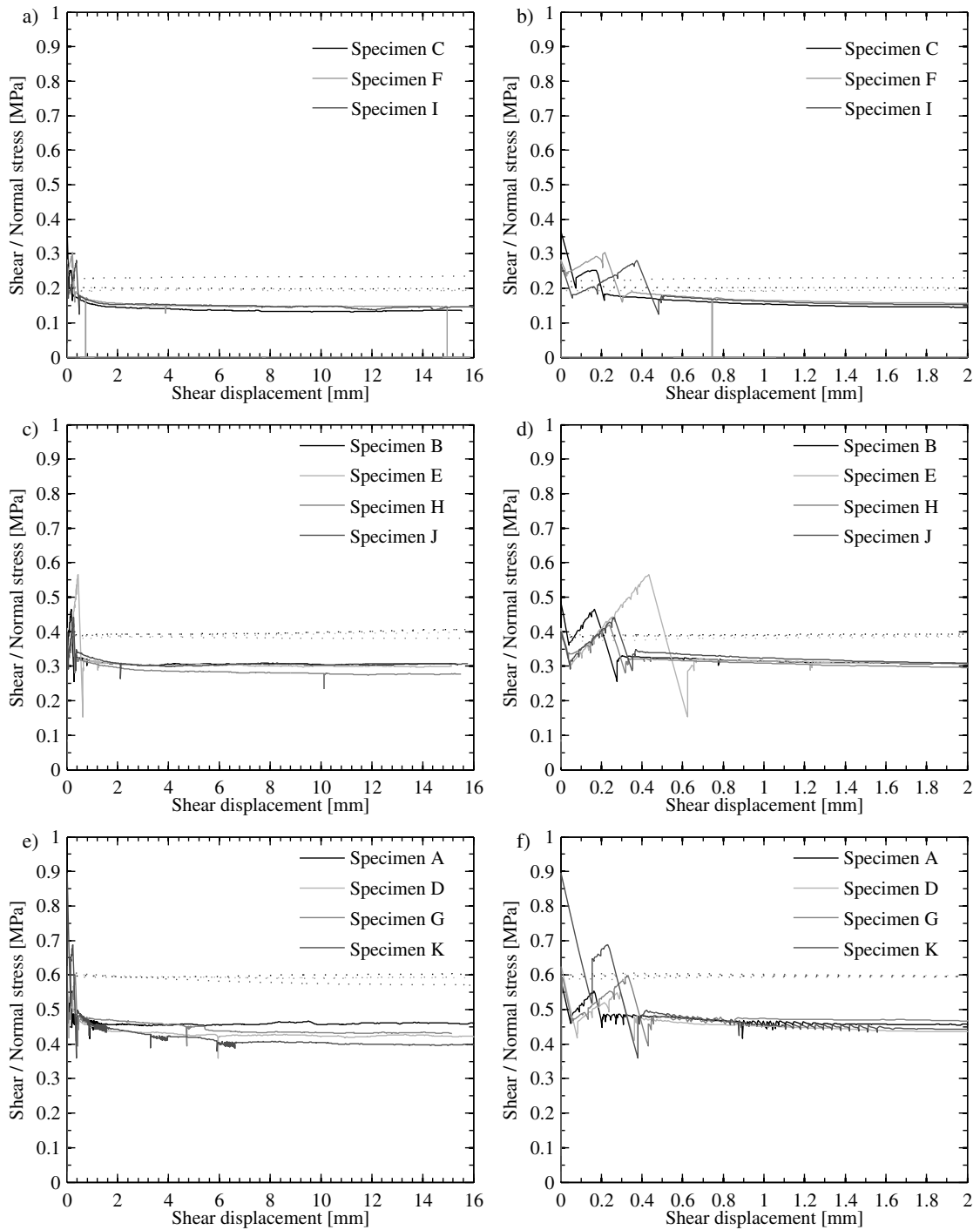


Figure 2.21: Shear tests for wallettes of TUC and TUD: Shear stress (solid lines) and normal stress (dotted lines) plotted against shear displacement. Full shear displacement range (a, c, e) and close-up of the displacement range between 0 and 2 mm (b, d, f).

2. Material tests for masonry spandrels

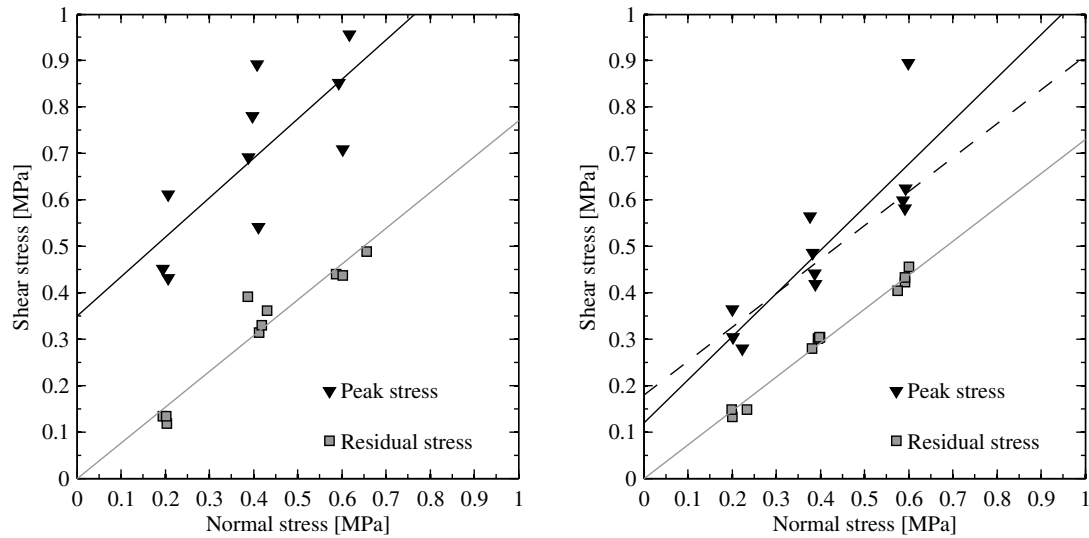


Figure 2.22: Shear tests: Peak and residual stress values including regression lines for TUA and TUB (a) and TUC and TUD (b).

2.5 Threaded steel bars

The horizontal force on TUB was applied by means of threaded steel bars with 10 mm diameter. At the beginning of the quasi-static cyclic test, the bars were pretensioned to 2.5 kN each. During the tests the stress in the bars varied according to the axial elongation of the spandrel. The threaded bars were purchased with a length of 3.0 m. From each bar a sample with 700 mm length was cut and then used for the tension test. The testing procedure was the same as for the reinforcing steel bars tested for the composite spandrels (Part II, Section 2.1). For reasons of completeness, the testing procedure is also outlined here.

2.5.1 Testing procedure

The cutting surfaces of the 700 mm long specimens were ground, the bars were weighted and the exact length of the undeformed bars measured. From these two measurements the effective area of each bar was determined assuming a steel density of $\rho = 7850 \text{ kg/m}^3$. The bars were tested in a Schenk $\pm 480 \text{ kN}$ universal testing machine. The clear length L_c of the specimens in the testing machine was 500 mm. Approximately at the centre of the clear length, an extensometer of type MFI-40 was mounted on the specimen. The extensometer had a gauge length of 300 mm and a displacement range of 20 mm.

The monotonic tensile tests were performed in displacement control. At $\varepsilon = 0.005$ and $\varepsilon = 0.02$ the displacement was held constant for two minutes to allow the stress to drop to a static value. At $\varepsilon = 0.007$ the bar was unloaded to about 10% of its yield strength. All aforementioned strain values refer to measurements with the extensometer. The loading velocity was 0.03 mm/s until the end of the unloading and 0.2 mm/s afterwards. All threaded bars were tested on 20.01.2010.

2.5.2 Test results

For the quasi-static cyclic tests, two bars of 2.30 m length were connected; the missing length was completed by a 1.0 m long D13 mm Stahlton bar. Bars E and A were used on the East face of the test unit (i.e. the front face featuring the LEDs); bars F and D were used on the West face of the test unit. Bar D ruptured at the end of the test. The following mechanical properties were determined from the stress-strain curves of the monotonic tensile tests on the reinforcing bars. All stress values are based on the nominal area of the bar.

D_{nom}	Nominal diameter.
D_{eff}	Effective diameter. Computed from weight and length of specimen assuming a steel density of $\rho = 7850 \text{ kg/m}^3$.
E_s	Modulus of elasticity: Computed from stress-strain points at $1/3$ and $2/3 f_{y,dyn}$ on the initial loading branch.
$f_{y,dyn}$	Dynamic yield stress: Stress at the transition from elastic behaviour to yield plateau (if present) or stress at 0.2% remaining strain (if no yield plateau present).
$f_{y,stat}$	Static yield stress: Computed as the dynamic yield stress $f_{y,dyn}$ minus the stress drop measured at $\varepsilon = 0.005$.
$f_{t,dyn}$	Dynamic tensile stress: Maximum measured stress.
$f_{t,stat}$	Static tensile stress: Computed as the dynamic tensile stress $f_{t,dyn}$ minus the stress drop measured at $\varepsilon = 0.02$.
A_{gt}	Percentage total elongation at maximum force.

The results of the tests are summarised in Table 2.9; the stress-strain relationships are shown in Fig. 2.23. Note the large difference between the nominal and the effective diameter. The nominal diameter is the outer diameter of the threaded bar. The effective diameter was computed from the weight and length of the specimen and an assumed density of 7850 kg/m^3 .

Table 2.9: Mechanical properties of threaded bars used as horizontal force system for TUB. All values are nominal values, i.e. they refer to the nominal bar area of 78.5 mm^2 .

Property	Bar E	Bar A	Bar F	Bar D	Mean \pm Stdev.
Position	East-North	East-South	West-North	West-South	
d_{nom} [mm]	10	10	10	10	
d_{eff} [mm]	8.90	8.90	8.90	8.90	8.90 ± 0.00
E_s [GPa]	134	135	133	133	134 ± 0.74
$f_{y,dyn}$ [MPa]	406	392	408	413	405 ± 8.95
$f_{t,dyn}$ [MPa]	453	449	453	456	453 ± 2.86
$f_{t,dyn}/f_{y,dyn}$ [-]	1.12	1.15	1.11	1.11	1.12 ± 0.02
$f_{y,stat}$ [MPa]	390	383	394	399	391 ± 6.73
$f_{t,stat}$ [MPa]	424	421	424	428	424 ± 2.99
$f_{t,stat}/f_{y,stat}$ [-]	1.09	1.10	1.08	1.07	1.08 ± 0.01
A_{gt} [%]	2.30	3.13	2.43	2.25	2.53 ± 0.41

2. Material tests for masonry spandrels

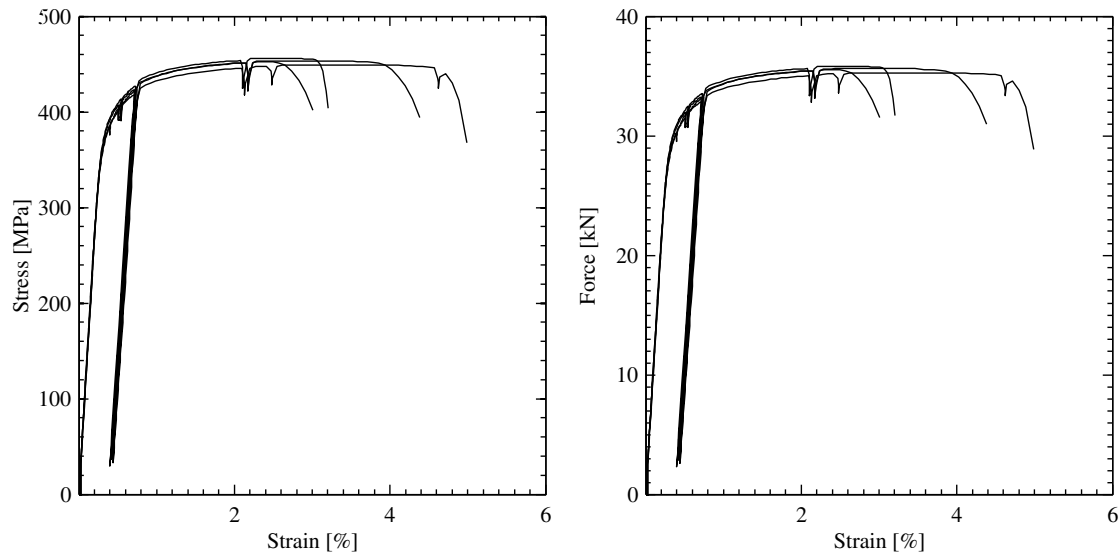


Figure 2.23: Tension tests on threaded bars used as horizontal force system for TUB: Stress-strain relationship (a) and force-strain relationship (b).

2.6 Timber

The timber lintels of TUA and TUB consisted each of four timber beams with an approximate width of 10 cm. The timber lintels were therefore slightly wider than the masonry wall (40 cm compared to 38 cm). The timber lintels were constructed from eight spruce beams that had approximate dimensions of 10x14x500 cm. The axes of the beams were parallel to the wood fibres. Each beam was cut into three pieces, which were 2.80, 1.58 and 0.70 m long. The middle piece was used for the construction of the lintels. The 2.80 m piece was used for material tests; the short piece of 0.70 m was not used.

Originally nine beams had been bought. They were classified as "timber" ("Bauholz"). For each of the beams the density of the different pieces was determined. One of the beams (Beam 2) had a considerably higher density than the others (593 kg/m^3 compared to the average density of the eight other beams of $477 \pm 42 \text{ kg/m}^3$). For this reason this beam was not used for the construction of the spandrels. Before cutting the 5 m long beams, the different pieces were labelled to be able to track which pieces came from the same beam. For the construction of the spandrel of TUA, the beams with numbers 1, 3, 4, 5 were used. For the construction of the spandrel of TUB, the beams with numbers 7, 6, 8, 9 were used. The numbers are given in the order the timber beams were arranged from the East face (with LEDs) to the West face (with LVDTs) of the test units.

The spandrel test units TUA and TUB were constructed between August 13 and 18, 2009 (Table 2.1). TUA was tested on September 30 to October 8, 2009; TUB on November 4 to 6, 2009. For organisational reasons the material tests on the timber samples were not carried out until January 2010. During this time the timber was stored in the structural engineering laboratory. The timber beams had been bought shortly before the construction of the test units; at this time they had just been cut. Between August 2009 and January 2010 the density of the timber beams decreased because their humidity decreased. Unfortunately, the density at the time of testing was not

determined. Table 2.11 summarises the densities of the timber specimens in August 2009 and January 2010. The ending "a" of a label refers to the specimen which was used for the construction of the spandrel. The timber beams in the spandrel experienced – as far it was visible to the naked eye – no permanent deformations. For this reason they were retained after the demolition of the spandrels and the same tests were carried out on these specimens as on those that were only used for the material tests. For the latter specimens the beam with a length of 2.80 m was halved and the two pieces were labelled with "b" and "d". Note that in August 2009 the density was determined on the 2.80 m long piece, which was cut in two only in January 2010. For this reason the density in August 2009 of the specimens "b" and "d" is the same. Specimens "c" with a length of 0.70 m were not used for any tests.

2.6.1 Test setup and testing procedure

The material tests conducted on the timber specimens were 4-point-bending tests. The standardised test in EN408 [DIN09] requires a free span of $18h$ and a distance between the two points where the force is applied of $6h$. For a beam height of 140 mm this corresponds to 2.52 m and 0.84 m, respectively. The tests conducted here used a shorter span: The free span between the supports was 1.0 m and the distance between the two points where the force is applied was 0.30 m; the distance between a support and a point where half the force was applied was therefore 0.35 m. The shorter span was chosen for two reasons: (i) a testing machine for the larger span was not readily available, (ii) it allowed to test also the beams that had been used for the construction of the spandrels and which were retained after the demolition of the test units.

The tests were conducted on a Walter & Bai universal testing machine using a load cell of 100 kN. Photos of the test setup are shown in Fig. 2.24. The following quantities were measured:

- The applied force and the movement of the piston of the testing machine.
- The deflection at mid span measured at midheight of the beam using an LVDT with a range of ± 25 mm. For the specimens with indices "a" and "d" also the deflections above the supports were measured, since when testing the series with index "b" it was observed that some local deformation occurred at the location of the supports. All deflections were measured at midheight of the beam.
- The elongation and contraction of the fibres in the constant moment region of the beam using two LVDTs with a range of ± 10 mm. The base length of both LVDTs was 150 mm. The vertical distance between the LVDTs was 100 mm; the vertical distance of each LVDT to the top or bottom edge of the beam was therefore around 18 – 20 mm.

The testing procedure was as follows:

- The LVDTs were installed and all measurements were set to zero.
- The load was applied as displacement-controlled load with a piston velocity of 0.05 mm/s.
- At a total load of 40 kN the piston was stopped and the two LVDTs measuring the elongation and contraction of the fibres removed.
- The loading was then continued until failure of the specimen. Failure was defined as the point when the maximum stress had been exceeded and the load dropped by a significant amount.

2. Material tests for masonry spandrels

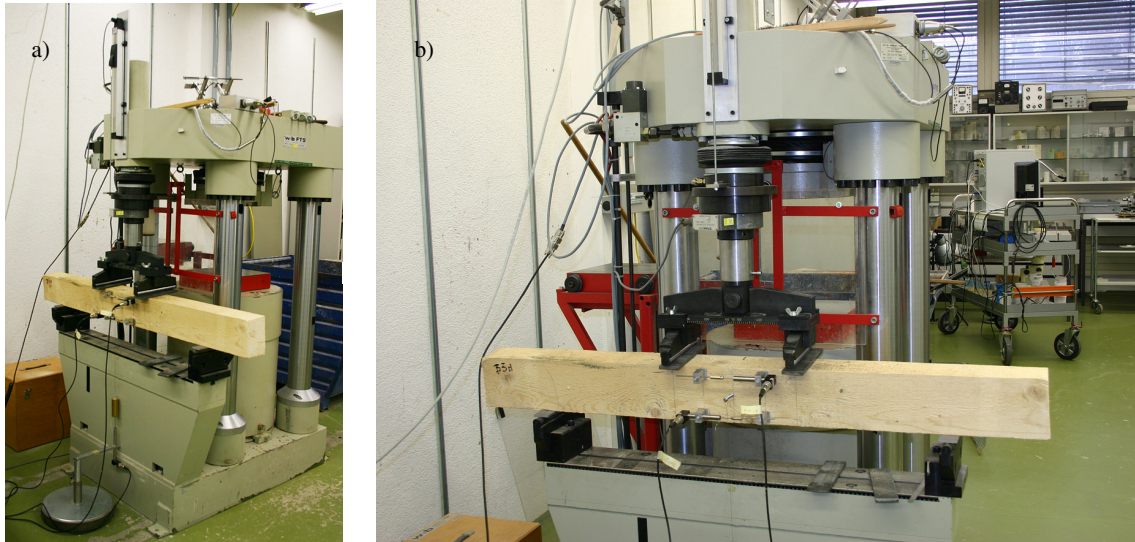


Figure 2.24: Setup for 4-point-bending tests on timber beams.

2.6.2 Failure modes

The failure modes of all timber beams were fairly similar, however, some differences could be observed. For some beams, single fibres ruptured one after the other. As a consequence, the failure was not sudden. The beam typically possessed a large deformation behaviour and the loss of strength after the maximum strength had been reached was rather gradual. An example of a beam with such a failure mode is shown in Fig. 2.25a. Other beams failed rather sudden and the failure surface crossed the entire section of the beam. An example of a beam with such a failure mode is shown in Fig. 2.25b. A further failure mode is shown in Fig. 2.25c.

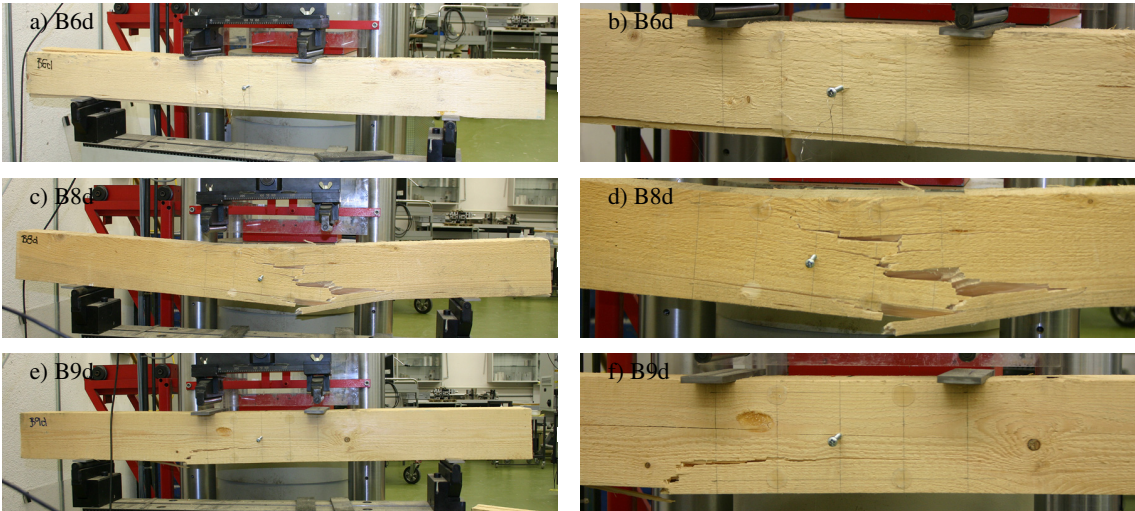


Figure 2.25: Photos of failure modes of timber beams.

2.6.3 Test results

The densities of the timber beams were first determined in August 2009, shortly before the test units TUA and TUB were constructed. The densities were determined a second time shortly before the 4-point-bending tests were carried out in January 2010. Over these months the humidity of the timber beams decreased leading to a reduction in density of up to 16 %. For most beams the reduction was, however, considerably smaller and it seems therefore reasonable that the properties determined from the material tests are representative for the timber lintels when TUA and TUB were tested. The densities in August 2009 and January 2010 are plotted in Fig. 2.26; the numerical values are summarised in Table 2.11.

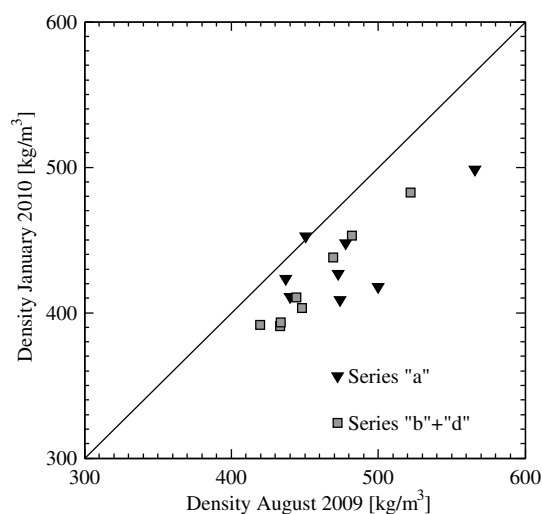


Figure 2.26: Variation of densities of timber beams.

From the measurements of the two horizontal LVDTs mounted within the central span, the curvature of the timber beam was computed. To do so, it was assumed that the curvature is constant within the central span. The moment within the central span was computed as $M = P/2 \cdot a$, where P is the total applied load and a is the distance from the outer support to the nearest point where the load is applied to the beam (i.e. $a = 0.35$ m). Since the horizontal LVDTs were removed when P reached approximately 40 kN, it is not possible to derive the entire moment-curvature relationship from this local curvature measure. For this reason, the curvature was back-calculated from the displacement at midspan assuming that the curvature profile was similar to the moment profile. If this assumption holds, the curvature φ_{Δ} within the central span can be computed as:

$$\varphi_{\Delta} = \frac{\Delta_{mid}}{1/2b^2 + ab + 2/3a^2} \quad (2.1)$$

where Δ_{mid} is the vertical deflection at midspan and b the half-width of the central span (i.e. $b = 0.15$ m). For the beams of series "b" the vertical deflection at midspan was taken equal to the displacement measured at midspan. For the beams of series "a" and "d" half the displacement measured above the supports was subtracted from the measurement at midspan in order to account for any local deformations at the supports. The moment-curvature relationships obtained for the two types of curvatures are plotted in Fig. 2.27. The curvatures that were computed from the measurements of the two horizontal LVDTs are plotted with solid lines. The curvatures that were

2. Material tests for masonry spandrels

derived from the displacement measurements are plotted with dashed lines. For most of the tested beams the agreement between the initial stiffnesses obtained from the two curvature measures is rather good. In general, the curvatures computed from the deformation data result in slightly smaller stiffnesses. For beams of group 1 and 4 the differences are rather large. It is possible that imperfections within the beam caused this difference.

Tables 2.10 and 2.11 summarise the mechanical properties of the timber beams in quantitative terms. The maximum stress was computed from the maximum moment assuming a linear stress distribution over the height of the beam and the position of the neutral axis at midheight. The E-Modulus of the beam was determined as secant modulus between the points corresponding to 10% and 33% of the beam strength. Similar to the curvature it was computed from both a local and a global deformation measures. The local E-Modulus was computed from the measured force and the curvature φ derived from the horizontal LVDT measurements assuming an elastic behaviour of the beam, where the relationship $M = \varphi \cdot EI$ holds. The global E-Modulus was computed from the measured force and the vertical deflection at midspan Δ_{mid} as:

$$E_{global} = \frac{dP}{48Id\Delta_{mid}} L^3(3\alpha - 4\alpha^3) \quad (2.2)$$

where dP and $d\Delta_{mid}$ refer to the increase in applied force and deflection, respectively, corresponding to the loading interval between 10% and 33% of the beam strength, L refers to the entire span of the beam ($L = 1.0$ m) and α is defined as the ratio a/L . The variation in particular of the E-moduli is rather large. For the back analysis of TUA and TUB it is recommended to use the mean values given at the end of Table 2.10.

Table 2.10: Timber beams: Dimensions, strengths and E-moduli of different beams and of spandrels in TUA and TUB.

Beam / Spandrel	Width [mm]	Height [mm]	Max. moment [kNm]	Max. stress [MPa]	E-Mod. local [GPa]	E-Mod. global [GPa]	Ratio E-Mod. [-]
B1	97	136	12.5 ± 0.5	41.9 ± 1.6	15.1 ± 7	7.1 ± 1.5	0.54 ± 0.23
B3	99	135	8.0 ± 1.1	26.7 ± 3.8	11.0 ± 2.8	7.6 ± 1.3	0.72 ± 0.20
B4	97	139	9.4 ± 1	29.9 ± 3.1	14.0 ± 7.7	5.6 ± 0.8	0.48 ± 0.23
B5	97	137	11.5 ± 0.9	38.1 ± 2.9	8.1 ± 1.3	6.6 ± 1.0	0.83 ± 0.18
B6	98	132	12.5 ± 0.8	44.0 ± 2.8	14.0 ± 2.3	7.6 ± 0.6	0.55 ± 0.09
B7	99	134	13.2 ± 0.3	44.4 ± 0.9	10.9 ± 0.6	8.0 ± 1.1	0.74 ± 0.11
B8	99	136	10.6 ± 2.1	34.9 ± 6.8	10.0 ± 0.6	8.0 ± 0.4	0.80 ± 0.04
B9	98	136	11.6 ± 1.2	38.5 ± 4	12.0 ± 1.4	8.6 ± 1.3	0.73 ± 0.19
TUA	390	137	41.5	34.1	12.1	6.7	0.56
TUB	394	135	48.0	40.4	11.7	8.1	0.69

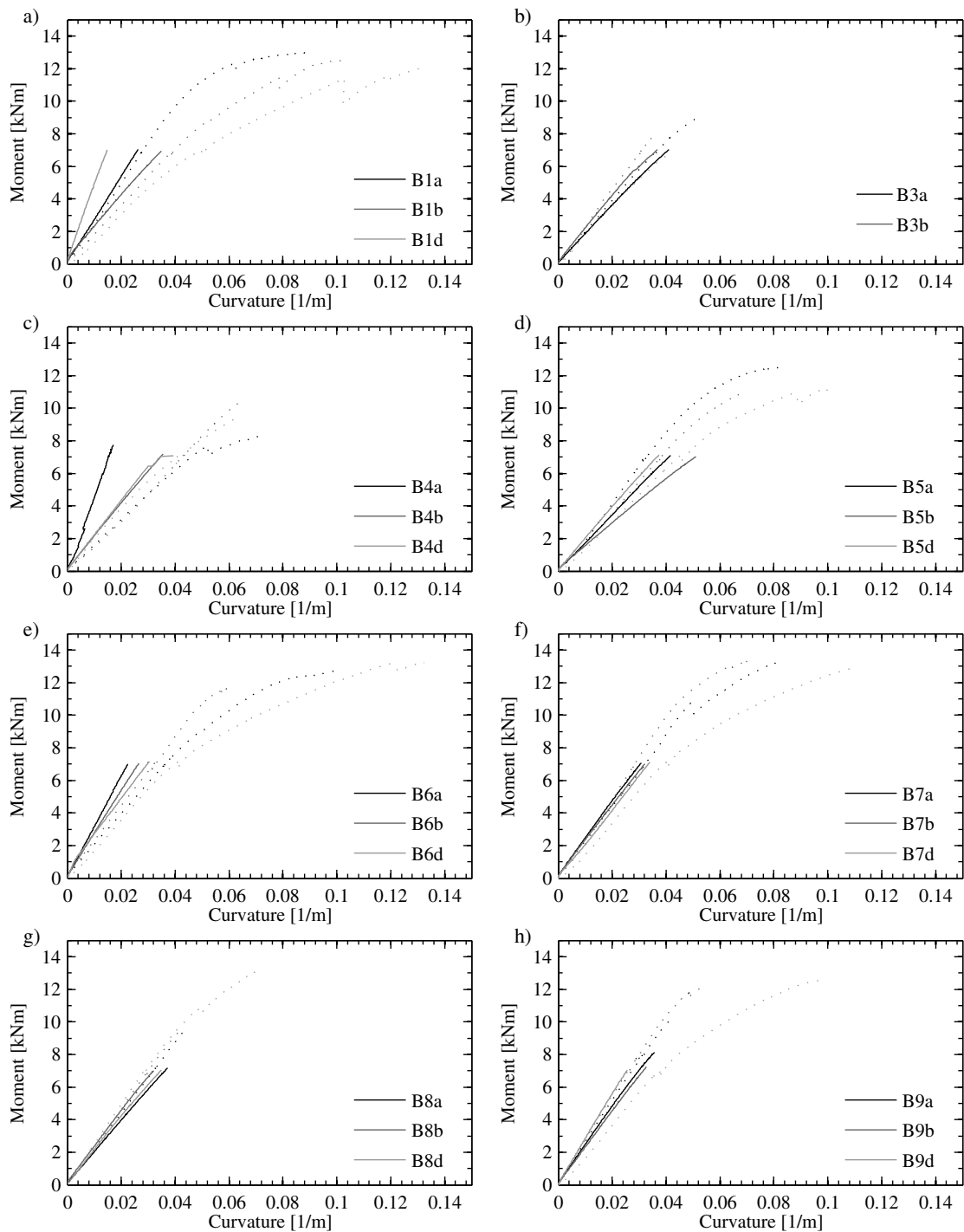


Figure 2.27: Moment-curvature relationships of timber beams obtained from 4-point-bending tests. The solid lines represent the curvature measured within the central span, the dashed lines represent the curvature φ_{Δ} , which was back-calculated from the deflection measurements.

2. Material tests for masonry spandrels

Table 2.11: Timber beams: Densities, strengths and E-moduli of individual test specimens.

Beam	Density August 09 [kg/m ³]	Density January 10 [kg/m ³]	Ratio densities [-]	Max. moment [kNm]	Max. stress [MPa]	E-Mod. local [GPa]	E-Mod. global [GPa]	Ratio E-Mod. [-]
B1a	451	453	1.00	13.0	43.4	12.8	8.7	0.68
B3a	440	411	0.93	9.1	30.4	8.8	6.7	0.76
B4a	500	418	0.84	8.4	26.8	23.0	5.2	0.22
B5a	474	409	0.86	12.5	41.3	8.4	7.8	0.93
B6a	437	423	0.97	12.7	44.6	16.3	7.3	0.45
B7a	473	427	0.90	13.3	44.9	11.5	7.7	0.67
B8a	566	498	0.88	9.3	30.5	9.4	7.6	0.82
B9a	478	448	0.99	10.3	34.0	11.5	9.0	0.78
B1b	444	406	0.91	12.5	41.9	9.6	6.3	0.66
B3b	433	379	0.88	8.1	26.9	10.1	9.1	0.90
B4b	448	408	0.91	10.3	32.9	9.4	5.2	0.55
B5b	434	391	0.90	10.8	35.7	6.7	6.4	0.94
B6b	419	379	0.90	11.7	41.0	14.0	8.3	0.59
B7b	469	422	0.90	13.3	44.9	10.7	9.3	0.86
B8b	522	493	0.94	9.6	31.4	10.6	8.0	0.75
B9b	482	452	0.94	12.1	39.9	10.9	9.6	0.88
B1d	444	415	0.93	12.0	40.2	23.0	6.1	0.27
B3d	433	402	0.93	6.9	22.9	14.2	7.1	0.50
B4d	448	398	0.89	9.4	30.1	9.8	6.5	0.66
B5d	434	395	0.91	11.3	37.2	9.3	5.8	0.62
B6d	419	404	0.96	13.2	46.5	11.7	7.3	0.63
B7d	469	454	0.97	12.9	43.4	10.3	7.1	0.69
B8d	522	472	0.90	13.0	42.7	10.1	8.4	0.83
B9d	482	454	0.94	12.6	41.6	13.6	7.1	0.52

3 Test results for masonry spandrels

This chapter summarises the test results for the masonry spandrels. For each spandrel the test observations and the most important graphs showing the results from the measurements with the hard-wired and optical instruments are given. The quantities computed from measurements, such as for example the shear force and the rotation of the piers, are defined in Section 3.1. For the masonry spandrels not only vertical but also horizontal forces were applied to the test units. In those cases where the horizontal force was applied at the beginning and kept constant throughout the loading history, a new load step LS 1b was introduced, which refers to the application of the horizontal load (axial load on the spandrel), while LS 1a refers to the application of the vertical loads (axial load on the piers). The exact setup varied slightly from unit to unit. For this reason, at the beginning of a section on a test unit, the exact setup concerning the application of the axial forces as well as the instrumentation is given.

During the discussion of the test observations and of the test results, reference to the loading direction is often made. The positive direction of loading is defined for a drift of the piers towards North while the negative direction of loading implies a drift of the piers towards South. The definition of the directions of loading is schematically depicted in Fig. 3.1. It shows the view of the East face on which the cracks were marked with a black pen and which is also the face shown on most photos.

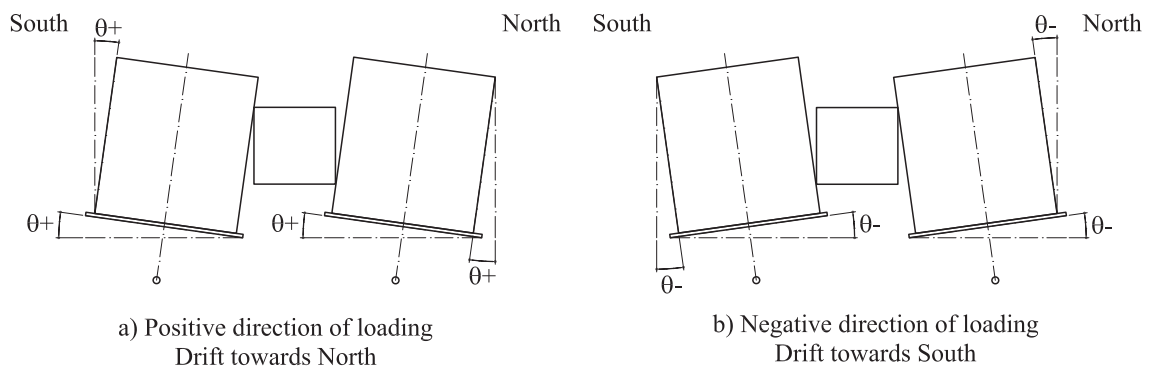


Figure 3.1: Positive (a) and negative (b) direction of loading. View from the East.

3.1 Definition of force and deformation quantities

This section defines the quantities used in the graphs showing the basic results from the hard-wired instruments and describes the standard graphs plotted for each test unit. Apart from the axial load applied to the spandrel (H_{sp}), all quantities were already defined in Section 3.1 of Part II. The definitions are repeated here for the sake of completeness.

3. Test results for masonry spandrels

Reaction forces at the supports

The reaction forces at the supports were measured by one compression load cell and four tension load cells (see Section 1.2). The total reaction force was computed as the sum of the five forces. Hence, for the North and South support, respectively, the reaction forces were computed as:

$$R_N = LC_N_C + LC_N_17 + LC_N_16 + LC_N_19 + LC_N_08 \quad (3.1)$$

$$R_S = LC_S_C + LC_S_15 + LC_S_0 + LC_S_24 + LC_S_22 \quad (3.2)$$

The reaction forces were set to zero before the test unit was lifted on the test stand.

Weight of the spandrel

The weight of the spandrel was computed as the sum of the two actuator forces and the two reaction forces:

$$W_{sp} = ACT_FORCE_N + R_N + ACT_FORCE_S + R_S \quad (3.3)$$

The weight of the spandrel includes the weight of all base steel plates and of the load transfer beams that were mounted with the test unit on the test stand as well as the portion of the weight of the lever beams carried by their outer supports before the test unit was lifted onto the test stand. The actuator forces were set to zero before the actuators were connected with the lever beams. Due to measurement errors of the load cells W_{sp} varied slightly over the duration of the test. For the computation of the shear force in the spandrel an average value of W_{sp} was defined and was kept constant for the entire duration of the test.

Shear force of the spandrel

The shear force of the spandrel was computed once from the North actuator force and the North reaction force and once from the South actuator force and the South reaction force. To obtain the shear force in the spandrel half the weight of the spandrel has to be subtracted:

$$V_N = ACT_FORCE_N + R_N - W_{sp}/2 \quad (3.4)$$

$$V_S = ACT_FORCE_S + R_S - W_{sp}/2 \quad (3.5)$$

Some unevenness of the base plates or slight misalignment of the lever beams could cause internal stresses in the test unit when placing the test unit on the test stand. These stresses correspond to an initial shear force, which Eqs. 3.4 and 3.5 can capture. Small differences between V_N and V_S result from (i) measurement errors and (ii) deviation of the actuator forces from the vertical axis at larger rotations. The final shear force is computed as the average of V_N and V_S :

$$V = (V_N + V_S)/2 \quad (3.6)$$

Axial force on piers

The axial force acting on each pier was computed from the forces in the four rods that pretensioned the load transfer beam against the base plate:

$$AFP_N = AFP_N_EN + AFP_N_ES + AFP_N_WN + AFP_N_WS \quad (3.7)$$

$$AFP_S = AFP_S_EN + AFP_S_ES + AFP_S_WN + AFP_S_WS \quad (3.8)$$

The nominal cross section of a pier was 0.38x2.07 m, which corresponds to 0.79 m². The nominal axial force per the piers varied between the tests. Three different load levels were used: 4x30 kN

(TUA up to cycle 12), 4x60 kN (TUA, TUB) and 4x80 kN (TUC, TUD). These axial forces correspond – excluding the weight of the load transfer beam and the selfweight of the pier – to 0.15, 0.30 and 0.40 MPa, respectively. The weight of the load transfer beam on top of the pier is approximately 4.4 kN, the weight of the pier down to midheight 18 kN. The additional axial stress at midheight of the pier due to the selfweight of the pier and the weight of the load transfer beam was therefore 0.03 MPa.

Axial force on spandrels

The axial force acting on each spandrel was computed from the forces in the two horizontal rod that applied an axial force onto the spandrel:

$$H_{sp} = H_E + H_W \quad (3.9)$$

Rotation of piers

The deformation demand on the spandrel is quantified in terms of the drift of the piers that are supported by the lever beams. The rotation of the lever beams is measured by the LVDTs mounted underneath the lever beams. For each lever beam the rotation is computed as follows:

$$\theta_N = (BEAM_N_S - BEAM_N_N)/l_{pier} \quad (3.10)$$

$$\theta_S = (BEAM_S_S - BEAM_S_N)/l_{pier} \quad (3.11)$$

The horizontal distance between the LVDTs corresponded to the length of a pier of the composite spandrel test units, i.e. $l_{pier} = 2100$ mm. The drift is defined as positive when the piers are displaced towards North (Fig. 3.1), i.e. for a positive rotation about an axis pointing from East to West. Since the velocity of the actuators was controlled via the displacement transducers mounted on the actuators themselves, the actual drifts of the two lever beams could differ slightly. This was mainly due to some small backlash within the actuators' hinges. The final drift was computed as the average of the rotation of the North and South lever beams:

$$\theta = (\theta_N + \theta_S)/2 \quad (3.12)$$

Spandrel displacement

The demand on the spandrel does not only depend on the pier rotations but also on the length of the spandrel and the piers. A "spandrel displacement" is computed as

$$\Delta_{sp} = \theta \cdot (l_{sp} + l_p) \quad (3.13)$$

where l_{sp} is the length of the spandrel ($l_{sp} = 1180$ mm) and l_p the length of the piers ($l_p = 2070$ mm) (see Figs. 1.1 and 1.2).

Deformation of the timber lintel of TUA and TUB

The deformations of the timber lintel were measured by two chains of LVDTs running along the top and bottom edges of the West face of the timber lintel. The measurements were recorded in units of [mm]. The base length of all LVDTs was 150 mm. The distance between the top and bottom chains of LVDTs was $d = 100$ mm and $d = 90$ mm for TUA and TUB, respectively (see Fig. 1.13). For each pair of LVDTs an average curvature is computed as:

$$\varphi_i = (SLAB_B_i - SLAB_T_i)/150 \text{ mm}/d \quad (3.14)$$

A curvature is defined as positive, when the strains at the bottom are larger than the strains at the top.

Standard plots

Based on the just defined quantities, the following standard plots were generated for all test units:

- Force-deformation hysteresis: Shear force V plotted against the drift θ . This graph is plotted for all cycles and for cycles with amplitudes up to $\pm 0.8\%$.
- Force-deformation hysteresis for North and South quantities: The quantities necessary to determine the shear force of the spandrel were overdetermined: The shear force in the spandrel could be computed based on the North actuator force and the North support force or based on the South actuator force and the South support force. As an overall measure the average shear force V was used. To judge the quality of the measurements the two computed shear forces are plotted separately as $V_N - \theta_N$ and $V_S - \theta_S$ curves.
- Axial force on piers: The axial force on the piers was supposed to remain constant. This was achieved by means of load followers. However, some variations occurred, which are shown in a graph plotting the total axial force on the North (AFP_N) and South (AFP_S) pier, respectively, against the rotation θ .
- Axial force on spandrel: For TUA and TUC the axial force on the spandrel was supposed to remain constant while for TUB and TUD the axial force on the spandrel depended on the axial elongation of the spandrel. The variation of axial load on the spandrel is shown in a graph plotting the total horizontal force H_{sp} against the rotation θ .
- Curvature distribution along the timber lintel (TUA and TUB only): From the two LVDT chains mounted on the West face of the timber lintel the curvature distribution φ_i along the timber lintel was computed. It was plotted for four drift levels, i.e. 0.4%, 0.8%, 1% and 2%. Plots for the negative and positive direction of loading are provided.

In addition to the results obtained from the hard-wired instruments, the data obtained from the optical measurements (see Section 1.3.2) was used to plot the deformed shape of the test unit for selected rotation demands. The data was obtained from the optical measurements over a duration of approximately one minute at each load step. The measurements were averaged over the recording time to obtain the deformations of the test unit at the load steps. Plots of the deformed shape of the test units are provided for first positive as well as the first negative peak of cycles with the following nominal rotation levels: 0.1%, 0.2%, 0.4% and 0.8%.

3.2 Masonry spandrel TUA

3.2.1 Specific test setup

The forces in all eight vertical rods were applied by D13 mm Stahlton bars that were tensioned by means of hollow core jacks. All eight jacks were connected to the same load follower. Since the variation of axial loads in the North and South pier was typically in opposite directions, this setup led to larger variations in the individual forces than if the jacks of one pier were connected to a different load follower than the jacks of the other pier. However, only two load followers were available and the second one was needed to control the forces in the horizontal rods, for which also D13 mm Stahlton bars were used. Both hollow core jacks that applied the forces to the two horizontal rods were connected to the same load follower. The LVDT instruments on the West

face of the lintel had all a base length of 150 mm. The distance between the top and bottom row of LVDT instruments was 100 mm (Fig. 1.13).

3.2.2 Test observations

At LS 0 the forces in the eight vertical and in the two horizontal rods were zero. As a first step the vertical rods were prestressed to a force of 40 kN each, which corresponds approximately to an axial stress in the piers of $\sigma = 0.15$ MPa (load step LS 1a). Including the selfweight of the masonry and the weight of the load transfer beam at the top, the axial stress level at midheight of the pier was approximately $\sigma = 0.18$ MPa. Then, the horizontal rods were prestressed to a force of 40 kN each, i.e. the total horizontal force was 80 kN (LS 1b). The vertical and horizontal forces were applied on 29.09.2009. The test unit was tested on four days: 30.09.2009 and 06.10.2009 to 08.10.2009. An overview on the load steps covered during each testing day is given in Table 3.1.

Table 3.1: TUA: Testing days and corresponding load steps.

Testing day	Load steps carried out
29.09.2009	LS 1a & LS 1b
30.09.2009	LS 2 - LS 15
06.10.2009	LS 12b - LS 15c
07.10.2009	LS 16 - LS 27
08.10.2009	LS 27 - LS 46

Axial stress in piers $\sigma = 0.18$ MPa, Horizontal force $H_{sp} = 80$ kN

At the onset of testing a thin crack above the timber lintel was present. It is believed that this crack formed because of some minor movement of the lintel either due to creeping or due to a variation of humidity. At the very first cycles thin vertical cracks between the edges of the lintel and the masonry formed. At LS 10, which was the first load step of the cycles with a nominal rotation of the lever beams of $\theta_{nom} = \pm 0.1\%$, a horizontal crack formed in the South pier at an elevation corresponding to the top face of the timber lintel. The crack reached from the edge of the timber lintel to about the vertical centre line of the pier. First cracks in the spandrel appeared at the top South edge of the spandrel when loading to LS 13. Thin flexural cracks at both ends of the spandrel formed in the then following cycle.

In the cycles with $\theta_{nom} = \pm 0.1\%$ cracks had appeared between the piers and the base steel plate as well as between the bottom rows of bricks. The maximum width of these cracks was 1 – 1.5 mm, which increased to 2 – 2.5 mm during the first two cycles with $\theta_{nom} = \pm 0.2\%$. These cracks reduced the effective rotational demand on the spandrel and were not intended. The bottom and top parts of the piers should remain virtually undamaged since the loading conditions of the piers do not represent a realistic loading scenario: The shear forces in the piers are zero and the moments are therefore constant. In a real situation this is not the case. It was therefore decided to continue the loading scheme with an increased axial stress of $\sigma = 0.33$ MPa in order to prevent the opening of such cracks.

Axial stress in piers $\sigma = 0.33$ MPa, Horizontal force $H_{sp} = 80$ kN

After the forces in the vertical rods were increased, the load steps LS 12 ($\theta_{nom} = 0.1\%$), LS 13 ($\theta_{nom} = -0.1\%$), LS 14 ($\theta_{nom} = 0.2\%$) and LS 15 ($\theta_{nom} = -0.2\%$) were repeated. To distinguish

3. Test results for masonry spandrels

these cycles from the cycles with an axial pier stress of $\sigma = 0.18$ MPa, the letter "b" was appended to their name. During these cycles only few new cracks formed in the spandrel. The most significant crack was a horizontal crack in the North pier located at an elevation corresponding to the top face of the timber lintel. Similar to the South pier, this crack extended approximately to the centre of the pier. Although the axial stress in the piers had been increased, the cracks at the base of the piers still opened up. The crack widths were slightly reduced but were still considered rather large. For this reason it was decided to repeat the load steps LS 12 to LS 15 again, this time reducing the horizontal force to half of its original value.

Axial stress in piers $\sigma = 0.33$ MPa, Horizontal force $H_{sp} = 40$ kN

The third repetition of the load steps LS 12 to LS 15 was indexed with the letter "c". The horizontal force was reduced at zero drift when loading from LS 15b to LS 12c. Shortly before reaching LS 15c a shear crack formed in the spandrel leading to a drop in force. The shear crack followed the mortar joints. At the South top edge of the spandrel the already existing flexural crack opened to a maximum crack width of 3 mm. At its North end, the timber lintel was pulled out of the surrounding masonry; the width of the vertical crack between lintel and masonry was 1.4 mm. Also the brick below the North end of the timber lintel was pulled out by a similar amount. It was decided to complete the test with this vertical and horizontal force configuration. Most of the main cracks within the spandrel had formed by this time. They were :

- For the positive direction of loading (Drift towards North): The flexural cracks at the North and South end of the spandrels.
- For the negative direction of loading (Drift towards South): The flexural cracks at the North and South end of the spandrel and the shear crack pointing from the North top edge to the South bottom edge of the spandrel.

The crack patterns in the two directions of loading were therefore different. In the following the two crack patterns are described in more detail based on Figs. 3.2 and 3.3. The former shows the crack pattern at the first peak with $\theta_{nom} = 0.4\%$ (LS 22) while the latter depicts the following peak LS 23 featuring $\theta_{nom} = -0.4\%$.

For the positive direction of loading the flexural crack at the North end of the spandrel was open at the top and closed approximately one brick below the timber lintel. At most rows of bricks, this crack concentrated within one single crack, at some rows it was distributed over a couple of cracks. This crack path only partially followed the mortar joints but went often through bricks. At the bottom it passed the timber lintel on its right and stopped one brick below the lintel. Since the axial force applied to the spandrel was kept constant and did not vary with the elongation of the spandrel, the spandrel became longer over the time of the loading process. For this reason the vertical crack next to the lintel, i.e. between lintel and masonry, did not close anymore. At the South end of the spandrel the flexural crack was closed at the top of the spandrel and opened up towards the bottom. At the top it appeared that only the topmost two rows of the spandrel were under compression; for all lower rows this flexural crack was open. Unlike at the North end, the flexural crack at the South end was divided into several parallel cracks, which at the height of the lintel concentrated again in the vertical crack between lintel and surrounding masonry while the lintel was pulled out of the surrounding masonry.



Figure 3.2: TUA: Crack pattern of spandrel at LS 22. Drift towards North with $\theta_{nom} = 0.4\%$.



Figure 3.3: TUA: Crack pattern of spandrel at LS 23. Drift towards South with $\theta_{nom} = -0.4\%$.

3. Test results for masonry spandrels

For the negative direction of loading the main deformation concentrated within the shear crack and the flexural cracks at the North and South ends of the spandrel. The shear crack pointed from the top North corner of the spandrel to the South end of the lintel. The flexural crack at the North end was open at the bottom and closed at the top. The crack was the widest next to the lintel. The brick that supported the lintel was pulled out of the surrounding masonry together with the lintel itself. The flexural crack at the South end was open at the top and closed approximately at the height of the lintel. The cracks surrounding the lintel suggested that for both directions of loading the support of the lintel within the pier corresponded only to a partial moment restraint. Over the entire duration of the test the lintel did not seem to undergo inelastic deformations.

As loading continued the crack pattern within the spandrel evolved only slightly. As the rotations got bigger, the flexural cracks became more and more straight, often causing cracks running through bricks. New types of cracks developed from LS 26 ($\theta_{nom} = 0.6\%$) onwards, when stair-stepped cracks appeared in the lower part of the piers starting from the lintel. This type of crack was probably caused by the pull-out forces transmitted by the lintel, which must have carried some net tension forces at its end. In addition, at LS 26 and LS 28 a shear crack formed in the lintel when loading in the positive direction (see Fig. 3.4). At this instant the shear crack was still rather thin, but became more and more dominant in the ensuing cycles. First cracks in bricks located within the compression diagonal in the spandrel occurred at LS 30 ($\theta_{nom} = 1\%$).

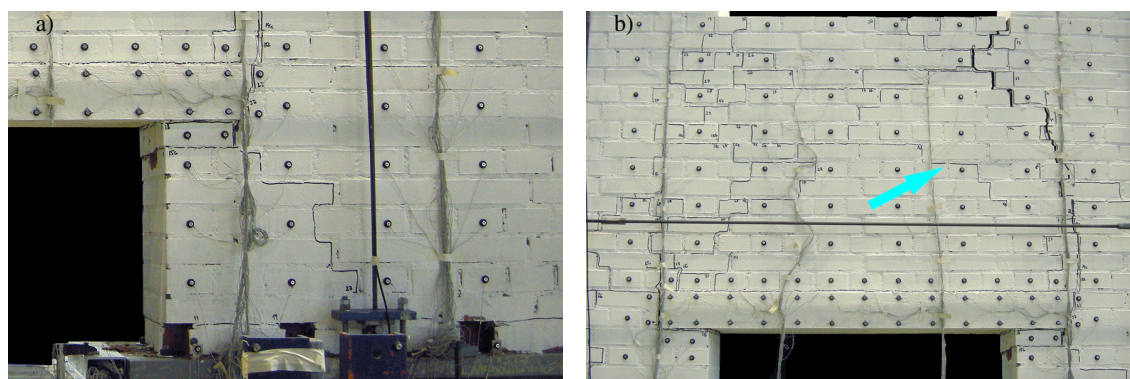


Figure 3.4: TUA: Stair-stepped cracks in the North pier at LS 28 (a) and onset of the formation of a shear crack running from the South top corner of the spandrel to the North bottom one at LS 28 (b). Drift towards North with $\theta_{nom} = 0.6\%$.

The stair-stepped cracks in the piers represented the onset of the formation of the failure mechanism: Due to the pull-out forces transmitted by the lintel the brick columns supporting the lintel rotated about their base, i.e. moving into the opening below the spandrel. As the rotation of these brick columns increased, the lintel and the masonry supported by the lintel lost their support. Particularly critical was the support at the South end of the lintel. To avoid a total collapse of the spandrel, the South end of the spandrel was loosely supported by the laboratory crane. The onset of failure occurred when loading to LS 46, which is the first peak of the cycles with $\theta_{nom} = \pm 2.5\%$. It was then decided to continue loading directly without stopping up to $\theta = 3.0\%$ when the final failure occurred. The photos taken at LS 46 show therefore the test unit at a drift of $\theta = 3.0\%$. Figure 3.5 shows the last peak in the negative loading direction (LS 45, $\theta_{nom} = 2.0\%$) before the failure at LS 46 (Fig. 3.6).

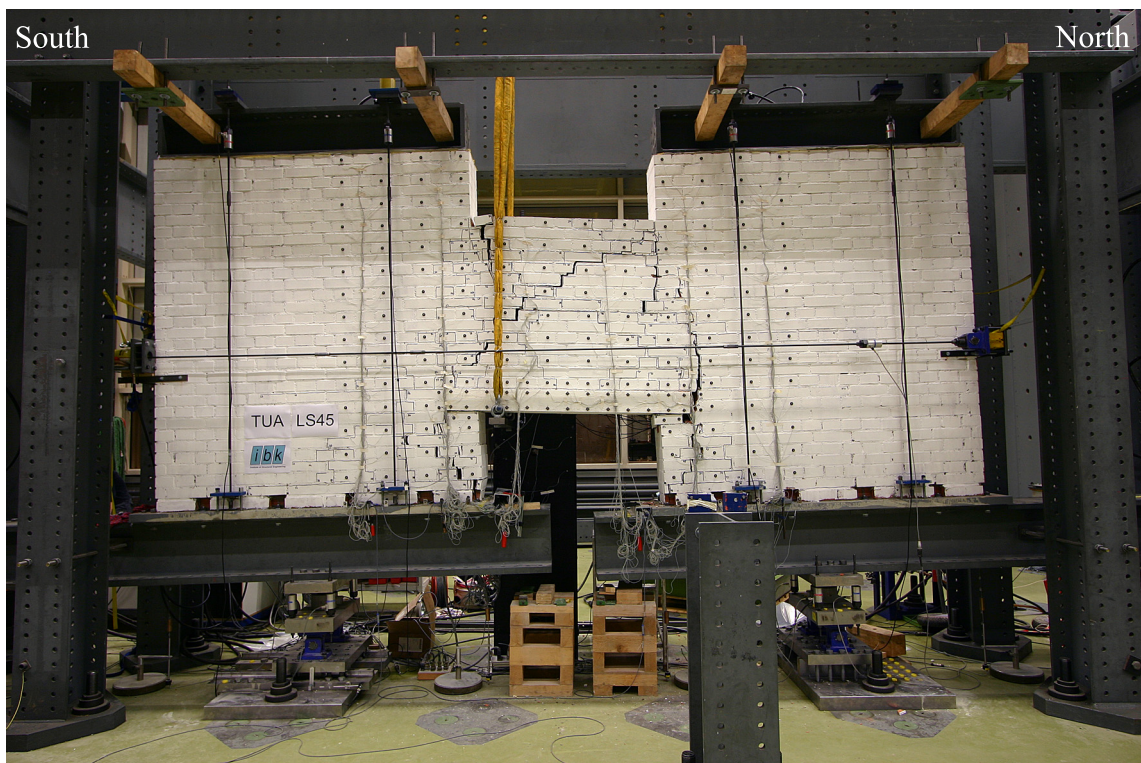


Figure 3.5: TUA: Crack pattern of spandrel at LS 45. Drift towards South with $\theta_{nom} = 2.0\%$.

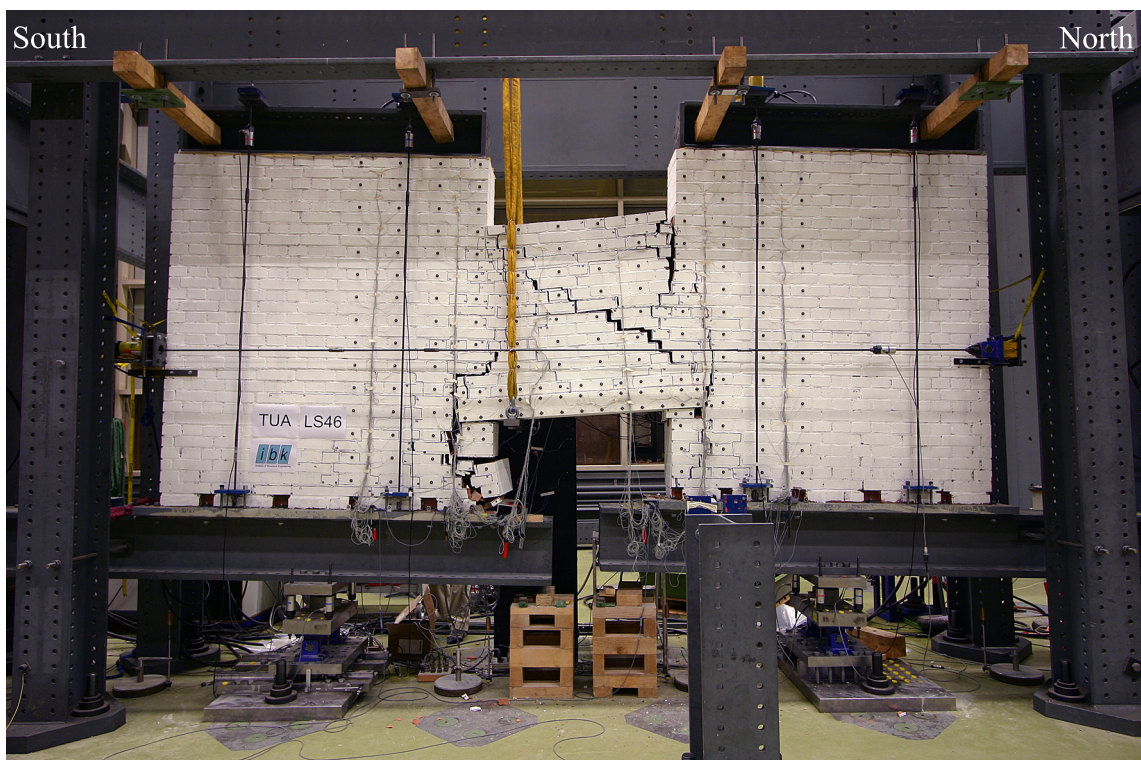


Figure 3.6: TUA: Crack pattern of spandrel at LS 46. Drift towards North with $\theta = 3.0\%$ (failure of TUA, $\theta_{nom} = 2.5\%$).

3.2.3 Test results

In this section key results of TUA are presented and briefly discussed often making reference to observations made during the test. The hysteretic behaviour of the test unit in terms of spandrel shear force vs. average rotation is presented first. Afterwards the variation of the axial load acting on the piers and on the spandrel is discussed. Finally the deformations experienced by the timber lintel are addressed in terms of local curvature distribution.

Hysteretic behaviour of TUA

The global hysteretic behaviour of the test unit is shown in Figs. 3.7 and 3.8. While in Fig. 3.7 both the rotation and the shear force acting on the spandrel are averaged, in Fig. 3.8 both quantities are calculated independently from the data stemming from the South and the North pier, respectively. The two curves in Fig. 3.8 feature only minor differences due to measuring errors (especially of the forces) and to a slightly different rotation of the two lever beams. Since the differences were only minor, the averaged hysteresis curve in Fig. 3.7 can be considered representative of the whole test and will be briefly discussed in the following.

The maximum shear force reached during the test was about 100 kN both for loading in the positive and negative direction and occurred at a drift of about 0.2%. Afterwards, the maximum shear force along the monotonic envelope of the loading cycles dropped relatively fast to a value of about 65 kN, which remained nearly constant over a large portion of the test. This drop in maximum shear force was due to two reasons: (i) cracking in the spandrel and (ii) reduction of the axial load acting on the spandrel. Regarding (ii) it shall be remembered that the cycles between LS 12 and LS 15 were repeated three times with different configurations of the axial load acting on the piers and on the spandrel (see previous section). The effect of these different combinations on the shear force - rotation relationship are illustrated in Fig. 3.9, which shows only the cycles between LS 12 and LS 15c during which the axial forces were modified. In Fig. 3.9 the hysteresis curve of all cycles are more or less linear-elastic up to a rotation of 0.1%, afterwards some non-linearities set in. These are due mostly to the unintended horizontal cracks that formed at the base of the piers (see previous section). However, upon unloading these cracks closed again yielding an almost nonlinear elastic behaviour during the cycles LS 12 to LS 15b. In this respect the behaviour of TUA during the cycles LS 12c-15c differed substantially; shortly before reaching the peak deformation during LS 14c and LS 15c significant cracking of the spandrel occurred (most notably at LS 15c with the formation of the shear crack in the spandrel) leading to a force reduction within the loading half-cycle.

Figure 3.10 shows the hysteresis curve of all cycles carried out with an average axial stress in the piers of $\sigma = 0.33$ MPa and an axial force in the spandrel of 40 kN. These loading conditions started at LS 12c and were kept constant until the end of test. A close-up of the same cycles up to a drift of $\pm 0.8\%$ is shown in Fig. 3.11. After cracking in the spandrel reached more or less its full extension at LS 23 ($\theta_{nom} = -0.4\%$), the peak value of the shear force for the following cycles remained almost constant at about 65 kN over a large range of drifts. This value is larger than the contribution V_N provided by the axial force in the spandrel alone. An upper limit for the latter can be estimated by means of Eq. 3.15 where H_{sp} is the axial force acting on the spandrel, h_{sp} is the height of the spandrel and l_{sp} is its span:

$$V_N = \frac{H_{sp} \cdot h_{sp}}{l_{sp}} = \frac{40\text{kN} \cdot 1.26\text{m}}{1.18\text{m}} = 42.7\text{kN} \quad (3.15)$$

The fact that the spandrel shear force was over a large range of drift demands larger than V_N suggests that both the cracked masonry and the timber lintel were able to carry shear over a large deformation range. With respect to Figs. 3.10 and 3.11 it is also noteworthy that the shear crack for loading in the positive direction, which occurred at a rotation of 0.6% (LS 26 and LS 28), did not cause any noticeable drop in shear force. Larger drops in shear force are noticeable for loading in the positive direction during the second cycle at $\theta_{nom} = 1.5\%$ (the shear force at LS 40 is noticeably lower than at LS 38) and at $\theta_{nom} = 2.0\%$ on the way to LS 46. Both drops are believed to be a consequence of the progressive degradation of the South support of the timber lintel that led to the failure mechanism shown in Fig. 3.6.

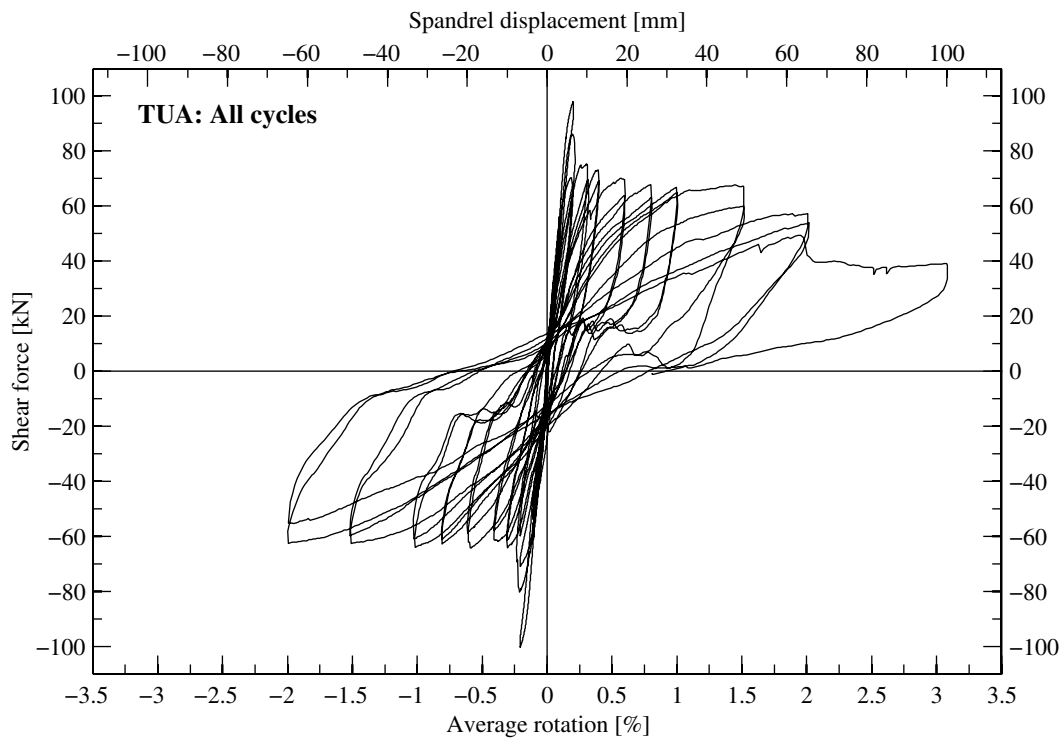


Figure 3.7: TUA: Force-rotation relationship for all cycles.

Variation of the axial load in the piers and spandrel of TUA

The variation of the axial force in the piers in function of the average rotation is shown in Fig. 3.12. Clearly noticeable are the two levels of axial load applied during the entire duration of the test: 140 kN per pier up to LS 15 and 260 kN afterwards. The load follower worked well limiting the maximum variation of the axial load to less than 5% of the target value.

The variation of the axial force in the spandrel in function of the average rotation is shown in Fig. 3.13. Clearly noticeable are the two levels of axial load applied during the entire duration of the test: 80 kN up to LS 15b and 40 kN afterwards. Also the second load follower worked well limiting the maximum variation of the axial load in the spandrel to less than 10% of the target value.

3. Test results for masonry spandrels

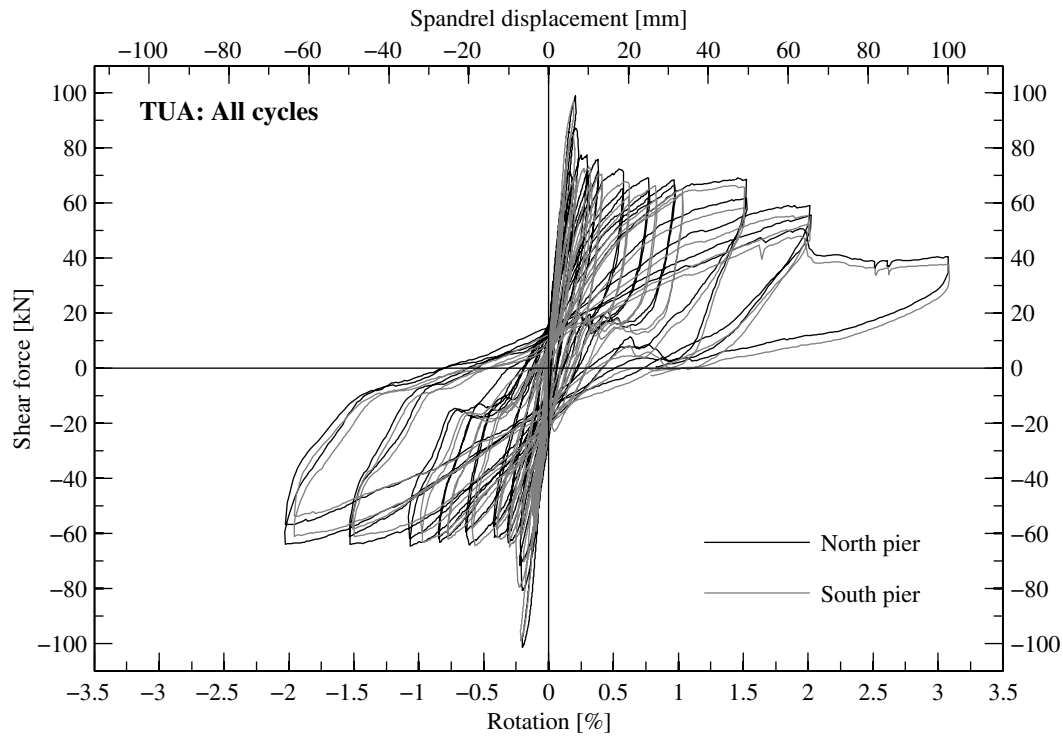


Figure 3.8: TUA: Force-rotation relationship for all cycles showing the non-averaged pier rotations and shear forces.

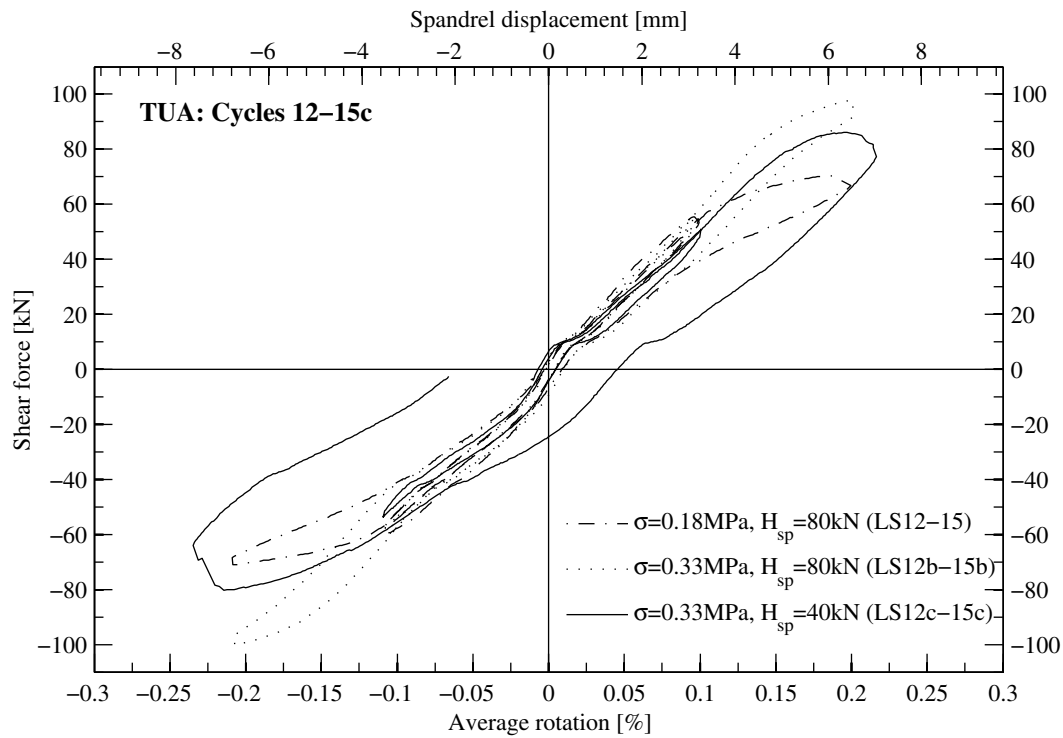


Figure 3.9: TUA: Force-rotation relationship for cycles LS 12-15c.

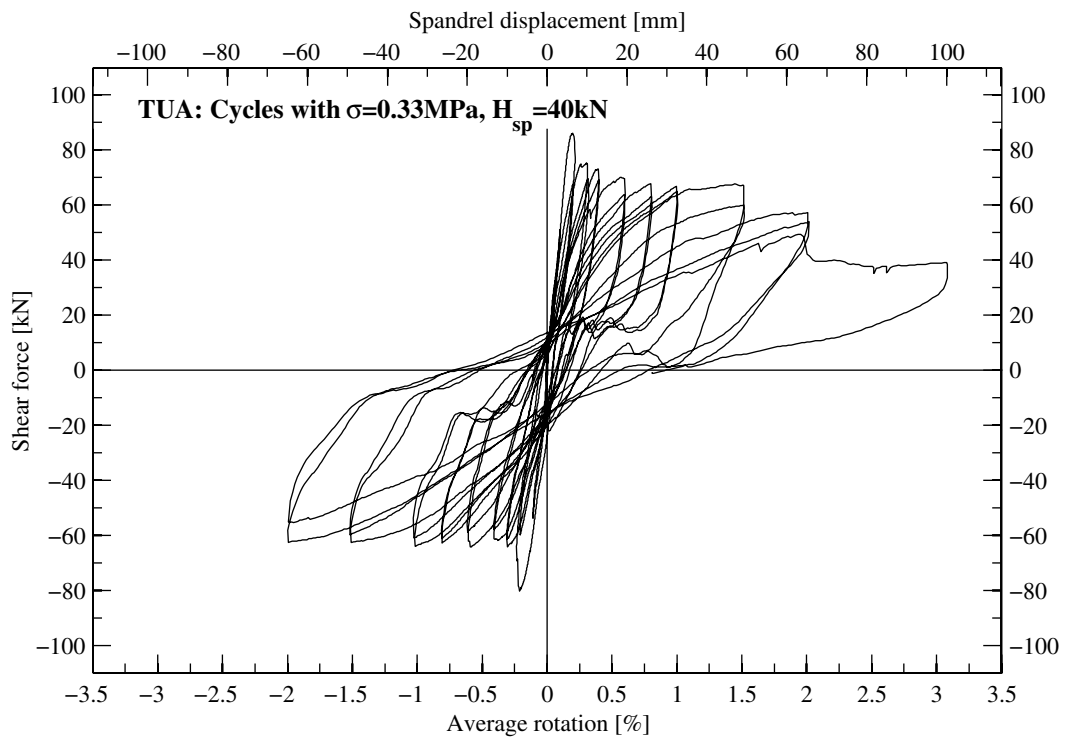


Figure 3.10: TUA: Force-rotation relationship for the cycles with $\sigma = 0.33 \text{ MPa}$ and $H_{sp} = 40 \text{ kN}$ (LS 12c to end).

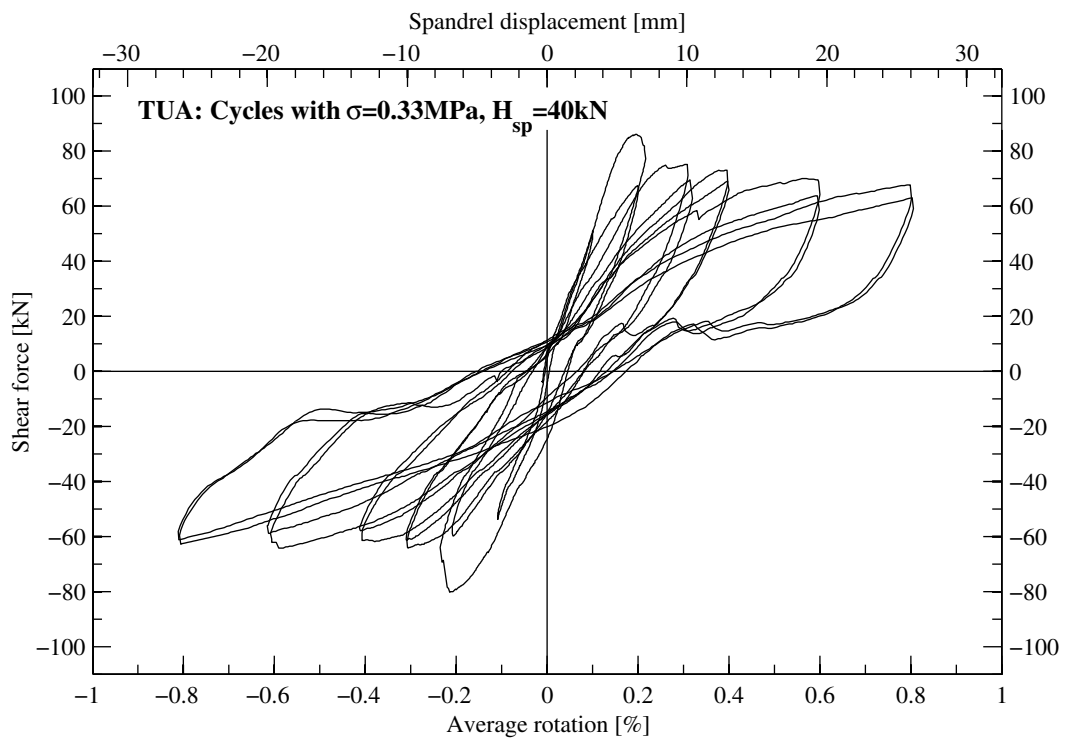


Figure 3.11: TUA: Force-rotation relationship for the cycles up to $\pm 0.8\%$ (LS 12c-33).

3. Test results for masonry spandrels

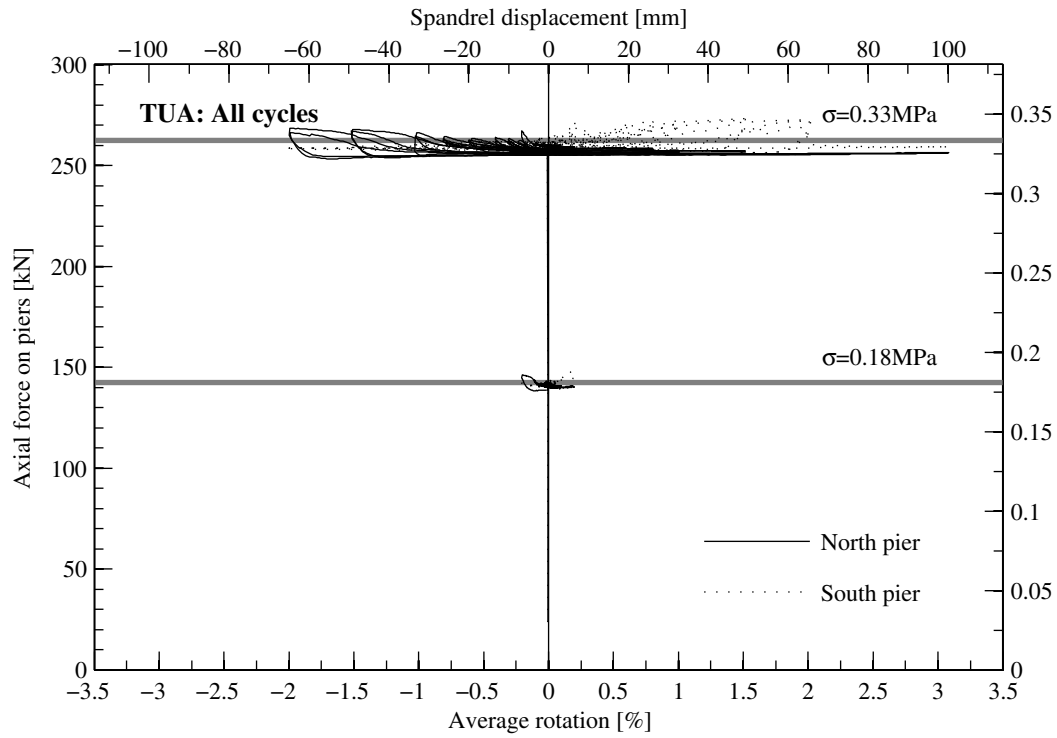


Figure 3.12: TUA: Axial force on piers - rotation relationship for all cycles.

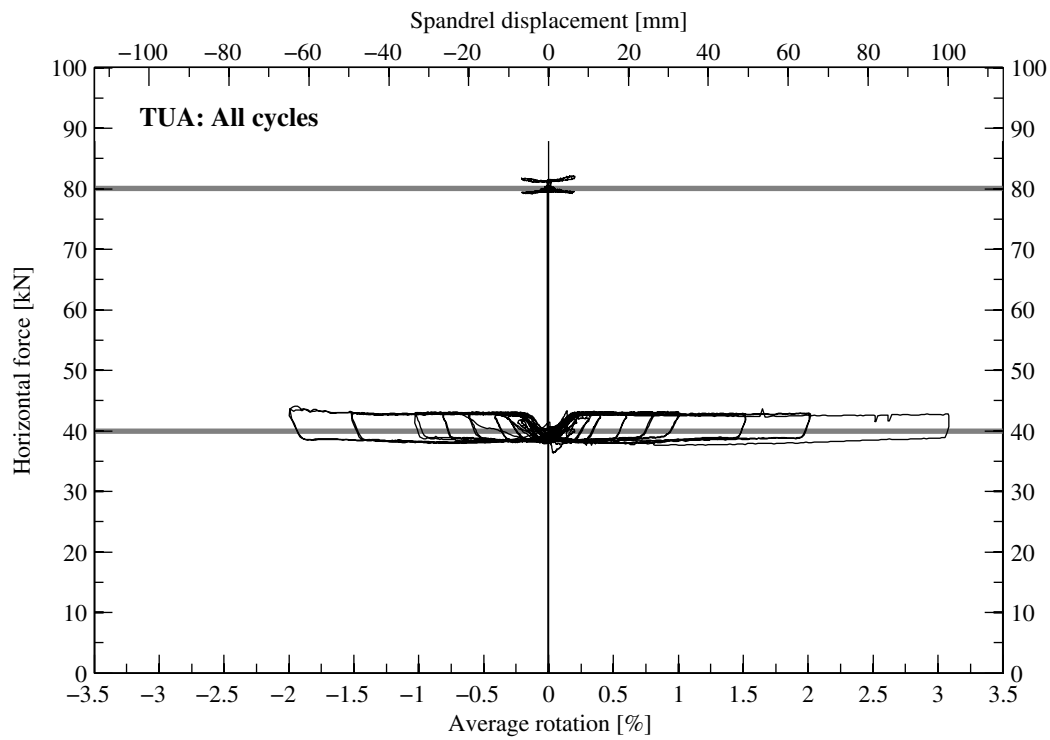


Figure 3.13: TUA: Horizontal force - rotation relationship for all cycles.

Local deformations of the timber lintel of TUA

The average curvatures of the timber lintel of TUA for in-plane bending of the spandrel can be computed from the readings of the chains of LVDTs mounted on the lintel. The curvature distribution along the lintel is plotted in Fig. 3.14 for selected load steps. Particularly noteworthy are the comparatively large curvatures at the North boundary for loading in the positive direction and at the South boundary for loading in the negative direction. In both cases the large curvatures correspond to the locations of negative bending. The large curvatures suggest at least a partial flexural restraint of the timber lintel by the masonry meaning a direct contribution of the former towards the shear carrying capacity of the spandrel. This hypothesis is in agreement with the observation made in the framework of the discussion of the hysteretic behaviour of TUA.

3. Test results for masonry spandrels

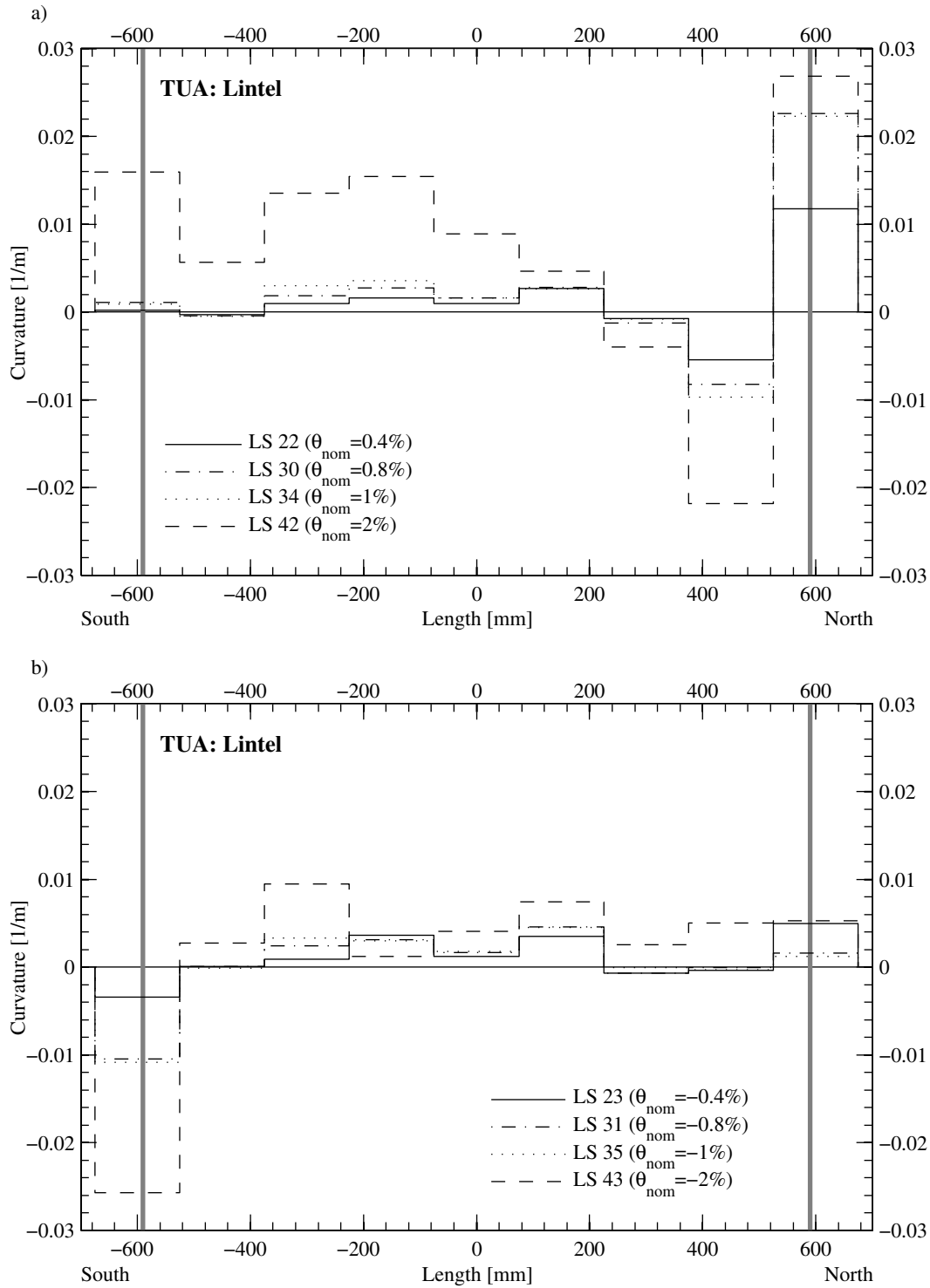
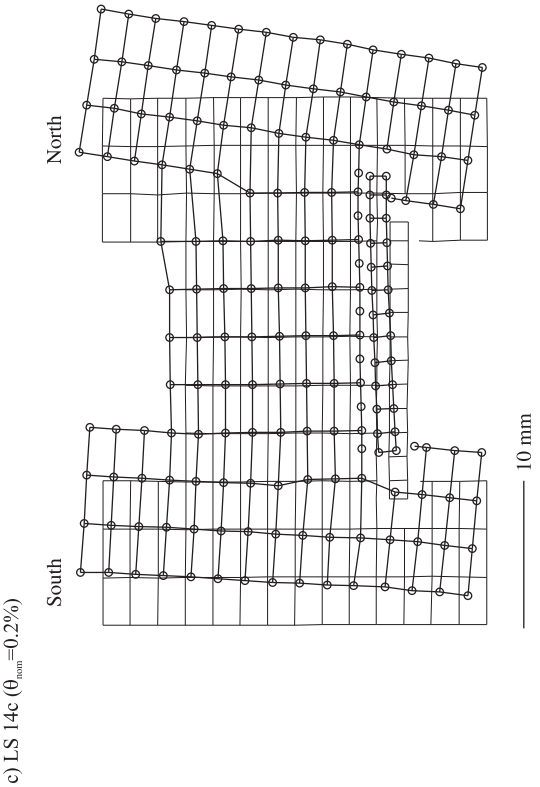
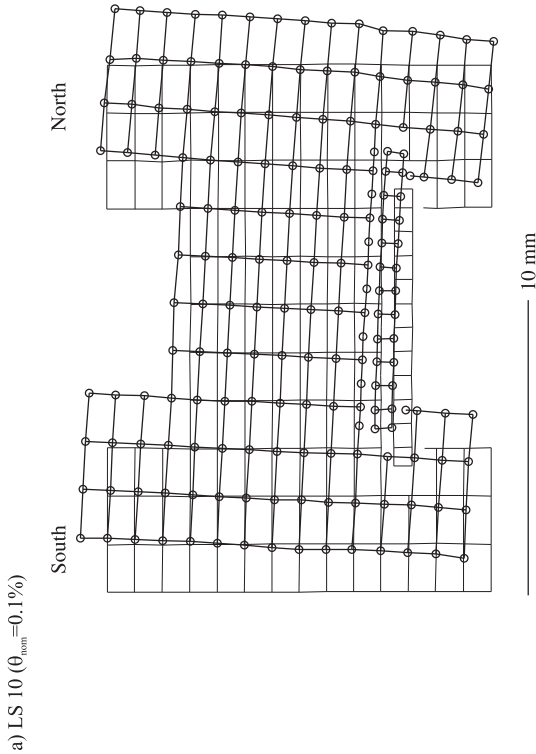
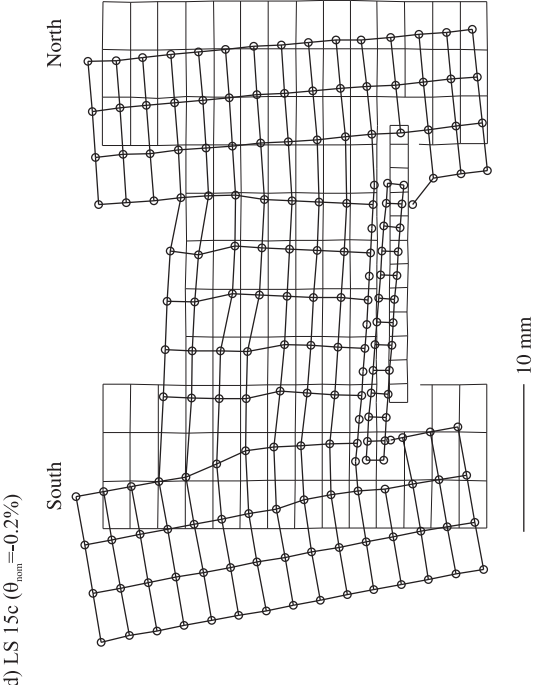
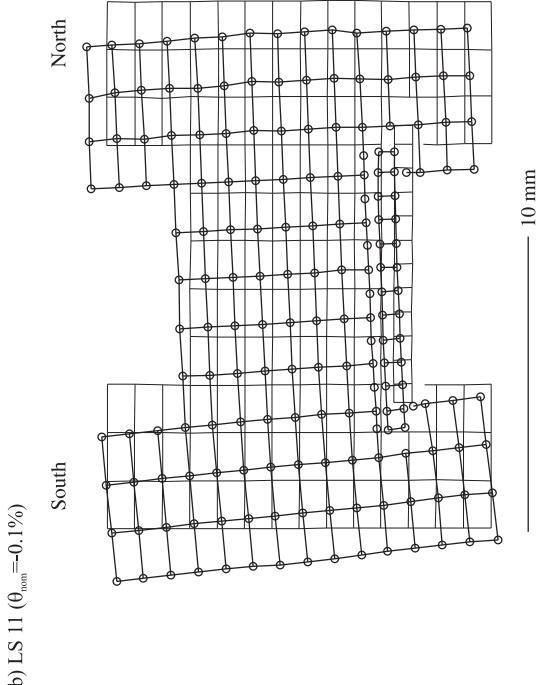


Figure 3.14: TUA: Curvature distribution along the lintel. The thick grey lines symbolise the edges of the piers. The lintel had a bearing length of 200 mm. The results of the LVDTs measuring across the interface of lintel and masonry are not included.

3.2.4 Deformation plots

Figure 3.15 shows the deformed shape of TUA at the first positive as well as the first negative peak of the cycles with amplitudes of $\theta_{nom} = \pm 0.1\%$, $\pm 0.2\%$, $\pm 0.4\%$ and $\pm 0.8\%$. With respect to the dimensions of the test unit, the deformations are amplified by factors ranging between 20 and 160 so that the magnitude of the plotted deformations is for all load steps approximately equal. Shown with thin lines is the undeformed state of the test unit at LS 0. For the cycles with amplitudes larger than $\theta_{nom} = \pm 0.2\%$ the plots show clearly the different deformation mechanisms for the two directions of loading: For the positive direction of loading (LS 14, 22 and 30) the masonry spandrel was accommodating the main part of the deformation demand in flexural cracks left and right of the spandrel. For the negative direction of loading (LS 15, 23 and 31) a shear crack crossing the entire spandrel is clearly visible. The figures show also that the brick below the North end of the timber lintel was pulled out of the surrounding masonry. For the positive direction of loading, the timber lintel remained almost straight, while some slight flexural deformations are noticeable for the negative direction of loading. For LS 10 and LS 11 the spandrel does not show any concentrated deformations, which is in agreement with the observation that at this load steps the masonry spandrel was still uncracked.

3. Test results for masonry spandrels



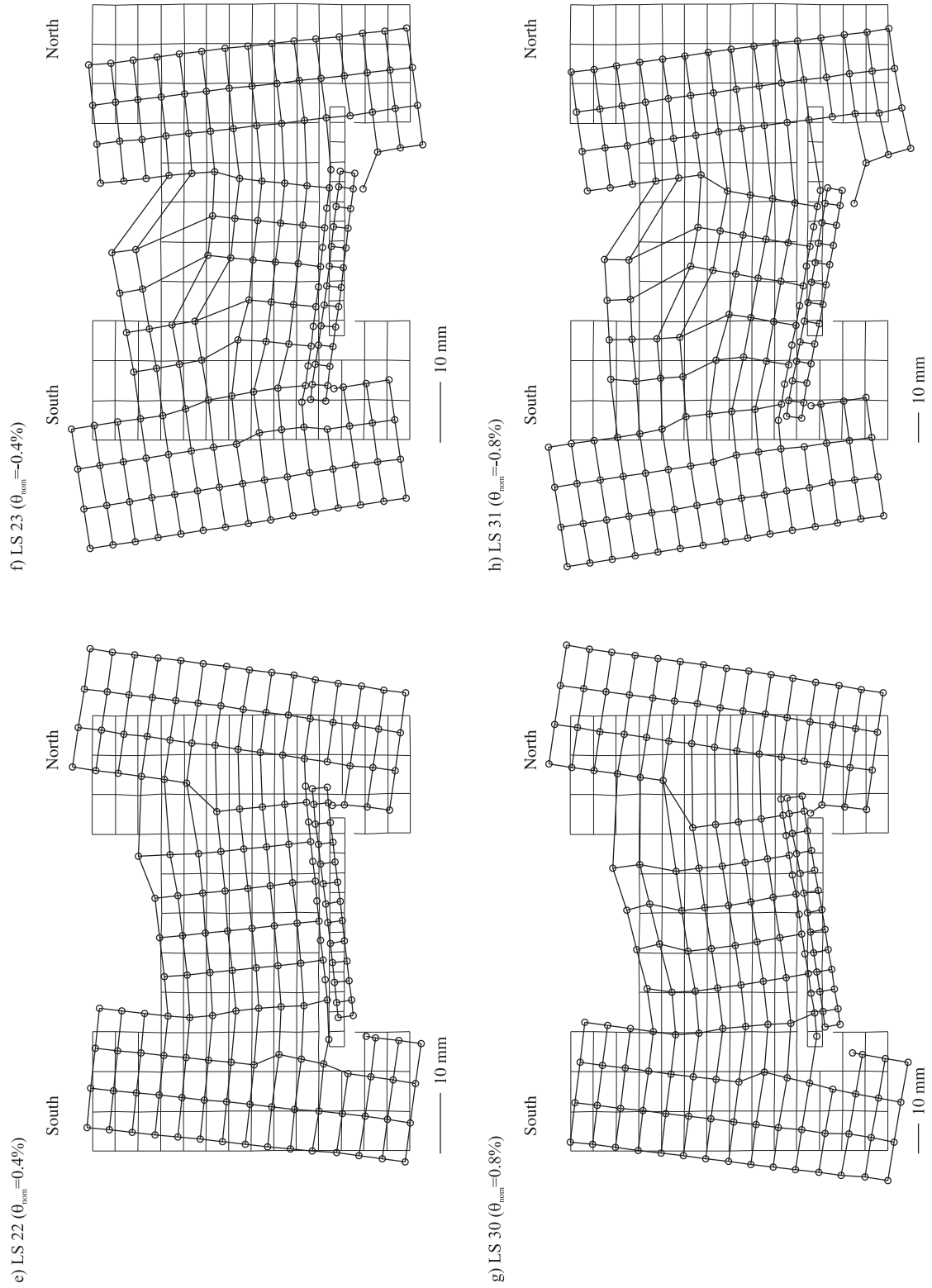


Figure 3.15: TUA: Deformed grid obtained from optical measurements at the first positive and the first negative peak of the cycles with $\theta_{nom} = \pm 0.1\%$, $\pm 0.2\%$, $\pm 0.4\%$ and $\pm 0.8\%$.

3.3 Masonry spandrel TUB

3.3.1 Specific test setup

The forces in all eight vertical rods were applied by means of hollow core jacks tensioning the D13 mm Stahlton bars. The four jacks on one pier were connected to the same load follower. The forces in the horizontal rods were not actively controlled but depended on the elongation of the spandrel. The horizontal rods were assembled from three threaded bars each. Two of these bars were threaded steel bars with 10 mm diameter and a length of 2.3 m each. These were connected by a coupling nut. Details on the material properties of these threaded bars are given in Section 2.5. For the missing length a one metre long D13 mm Stahlton bar was used at the North end of the test unit. This is the type of bar that was also used for the horizontal rods for TUA and had therefore the advantage that the support for the horizontal forces at the North end did not need to be modified. The support at the South end was also identical to that of TUA since it was not dependent on the diameter of the bar. The load cells were placed between the D10 mm and D13 mm bars. In order to straighten the bars and not to obstruct the view on the LEDs, the horizontal rods were post-tensioned to 2.5 kN each at the beginning of the test. The instrumentation was identical to that of TUA. Note that the distance between the top and bottom row of LVDTs on the timber lintel was only 9 cm; for TUA this distance was 10 cm. The latter had to be reduced since the timber lintel was only about 135 mm high instead of 140 mm.

3.3.2 Test observations

At LS 0 the forces in the eight vertical rods were zero; the forces in the two horizontal steel rods were 2.5 kN each. As a first step the vertical rods were prestressed to a force of 60 kN each, which corresponds approximately to an axial stress in the piers of $\sigma = 0.33$ MPa. This load step LS 1 was applied on 03.11.2009. The test unit was tested on the following three days (04 to 06.11.2009). An overview on the load steps covered during each testing day is given in Table 3.2.

Table 3.2: TUB: Testing days and corresponding load steps.

Testing day	Load steps carried out
03.11.2009	LS 1
04.11.2009	LS 2 - LS 19
05.11.2009	LS 20 - LS 35
06.11.2009	LS 36 - LS 39

Before the onset of testing a very fine crack was detected and marked at the top and sides of the timber lintel. During the first load steps a small crack at the base of the piers developed (analogue to the base cracks described in Section 3.2.2 for $\sigma = 0.18$ MPa and $H_{sp} = 80$ kN). However, the maximum crack width did not exceed 0.5 mm and testing was therefore continued. The first short crack in the spandrel appeared when loading to LS 13 (last peak of cycles with $\theta_{nom} = \pm 0.1\%$). The crack was located at the South top corner of the spandrel and followed the mortar joints. Flexural cracks at both ends of the spandrel appeared during the cycles with $\theta_{nom} = \pm 0.2\%$ (LS 14-17). The cracks were rather vertical and passed through several bricks. For both directions of loading the lintel was pulled out of the surrounding masonry by about 2 mm indicating that the spandrel was growing in length. As a result the axial force in the horizontal rods

was increasing. Figure 3.16 shows the crack pattern at LS 23 ($\theta_{nom} = -0.4\%$). Figure 3.17 shows for the same load step a close-up photo of the lintel ends. For the negative direction of loading the lintel is pulled out of the North support (Fig. 3.17b). At LS 30 a small stair-stepped crack formed in the lower part of the South pier. At LS 31 the equivalent crack formed in the North pier. These cracks correspond to those that formed in TUA at LS 26 and marked the onset of the development of the failure mechanism of the support of the timber lintel.

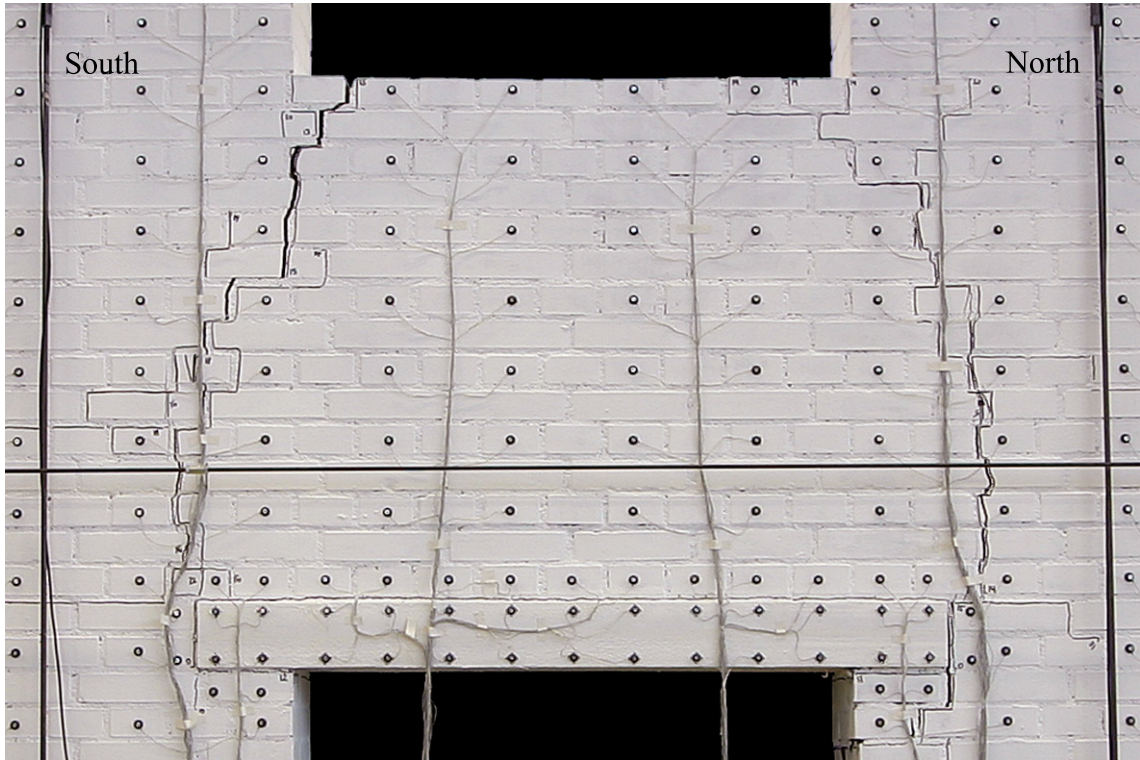


Figure 3.16: TUB: Crack pattern of spandrel at LS 23. Drift towards South with $\theta_{nom} = -0.4\%$.

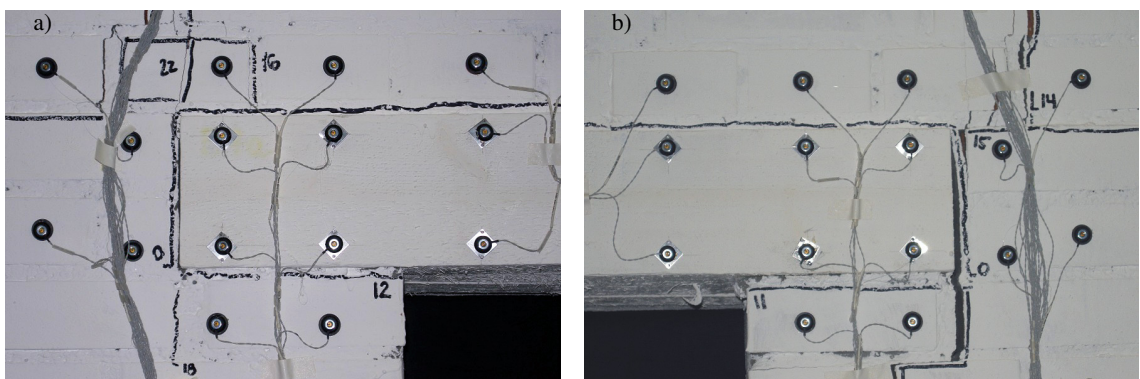


Figure 3.17: TUB: South (a) and North (b) ends of lintel at LS 23. Drift towards South with $\theta_{nom} = -0.4\%$.

During the cycles with $\theta_{nom} = \pm 1.0\%$ (LS 34-37) the bricks supporting the lintel at its North end deteriorated significantly. Most likely due to the large shear stresses that were generated by the pull-out forces of the lintel, the bricks supporting the lintel detached from other bricks or broke in two. Compared to the North support, the South support of the lintel was still in rather good

3. Test results for masonry spandrels

condition (Fig. 3.18). Starting at LS 37 the North end of the spandrel was loosely supported by the laboratory crane to avoid a catastrophic collapse of the spandrel onto the floor. The test unit failed shortly afterwards when loading to LS 39 ($\theta_{nom} = -1.5\%$). Almost simultaneously did the North support fail and the West horizontal D10 threaded bar fracture. It was not possible to say which of the two failure mechanisms occurred first. The bar that fractured was the one with label "D" (see Section 2.5). After the failure the spandrel still carried its own weight; the crane support was not activated. Figures 3.19 and 3.20 show the crack pattern at the last two load steps of TUB.

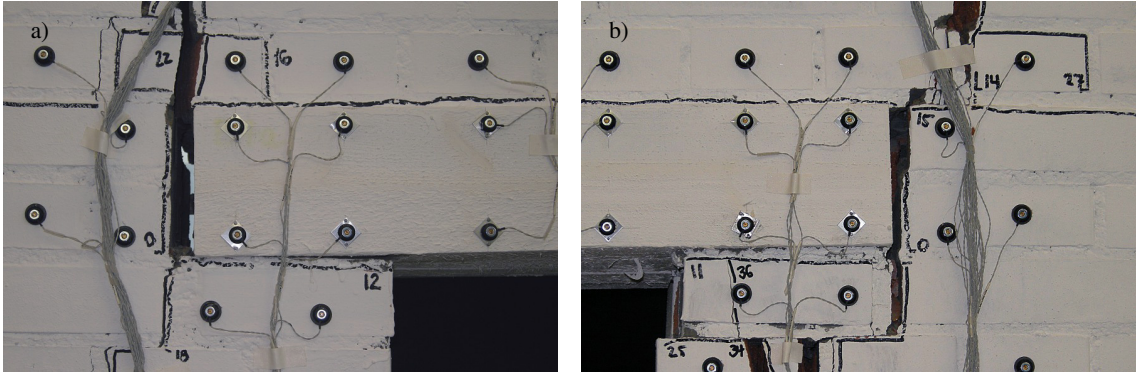


Figure 3.18: TUB: South (a) and North (b) ends of lintel at LS 36. Drift towards North with $\theta_{nom} = 1.0\%$.



Figure 3.19: TUB: Crack pattern of spandrel at LS 38. Drift towards North with $\theta_{nom} = 1.5\%$.

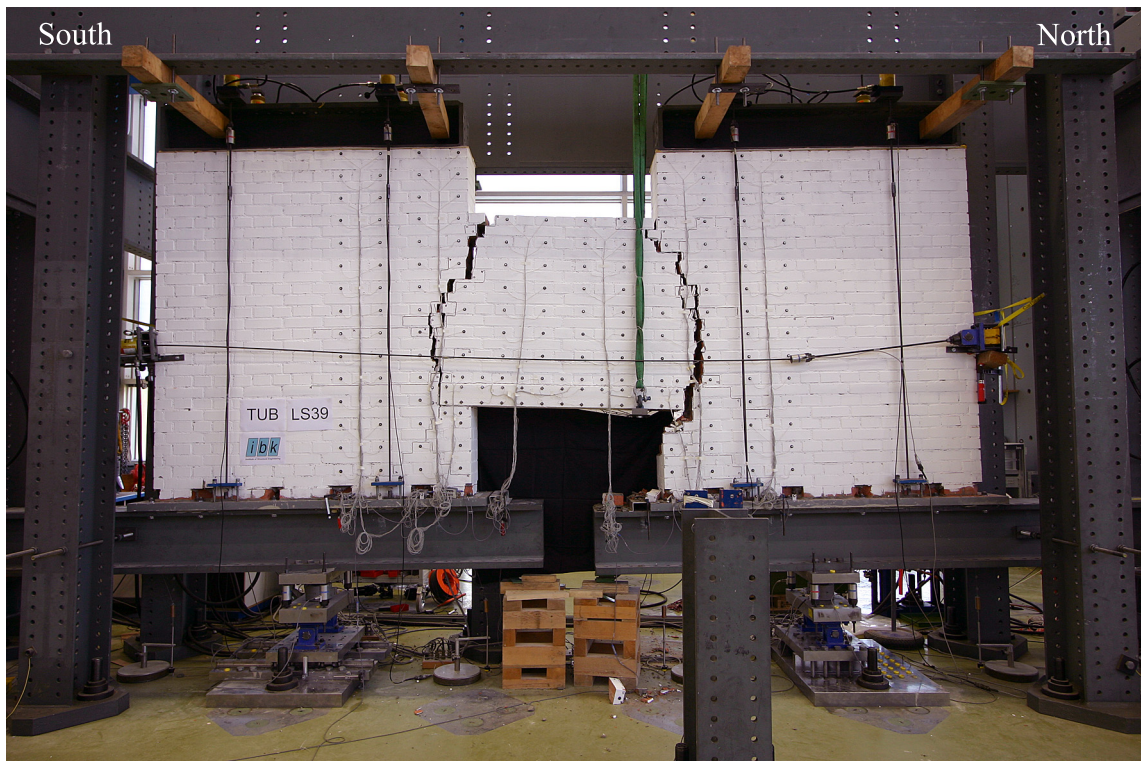


Figure 3.20: TUB: Crack pattern of spandrel at LS 39. Drift towards South with $\theta_{nom} = -1.5\%$ (failure of TUB).

3.3.3 Test results

In this section key results of TUB are presented and briefly discussed often making reference to observations made during the test. The hysteretic behaviour of the test unit in terms of spandrel shear force vs. average rotation is presented first. Afterwards the variation of the axial load acting on the piers and on the spandrel is discussed. Finally the deformations experienced by the timber lintel are addressed in terms of local curvature distribution.

Hysteretic behaviour of TUB

The global average hysteretic behaviour of the test unit is shown in Fig. 3.21 and a close-up of the same cycles up to a drift of $\pm 0.8\%$ is shown in Fig. 3.22. As it was the case for TUA, the hysteretic behaviour calculated independently from the data stemming from the South and the North pier, respectively (see Fig. 3.23), confirms that the averaged hysteresis curve in Fig. 3.21 can be considered representative of the whole test and it will be briefly discussed in the following.

The hysteresis curve of TUB shows a nearly elastic behaviour up to a $\pm 0.1\%$ rotation reaching identical shear strengths in the positive and in the negative loading direction, i.e. 69 kN (LS 10) and -69 kN (LS 11). When loading to LS 14 first significant cracking of the spandrel occurred (see previous section) and a peak shear force of 82 kN could be reached at $\theta = 0.14\%$. At this point the axial load in the spandrel was 5 kN (see Fig. 3.25), i.e. significantly lower compared to the axial load applied to TUA at the beginning of the test. This could explain the fact that in TUB no shear crack in the spandrel developed, however, it is worth noting that the shear force for which

3. Test results for masonry spandrels

a shear crack formed at LS 15c of TUA (see Fig. 3.9) was basically the same as the maximum force reached by TUB. When LS 14 was reached at $\theta_{nom} = 0.2\%$ the shear force had dropped to 75 kN. During the following reversal to LS 15 further significant cracking of the spandrel occurred ($\theta = 0.06\%$, $V = -48$ kN) and by the time LS 15 was reached at $\theta_{nom} = 0.2\%$ the shear force had "increased" to just -56 kN. Afterwards, the maximum shear force reached during reversals of the same amplitude was constantly about 5 to 8 kN larger for loading in the positive direction than for loading in the negative direction.

For cycles with θ_{nom} larger than $\pm 0.2\%$ an increase in the peak shear force can be noticed. The increase in shear force is due to the increase of axial load in the spandrel (see Fig. 3.25) triggered by the axial elongation of the spandrel due to opening of the cracks. For example, at LS 38 ($\theta_{nom} = 1.5\%$) a shear force of 78 kN could be reached; at the same time the axial load in the spandrel was 66 kN (see Fig. 3.25). The theoretical maximum contribution of the axial load to the shear strength was hence 71 kN (see Section 3.2.3) suggesting, similarly to TUA, a direct residual contribution of the masonry and of the timber lintel to the shear strength of the spandrel despite the large cracks characterising the deformed shape of TUB at LS 38 (see Fig. 3.19). At lower drifts, the direct contribution of masonry and lintel was probably even larger due the minor damage. To this purpose consider e.g. LS 30 ($\theta_{nom} = 0.8\%$) featuring a shear force of 79 kN and an axial load in the spandrel of 54 kN. On the way to LS 39 the maximum shear force reached by the test unit was -66 kN with an axial load in the spandrel of 68 kN when failure occurred as described in the previous Section 3.3.2.

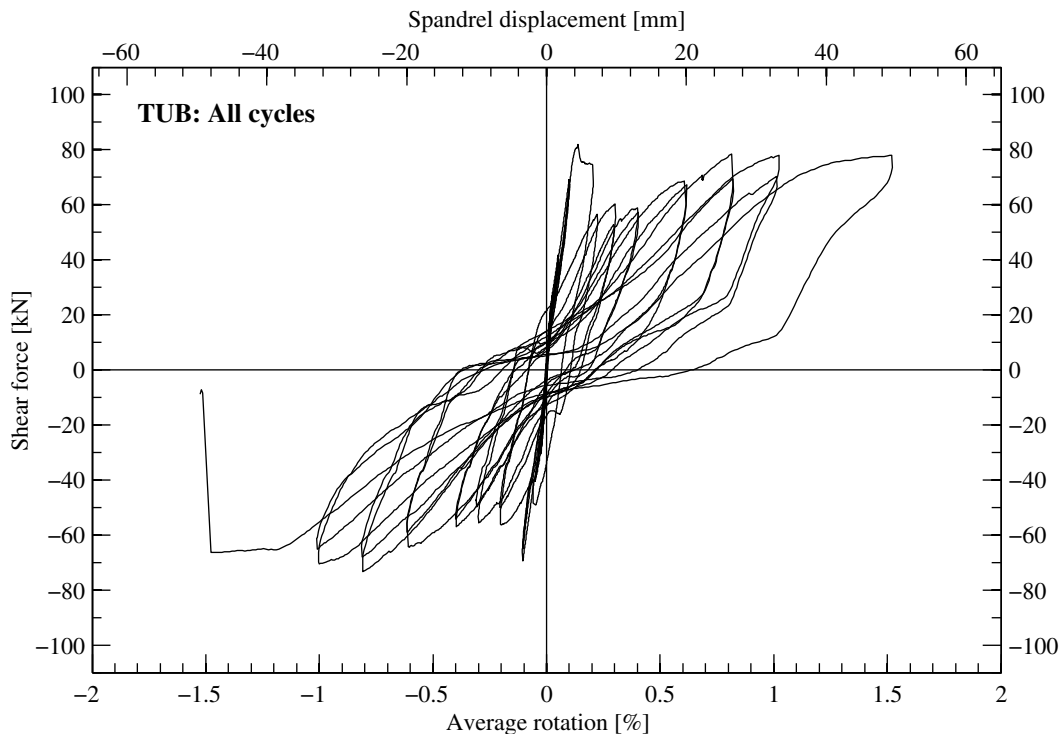


Figure 3.21: TUB: Force-rotation relationship for all cycles.

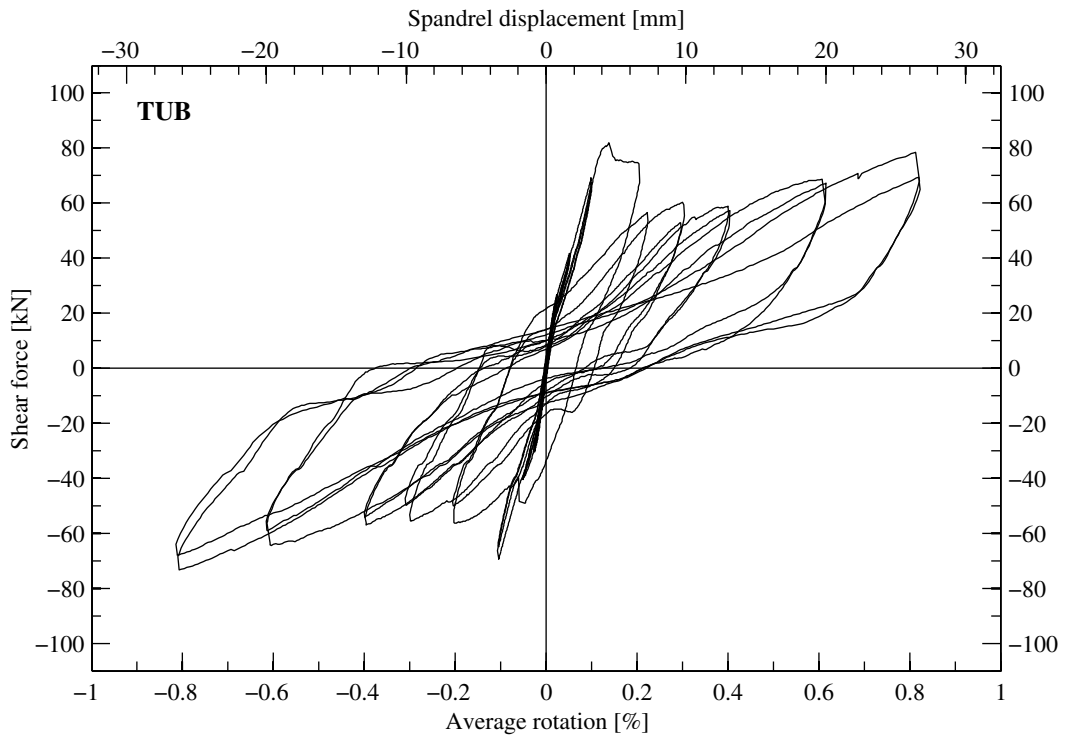


Figure 3.22: TUB: Force-rotation relationship for the cycles up to $\pm 0.8\%$ (LS 2-33).

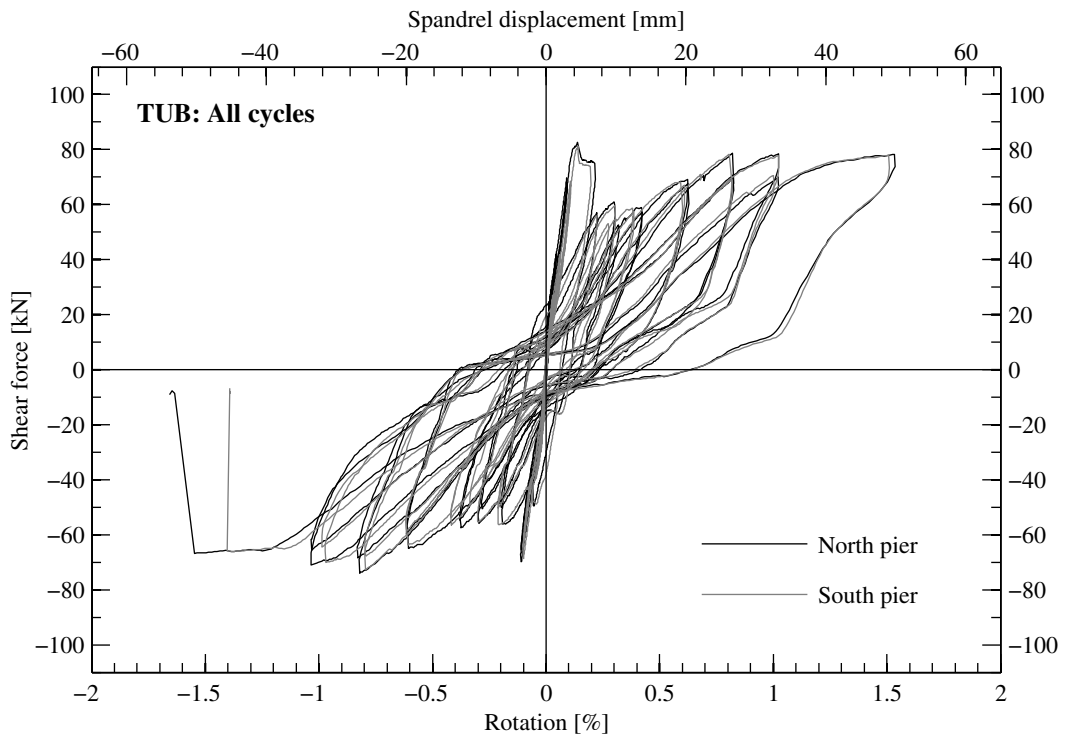


Figure 3.23: TUB: Force-rotation relationship for all cycles showing the non-averaged pier rotations and shear forces.

Variation of the axial load in the piers and spandrel of TUB

The variation of the axial force in the piers in function of the average rotation is shown in Fig. 3.24. The deviance to the target value of 264 kN is even smaller compared to TUA due to the fact that for TUB two independent load followers could be used; one to control the axial load of each pier. Also in this case the maximum variation of the axial load was always less than 5% of the target value.

The variation of the axial force in the spandrel in function of the average rotation is shown in Fig. 3.25. The horizontal lines labelled $F_{y,dyn} = 61$ kN and $F_{u,dyn} = 71$ kN represent the dynamic yield and the ultimate strength of the D10 mm threaded bars, respectively. The third line represents the static value of the ultimate strength of these threaded bars ($F_{u,stat} = 67$ kN). These values corresponds to average values measured during the material tests on the bars (see Section 2.5). As long as no cracking of the spandrel occurred, the total force in the horizontal rods remained basically constant at 5 kN which corresponds to the initial post-tensioning. As soon as cracks occurred in the spandrel at a rotation between ± 0.1 and $\pm 0.2\%$ the increase in force is clearly noticeable and is nearly proportional to the rotation. It is noteworthy that the force at zero rotation tended to increase with increasing amplitude of the cycles suggesting a permanent elongation of the spandrel. In cycles with $\theta_{nom} = \pm 1.5\%$ the yielding of the horizontal bars is clearly visible. The maximum attained force in the threaded bars was larger than $F_{u,stat}$ but smaller than $F_{u,dyn}$.

At the end of the test of TUB the axial load in the spandrel was larger than in TUA at onset of shear cracking in the spandrel. Despite this fact no shear cracking of the spandrel occurred in TUB as clearly shown in Fig. 3.20.

Local deformations of the timber lintel of TUB

The curvature distribution along the timber lintel (Fig. 3.26) suggests that the timber lintel of TUB was subjected to smaller deformations than the timber lintel of TUA (Fig. 3.14). Unlike for TUA, there was no clear change in signs of curvatures when changing the direction of loading. It is likely that the different failure mechanism of the URM spandrels of TUA and TUB imposed a different deformation demand on the timber lintels. A more in-depth analysis of this observation will be carried out in a future study.

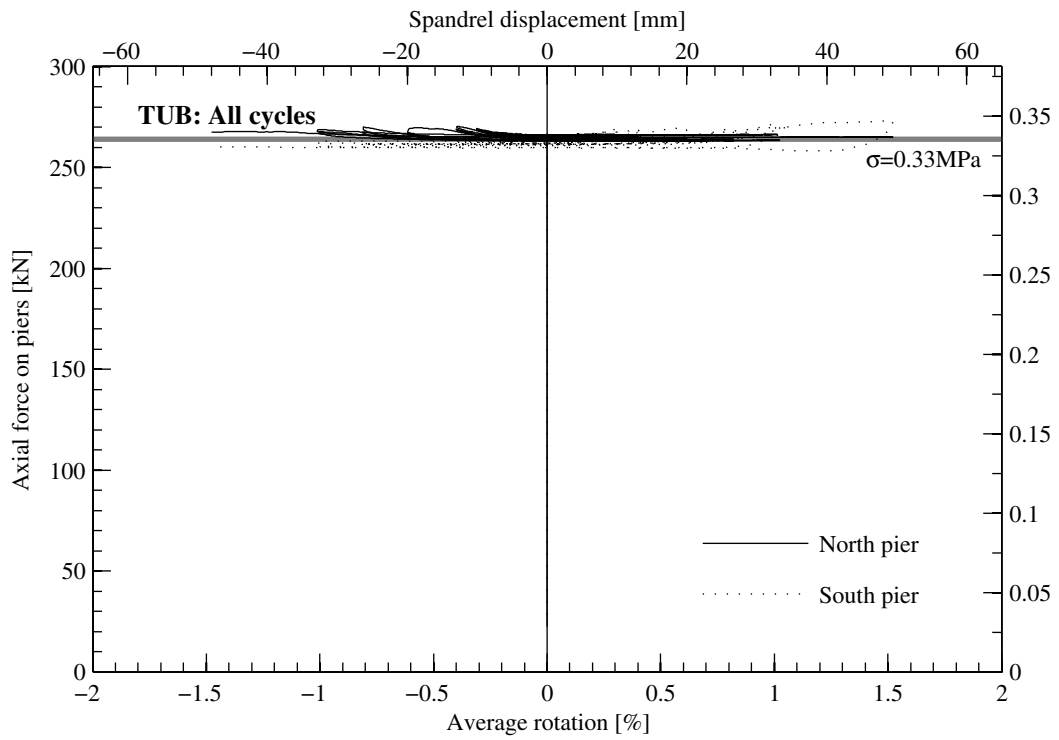


Figure 3.24: TUB: Axial force on piers - rotation relationship for all cycles.

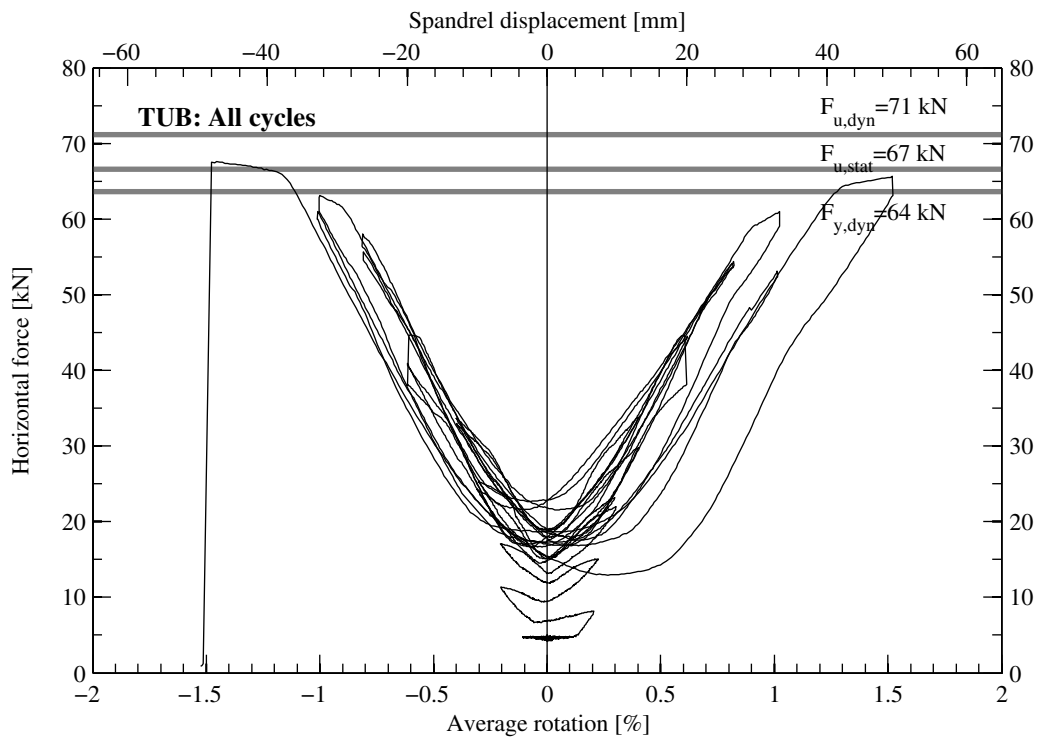


Figure 3.25: TUB: Horizontal force - rotation relationship for all cycles.

3. Test results for masonry spandrels

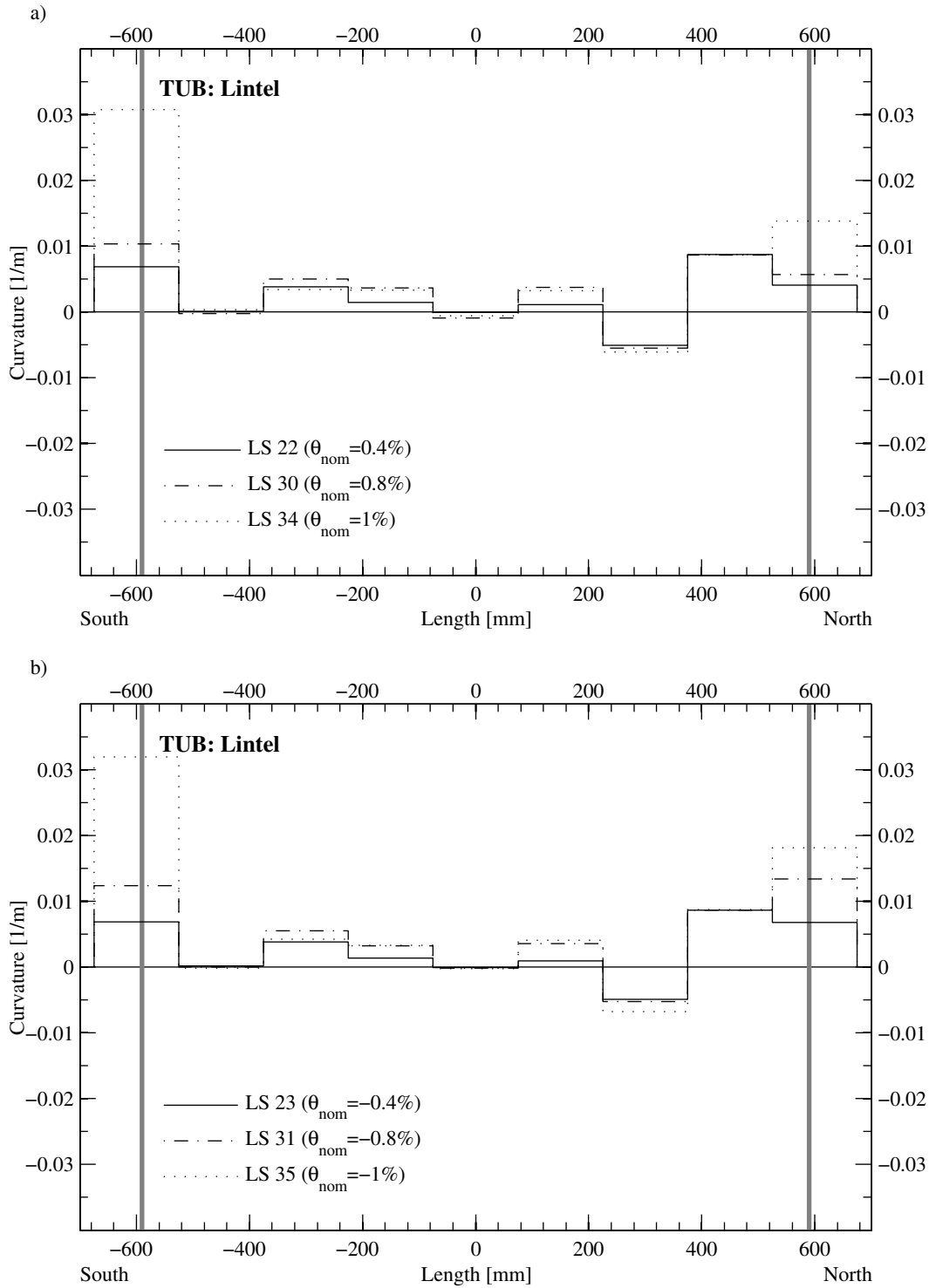


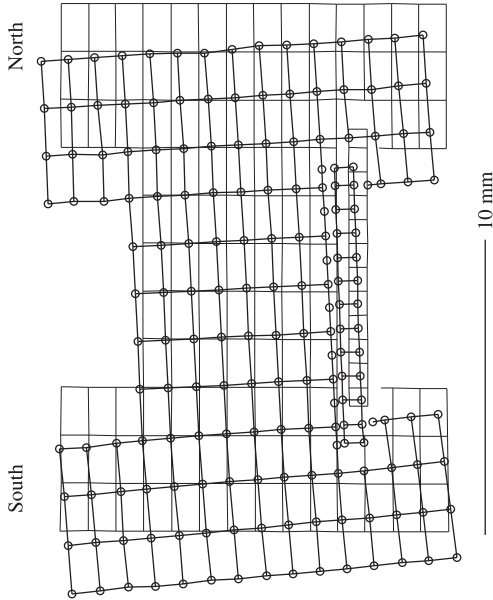
Figure 3.26: TUB: Curvature distribution along the lintel. The thick grey lines symbolise the edges of the piers. The lintel had a bearing length of 200 mm. The results of the LVDTs measuring across the interface of lintel and masonry are not included.

3.3.4 Deformation plots

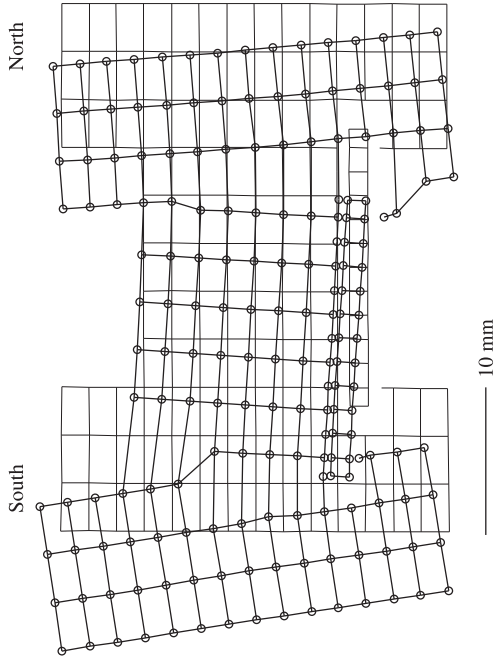
Figure 3.27 shows the deformed shape of TUB at the first positive as well as the first negative peak of the cycles with amplitudes of $\theta_{nom} = \pm 0.1\%$, $\pm 0.2\%$, $\pm 0.4\%$ and $\pm 0.8\%$. With respect to the dimensions of the test unit, the deformations are amplified by factors ranging between 20 and 160 so that the magnitude of the plotted deformations is for all load steps approximately equal. Shown with thin lines is the undeformed state of the test unit at LS 0. The deformation plots for TUB show how the flexural mechanism of the masonry spandrel evolved: At LS 10 and LS 11, the spandrel was still uncracked. In the following, flexural cracks formed at both ends of the spandrel and grew wider with increasing rotation demand while the body of the spandrel remained virtually undeformed. The timber lintel was subjected to slight bending for loading in the positive direction but remained almost straight for loading in the negative direction.

3. Test results for masonry spandrels

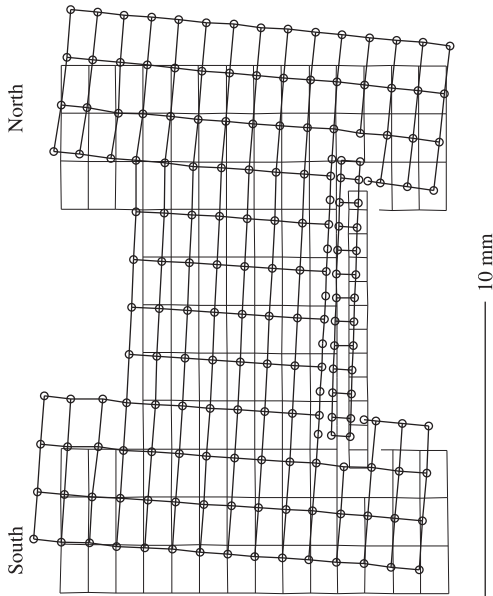
b) LS 11 ($\theta_{\text{min}} = -0.1\%$)



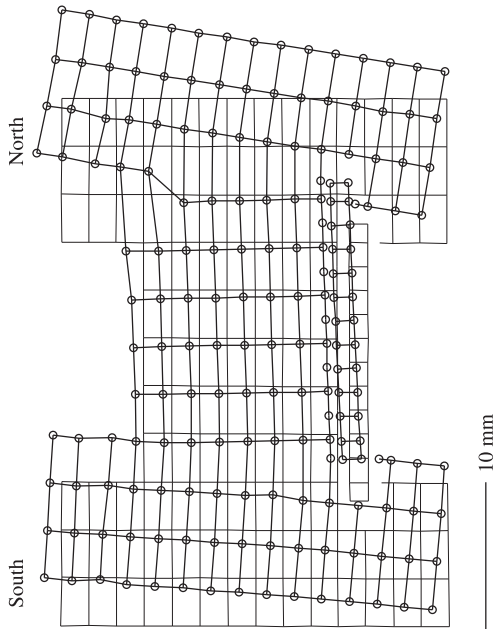
d) LS 15 ($\theta_{\text{min}} = -0.2\%$)



a) LS 10 ($\theta_{\text{min}} = 0.1\%$)



c) LS 14 ($\theta_{\text{min}} = 0.2\%$)



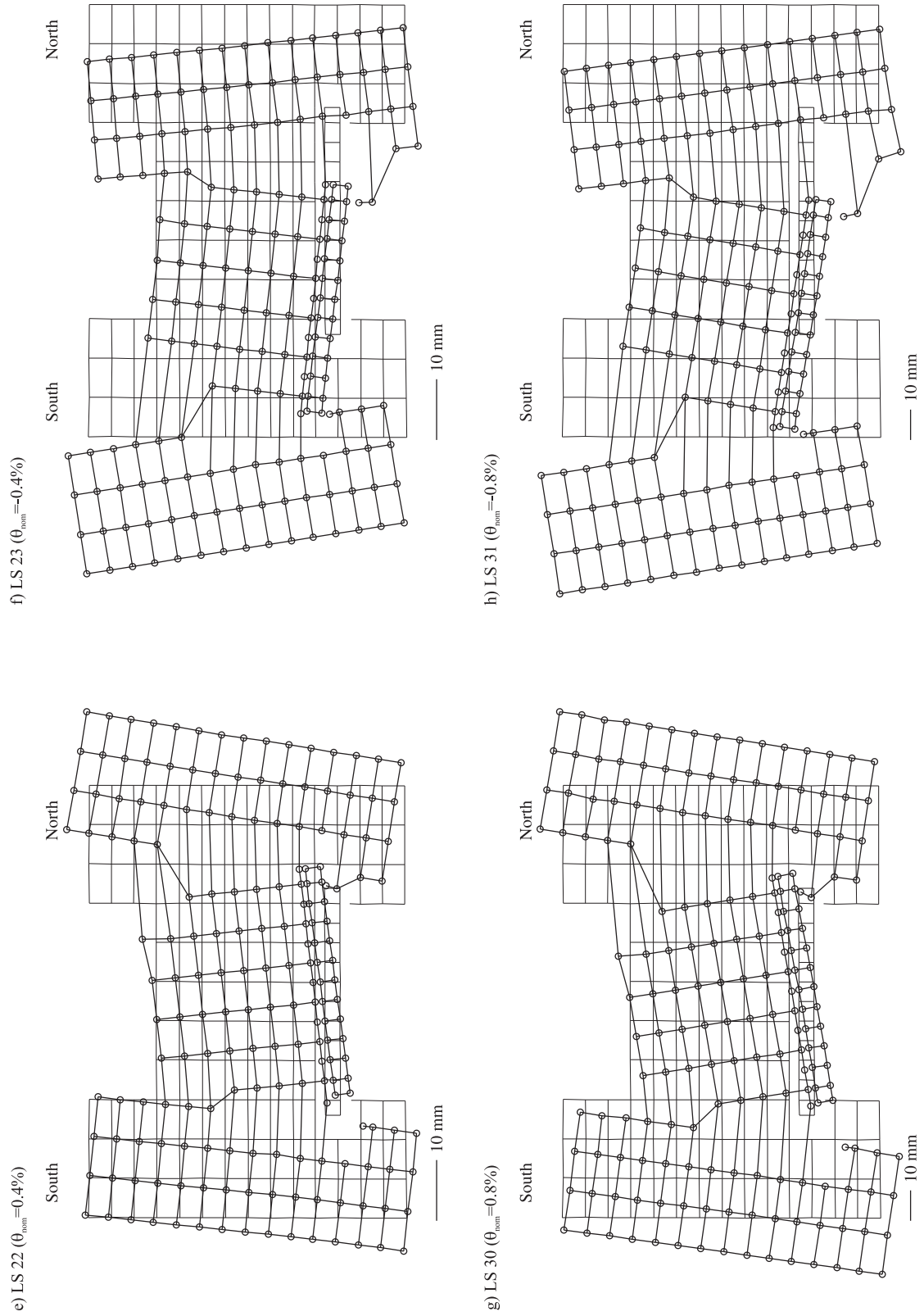


Figure 3.27: TUB: Deformed grid obtained from optical measurements at the first positive and the first negative peak of the cycles with $\theta_{nom} = \pm 0.1\%$, $\pm 0.2\%$, $\pm 0.4\%$ and $\pm 0.8\%$.

3.4 Masonry spandrel TUC

3.4.1 Specific test setup

The forces in the horizontal rods applying the axial load on the spandrel were kept constant during the entire tests by means of one load follower. As for TUA, the horizontal rods were assembled from D13 mm Stahlton bars of different length that were connected by means of coupling nuts. The load cells were placed between two of these bars. The LVDTs that for TUA and TUB had been used to measure the deformations of the West face of the timber lintel were discarded for TUC. The forces in all eight vertical rods were applied by means of hollow core jacks. The four jacks on one pier were connected to the same hand pump. A safety valve mounted between hand pump and hollow core jacks ensured that the forces in the rods could not exceed about ~ 80 kN per rod. If the forces dropped below ~ 75 kN per rod, the hollow core jacks were pumped up by means of the hand pump. This setup replaced the load followers used for TUA and TUB. An alternative setup was required since only two load followers were available. This setup was considered superior to the one used for TUA, where the eight hollow core jacks on both piers were controlled by the same load follower. Furthermore, the capacity of the load followers in terms of maximum output pressure would have not been enough to post-tension the vertical rods to 80 kN each.

3.4.2 Test observations

At LS 0 the forces in the eight vertical and in the two horizontal rods were zero. As a first step the vertical rods were prestressed to a force of 80 kN each, which corresponds approximately to an axial stress in the piers of $\sigma = 0.43$ MPa. This load step was called LS 1a. Then, the horizontal rods were prestressed to a force of 40 kN each, i.e. the total horizontal force was 80 kN. This load step was called LS 1b. The vertical and horizontal forces were applied on 20.12.2009. The test unit was tested on two days: 21.12.2009 and 23.12.2009. An overview on the load steps covered during each testing day is given in Table 3.3.

Table 3.3: TUC: Testing days and corresponding load steps.

Testing day	Load steps carried out
20.12.2009	LS 1a & LS 1b
21.12.2009	LS 2 - LS 19
23.12.2009	LS 20 - LS 45

The first crack in the spandrel appeared at LS 3 ($\theta_{nom} = -0.025\%$). Its onset was located between the sixth and seventh brick of the arch (counting from the South end to the North end of the arch). The crack reached vertically upwards to about midheight of the spandrel. Small cracks appeared also at the base of the piers, as they had also been observed for TUA and TUB. However, the width of these cracks remained always rather small. At LS 6 and LS 8 ($\theta_{nom} = 0.05\%$) this crack grew in length but turned from a flexural crack into a shear crack (stair-stepped crack). At LS 9 a second crack formed within the spandrel, which was almost symmetrical to the first flexural crack albeit shorter and it ended just above the arch. At LS 10 ($\theta_{nom} = 0.1\%$) the already existing stair-stepped crack grew in length and now spanned the entire spandrel. Two rows above this crack a second shear crack developed. At LS 15 ($\theta_{nom} = -0.2\%$) a shear crack in the opposite direction as the existing two developed; the new shear crack pointed from the top North corner to

the bottom South corner of the spandrel. With this crack the crack pattern of the spandrel turned rather symmetrical with respect to the central axis of the spandrel. The formation of the cracks up to LS 15 can be tracked in Fig. 3.28. The extension that a particular crack reached at a specific load step is marked on the test unit by means of a short cross-line and the number of the corresponding load step.

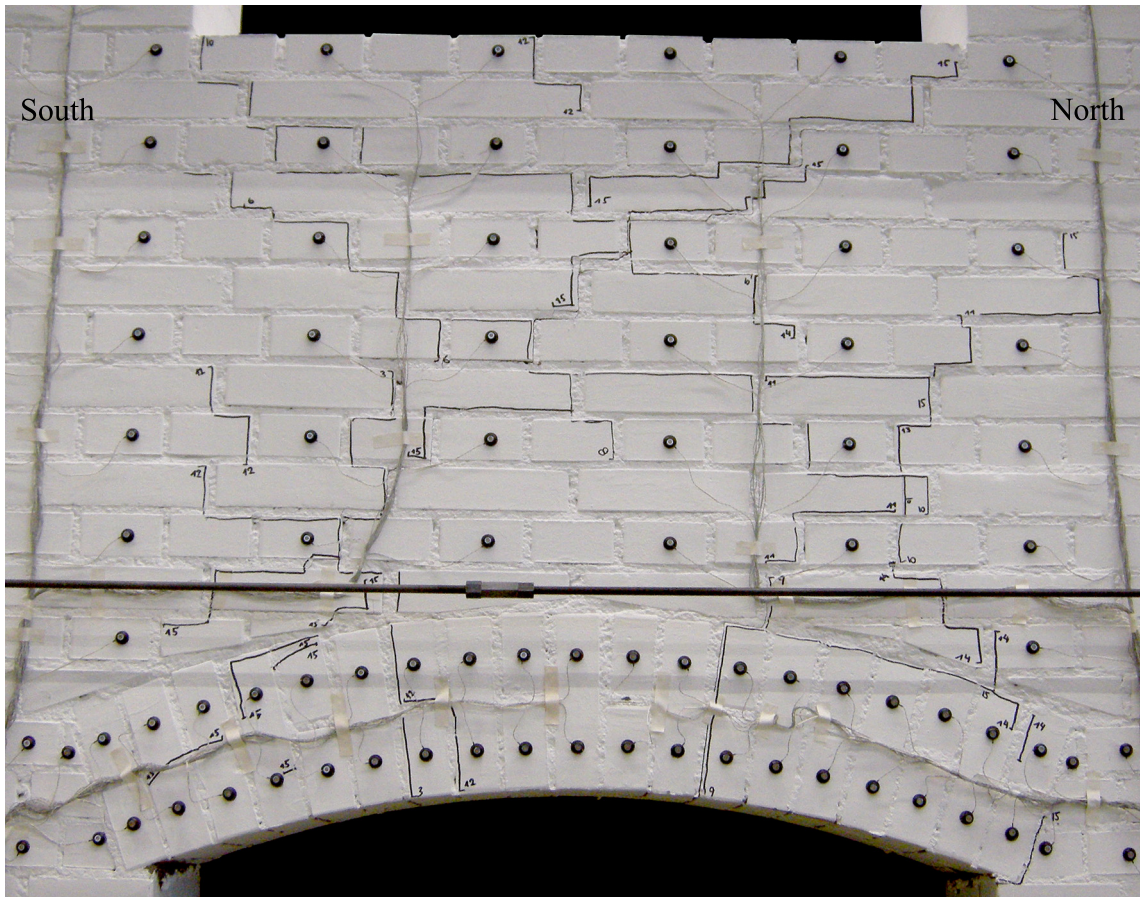


Figure 3.28: TUC: Crack pattern of spandrel at LS 15. Drift towards South with $\theta_{nom} = 0.2\%$.

During the cycles with $\theta_{nom} = \pm 0.3\%$ (LS 18-21) the shear cracks opened up significantly and the shear force carried by the spandrel dropped. With increasing deformation demand, the hinges in the arch became apparent: The hinges formed at about the location of the first flexural cracks, i.e. at approximately one third and two thirds of the arch length. Additional small cracks developed; the diagonal shear cracks, however, remained the widest cracks within the spandrel. Figure 3.29 shows the crack pattern at LS 22 ($\theta_{nom} = 0.4\%$) while Fig. 3.30 shows the crack pattern at LS 23 ($\theta_{nom} = -0.4\%$).

In the following the damage to the arch increased with each cycle. New cracks formed also in the spandrel. Apart from the diagonal shear cracks most other cracks remained rather thin. This is particularly evident on photos taken from the back (West face) of the spandrel where the cracks were not marked with a pen (Fig. 3.31 and Fig. 3.32). The photos also show that the damage to the spandrel is not symmetric about the spandrel axis. The shear crack opening for loading in the positive direction (on Fig. 3.32a it is the crack starting in the top left corner) does not end at the end

3. Test results for masonry spandrels

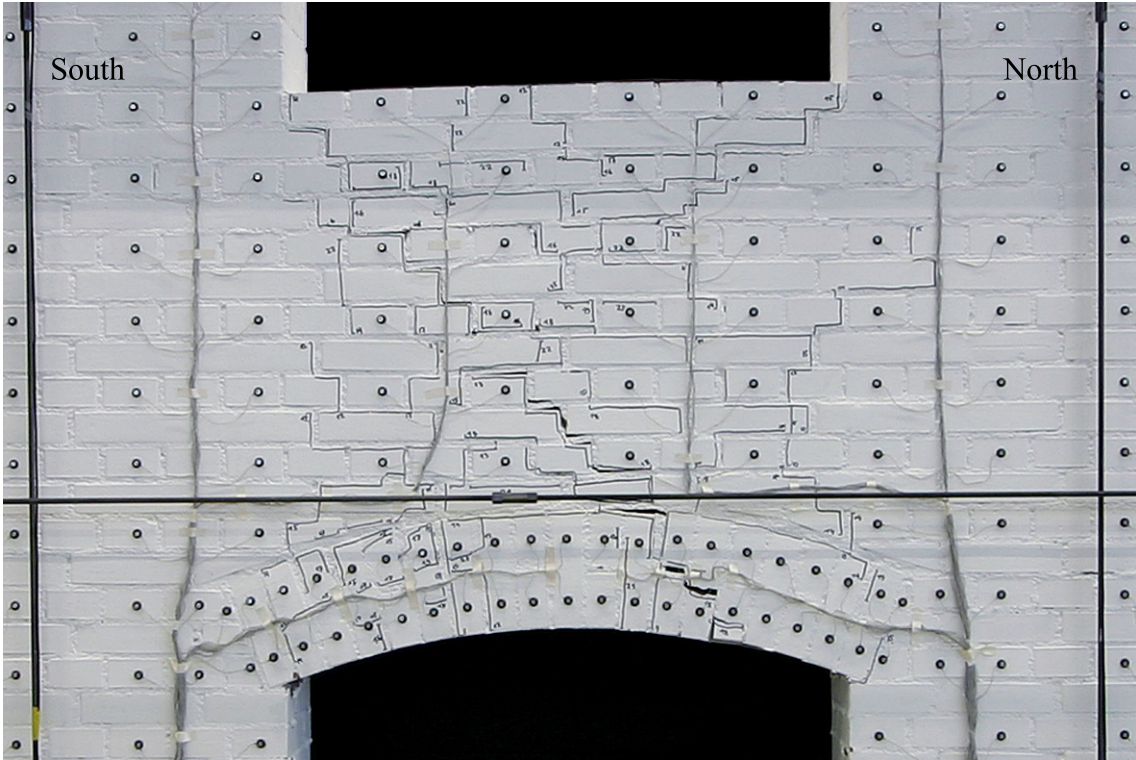


Figure 3.29: TUC: Crack pattern of spandrel at LS 22. Drift towards North with $\theta_{nom} = 0.4\%$.

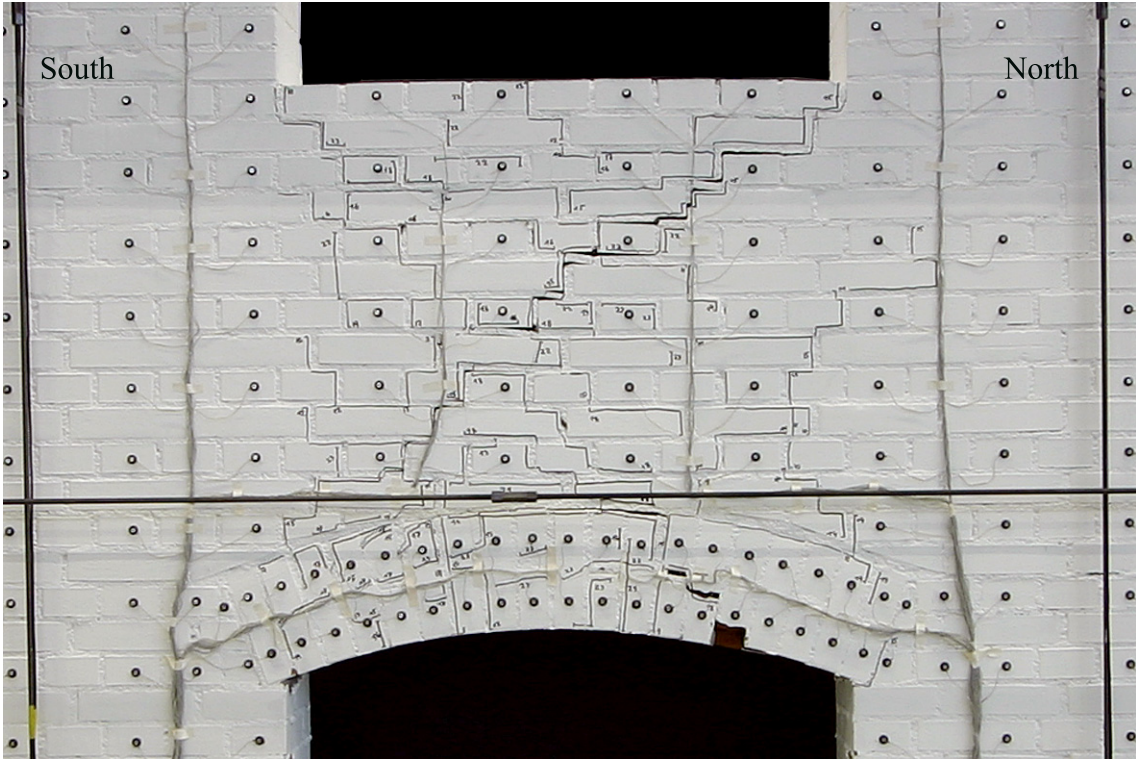


Figure 3.30: TUC: Crack pattern of spandrel at LS 23. Drift towards South with $\theta_{nom} = -0.4\%$.

of the arch but about one third of the span inwards. At this location the arch is heavily damaged and pieces of bricks have started to fall off the arch. For loading in the negative direction (Fig. 3.31) the shear crack points to the South end of the arch and the compression strut passes through the South most bricks of the arch, which have fractured under the large compressive stresses. Due to the large rotation demands, the top bricks of the spandrel became more and more disjointed until almost all bricks were loose.

Failure was caused by the collapse of the arch. Figure 3.33 shows LS 42 ($\theta_{nom} = 2.0\%$), which corresponds to the last load step where the arch – at least the East face – was still more or less intact. As loading continued first the lower half of the arch collapsed on the way from LS 43 to LS 44. The part of the arch that collapsed at that point can be easily made out on Fig. 3.33. Afterwards, also the upper half of the arch collapsed on the way to LS 45 ($\theta_{nom} = -2.0\%$) as shown in Fig. 3.34. When loading to LS 45 it was decided to load beyond the nominal maximum rotation since the spandrel was already very heavily damaged and further cycles were no longer particularly meaningful. The maximum applied rotation was about $\theta = -3.5\%$; the photos labelled with LS 45 were taken at this rotation (Fig. 3.34).

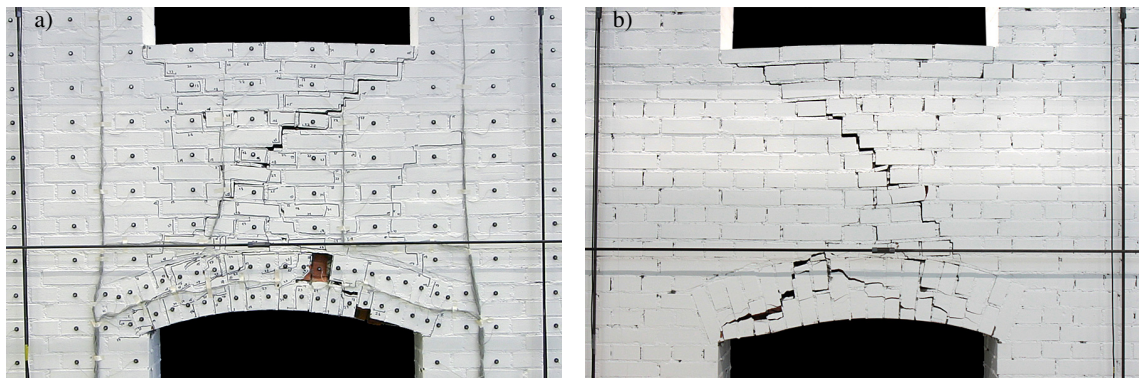


Figure 3.31: TUC: Front (East, a) and back (West, b) face of the spandrel at LS 31. Drift towards South with $\theta_{nom} = -0.8\%$.

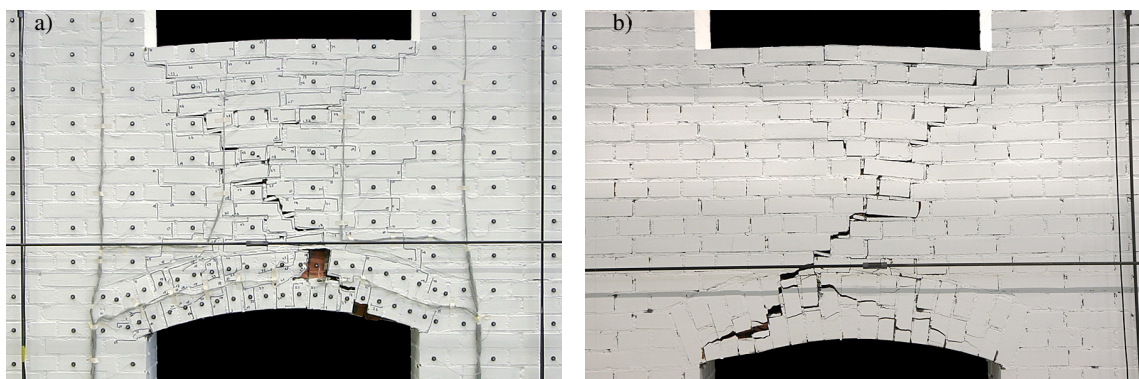


Figure 3.32: TUC: Front (East, a) and back (West, b) face of the spandrel at LS 32. Drift towards North with $\theta_{nom} = 0.8\%$.

3. Test results for masonry spandrels

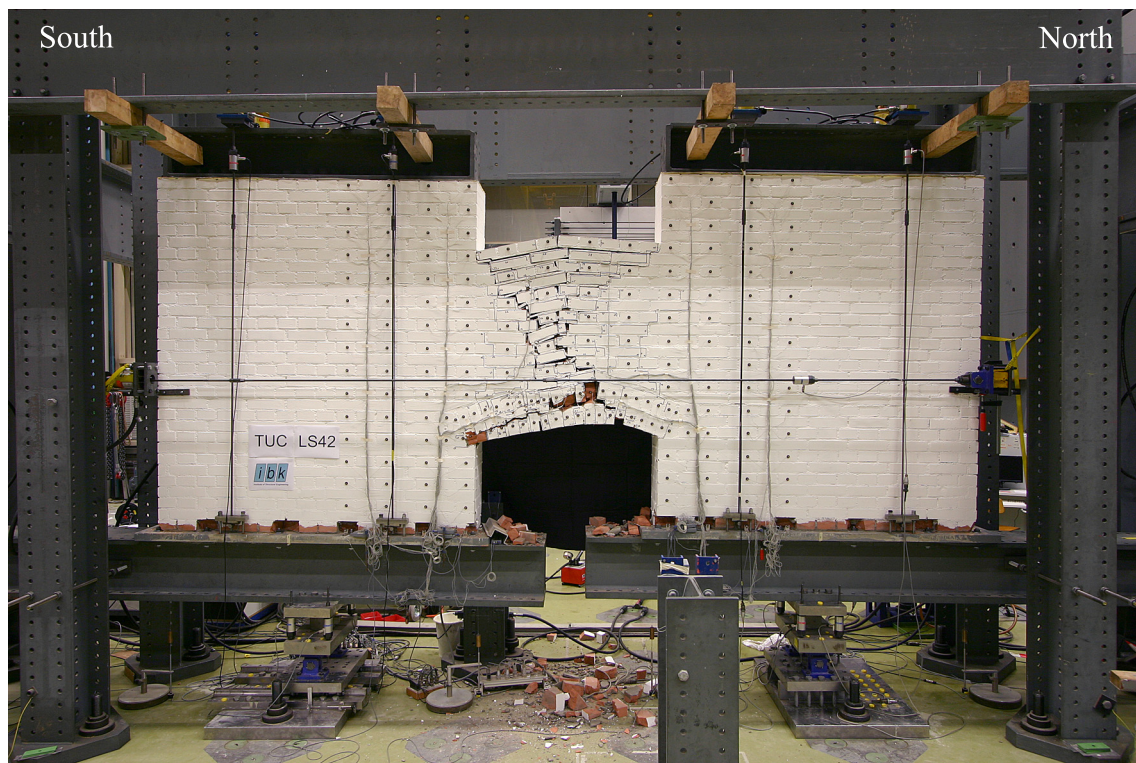


Figure 3.33: TUC: Crack pattern of spandrel at LS 42. Drift towards North with $\theta_{nom} = 2.0\%$.



Figure 3.34: TUC: Crack pattern of spandrel at LS 45. Drift towards South with $\theta = -3.5\%$ (failure of TUC, $\theta_{nom} = -2.0\%$).

3.4.3 Test results

In this section key results of TUC are presented and briefly discussed often making reference to observations made during the test. The hysteretic behaviour of the test units in terms of spandrel shear force vs. average rotation is presented first. Afterwards the variation of the axial load acting on the piers and on the spandrel is discussed.

Hysteretic behaviour of TUC

The global average hysteretic behaviour of the test unit is shown in Fig. 3.35 and a close-up of the same cycles up to drifts of $\pm 0.8\%$ is shown in Fig. 3.36. As it was the case for TUA and TUB, the hysteretic behaviour calculated independently from the data stemming from the South and the North pier, respectively (see Fig. 3.37), confirms that the averaged hysteresis curve in Fig. 3.35 can be considered representative of the whole test and will be briefly discussed in the following.

Despite some cracks in the spandrel forming at smaller rotations the hysteresis curve of TUC shows an almost elastic behaviour up to a $\pm 0.05\%$ -rotation and only a small deviation from the same nearly elastic behaviour up to a $\pm 0.10\%$ -rotation reaching almost identical shear strengths in the positive and in the negative loading direction, i.e. 80 kN (LS 10) and -78 kN (LS 11). On the way to LS 14 further cracking of the spandrel occurred leading to the first prominent inelastic behaviour of the test unit. At LS 14 ($\theta_{nom} = 0.2\%$) the shear force was 78 kN. During the following reversal a peak shear force of -83 kN could be reached at $\theta = -0.18\%$ before "dropping" to -76 kN at LS 15 ($\theta_{nom} = -0.2\%$). At this stage it is worthwhile mentioning that this value is already smaller than the upper limit of the contribution V_N that could be provided by the axial force in the spandrel. As in the case of TUA and TUB, V_N is estimated by means of Eq. 3.16 where H_{sp} is the axial load acting on the spandrel, h_{sp} is the height of the spandrel and l_{sp} is its span.

$$V_N = \frac{H_{sp} \cdot h_{sp}}{l_{sp}} = \frac{80\text{kN} \cdot 1.26\text{m}}{1.18\text{m}} = 85.4\text{kN} \quad (3.16)$$

During the two cycles with $\theta_{nom} = \pm 0.3\%$ the peak shear force reached at every load step dropped significantly. In the positive loading direction the peak shear force dropped to 47 kN at LS 18 and further down to 44 kN at LS 20. In the negative direction the drop during the first cycle was smaller (-59 kN at LS 19), however that during the second cycle was larger leading to a shear force of -48 kN at LS 21, which is almost of the same magnitude as the shear force at LS 20. The remaining shear strengths at the end of the second cycle at $\theta_{nom} = \pm 0.3\%$ were hence just 55% and 57% of the maximum shear force ever reached for loading in the positive and the negative direction, respectively. These values are also quite smaller than V_N suggesting that by that time the lever arm of the internal forces of the spandrel had already reduced significantly.

At LS 22, which corresponds to the first cycle with $\theta_{nom} = \pm 0.2\%$, the shear force was 37 kN and at the immediately following LS 23 it was -43 kN. During the ensuing cycles at $\theta_{nom} = \pm 0.6\%$ and $\pm 0.8\%$ the drop in strength was relatively minor and at LS 30 ($\theta_{nom} = 0.8\%$) 31 kN could be measured while at LS 31 ($\theta_{nom} = -0.8\%$) the shear force was still -41 kN. For larger amplitudes of the cycles a steady decrease of the shear strength could be observed and during the first cycle at $\theta_{nom} = \pm 2.0\%$ values of just 10 kN (LS 42, see Fig. 3.33) and -15 kN (LS 43) occurred, despite the axial load of the spandrel still being about 80 kN (see Fig. 3.39).

3. Test results for masonry spandrels

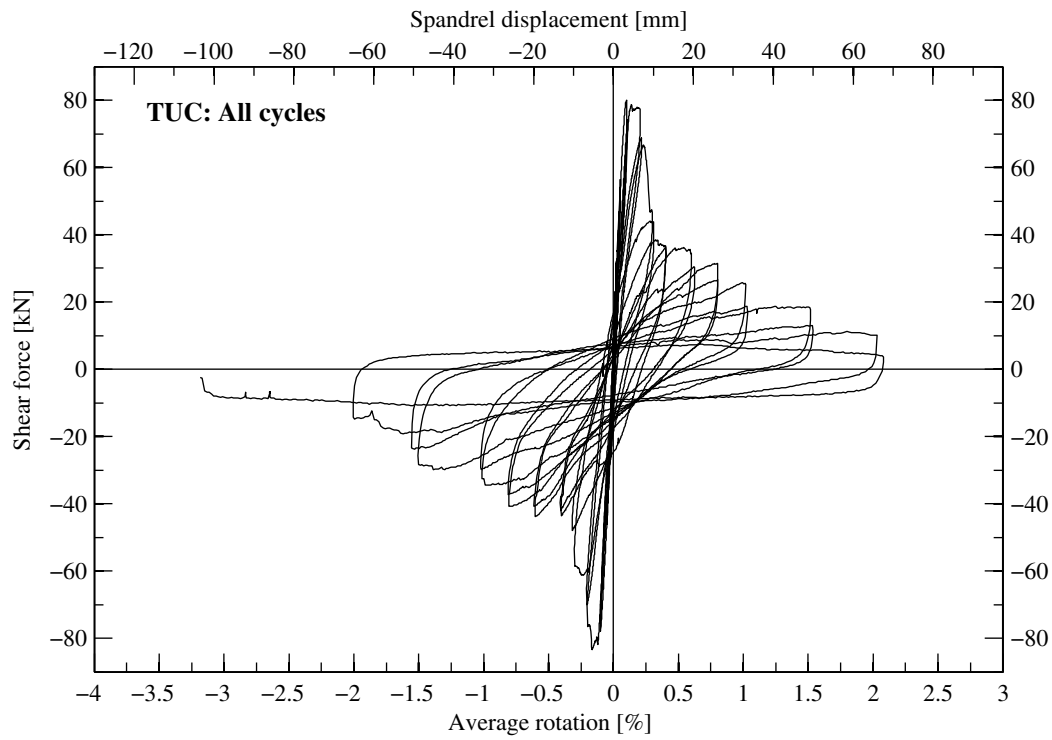


Figure 3.35: TUC: Force-rotation relationship for all cycles.

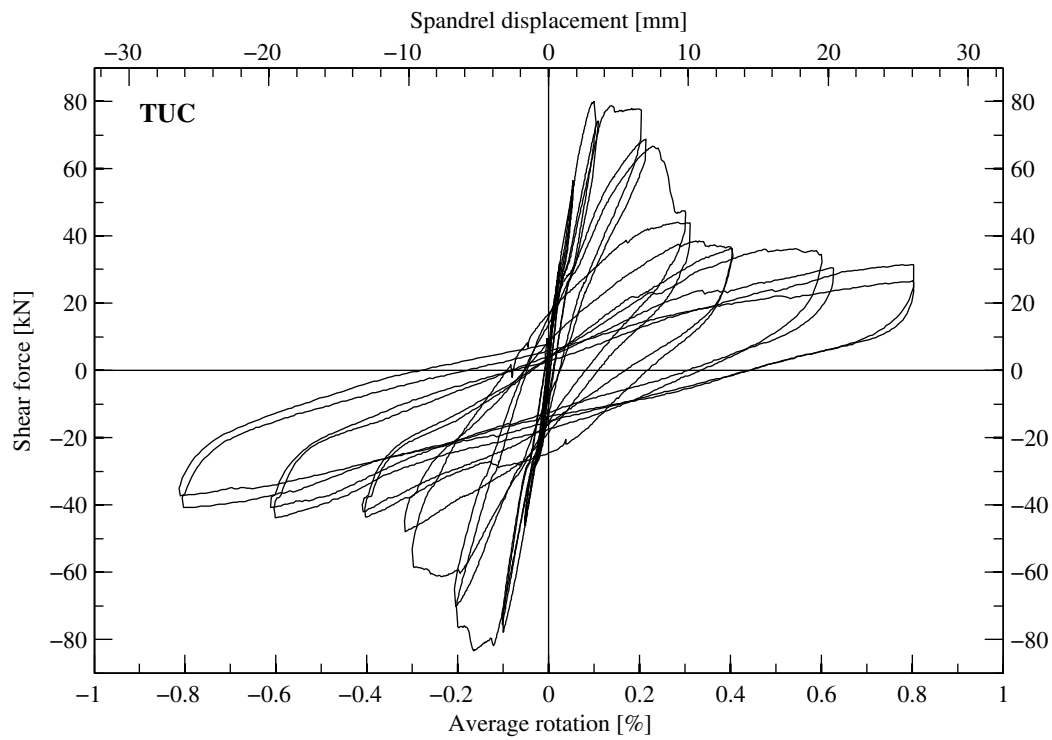


Figure 3.36: TUC: Force-rotation relationship for the cycles up to $\pm 0.8\%$ (LS 2-33).

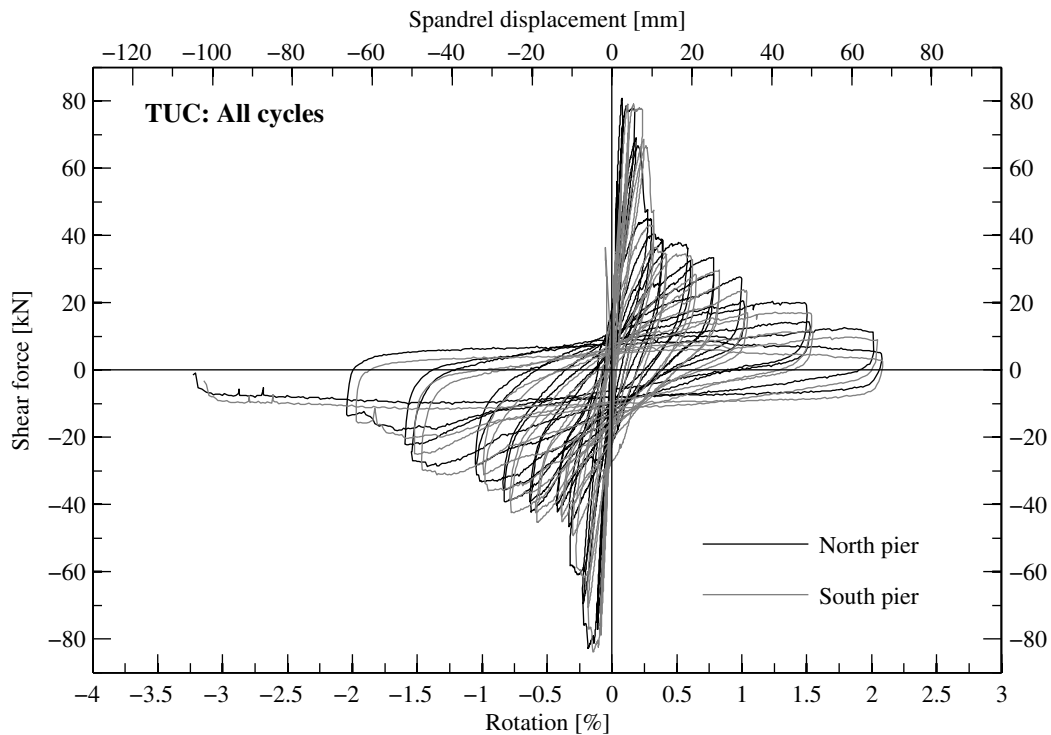


Figure 3.37: TUC: Force-rotation relationship for all cycles showing the non-averaged pier rotations and shear forces.

Variation of the axial load in the piers and spandrel of TUC

The variation of the axial force in the piers in function of the average rotation is shown in Fig. 3.38. The deviance to the target value of 364 kN is generally very small proving the reliability of the manual load controlling system used in the framework of TUC. The maximum variation of the axial load is over the majority of test duration negligible. Just at two locations a somewhat larger variation is noticeable due to a slight mismanagement of the hand pumps driving the hollow core jacks of the vertical rods.

The variation of the axial force in the spandrel in function of the average rotation is shown in Fig. 3.39. The load follower was able to limit the maximum variation of the axial load to about 5% of the target value of 80 kN. Just on the way to LS 45 the axial load reduced significantly starting at a rotation of -2.5% due to the axial crushing of the spandrel and due to the oil flow of the load follower not being enough to compensate the shortening of the spandrel. Noteworthy is the hysteretic behaviour of the spandrel axial load showing consistently larger values during the loading phase compared to the unloading phase of every half-cycle. This behaviour was due to the friction of the hollow core jacks in charge of the tensioning of the horizontal rods.

3.4.4 Deformation plots

Figure 3.40 shows the deformed shape of TUC at the first positive as well as the first negative peak of the cycles with amplitudes of $\theta_{nom} = \pm 0.1\%$, $\pm 0.2\%$, $\pm 0.4\%$ and $\pm 0.8\%$. With respect

3. Test results for masonry spandrels

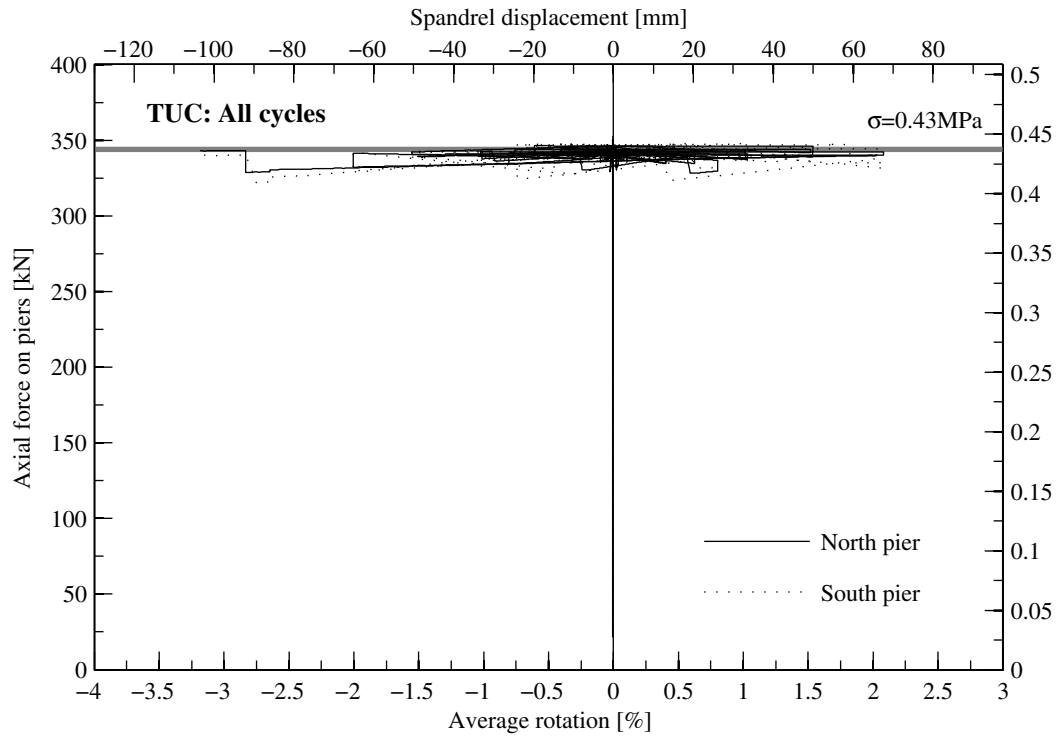


Figure 3.38: TUC: Axial force on piers - rotation relationship for all cycles.

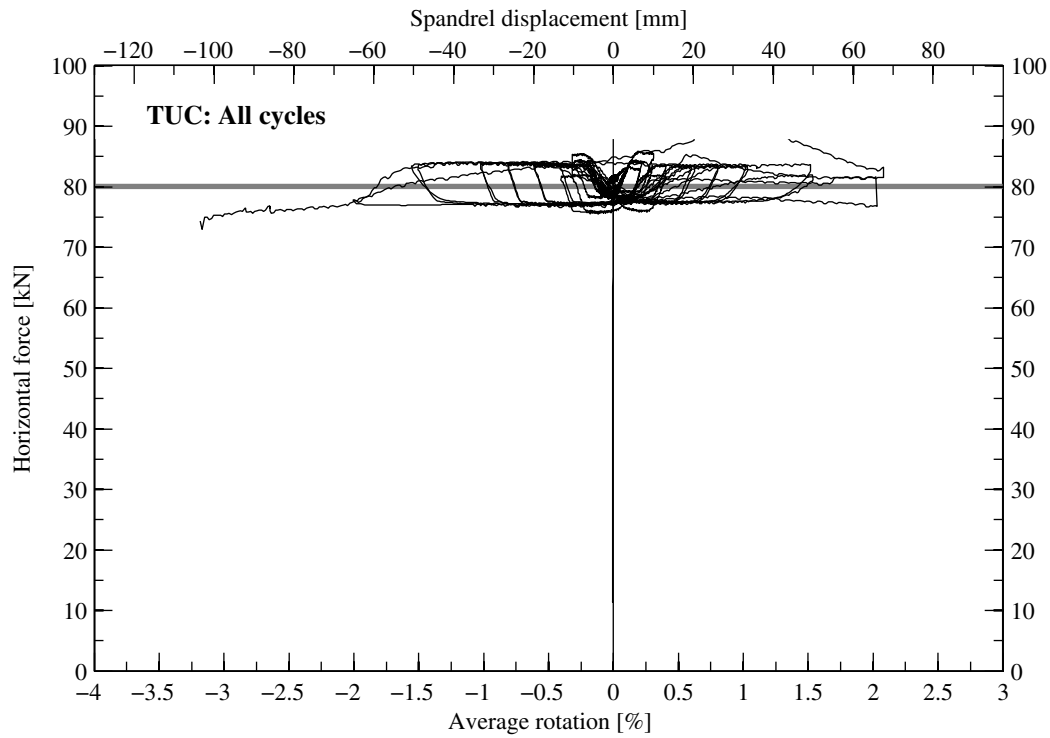
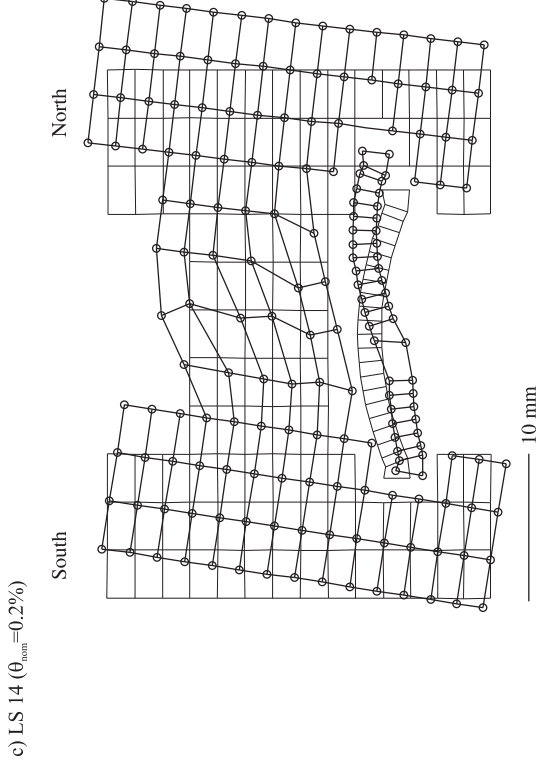
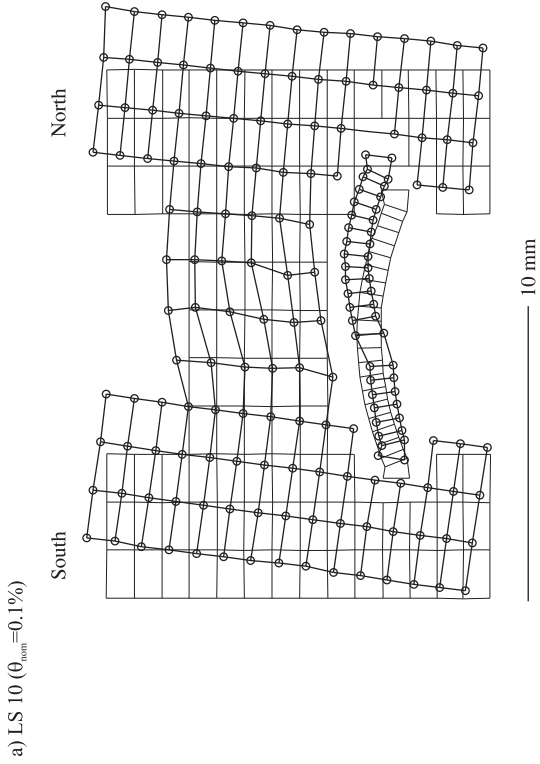
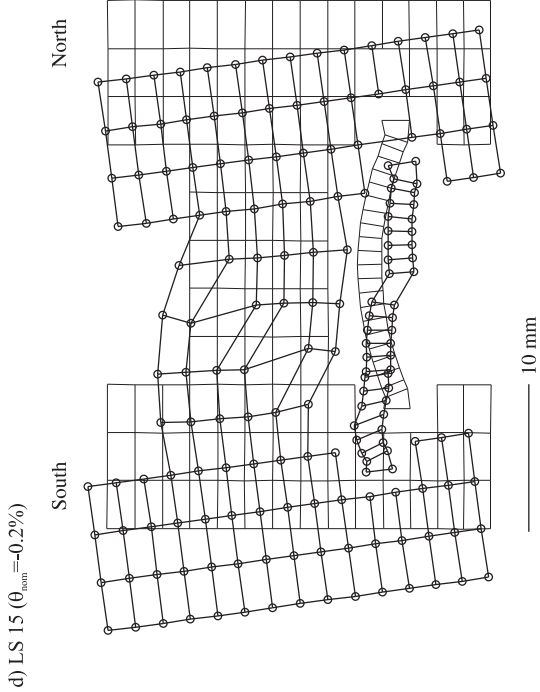
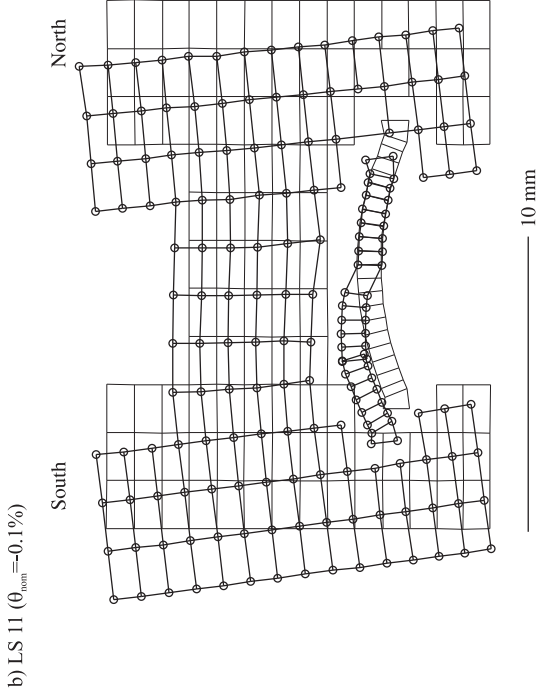


Figure 3.39: TUC: Horizontal force - rotation relationship for all cycles.

to the dimensions of the test unit, the deformations are amplified by factors ranging between 20 and 160 so that the magnitude of the plotted deformations is for all load steps approximately equal. Shown with thin lines is the undeformed state of the test unit at LS 0. The deformation plots show very well the evolution of the hinges in the arch: For the cycles with $\theta_{nom} = \pm 0.1\%$ and $\pm 0.2\%$ the deformation of the arch for the positive and negative direction of loading is almost symmetric. For loading in the positive direction, a positive plastic hinge formed at about one third of the arch length away from the South edge of the spandrel. For loading in the negative direction, a positive plastic hinge formed at about one third of the arch length away from the North edge of the spandrel; and additionally also a negative plastic hinge can be identified at about two thirds of the arch length away from the North edge of the spandrel. During the cycles with $\theta_{nom} = \pm 0.4\%$ and $\pm 0.8\%$, the deformation concentrated more and more in the hinge which was closest to the North pier. The hinge seemed to develop a sliding mechanism rather than a flexural mechanism. The masonry spandrel above the arch showed for both directions of loading a concentration of the deformation in a diagonal shear crack. The curved top edge of the spandrel suggests that the two parts of the spandrel that were divided by the shear crack were also subjected to flexural deformations.

3. Test results for masonry spandrels



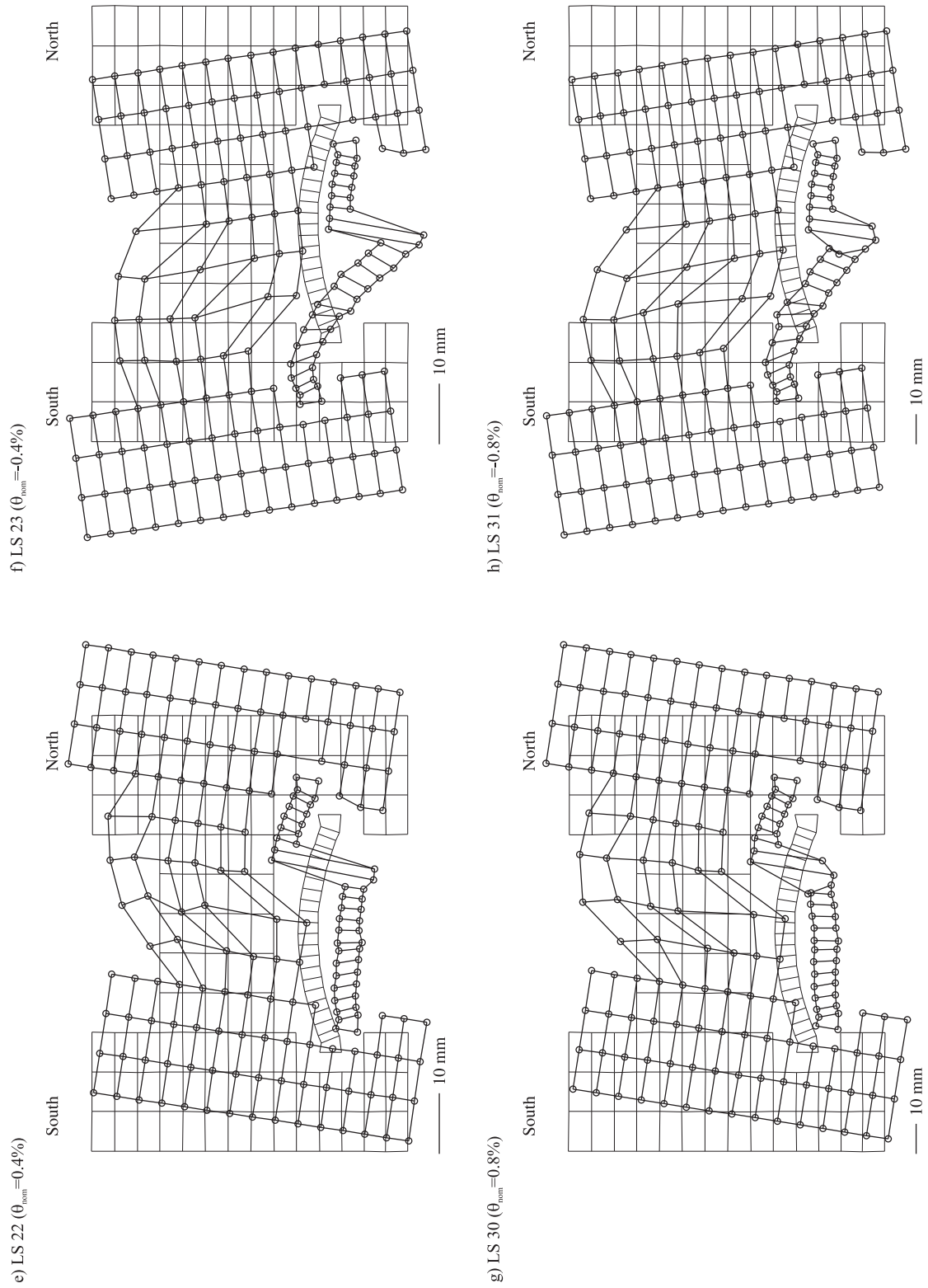


Figure 3.40: TUC: Deformed grid obtained from optical measurements at the first positive and the first negative peak of the cycles with $\theta_{nom} = \pm 0.1\%$, $\pm 0.2\%$, $\pm 0.4\%$ and $\pm 0.8\%$.

3.5 Masonry spandrel TUD

3.5.1 Specific test setup

For the vertical forces applied to the piers the same setup as for TUC was used, i.e. the eight vertical rods were post-tensioned by means of hollow core jacks. The pressure of the hollow core jacks was controlled by means of safety valves and hand pumps. For the horizontal rods a new setup was designed. In principle, the setup was similar to that of TUB, i.e. the forces in the horizontal bars were not kept constant by means of a load follower but varied according to the elongation of the spandrel. For TUD, however, the horizontal bars consisted of D32 mm Dywidag steel bars, which were considerably stiffer than the D10 mm threaded bars used for TUB. The Dywidag bars were initially prestressed to a force of ~ 10 kN each.

3.5.2 Test observations

At LS 0 the forces in the eight vertical were zero; the forces in the two horizontal steel rods were 10 kN each. As a first step the vertical rods were prestressed to a force of 80 kN each, which corresponds at midheight of the piers approximately to an axial stress in the piers of $\sigma = 0.43$ MPa. This load step was called LS 1 and was applied on 13.01.2010. The test unit was tested on this and the following two days (13 to 15.01.2010). An overview on the load steps covered during each testing day is given in Table 3.4.

Table 3.4: TUD: Testing days and corresponding load steps.

Testing day	Load steps carried out
13.01.2010	LS 1 - LS 15
14.01.2010	LS 16 - LS 35
15.01.2010	LS 20 - LS 48

During the cycles with $\theta_{nom} = \pm 0.05\%$ the first flexural cracks appeared. The cracks started within the arch at about one third and two thirds of the arch length and reached within the spandrel. These first cracks are very similar to those observed for TUC. In the following, however, the flexural cracks grew in length and also, in particular at the North end of the spandrel, branched out into several smaller cracks. The formation of the cracks up to LS 15 can be tracked in Fig. 3.41. The extension that a particular crack reached at a particular load step is marked on the test unit by means of a short cross-line and the number of the corresponding load step.

Only at LS 19 ($\theta_{nom} = -0.3\%$) a first shear crack formed. At this instant the forces in the horizontal rods were approximately 40 kN each, i.e. of similar magnitude as the constant horizontal forces applied to TUC. The shear crack in the opposite direction appeared at LS 20. As loading continued the shear cracks dominated more and more the crack pattern. The flexural cracks were still open but not as wide as the shear cracks. Figures 3.42 and 3.43 show the crack pattern at LS 22 ($\theta_{nom} = 0.4\%$) and LS 23 ($\theta_{nom} = -0.4\%$), respectively.

Figures 3.44 and 3.45 show the crack pattern of the front and back face of the spandrel at LS 30 and LS 31, respectively, i.e. at the first two peaks of the cycles with $\theta_{nom} = \pm 0.8\%$. For both directions of loading the damage to the spandrel was concentrated in the upper half of the

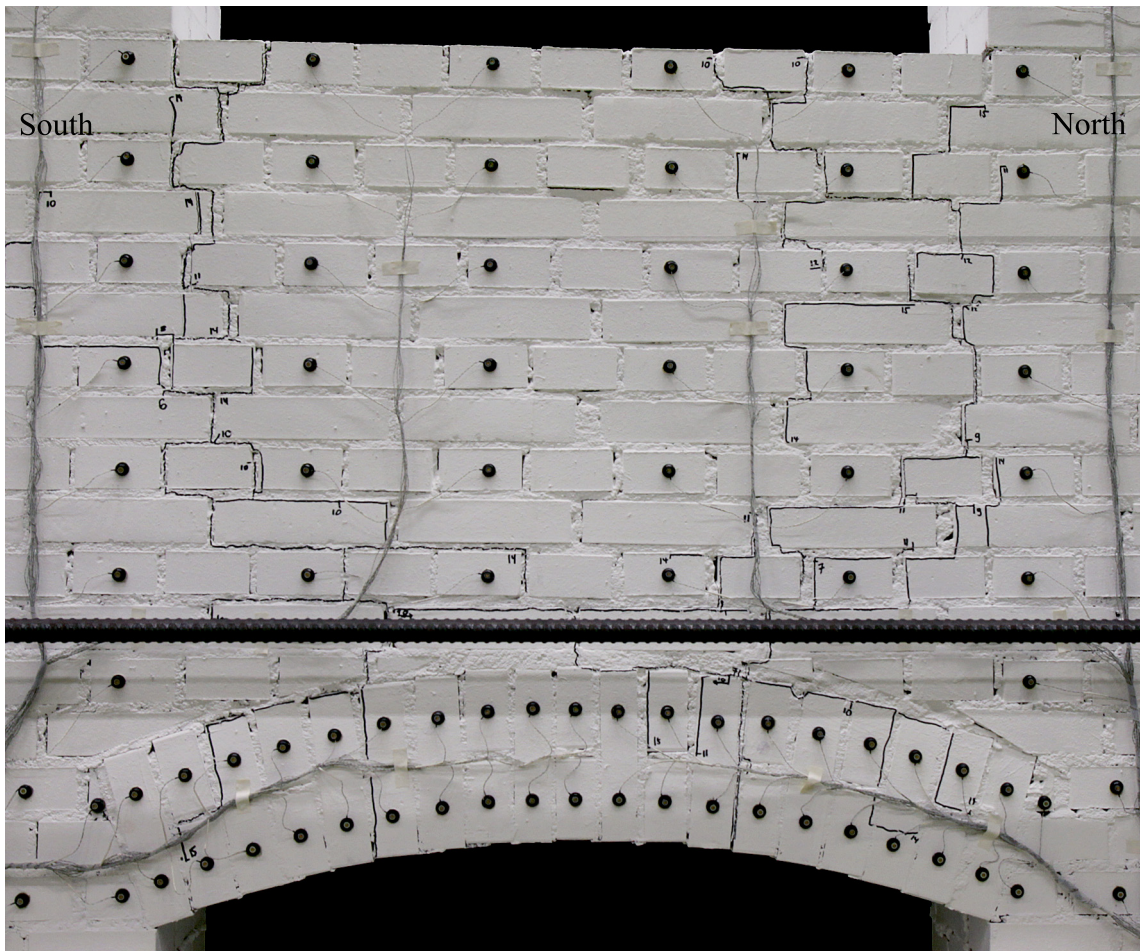


Figure 3.41: TUD: Crack pattern of spandrel at LS 15. Drift towards South with $\theta_{nom} = 0.2\%$.

spandrel, the damage to the arch was at this point of loading still rather limited. This is different to TUC, where at this instant during the loading history, the damage to the arch was already quite substantial (see Figs. 3.31 and 3.32). The limited damage to the lower part of the spandrel and to the arch was mostly due to the rather large horizontal force in the steel bar. At LS 30 and LS 31 the sum of the forces in the two horizontal bars was 114 kN and 107 kN, respectively. The constant horizontal force applied to TUC was 80 kN and therefore at this load step considerably smaller. Nevertheless, hinges formed also in the arch of TUD. This is particularly evident in Fig. 3.44b where a wide flexural crack is visible in the arch at about one third of the span inwards from the right (South) end of the spandrel. In the following cycles the mechanisms involved remained the same. However, the spandrel and the arch were increasingly damaged and softened. The integrity of the arch suffered in particular due to the horizontal cracks running through the bricks of the arch as shown in Fig. 3.46. The latter depicts the deformed shape of the test unit at LS 45 ($\theta_{nom} = -2.0\%$) which is the last load step in the negative direction during which the arch – at least the East face – was still more or less intact. As a consequence of these horizontal cracks the lower part of the bricks often fell down when the loading direction was reversed. At the end of the test the front row of the central part of the arch collapsed (LS 50, Fig. 3.47).

3. Test results for masonry spandrels

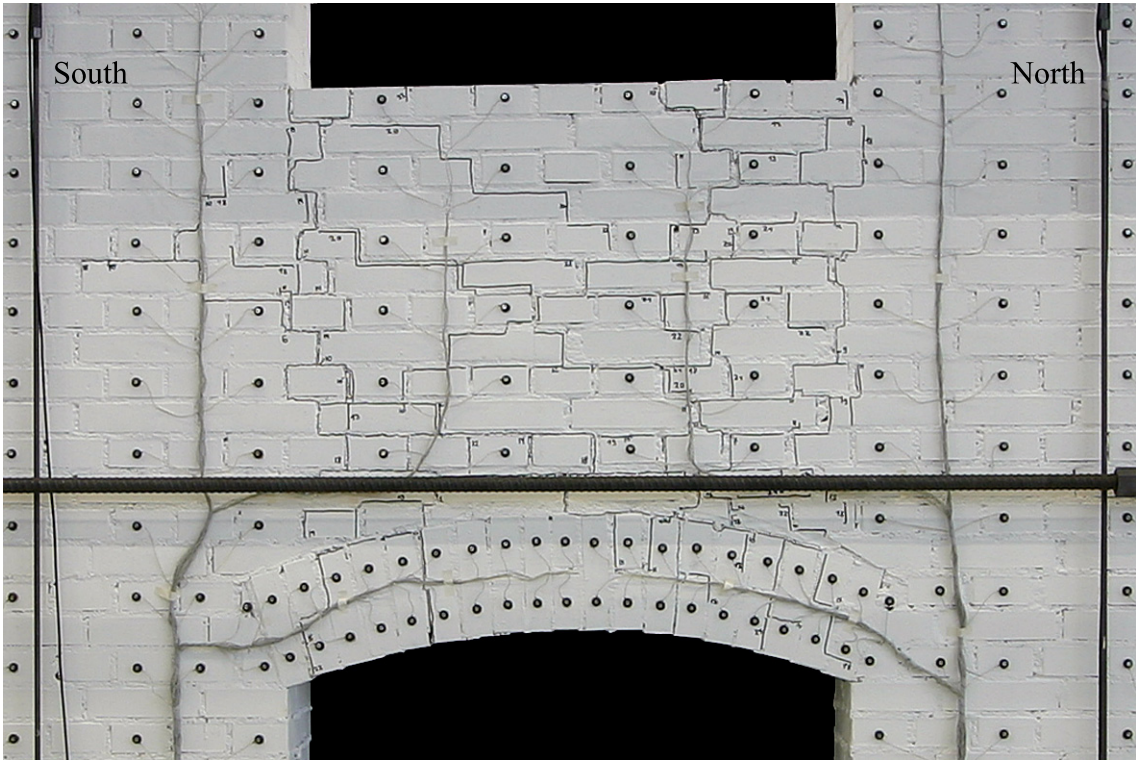


Figure 3.42: TUD: Crack pattern of spandrel at LS 22. Drift towards North with $\theta_{nom} = 0.4\%$.

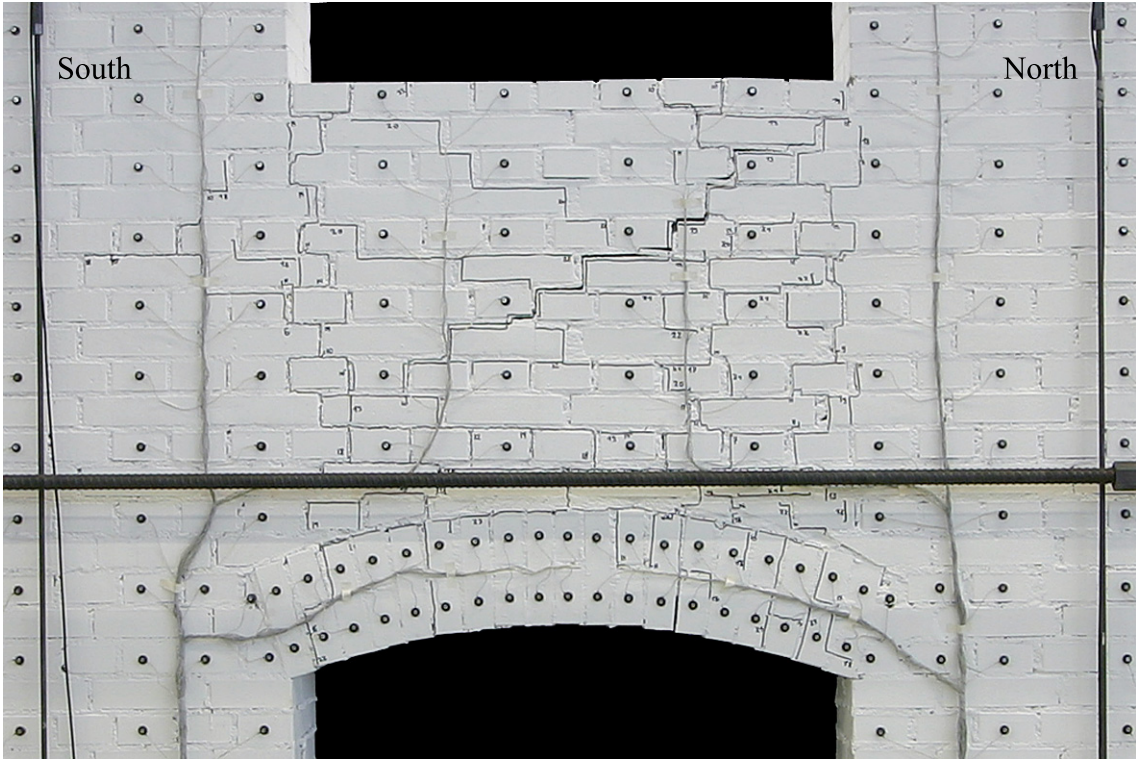


Figure 3.43: TUD: Crack pattern of spandrel at LS 23. Drift towards South with $\theta_{nom} = -0.4\%$.

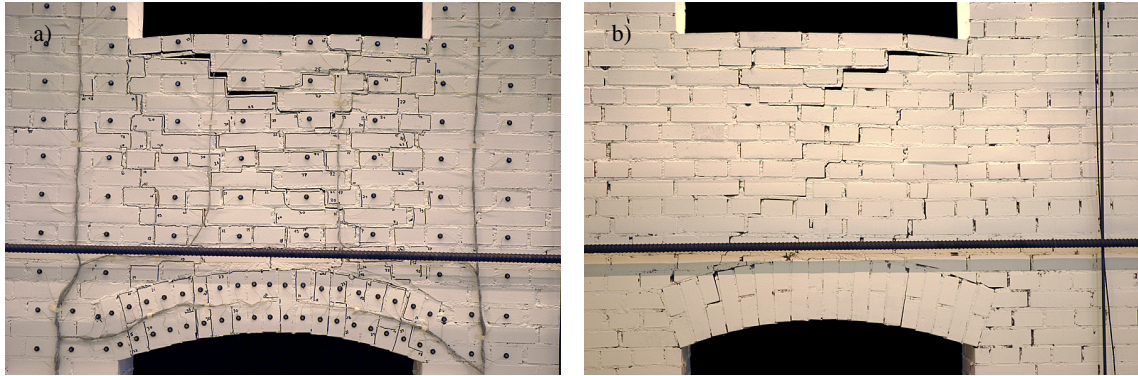


Figure 3.44: TUD: Front (East, a) and back (West, b) face of the spandrel at LS 30. Drift towards North with $\theta_{nom} = 0.8\%$.

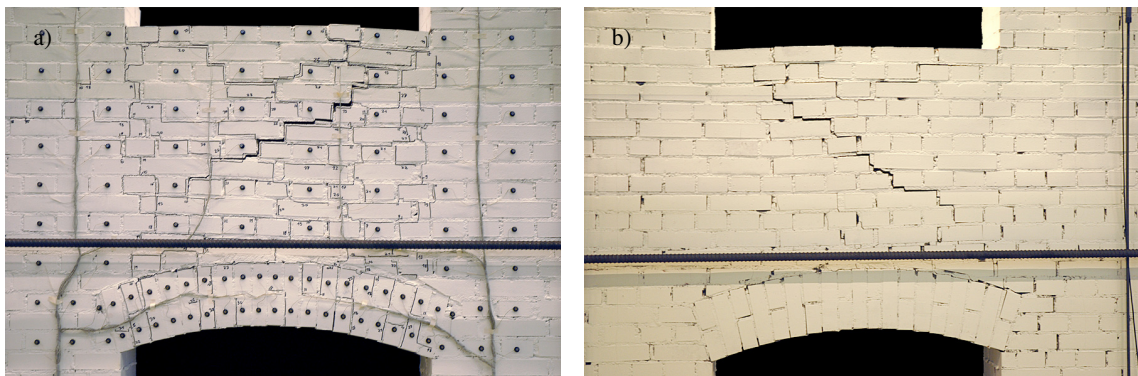


Figure 3.45: TUD: Front (East, a) and back (West, b) face of the spandrel at LS 31. Drift towards South with $\theta_{nom} = -0.8\%$.

3. Test results for masonry spandrels

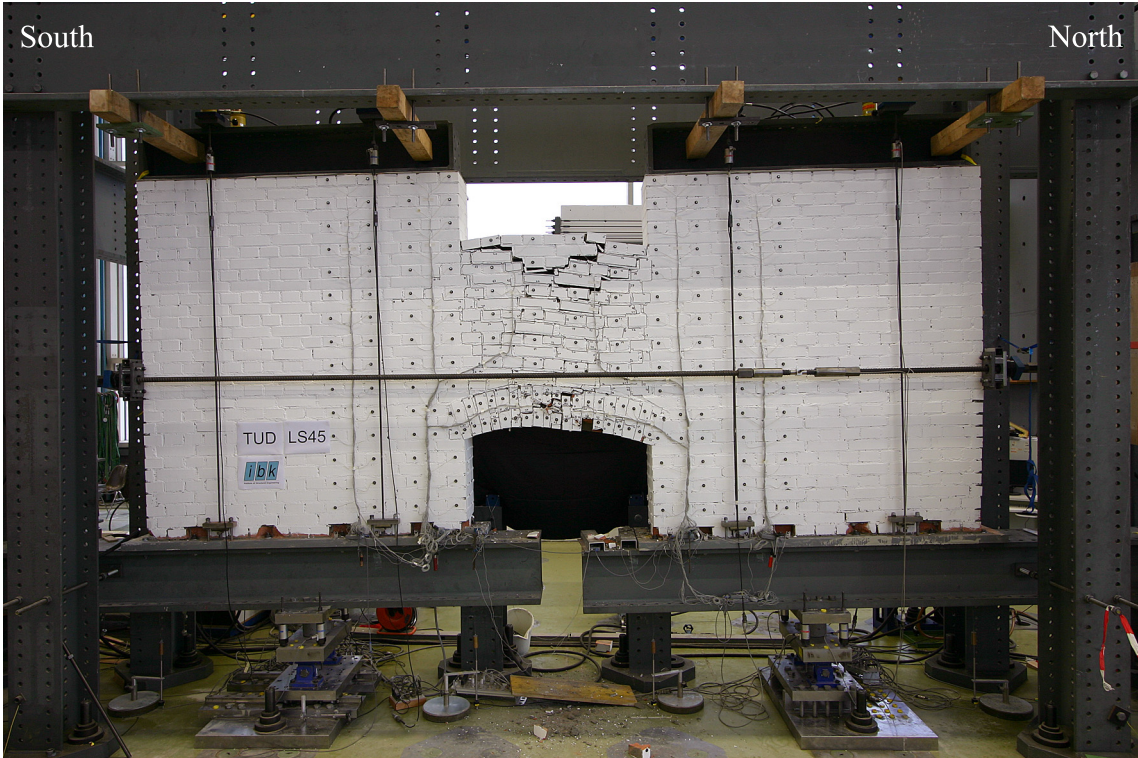


Figure 3.46: TUD: Crack pattern of spandrel at LS 45. Drift towards South with $\theta_{nom} = -2.0\%$.

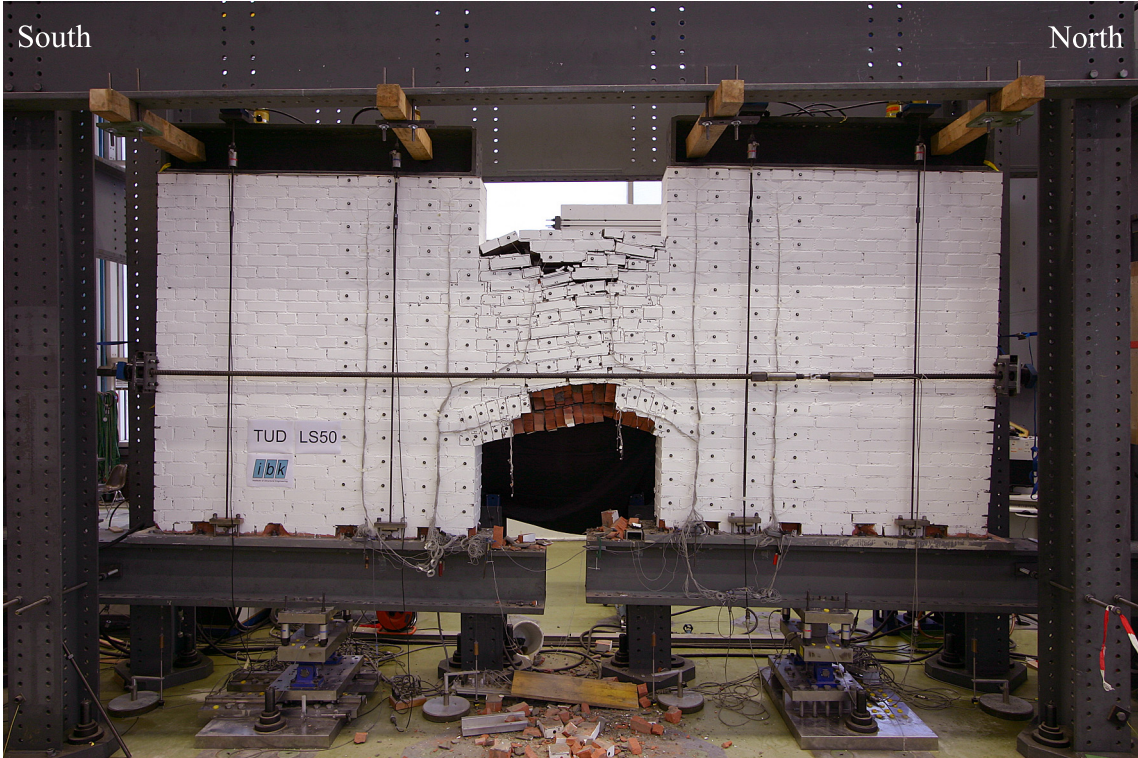


Figure 3.47: TUD: Crack pattern of spandrel at LS 50. Drift towards North with $\theta = 2.5\%$ (failure of TUD, $\theta_{nom} = 3.0\%$).

3.5.3 Test results

In this section key results of TUD are presented and briefly discussed often making reference to observations made during the test. The hysteretic behaviour of the test units in terms of spandrel shear force vs. average rotation is presented first. Afterwards the variation of the axial load acting on the piers and on the spandrel is discussed.

Hysteretic behaviour of TUD

The global average hysteretic behaviour of the test unit is shown in Fig. 3.48 and a close-up of the same cycles up to drift of $\pm 0.8\%$ is shown in Fig. 3.49. As it was the case for TUA to TUC, the hysteretic behaviour calculated independently from the data stemming from the South and the North pier, respectively (see Fig. 3.50), confirms that the averaged hysteresis curve in Fig. 3.48 can be considered representative of the whole test and will be briefly discussed in the following.

The hysteresis curve of TUD shows an almost elastic behaviour up to a $\pm 0.05\%$ -rotation. During the cycles at $\theta_{nom} = \pm 0.1\%$ the increase of the flexural cracking in the spandrel led to the first noticeable inelastic behaviour of the test unit. The shear force at LS 10 and 11 was 74 kN and -71 kN, respectively, and the axial force in the spandrel increased slightly to 30 kN and 28 kN, respectively. During the cycles at $\theta_{nom} = \pm 0.2\%$ the thickness of the flexural cracks increased leading to an increase of the axial load in the spandrel. At LS 14 ($\theta_{nom} = 0.2\%$) the axial load was 56 kN and the shear force 74 kN, i.e. similar to the shear force at LS 10. At LS 15 ($\theta_{nom} = -0.2\%$) the axial load was 54 kN and the shear force -66 kN which is slightly smaller than the force at LS 11.

Shear cracks in the spandrel occurred during the cycles at $\theta_{nom} = \pm 0.3\%$. However, during the first half cycle at this amplitude, LS 18 could be reached with no shear cracks and the shear force at maximum deformation was 77 kN, i.e. the largest value measured during the entire test. At this stage the axial load in the spandrel was 81 kN. In the following negative loading to LS 19 the first shear crack occurred at $\theta = -0.22\%$. Just before shear cracking the shear force was -56 kN and "reduced" rapidly afterwards. At LS 19 ($\theta_{nom} = -0.3\%$) the shear force was just -45 kN and the axial load in the spandrel was 68 kN. The first shear crack in the positive loading direction occurred at $\theta = 0.29\%$ shortly before reaching LS 20. Just before shear cracking took place the shear force was 70 kN and reduced rapidly to 55 kN at LS 20 ($\theta_{nom} = 0.3\%$). At this stage the axial load in the spandrel was 83 kN. For the sake of completeness, it is worth mentioning that at LS 21 the shear force was -40 kN and the axial load 64 kN.

The peak shear force recorded at maximum amplitude of the cycles ranging from $\theta_{nom} = \pm 0.4\%$ to $\theta_{nom} = \pm 1.0\%$ was more or less constant showing a value of about 50 kN for loading in the positive direction and -45 kN for loading in the negative direction. During the same cycles the axial load in the spandrel increased steadily almost proportional to the amplitude (see Fig. 3.52) reaching values of 128 kN and 121 kN at LS 34 ($\theta_{nom} = 1.0\%$) and LS 35 ($\theta_{nom} = -1.0\%$), respectively.

At LS 38 ($\theta_{nom} = 1.5\%$) the largest axial load in the spandrel was recorded (174 kN). This led to a temporary increase of the peak shear force to 60 kN. From LS 38 onwards the peak axial load in the spandrel decreased steadily suggesting that the axial crushing of the spandrel had started. As a consequence of the reduction of the axial load, the shear strength of the spandrel also reduced.

3. Test results for masonry spandrels

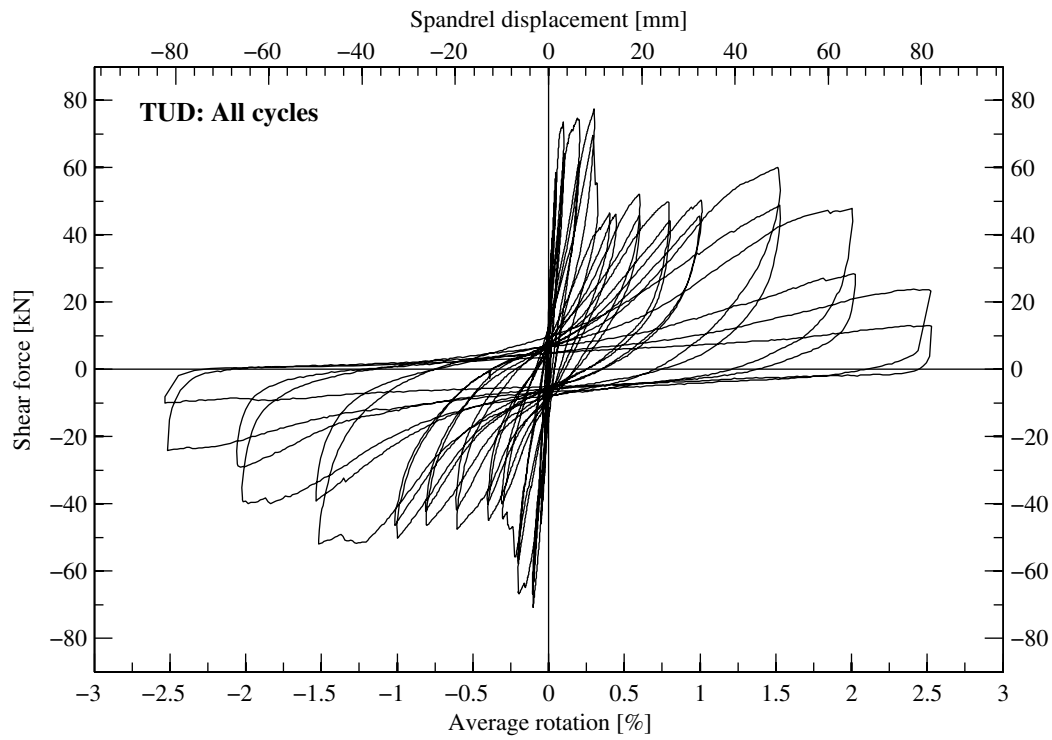


Figure 3.48: TUD: Force-rotation relationship for all cycles.

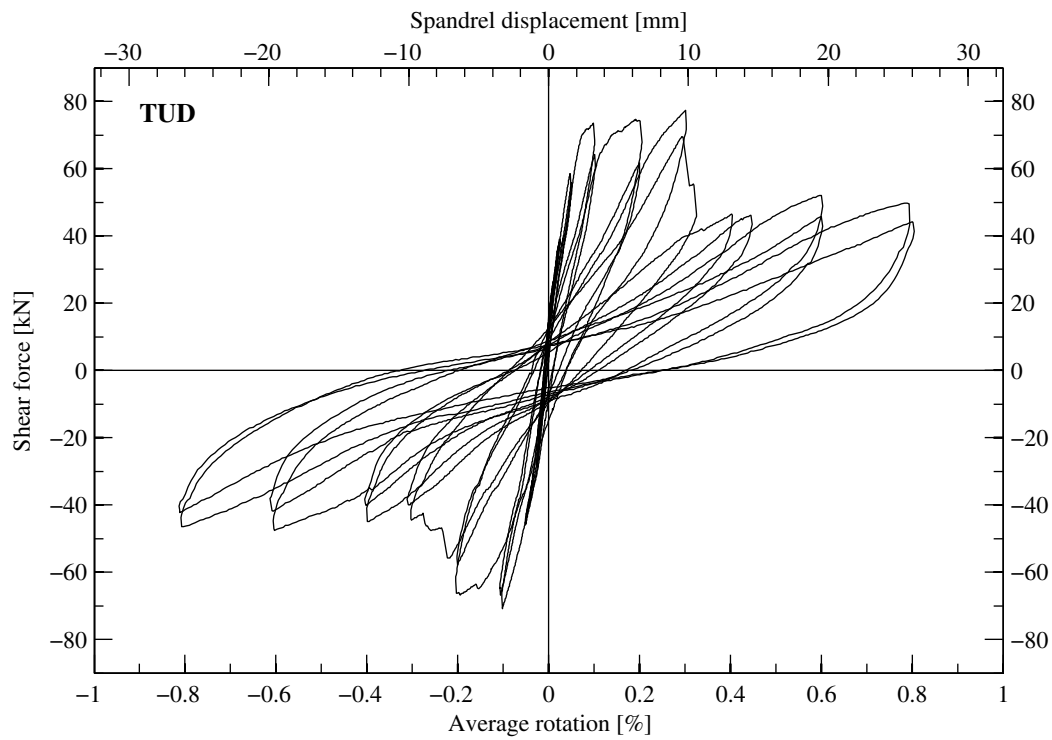


Figure 3.49: TUD: Force-rotation relationship for the cycles up to $\pm 0.8\%$ (LS 2-33).

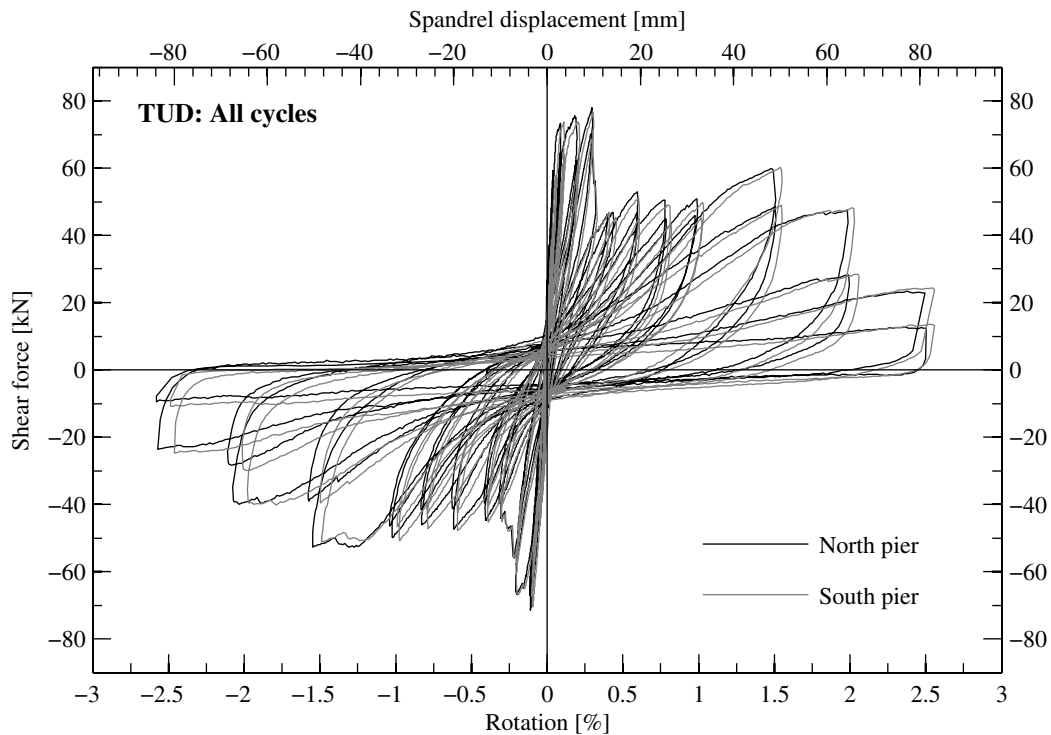


Figure 3.50: TUD: Force-rotation relationship for all cycles showing the non-averaged pier rotations and shear forces.

Variation of the axial load in the piers and spandrel of TUD

The variation of the axial force in the piers in function of the average rotation is shown in Fig. 3.51. The deviance to the target value of 340 kN was generally very small in the South pier. On the contrary, the maximum variation of the axial force in the North pier was somewhat larger. The force drops in the North pier were caused by a leakage of the hydraulic pump in charge of stressing the vertical rods. This made it difficult to keep the axial force constant. However, it is believed that these variations of axial load had negligible effect on the behaviour of the test unit. In this framework it is worth noting that no cracks occurred in the Nord pier (see Fig. 3.47).

The variation of the axial force in the spandrel in function of the average rotation is shown in Fig. 3.52. The dependence of the axial force on the average rotation has already been discussed in the previous section on the hysteretic behaviour of TUD. Figure 3.52 shows in addition that the force at zero rotation tended to increase with increasing amplitude of the cycles suggesting a permanent elongation of the spandrel.

3.5.4 Deformation plots

Figure 3.53 shows the deformed shape of TUD at the first positive as well as the first negative peak of the cycles with amplitudes of $\theta_{nom} = \pm 0.1\%$, $\pm 0.2\%$, $\pm 0.4\%$ and $\pm 0.8\%$. With respect to the dimensions of the test unit, the deformations are amplified by factors ranging between 20 and 160 so that the magnitude of the plotted deformations is for all load steps approximately equal.

3. Test results for masonry spandrels

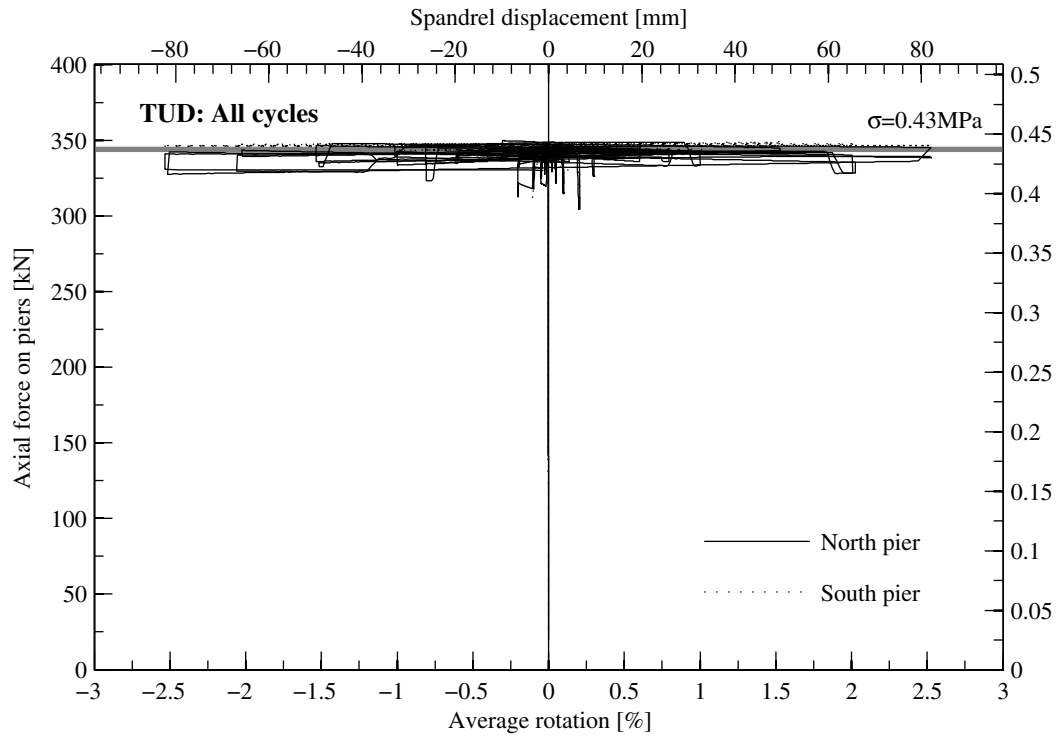


Figure 3.51: TUD: Axial force on piers - rotation relationship for all cycles.

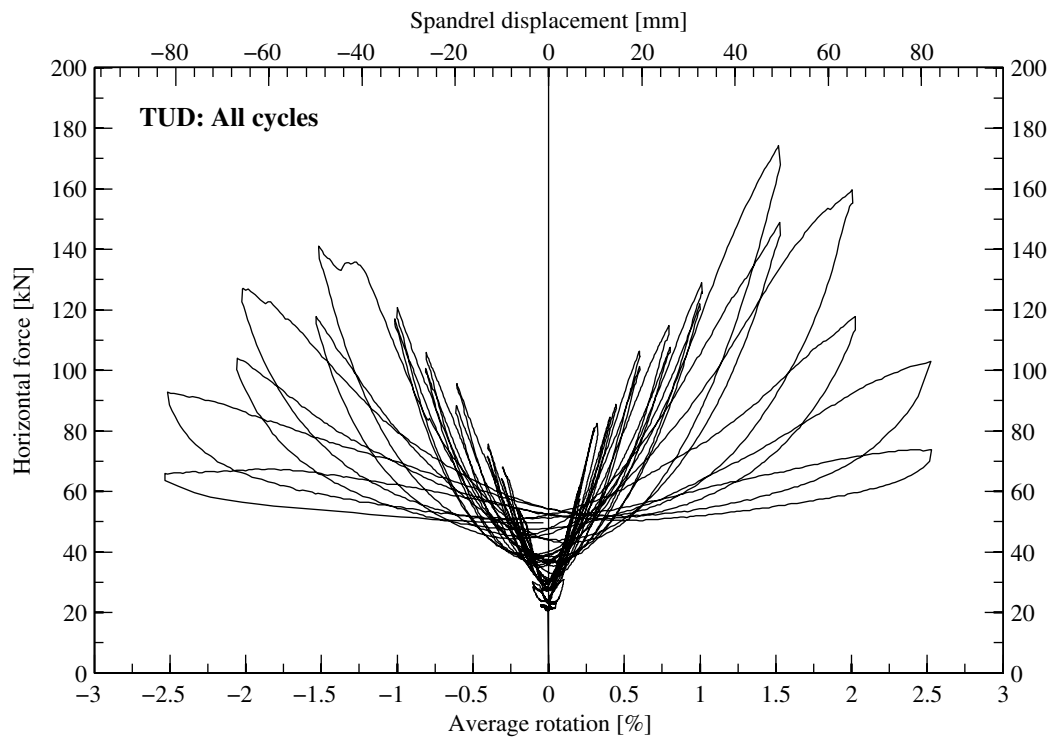


Figure 3.52: TUD: Horizontal force - rotation relationship.

Shown with thin lines is the undeformed state of the test unit at LS 0. Unlike for TUC, the deformed shape of the arch of TUD remained very similar during all cycles with amplitudes between $\theta_{nom} = \pm 0.1\%$ and $\pm 0.8\%$: Positive and negative plastic hinges developed for both directions of loading. Significant sliding movement between the bricks of the arch was not noticeable. The deformation mechanism of the masonry spandrel above the arch changed, however, during these cycles: For cycles with $\theta_{nom} = \pm 0.1\%$ and $\pm 0.2\%$ the deformation demand was mainly accommodated in flexural cracks at both ends of the spandrel while for larger rotation demands most of the deformation concentrated in large shear cracks.

3. Test results for masonry spandrels

